Heterostructured Thin Films of Coordination Polymers: Study on Growth and Electrical Conductance

विद्या वाचस्पति की

उपाधि की अपेक्षाओं की आंशिक पूर्ति में प्रस्तुत शोध प्रबंध

A thesis submitted in partial fulfillment of the requirements

for the Degree of Doctor of Philosophy

द्वारा / by

Pooja Sindhu/ पूजा सिंधु

पंजीकरण सं. / Registration No.: 20183595

शोध प्रबंध पर्यवेक्षक / Thesis Supervisor:

Prof. Nirmalya Ballav/ प्रो. निर्माल्य बल्लव

भारतीय विज्ञान शिक्षा एवं अनुसंधान संस्थान पुणे

INDIAN INSTITUTE OF SCIENCE EDUCATION AND RESEARCH, PUNE

2023

Dedicated to

My Family

and

True Friends

my eternal pillars of strength…

भारतीय विज्ञान शिक्षा एवं अनुसंधान संस्थान, पुणे
INDIAN INSTITUTE OF SCIENCE EDUCATION AND RESEARCH (IISER), PUNE
(An Autonomous Institution, Ministry of Human Resource Development, Govt. of India)

Date: 29-Nov-2023

Certificate

Certified that the work incorporated in the thesis entitled ***"Heterostructured Thin Films of Coordination Polymers: Study on Growth and Electrical Conductance"*** submitted by ***Ms. Pooja Sindhu*** was carried out by the candidate, under my supervision. The work presented here or any part of it has not been included in any other thesis submitted previously for the award of any degree or diploma from any other university or institution.

Prof. Nirmalya Ballav
(Research Supervisor)

nballav@iiserpune.ac.in Tel: +91 (020) 2590 8215 www.iiserpune.ac.in

भारतीय विज्ञान शिक्षा एवं अनुसंधान संस्थान, पुणे
INDIAN INSTITUTE OF SCIENCE EDUCATION AND RESEARCH (IISER), PUNE
(An Autonomous Institution, Ministry of Human Resource Development, Govt. of India)

Date: 29-Nov-2023

Declaration

I *Ms. Pooja Sindhu* declare that this written submission represents my ideas in my own words and where others' ideas have been included; I have adequately cited and referenced the original sources. I also declare that I have adhered to all principles of academic honesty and integrity and have not misrepresented or fabricated or falsified any idea/data/fact/source in my submission. I understand that violation of the above will be the cause for disciplinary action by the Institute and can also evoke penal action from the sources which have thus not been properly cited or from whom proper permission has not been taken when needed.

The work reported in this thesis is the original work done by me under the guidance of *Prof. Nirmalya Ballav.*

Ms. Pooja Sindhu

(ID: 20183595)

nballav@iiserpune.ac.in Tel: +91 (020) 2590 8215 www.iiserpune.ac.in

Acknowledgement

I would like to express my deepest gratitude to my supervisor, Prof. Nirmalya Ballav, for the incredible support, encouragement, and unwavering belief in me throughout the past five years. Under his guidance, I could surpass my own boundaries towards achieving excellence in my endeavours which has fostered my academic understanding. His keen attention to details, punctuality, positive outlook, and ability to see beyond the conventional have been truly inspiring, and I aspire to adopt these qualities.

I am grateful to my Research Advisory Committee (RAC) members, Prof. V. G. Anand (IISER Pune) and Dr. Kirandeep Singh (NCL, Pune) for their invaluable suggestions during the annual RAC meetings that helped improving my work. I would also like to thank my collaborators, Dr. Kartick Tarafder and his student K.S. Ananthram for the extensive theoretical calculations which helped me to get an in-depth understanding of my work. I would thank Dr. Anil Jain (BARC, Mumbai) for Rietveld refinement which provided enormous structural insights about the materials. I would like to express my gratitude to Prof. Shaibal Sarkar (IIT, Bombay) for giving me opportunity to visit his lab and get the experience in low-temperature conductivity measurement with his wonderful students (Sudeshna and Sushmita). I also would like to thank Dr. Pramod Pillai, Prof. Sujit K. Ghosh, Prof. R. Vaidhyanathan, Prof. Surjeet Singh, Dr. Shouvik Datta and Dr. Atikur Rahman for allowing to access their lab facilities.

I would like to thank the former and present Directors of IISER Pune for providing best infrastructural facilities to carry out my research. I extend my gratitude to the former and present Chair Chemistry and all the faculty members in the department.

I thank Mr. Yathish T. S., Mr. Sudhir Lone, Mr. Mahesh Jadhav, Mr. Anil Prathamshetti, Mr. Nilesh Dumbre, Mrs. Megha Paygude, Mr. Parveen Nasa, Mr. Nitin Dalvi, Mr. Ravindra Mahlot and Mr. Sandip Kanade for the technical support which helped me to carry out my research activities smoothly at IISER Pune. I am thankful to Dr. Umeshareddy Kacherki for library support and Mr. Sachin Behra (late), Mr. Naveen and Mr. Shailesh Patil for IT support. I would like to thank Mr. Mayuresh Kulkarni, Mr. Sanjay Meena, Mr. Ganesh Dimbar, Mr. Prabhakar Anagare, Mr. Tushar Kurulkar, Mr. Swapnil Bukhtar, Mr. Alok Mishra, Mr. Rajan Kumar Sahoo, Mrs. Deepali Dalvi and Ms. Sayalee Damle for administrative support.

I am grateful to have interacted with former as well the current lab members at Interfacial Materials Chemistry (IMC) (Dr. Barun Dhara, Dr. Ranguwar Rajendra, Dr. Plawan K. Jha, Dr.

Shammi Rana, Dr. Kriti Gupta, Dr. Debashree Roy, Vikash, Anupam, Dr. Syed, Ashwini, Pranay, Manish, Sujit, Jai, Gopi, Ishan, Aswani, Nahid, Umashis, Ajay, Sauvik, Rimpa, Kalyani, Aradhana and Aniruddha). It was a privilege to have worked and learnt a great deal from all the lab members at IMC. A special mention to Anupam Prasoon for mentoring me during the early stages of my PhD journey and engaging in countless scientific discussions that greatly enriched my knowledge and understanding. I would be forever eternally grateful for his support and encouragement which helped me to evolve as a strong and independent researcher. I thank Dr. Debashree Roy and Pranay Ninawe for adding special memories to my PhD journey.

I am indebted to all my teachers who have directly or indirectly influenced my PhD journey, especially, Dr. Prabhat Kumar, Dr. Sandipan Halder, Dr. Ashis K. Jena, Dr. Swagatika Sahu, Dr. A. K. Chaudhary (late), Dr. Ranjit, Dr. Arijit Kumar De, Sahendra Sir and Kuldeep Sir. A special note of thanks to my first ever chemistry teacher, Kuldeep Sir, for igniting a keen interest within me for the subject. I have learned that teaching is an art by attending wonderful lectures of Dr. Muhammed Musthafa and Dr. Angushuman Nag at IISER Pune.

I thank my friends, Abhishek, Keerti, Arnab, Tumpa, Habib, Sanchayita, Tejaswini, Kamesh, Pragya, Manisha, Ankit, Vijay, Sravan and Sumanta for making life interesting and memorable at the campus. Special mention to Abhishek (for always being a motivation), Arnab (for helping me in every situation), and Sumanta (for being available whenever I needed) for adding new chapters to my PhD journey. I am blessed to have a new family as Yogita di, Babita di and Govind bhaiya at the campus. I am grateful to have friends (Lalita, Vandana, Tapan, Amit, Prakash, Anuj, Manav, Bhanu, Swagata, Tannistha, Nidhi, Ankita, Tejaswini, Gulshan, Sarita, Mayank) who have remained an integral part of my life, despite of embarking on diverse paths.

This acknowledgment would be incomplete without the mention of my parents, brother (Deepak), sister-in-law (Sonica) and the little one (Sanaya), who have been my unwavering supporters and strongest cheerleaders. I thank them for shaping me for who I am today with their unconditional support and unmeasurable love and allowing me to flourish without ever limiting my potential.

Last but not the least, I thank my God for his invisible but powerful presence, mysterious wisdom and unconditional guidance in the darkest hours of my life.

Above all, I thank CSIR for the fellowship, DST, Infosys and SERB for financial support.

Pooja Sindhu

A. Publications Included in Thesis:

1. Emergent Interface in Heterostructured Thin Films of Cu(II) and Cu(I) Coordination Polymers

P. Sindhu, A. Prasoon, S. Rana, N. Ballav

J. Phys. Chem. Lett. ***2020****, 11, 6242−6248*

2. Thin Films of MOF-on-Guest@MOF: A Simple Strategy of Designing Electronic Heterostructures

P. Sindhu, N. Ballav

Inorg. Chem. ***2023,*** *62, 10887−10891*

3. Charge-Transfer Interface of Insulating Metal-Organic Frameworks with Metallic Conduction

P. Sindhu, K. S. Ananthram, A. Jain, K. Tarafder, N. Ballav

Nat. Commun. ***2022****, 13, 7665*

4. Insulator-to-Metal-like Transition in Thin Films of a Biological Metal-Organic Framework

P. Sindhu, K. S. Ananthram, A. Jain, K. Tarafder, N. Ballav

Nat. Commun. ***2023****, 14, 2857*

5. Bistable Interface: Reversible Switching of Rectifying to Non-Rectifying Current across Heterostructured Thin Films of MOFs

P. Sindhu, S. Saha, U. Bhoi, N. Ballav

Under Review ***2023***

B. Other Publications:

1. Perspective on the Interfacial Reduction Reaction

S. Rana, **P. Sindhu**, N. Ballav

Langmuir **2018**, *35*, 9647−9659

2. Direct Layer-by-Layer Growth of Crystalline Ag-TCNQ Thin Films on Functionalized Au Substrate: How Critical Is the pH of Ag(I)Solution?

A. Sathish Lathika, S. Rana, A. Prasoon, **P. Sindhu**, D. Roy, N. Ballav

J. Phys. Chem. Lett. **2020**, *11*, 10548−10551

CP	Coordination Polymer
MOF	Metal-Organic Framework
TMO	Transition Metal Oxide
LbL	Layer-by-Layer
MUDA	Mercaptoundecanoic Acid
SAM	Self-Assembled Monolayer
Cu	Copper
Pt	Platinum
Au	Gold
FTO	Fluorine-doped Tin Oxide
PET	Polyethylene terephthalate
EtOH	Ethanol
DMF	Dimethylformamide
TCNQ	7,7,8,8-Tetracyanoquinodimethane
BTC	Benzene-1,3,5-tricarboxylic Acid
BPyDC	2,2′-bipyridine-4,4′-dicarboxylic acid
Cys	Cysteine
IRR	Interfacial Reduction Reaction
I-V	Current-Voltage
EGaIn	Eutectic Gallium Indium
SMU	Source Measure Unit
Ω	Ohm
S	Siemens
RR	Rectification Ratio
HRS	High Resistance State
LRS	Low Resistance State
IMT	Insulator-to- Metal Transition
IMLT	Insulator-to-Metal-like Transition
A	Ampere (Current)
V	Voltage
R	Resistance

eV	Electron Volt
C	Capacitance
RT	Room Temperature
HT	High Temperature
DFT	Density Functional Theory
DOS	Density of States
PDOS	Partial Density of States
HOMO	Highest Occupied Molecular Orbital
LUMO	Lowest Unoccupied Molecular Orbital
CT	Charge Transfer
UV-vis	Ultraviolet-Visible Spectroscopy
FESEM	Field Emission Scanning Electron Microscopy
TEM	Transmission Electron Microscopy
HRTEM	High Resolution Transmission Electron Microscopy
SAED	Selected Area Electron Diffraction
FFT	Fast Fourier Transform
IFFT	Inverse Fast Fourier Transform
EDXS	Energy Dispersive X-Ray Spectroscopy
PXRD	Powder X-Ray Diffraction
GIXRD	Grazing Incidence X-Ray Diffraction
XPS	X-Ray Photoelectron Spectroscopy
EPR	Electron Paramagnetic Resonance
MQ	Millipore Water
mg	Milligram
mM	Millimolar
µm	Micrometre
^{o}C	Degree Celsius
K	Kelvin
min	Minutes
h	Hour

Introduction to Heterostructured Thin Films of Coordination Polymer

1.1 Introduction

A heterostructure consists of two or more different materials having distinct properties or structures. It can be classified into two categories based on their lattices: (i) lattice-matched heterostructure and (ii) lattice-mismatched heterostructure[1] (Figure 1.1). Heterostructures have gathered significant attention from researchers in last two decades due to the emergence of unique properties at the interface. The interfacial properties were observed to be strikingly different from their bulk counterparts and strongly depend on the nature of material, interlayer coupling and/or chemical interaction at the interface, morphological characteristics, and environmental conditions during fabrication. By carefully engineering the composition and arrangement of these interfaces, scientists have been able to unlock a wide range of fascinating phenomena and applications such as emergent magnetism, metallic conduction, high-mobility electron gas, and finally culminating to superconductivity.[2-8]

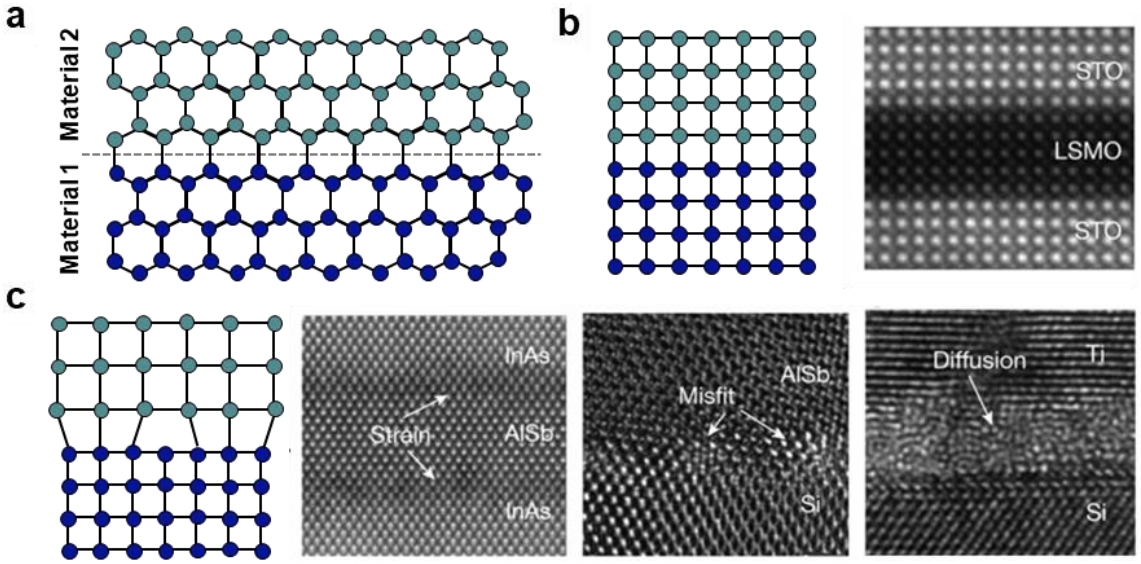

Figure 1.1. *(a) Schematic representation of heterostructure consists of different materials. (b) A lattice-matched heterostructure (STO/LSMO; STO, $SrTiO_3$; LSMO, $La_{0.7}Sr_{0.3}MnO_3$) grown using pulsed laser deposition with one-to-one bonding at the interface and (c) a schematic illustration of a lattice-mismatched heterostructure with the examples showing strain, misfit and diffusion at the interface (Adopted from Ref. 1 © Nature Publishing Group).*

"Interface is a device"- the famous phrase has coined by Nobel laureate Herbert Kroemer referring to the astonishing success of devices based on semiconductor thin films for photonic and electronic applications that started over a half-century ago. Later on, it was realized true for other class of materials such as transition metal oxides (TMOs) and organic molecules[9]. The interface between two

electrical insulating and non-magnetic transition metal oxides was observed to be metallic, magnetic as well as superconducting.[5, 7-8] An exemplary work by Hwang et al. is the oxide heterostructure of electrically insulating lanthanum aluminate ($LaAlO_3$) and strontium titanate ($SrTiO_3$) where the termination layer at the interface was controlled at the atomic scale and interaction at the interface was observed to play a crucial role for the emergence of unique interfacial phenomenon[5] (Figure 1.2a & b). The $(AlO_2)^-/(SrO)^0$ interface, a hole-doped interface, was found to be insulating, whereas the $(LaO)^+/(TiO_2)^0$ interface, an electron-doped interface, was realized to be metallic due to electron transfer from the top layer, $(LaO)^+$, into the vacant 3d Ti^{4+} states across the interface, with extremely high carrier density and high carrier mobility exceeding 10,000 $cm^2\ V^{-1}\ s^{-1}$ - the phenomenon known as electronic reconstruction (ER) or the generation of 2D-electron gas (2DEG) at the interface[5] (Figure 1.2a & b). The emergence of metallic interface was further observed in other oxide heterostructures such as $LaVO_3/SrTiO_3$, $LaAlO_3/SrTiO_3$ and $LaTiO_3/SrTiO_3$[10-12], and quasi-two-dimensional electron gas (q-2DEG) leading to metallic interface was confined mainly at the interface of $(LaO)^+/(TiO_2)^0$.

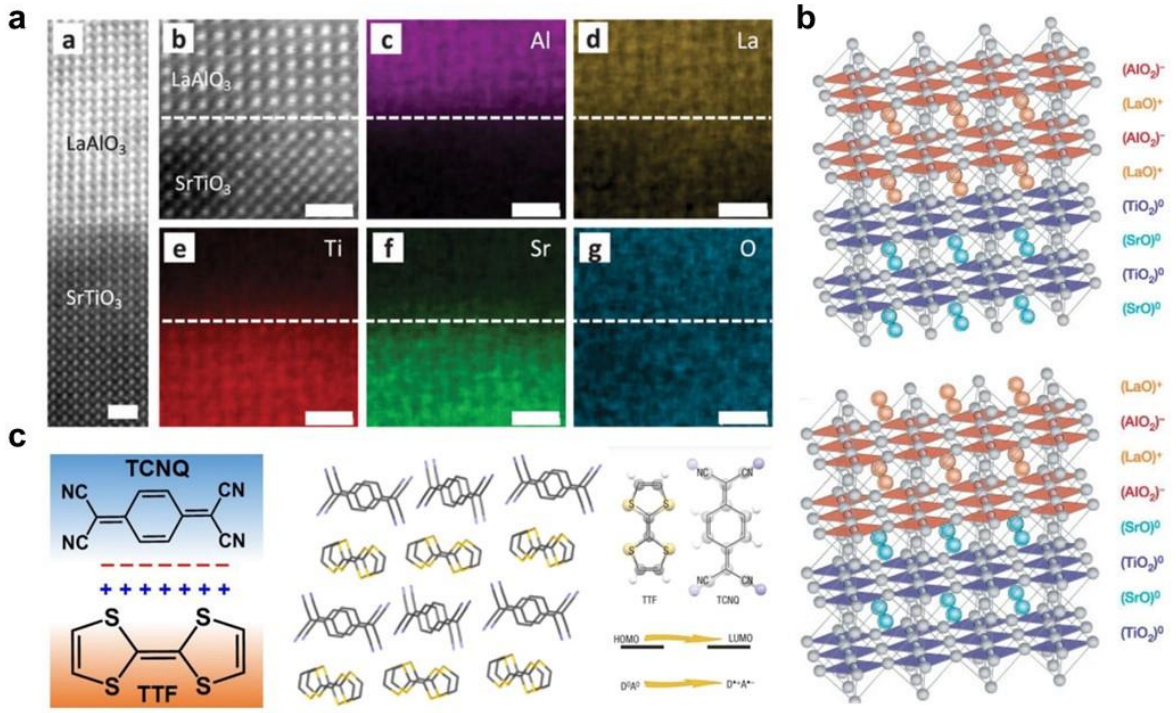

Figure 1.2. *(a) High resolution scanning transmission electron microscopy (STEM) image of $LaAlO_3/SrTiO_3$ interface along with high-magnification STEM image, showing the detailed microstructures close to the interface and atomically resolved chemical mapping of Al, La, Ti, Sr, and O respectively. Scale bars are 1 nm for all images (Adopted from Ref. 11 © Nature Publishing Group). (b) Schematic of the resulting $(LaO)^+/(TiO_2)^0$ interface and $(AlO_2)^-/(SrO)^0$ interface (bottom), showing the composition of each layer and the*

ionic charge state of each layer (Adopted from Ref. 5 © Nature Publishing Group). (c) Schematic of interface between two organic crystals (TCNQ and TTF) where metallic conduction was found due to the charge transfer (Adopted from Ref. 13 © Nature Publishing Group).

Similarly, the interface was observed to be metallic in electrically insulating organic crystals of TCNQ (7,7,8,8-tetracyanoquinodimethane) and TTF (tetrathiafulvalene) fabricated by lamination method. The metallic conduction at interface with a remarkably high carrier density 10^{14} cm^{-2}, arises mainly due to electron transfer from the highest occupied molecular orbital (HOMO) of TTF molecule to the lowest unoccupied molecular orbital (LUMO) of TCNQ molecule (Figure 1.2c).[13] Furthermore, the conducting interface was found in other organic heterostructures such as Rubrene-TCNQ, Rubrene-PDIF-CN_2 (PDIF-CN_2 = *N*;*N'*-bis(n-alkyl)-(1,7 and 1,6)-dicyanoperylene-3,4:9,10-bis(dicarboximide)) and TMTSF-TCNQ (TMTSF = tetramethyltetraselenafulvalene).[14-16] Therefore, integrating dissimilar materials with well-defined interfaces is essential for creating functional devices by design and has been a longer pursuit of the material science community. Exploring such intriguing design into a different yet fascinating class of materials, namely coordination polymers (CPs), including metal-organic frameworks (MOFs), holds great potential due to their tunable structures and wide range of properties.[17]

1.2 Coordination Polymers

A coordination compound with repeating coordination entities extending in 1-, 2-, or 3-dimensions, consisting of metal centers and organic linkers are known as coordination polymers.[18] A vast range of metal centers and organic linkers makes it a highly versatile class of material and provides an opportunity to render the desired properties such as structure, internal porosity, stiffness, surface functionalities and chemical interaction with guest molecules.[19] Along with the structural tunability, it has various other properties such as high crystallinity, thermal stability, water stability, porosity and high surface area which offer tremendous diversity in applications such as gas storage, gas sensing and separation, catalysis, drug delivery, water purification and storage, energy storage and many more.[19] Therefore, CPs have emerged as potential candidates in material science for various applications such as gas adsorption and separation, sensing and catalysis. However, they have received less attention in the field of electronics, optoelectronics and other energy storage/conversion devices. They have great advantages to be considered as active materials in such fields. First, they have highly ordered structure determined by the coordination geometry of the metal and the topology of the linkers which provides the high chemical and thermal stability.[20] Second, they have highly defined pores which eliminate the

disorder, considered to be a major factor for poor mobility and low carrier concentration.[20] Third, they have high structural tunability due the synthetic flexibility which can eventually tune their intrinsic properties such as electrical, optical and mechanical.[20] Although, CPs are often found to be electrically insulating in nature likewise TMOs due to the poor overlap of metal d-orbitals with s/p-orbitals of organic linker.[21] In the last decade, novel design strategies have been implemented to confer reasonable electrical conductivity in CPs including MOFs such as selection of redox-active linkers, hybridization of CPs with other conductive media, composite formation with conducting polymers, incorporation of redox-active guest molecules and many more.[22-33] The electrical transport in CPs has been understood as follows: (i) through-bond, (ii) through-space, (iii) extended conjugation, (iv) redox-hopping, and (v) guest-promoted transport − nicely summarized by Dincă et al. (Figure 1.3).[27, 34]

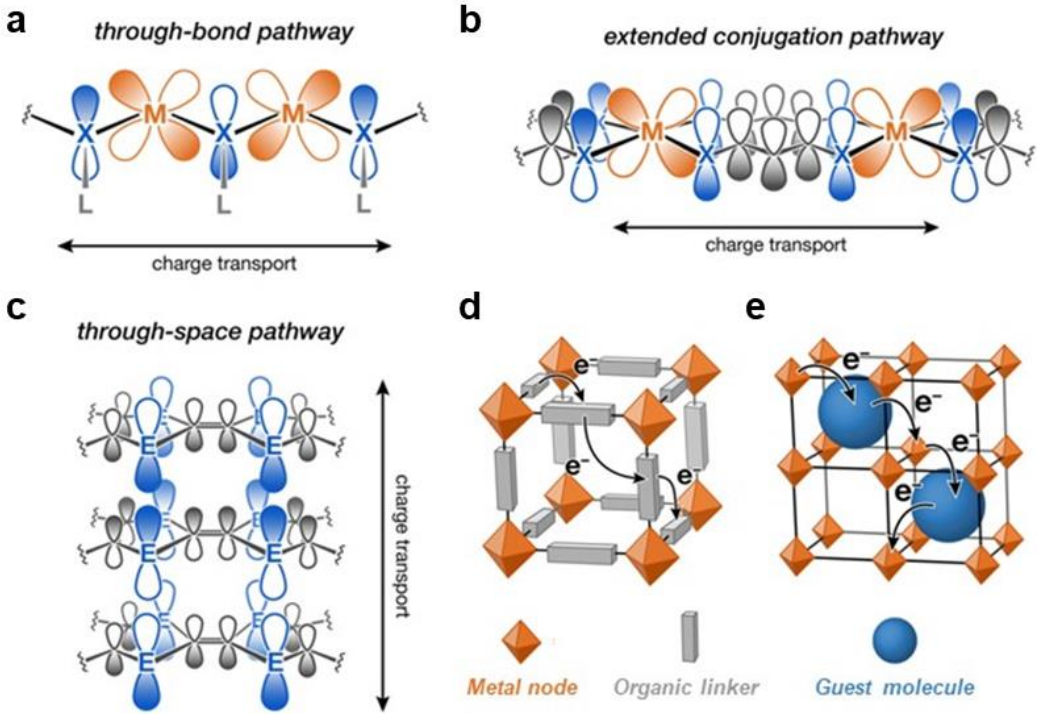

Figure 1.3. *(a) Different pathways for the charge transfer in CPs including MOFs such as (a) through-bond (b) through-space (c) extended conjugation, (d) redox hopping and (e) guest-promoted (Adopted from Ref. 34 © American Chemical Society).*

In the through-bond pathway, charge transport was realized through the continuous networks of coordination bonds between the metal and ligand functional groups (Figure 1.3a). Here, CPs/MOFs with good-orbital overlap between metal and ligand with well-matched energy levels can result in small band gaps and high charge mobilities, eventually leading to high electrical conductivity.[34] Most

commonly in this category, metal with the electropositive linkers containing thiol (sulphur), hydroxy (oxygen) and amine (nitrogen) functionalities results in improved orbital overlap and energy matching.[34] In the through-space pathway, the π-π interaction between organic linkers results in sufficient orbital overlap, finally leading to enhanced electrical conductivity (Figure 1.3b)[34], whereas in the extended conjugation pathway, ligands containing chelating functional groups conjugated with the organic core and linked with the transition metals was realized to be the factor to enhance electrical conductivity (Figure 1.3c).[34] Here, 2D CP/MOF structures have extended π−d conjugation within the planes with the sp^2-hybridization similar to the graphene structure, therefore proposed as metal-organic analogs of graphene. In the redox hopping pathway, charge carriers are localized between discrete or non-bonded sites and hop between neighboring sites (Figure 1.3d). Redox hopping can be realized in various ways such as metal-based hopping, linker-based hopping, and mixed metal- and linker-based hopping.[34] In guest-promoted pathway, the charge transport can be improved by introducing guest molecules in the framework such as iodine/polyiodides, organic/organometallic molecules (Ferrocene, TCNQ and related molecules), conductive polymers/oxides (polypyrrole, polyaniline and perovskite quantum dots) and nanoparticles (Ag, Au) (Figure 1.3e).[34] Therefore, guest molecules act as a bridge between metal secondary building units (SBUs) and the charge transport carried out by through-bond pathways.[27, 34] Moreover, selection of metal or organic linker and the spatial arrangement of metal and ligand in CPs/MOFs play a vital role in their electronic properties.[35-38] Electrical conductivity of MOFs was found to be affected upon changing the metals in M_2(DOBDC)$(DMF)_2$ (M = Mg^{2+}, Mn^{2+}, Fe^{2+}, Co^{2+}, Ni^{2+}, Cu^{2+}, Zn^{2+}), M_2(DSBDC)$(DMF)_2$ (M = Mn^{2+}, Fe^{2+}) and M_2Cl_2(BTDD)$(DMF)_2$ (M = Mn^{2+}, Fe^{2+}, Co^{2+}, Ni^{2+}) and M(1,2,3-triazolate)$_2$ (M = Mg^{2+}, Mn^{2+}, Fe^{2+}, Co^{2+}, Cu^{2+}, Zn^{2+}, Cd^{2+}) where H_4DOBDC = 2,5-dihydroxybenzene-1,4-dicarboxylic acid; DMF = *N*,*N*-dimethylformamide); H_4DSBDC = 2,5-disulfhydrylbenzene-1,4-dicarboxylic acid); H_2BTDD = bis(1*H*-1,2,3-triazolo[4,5-b],[4′,5′-*i*]dibenzo[1,4]dioxin).[35] Lower band gap values were observed for MOFs with Fe^{2+}, Cu^{2+} as compared to other metals (Figure 1.4). In M_2(DOBDC)$(DMF)_2$, the closed-shell ions such as Mg^{2+} and Zn^{2+}, have little contribution in VB (valence band) and CB (conduction band), whereas, open-shell ions such as Mn^{2+}, Fe^{2+}, Ni^{2+}, and Cu^{2+} have significant contribution towards VB and CB. Metals ions with more electronegative nature such as Cu^{2+}, have a greater contribution towards CB, therefore lower the E_{CBM} (CBM; conduction band minimum), whereas more electropositive metals contribute more towards VB and raise the E_{VBM} (VBM; valence band maximum) (Figure 1.4).[35] Therefore, metal ions can greatly affect the electrical conductivity by changing the band gap in MOFs.[35]

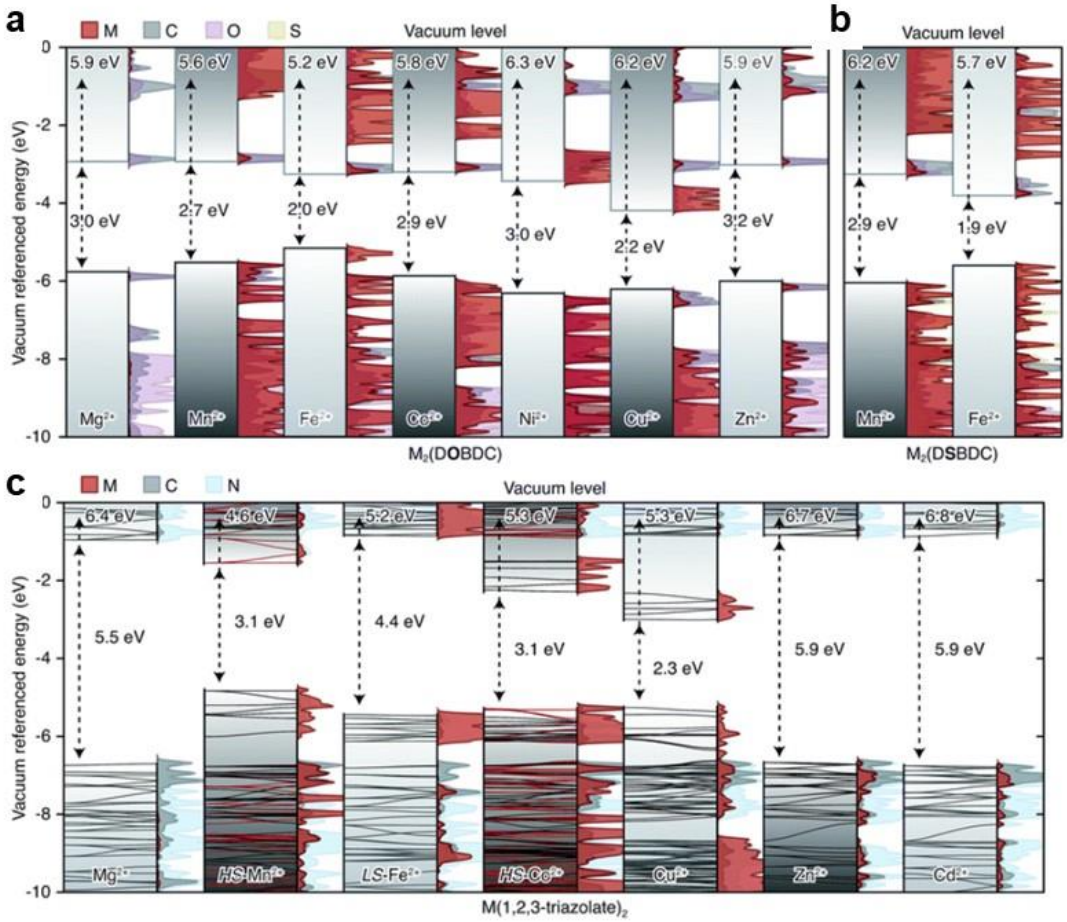

Figure 1.4. *Calculated energy bands and projected density of states (PDOS) of (a) M_2(DOBDC), (b) M_2(DSBDC), and (c) M(1,2,3-triazolate)$_2$ are presented with the E_{VBM} (top) and band gap values and the electron energies are referenced to the vacuum level. (Adopted from Ref. 35 © The Royal Society of Chemistry).*

Additionally, ligands also can influence the electrical conductivity to great extent. $Ni_3(HITP)_2$ (HITP = 2,3,6,7,10,11-hexaiminotriphenylene) has a semiconducting nature with bulk electrical conductivity (~ 40 S/cm); and replacing HITP with the smaller HIB (hexaiminobenzene) ligand leading to metallic nature with bulk electrical conductivity (~ 8 x 10^4 S/cm) which was surmised due to the reduction of distance between neighboring metals/ligands and therefore, provides a better overlap between their electronic wave functions (Figure 1.5).[37-38] Spatial arrangement of metal and ligand has been observed to be the factor influencing electrical conductivity in CPs such as Cu-TCNQ.[36] It exists in two phases: Cu-TCNQ (Phase-I) and Cu-TCNQ (Phase-II) and the electrical conductivity value of Cu-TCNQ (Phase-I) (~ 0.25 S cm^{-1}) was observed to be higher than Cu-TCNQ (Phase-II) (~ 1.3 × 10^{-5} S cm^{-1}). The main reason for different electrical conductivity in Cu-TCNQ (Phase-I) and (Phase-II) is due to the completely different spatial arrangements of TCNQ ligands in the two structures (Figure 1.6).[36]

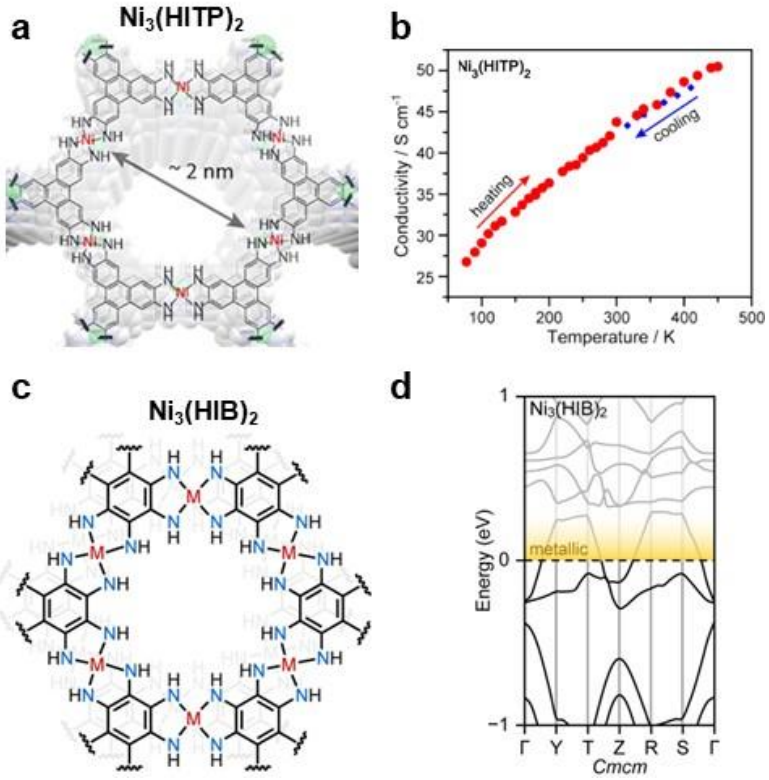

Figure 1.5. *(a) Chemical structure and (b) Variable-temperature van der Pauw conductivity measurement of $Ni_3(HITP)_2$ thick film on quartz (Adopted from Ref. 38 © American Chemical Society). (c) Chemical structure and (d) calculated electronic band structure of bulk $Ni_3(HIB)_2$ (Adopted from Ref. 37 © American Chemical Society).*

In Cu-TCNQ (Phase-I), Cu atoms are coordinated with four nitrogen atoms of four different TCNQ molecules in a highly distorted tetrahedral environment with N−Cu−N angles of 92° and 142°. Neighboring TCNQ ligands are rotated by 90° with respect to each other and the quinoid rings of TCNQ are arranged in a columnar stack with interplanar distance of 3.24 Å, which is even smaller than the van der Waals distance of 3.4 Å in graphite.[36]

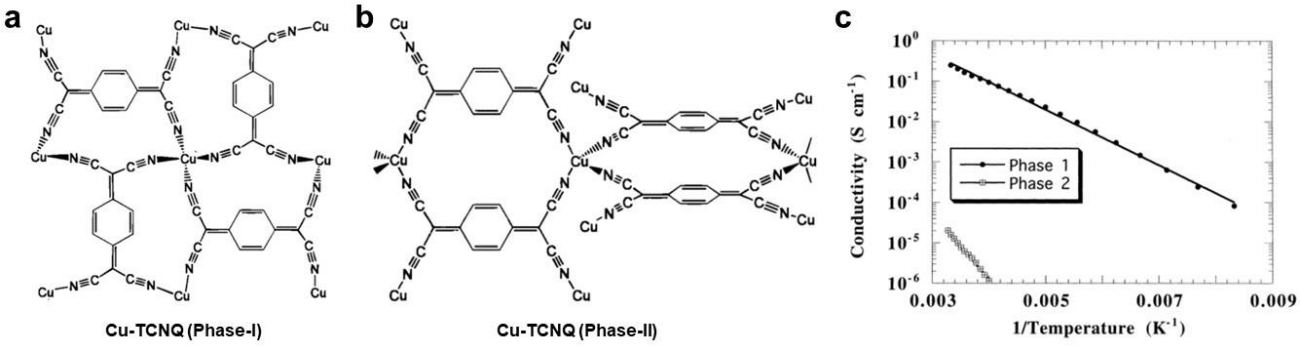

Figure 1.6. *Chemical structure of Cu-TCNQ CP in (a) phase-I, (b) phase-II and (c) Conductivity versus temperature of bulk Cu-TCNQ Phase-I and phase-II on pressed pellets (Adopted from Ref. 36 © American Chemical Society).*

In Cu-TCNQ (Phase-II), Cu atoms are more likely arranged in a tetrahedral geometry with N−Cu−N angles of 103° and 114.7°. Neighboring TCNQ ligands are parallel to each other and the shortest face-to-face distance between nearest TCNQ neighbors is 6.8 Å.[36]

Following the aforementioned advancements, additional development is required for CPs to emerge as a potential material for electronic and optoelectronic applications. Designing a heterostructure of CPs to study the electrical transport properties at the interface can provide a new dimension in the field, likewise oxide heterostructures. In order to investigate electron transport properties across heterostructures of CPs, a thin film configuration has been realized to be an ideal one.

1.3 Brief Overview on Thin Films

Thin film refers to a well-ordered and densely packed layer of material (organic/inorganic) deposited on a substrate. Thin films have a thickness ranging from 5 nm to a few microns, whereas below 5 nm are considered ultra-thin films. In literature, thin films are known to exhibit distinctive surface properties that deviate from their bulk counterparts due to their increased surface area-to-volume ratio, dimensional constraints, chemical interaction, microstructure, and geometry.[39] The increased surface area allows for enhanced interactions with the surrounding environment, making thin films susceptible to surface effects, and interfacial phenomena. Additionally, quantum confinement effects, atomic arrangement and interfacial interactions can alter crystal structure, defect formation, electronic band structures, and energy levels, eventually affecting the electronic and opto-electronic properties.[40]

The properties of thin films, including electrical, optical, magnetic, and mechanical, can be precisely controlled and tailored by adjusting the composition, thickness, orientation and microstructure.[39-40] Such tunability allows for designing and optimizing thin films for specific applications, making them ideal for device applications. Thin films are utilized for various applications such as integrated circuits, transistors, microelectronics, optical coatings, sensors, data storage, solar cells, batteries, and fuel cells.[39-40] Thin films have revolutionized various industries by enabling the development of advanced technologies and devices. Overall, the broad range of thin film applications demonstrates their versatility, enabling advancements in electronics, optics, energy, sensing, coatings, storage, and micro/nanotechnology.[39-41]

The fabrication of high-quality thin film is a prerequisite for various technological applications, including electronic and opto-electronic devices. There are several conventional techniques available for the depositing thin films; however, considerable attention has been given to exploring alternative methods that are cost-effective, more reliable, and capable of yielding high-quality films. Additionally, the choice of deposition method depends on factors such as the desired film properties, substrate material, film thickness, and specific application.

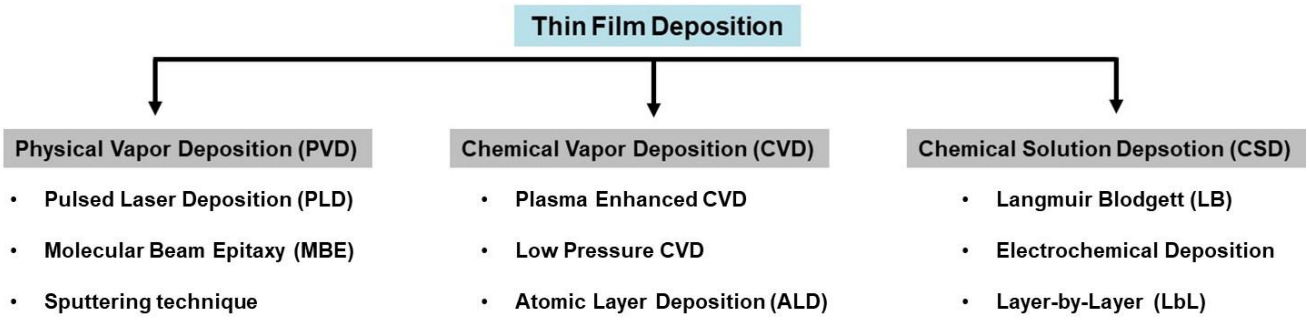

Figure 1.7. *Classification of thin film deposition techniques.*

Thin film deposition techniques[42] are broadly classified into three categories as follows:

1. Physical Vapor Deposition (PVD): In this technique, the desired material is vaporized into atomic or molecular species by physical means (ion bombardment, laser ablation, or evaporation). Vaporized species undergo condensation on a substrate to deposit thin film, whereby no chemical reaction occurs (Figure 1.7).[42]

2. Chemical Vapor Deposition (CVD): It involves plasma/reduced pressure to break down precursor gases into reactive species, which undergo chemical reactions to deposit a thin film on a substrate (Figure 1.7).[42]

3. Chemical Solution Deposition (CSD): Precursor solution is deposited on the substrate by various methods like spin coating, spray coating, dip coating, liquid-phase epitaxy (layer-by-layer), electrodeposition, and so on (Figure 1.7).[39, 42]

Having precise control over various parameters is crucial to achieving the desired properties; the layer-by-layer (LbL) method is perhaps the most robust because of its simplicity as well as growth via liquid phase epitaxy, leading to fabrication of highly crystalline, orientated, monolithic thin films of CPs at ambient conditions.[43-44] This method includes functionalizing the substrate by an appropriate self-

assembled monolayer (SAM) followed by LbL growth cycles to fabricate a well-oriented and highly crystalline thin film of CPs.

1.4 Functionalization of Substrate by Self-assembled Monolayers

Self-assembled monolayer refers to a single layer of organic molecules assembled/organized spontaneously on a surface in a highly-ordered and well-defined manner by means of physical or chemical adsorption from the solution and gas phase (Figure 1.8a).[45] This phenomenon is driven by intermolecular forces such as van der Waals, hydrogen bonding, and electrostatic interactions. The organic molecules or ligands forming SAMs consists of a "head group" and a "tail/terminal group" separated by a long alkyl chain (spacer) (Figure 1.8b).[45-46] Headgroups have a distinct affinity towards substrates; therefore, a wide range of headgroups available that can selectively bind to specific metals, metal oxides, and semiconductors. SAM has a typical thickness of 1-3 nm and can be used to functionalize a variety of substrates like Au, Ag, Cu, Pt, Si, Pd, Cr, Ni, Ti, and many more.[45] SAMs are well-studied for investigation in the field of nanoscience and technology due to their (i) easy preparation at ambient conditions without the need for ultrahigh vacuum (UHV) or any other sophisticated instrument/technique; and (ii) they can functionalize all sizes of objects including thin films, nanowires, and other nanostructures. (iii) Orientation and structure of SAM are dependent on the spacer chain length in the absorbate molecule. (iv) Surface properties and functionalities can be modulated by changing the chemical functionality at the tail group, such as -COOH, -OH, $-NH_2$, -SH, $-CH_3$, and so on. (v) SAM can link the external environment to the optical and electronic properties of the substrate[47] and (vi) can bridge the molecular-level structure to macroscopic interfacial phenomena, which is critical for various applications.[45]

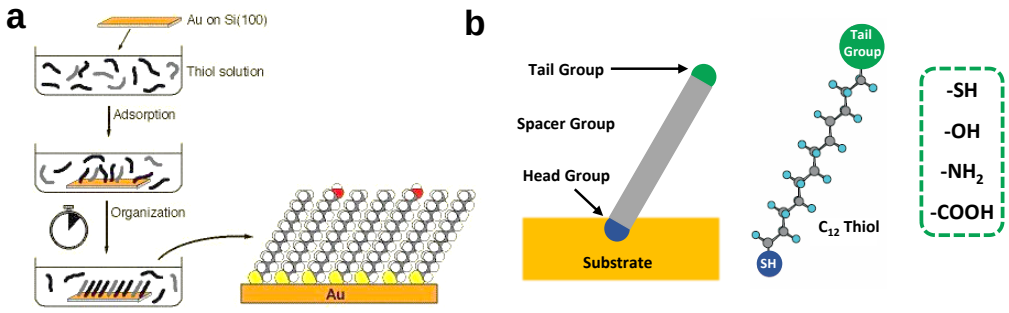

Figure 1.8. *Schematic illustration of (a) SAM formation involving adsorption process followed by self-organization (https://i.stack.imgur.com/hW8ea.jpg). (b) SAM consists of a head group, a terminal sulphur group and a long alkyl chain (spacer group) on the Au substrate with different functionalities at head groups.*

Alkanethiols are the most widely studied class of SAMs on various substrates such as gold, silver, copper, palladium, platinum, and mercury due to the high affinity of thiols towards the noble and coinage metals. Mainly, Mercaptoundecanoic acid (MUDA), Mercaptoundecanol (MUD), Benzene-1,4-dithiol (BDT), Dodecanethiol (DDT), and Biphenyl-4,4′-dithiol (BPDT) thiol molecules are used to functionalize Au substrate due to the strong Au-S interaction.[45] Furthermore, the nanoscale patterning of organic thiol molecule on a surface can be achieved by electron-beam lithography (EBL), micro-contact printing (μCP), photo-lithography, and inkjet printing.[45, 48] Therefore, SAMs are crucial for studying the interfacial phenomena and are used as essential interlayers and electronically active layers in organic electronic devices, such as organic photovoltaics, non-volatile memories, and organic thin film transistors.

Some substrates need other techniques for functionalization such as oxygen plasma treatment and chemical treatments (Piranha treatment). Such treatments are mainly used for SiO_2 coated Si substrate, fluorine-doped tin oxide-coated glass (FTO), indium-doped tin oxide-coated glass (ITO) and glass substrate to increase the oxygen functionalities at the surface. These substrates are vital for the electronic and opto-electronic applications, such as field-effect transistor (FET), solar cell, photodetector, photodiode and so on.

1.5 Thin Films of Coordination Polymers by LbL Approach

Layer-by-layer deposition technique involves the sequential deposition of alternating layers of two or more materials (metal connector and organic linker) onto a functionalized substrate in a layer-by-layer manner (Figure 1.9).[49-50] It includes various methods like dipping, spraying, pumping, spin coating, and the quartz crystal microbalance (QCM) system-based method.[44, 49]

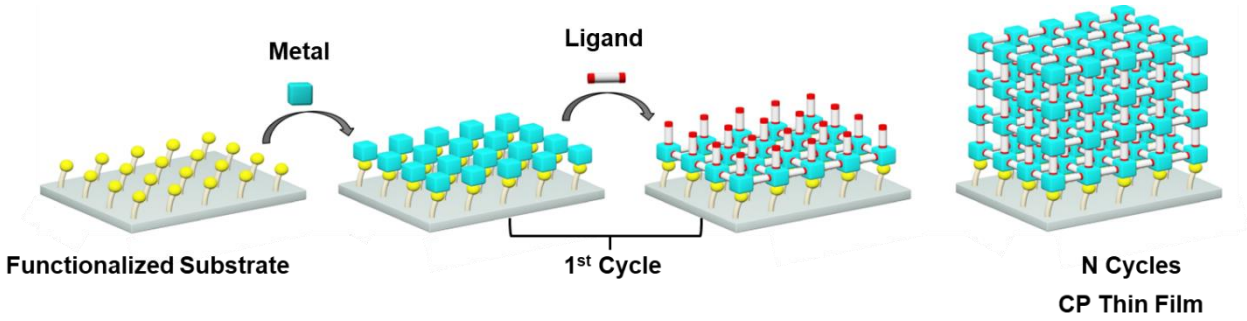

Figure 1.9. *Schematic representation of LbL method showing the sequential deposition of metal connectors and organic linkers in each cycle (Adopted from Ref. 50 © Nature Publishing Group).*

The dipping method is the most widely utilized for LbL assembly to grow oriented films of CPs due to its simplicity and robustness. LbL technique enables the growth of highly crystalline and orientated coordination thin films. It effectively prevents the interpenetration of the coordination network within the thin film structure and provides precise control over important parameters, including dipping time, reaction temperature, and concentration of precursor solutions which directly influence the thickness of the thin film and facilitates the exploration of desired properties.[49, 51] In the LbL approach, a functionalized substrate is sequentially dipped into the solution of desired materials (typically metal and ligand precursor) with the involvement of washing steps in between to remove unbound or unreacted molecules from the substrate followed by drying step (Figure 1.10).

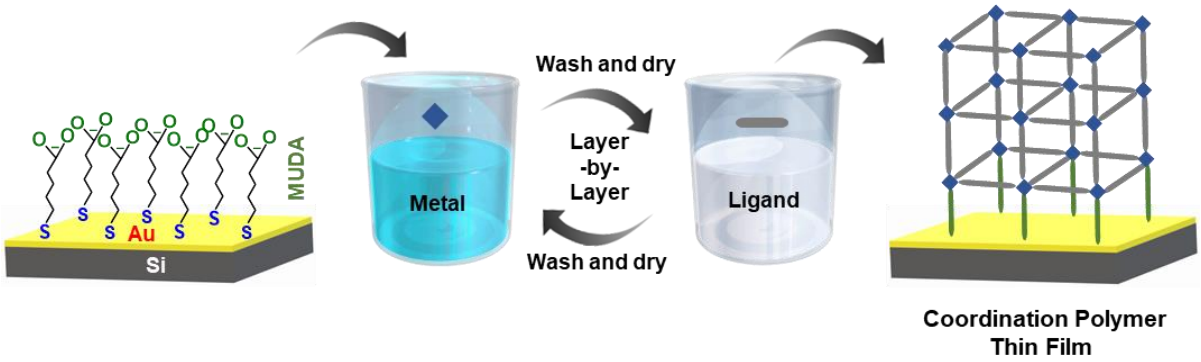

Figure 1.10. *Schematic diagram of LbL growth for the fabrication of coordination polymer thin film on functionalized Au substrate.*

In the last few decades, LbL has significantly gathered the attention of researchers and extensively explored to grow thin films of CPs on top of conducting as well as non-conducting substrates. Ligands with carboxylate or pyridine functionalities and copper or zinc metals are majorly studied to grow thin films of CPs through LbL approach.[51] Only recently, different metals other than Cu or Zn such as Ag, Fe, Zr and other functionalities like -NH_2, -SH, -CN are being explored. The functional groups of ligands play a crucial role in shaping the coordination environment, geometry, and oxidation state of the metal, thereby influencing the physical properties of CPs. The widely observed copper paddlewheel-shaped [$Cu_2(-COO)_4$] secondary building unit (SBU) is a result of the favorable reaction with carboxylate functionalities. Notably, the presence of coordinated guest molecules, primarily solvents, within the Cu_2 paddlewheel SBUs can be removed after activation, creating open metal sites (OMS) of Cu(II) ions.[52] These OMS serve diverse purposes, including gas storage, separation, catalysis, and electrical conductivity. A notable example is HKUST-1, known for its paddlewheel topology, where the ligand connects to the metal node via carboxylate linkers. Incorporating the redox-

active molecule, tetracyanoquinodimethane (TCNQ), into the pores of HKUST-1 induces conductivity through the facilitation of effective charge pathways at the metal nodes.[22] Copper ions within CPs can adopt various oxidation states, with Cu(II) and Cu(I) being the most common. Cu(II) ions are the predominant choice for constructing CPs due to their stability and ability to form strong coordination bonds with organic ligands. Cu(I) ions are less common but can also be used to create interesting materials with distinct properties, for example, Cu-TCNQ. Common ligands include carboxylates (e.g., terephthalate, benzenedicarboxylate), nitrogen-containing ligands (e.g., pyrazine, bipyridyl), Cyano (tetracyanoquinodimethane), hydroxyl (hexahydroxytriphenylene) and other organic linkers. Functionalized Au substrate, SiO_2 coated silicon substrate, fluorine-doped tin oxide-coated glass substrate (FTO) and indium tin oxide-coated glass substrate (ITO) are commonly used as substrates in the LbL technique.[44, 53]

1.6 Heterostructured Thin Films of Coordination Polymers by LbL Approach

Apart from aforementioned advantages, LbL method allows us to modulate metal ions or organic linkers during the growth of thin film, which is imperative for the growth of heterostructure and makes this method ideal for studying the growth of heterostructured thin films of CPs also referred as liquid-phase heteroepitaxy (Figure 1.11 and 1.12).[54] The heterostructured thin films of CPs can be grown by adopting various design strategies: (i) changing metal node,[55-59] (ii) changing organic linker,[59-67] (iii) changing both metal node and organic linker,[56] (iv) introducing post-synthetic modification including incorporation of guest molecules.[68-70] We have summarized salient features of various heterostructured thin films of CPs fabricated by the LbL method (Table 1.1).

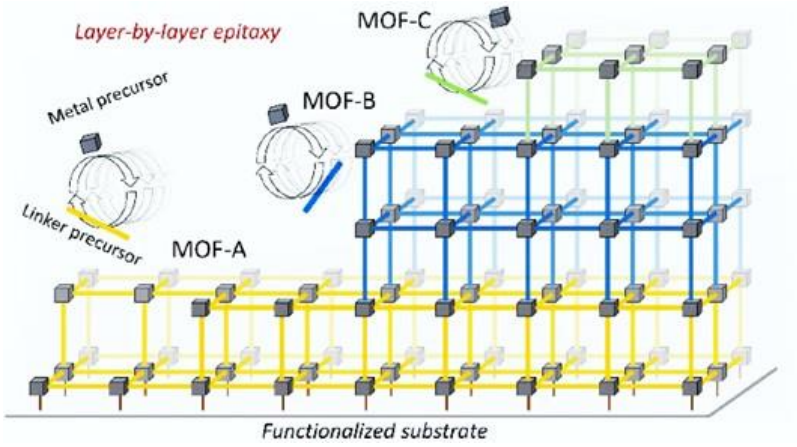

Figure 1.11. *LbL epitaxy to fabricate heterostructured thin films of CPs/MOFs on a functionalized substrate (Adopted from Ref. 54 © Springer Publication Group).*

In literature, the study of heterostructured thin films of CPs predominantly involves copper (Cu) or zinc (Zn) metals and ligands with carboxylate or pyridine functionalities (Table 1.1). It is interesting to note that despite the presence of different metal ions, specifically copper (Cu) and zinc (Zn), metals maintain same oxidation states. Consequently, the fabrication of heterostructured thin films composed of coordination polymers (CPs) with different oxidation states of metal ions such as Cu(II) and Cu(I) represents a novel avenue for further exploration, thereby introducing a new design strategy for the generation of heterostructured thin films.

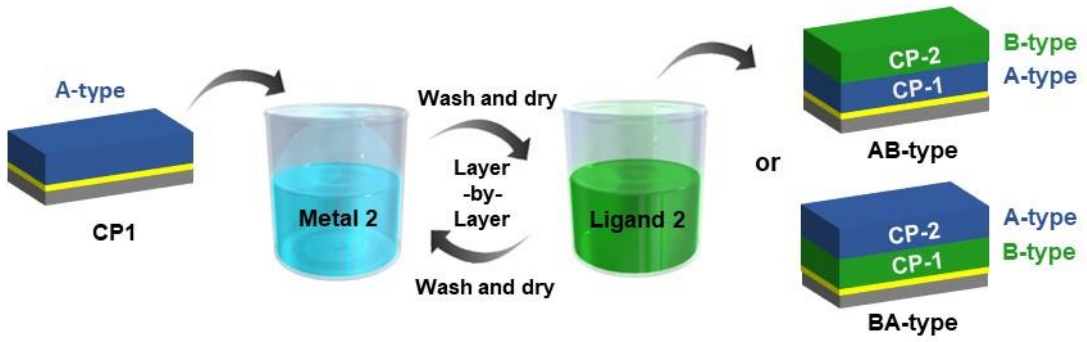

Figure 1.12. *Schematic diagram of LbL growth for the fabrication of AB- or BA-type heterostructured thin films of CPs on functionalized Au substrate by changing the sequence of layer deposition.*

Combining CPs with distinct lattice constants presents a significant challenge as per the norms of conventional heteroepitaxy. Typically, the lattice constant of the material grown must closely align with that of the underlying substrate within 2%.[71] Deviations in lattice constants may strain the deposited layer, leading to growth termination. In literature, a heterostructured thin film with the 20% lattice constant mismatch was realized by LbL method.[62] Interestingly, subsequent studies demonstrated the fabrication of a complete lattice mis-matched heterostructured thin film of CPs through the LbL method.

Sr. No	Metal ion	Ligand	Coordination Motif	Design Strategy	Remark
1.	Cu(II) and Zn(II)	NDC and DABCO	-COO---Cu -COO---Zn	Changing metal nodes	TF fabrication by LbL[55]
2.	Cu(II) and Zn(II)	NDC, DABCO BME-BDC and F_4BDC	-COO---Cu -COO---Zn	Changing metal nodes; and changing both metal nodes and organic linkers	TF fabrication by LbL and study of growth orientation[56]

3.	Cu(II)	BDC, NH_2-BDC and DABCO	-COO---Cu	Introducing post-synthetic modification	TF fabrication by LbL followed by PSM (tBITC) and selective gas adsorption[70]
4.	Cu(II)	NDC, NH_2-BDC and DABCO	-COO---Cu	Introducing post-synthetic modification	TF fabrication by LbL followed by PSM (succinic acid anhydride) and selective gas adsorption[69]
5.	Cu(II)	BDC, NH_2-BDC, NDC and DABCO	-COO---Cu	Introducing post-synthetic modification	TF fabrication by LbL followed by chemo-selective and location specific PSM (FPI) and gas adsorption study[68]
6.	Cu(II)	BTC, NDC and DABCO	-COO---Cu	Changing organic linkers	TF fabrication by LbL and gas adsorption study[61]
7.	Cu(II)	BPDC, BiPy and AB-BPDC	-COO---Cu	Changing organic linkers	TF fabrication by LbL and optically triggered guest adsorption[60]
8.	Zn(II)	H_2mipcapz and H_2dmcapz	-COO---Zn	Changing organic linkers	TF fabrication by LbL and selective membrane application[63]
9.	Cu(II)	BDC, NDC and BPDC	-COO---Cu	Changing organic linkers	TF fabrication by LbL and size selective loading of nano-particles[62]
10.	Zn(II)	MI, DM, DE and ME	-COO---Zn	Changing organic linkers	TF fabrication by LbL and adsorption selectivity[64]
11.	Zn(II)	Pd-DCP and ADB	-COO---Zn	Changing organic linkers	TF fabrication by LbL and optoelectronic properties[65]
12.	Cu(II)	BTC and H_8L2	-COO---Cu	Changing organic linkers	TF fabrication by LbL and importance of epitaxial orientation[66]
13.	Cu(II)	BTC, NDC and DABCO	-COO---Cu	Changing organic linkers	TF fabrication by LbL by functionalizing hetero-junction and

					new approach for fabrication of lattice mismatched heterostructures[67]
14.	Co(II) and Zn(II)	Hmim	-N---Co -N---Zn	Changing metal nodes	TF fabrication by LbL and selective gas membrane[57]
15.	Cu(II), Co(II) and Zn(II)	BDC, BPDC, BPYDC	-COO---Cu -COO---Co -COO---Zn	Changing metal nodes	TF fabrication by LbL on $Cu(OH)_2$ and Ag-NPs within aligned pores[59]
16.	Eu(III) and Tb(III)	BTC	-COO---Eu -COO---Tb	Changing metal nodes	TF fabrication by LbL and its photoluminescence properties[58]

Table 1.1. *Salient features of heterostructured thin films of CPs fabricated by LbL approach where* ***TF*** *= thin film,* ***NDC*** *= 1,4-naphthalenedicarboxylate;* ***DABCO*** *= 1,4-diazabicyclo(2.2.2)octane;* ***BME-BDC*** *= 2,5-bis(2-methoxyethoxy)benzene dicarboxylate;* ***F_4BDC*** *= tetrafluorobenzenedicarboxylate;* ***BDC*** *= 1,4-benzenedicarboxylate;* ***PSM*** *= Post-synthetic modification;* ***tBITC*** *= tert-butyl isothiocyanate;* ***NH_2-BDC*** *= 2-amino-1,4-benzenedicarboxylate;* ***FPI*** *= 4-fluorophenyl isothiocyanate;* ***BTC*** *= benzene tricarboxylic acid;* ***BPDC*** *= biphenyl-4,4'-dicarboxylic acid,* ***BiPy*** *= 4,4'-bipyridine;* ***AB-BPDC*** *= 2-azobenzene 4,4'-biphenyldicarboxylic acid;* ***H_2mipcapz*** *= 3-methyl-5-isopropyl-4-carboxypyrazole;* ***H_2dmcapz*** *= 3,5-dimethyl-4-carboxypyrazole;* ***MI*** *= 3-methyl-5-isopropyl-4carboxypyrazolate;* ***DM*** *= 3,5-dimethyl-4-carboxypyrazolate;* ***DE*** *= 3,5-diethyl-4-carboxypyrazolate;* ***ME*** *= 3-methyl-5-ethyl-4-carboxypyrazolate;* ***Pd-DCP*** *= Pd(II) 5,15-diphenyl-10,20-di(4-carboxyphenyl) porphyrin;* ***ADB*** *= 4,4'-(anthracene-9,10-diyl)dibenzoate;* ***H_8L2*** *= 1,2,4,5-tetrakis [4 - (3',5'-dicarboxy-1,1'-biphenyl)] - 3,6 dimethyl - benzene;* ***Hmim*** *= Methylimidazole;* ***BPYDC*** *= 2,2'-bipyridine-5,5'-dicarboxylate;* ***TCNQ*** *= tetracyanoquinodimethane.*

1.7 Outline and Scope of Thesis

This thesis entitled "***Heterostructured Thin Films of Coordination Polymers: Study on Growth and Electrical Conductance***" primarily focuses on the fabrication of lattice-matched and lattice-mismatched heterostructured thin films of CPs and thorough investigation of electrical transport properties across the thin films. Herein, we have fabricated the lattice-matched and lattice-mismatched heterostructured thin films of CPs involving metals with different oxidation states Cu(II) or Cu(I) and different ligands with distinctive functionalities or coordination motifs on functionalized Au and FTO substrates by employing LbL method. Electrical transport measurements were conducted for the first

time to explore the emergence of interfacial properties on heterostructured CP thin films. Overall, four Cu-based heterostructured thin films of CPs are explored in this thesis, with one lattice-matched and three lattice-mismatched structures. In chapter-2, lattice-mismatched heterostructure thin films of Cu(II)-BTC (BTC = 1,3,5-benzenetricarboxylate) and Cu(I)-TCNQ (TCNQ = 7,7,8,8-tetracyanoquinodimethane) have been studied and electrical transport measurements across the thin films revealed rectification of current assigned to be due to the formation of p-n junction interface.[72] Similarly, a current rectification was realized in a lattice-matched heterostructured thin film of Cu(II)-BTC and TCNQ@Cu-BTC with the formation of p-n junction in chapter-3.[73] In chapter-4, an unusual metallic conduction was identified in the lattice-mismatched heterostructure thin film of Cu(II)-BPyDC (BPyDC = 2,2′-bipyridine-4,4′-dicarboxylate) and Cu(I)-TCNQ, attributed to be due to charge-transfer across the interface[74] and in chapter-5, an interesting effect of current rectification along with resistive switching at elevated temperature was observed in a lattice-mismatched heterostructured thin film of Cu(II)$(Cys)_2$ (Cys = Cysteine) and Cu(I)-TCNQ where both CPs show thermally driven resistive switching behaviour.[75] In all the cases, emergence of unique interfacial properties was realized in resultant heterostructured thin films. Therefore, the obtained results open up new avenues for the design and development of functional materials in thin film configurations for various electronic and electrochemical device applications, specifically, flexible electronics (flexible displays, sensors, and wearable electronics), memory devices (resistive switching or phase change), field-effect transistors (FET), photodetectors and photovoltaics.

This thesis further contains following chapters,

Chapter-2. *Emergent Interface in Lattice-mismatched Heterostructured Thin Films of Cu(II)-BTC and Cu(I)-TCNQ*

In this chapter, we have fabricated high-quality thermally stable lattice-mismatched AB- and BA-type heterostructured thin films of cubic Cu(II)-BTC (A-type) and tetragonal Cu(I)-TCNQ (B-type) CPs on the functionalized Au substrate by the LBL method. Successful growth of Cu(I)-TCNQ on top of Cu(II)-BTC was possible due to spontaneous reduction of Cu(II) to Cu(I) at the solid-liquid interface, namely interfacial reduction reaction (IRR). Notably, electrical transport measurements across AB- and BA-type heterostructured thin films revealed rectification of current (~10^2) at 300 K and an enhanced current rectification ratio (~10^3) at 400 K. Such an interestingly new observation was attributed to the formation of a well-defined interface of Cu(II)-BTC and Cu(I)-TCNQ resembling a

p-n junction−a hitherto unreported phenomenon that is anticipated to open enormous opportunities for the heterostructured thin films of CPs, likewise celebrated interfaces of oxide heterostructures.[72]

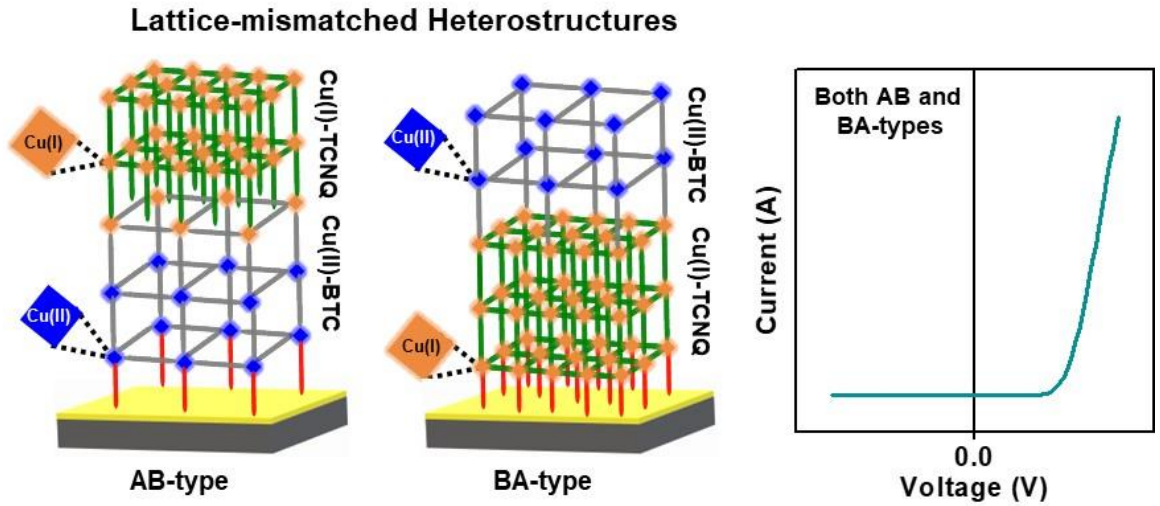

Publication from this chapter:

Emergent Interface in Heterostructured Thin Films of Cu(II) and Cu(I) Coordination Polymers

P. Sindhu, A. Prasoon, S. Rana, N. Ballav

J. Phys. Chem. Lett. ***2020****, 11, 6242−6248 (Adopted from Ref. 58 © American Chemical Society)*

Chapter-3. *Electrical Transport Properties in Lattice-matched Electronically Heterostructured Thin Films*

In this chapter, a novel design strategy was explored to deposit lattice-matched heterostructured thin film of CPs, so called electronic heterostructure by introducing guest molecules inside the pores. Depositing thin films of pristine CP on top of a lattice-matched and molecularly-doped CP could provide a new path for generating electronic heterostructures of MOFs with well-defined interfaces. Lattice-matched heterostructured thin film of Cu(II)-BTC (top-layer)/TCNQ@Cu-BTC (bottom-layer) system is fabricated by sequential deposition on functionalized Au substrate by LbL approach and clear-cut rectification (~10^5) of electrical current across the thin film was observed at room-temperature. Interestingly, the electrical current rectification ratio (~10^6) was found to be significantly influenced by the effect of temperature (400 K), resulting in a remarkable figure in the domain of CPs including MOFs. Such CP-on-Guest@CP systems can be further improvised by utilizing the accessible pores in the pristine CP layers; therefore, we have explored Fc@Cu-BTC (top-layer)/TCNQ@Cu-BTC

system by utilizing accessible pores of top layer by ferrocene (Fc = $Fe(C_5H_5)_2$) and realized to have an anomalous interfacial effect of tunable electrical rectification at ~340 K. Such electronic heterostructure of pristine and molecularly-doped CPs could provide new avenues for electronic device applications.[73]

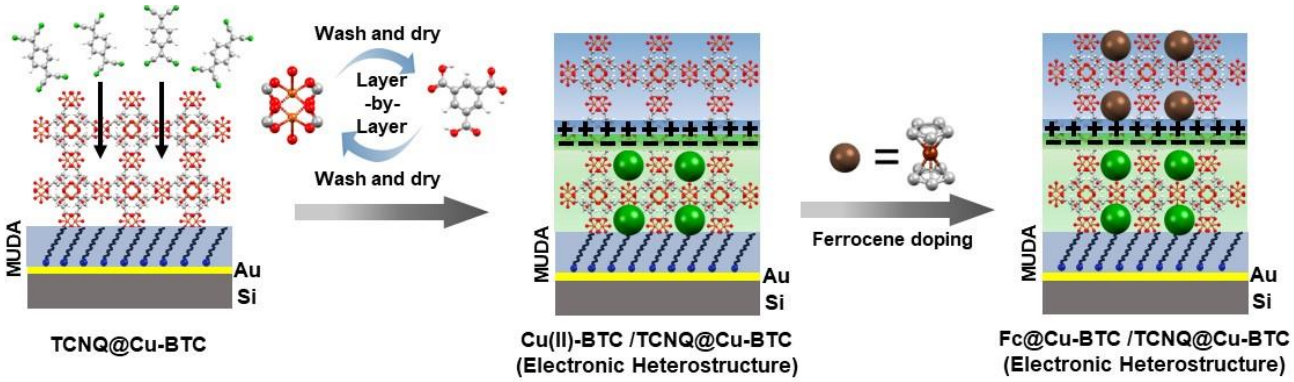

Publication from this chapter:

Thin Films of MOF-on-Guest@MOF: A Simple Strategy of Designing Electronic Heterostructures

P. Sindhu, N. Ballav

Inorg. Chem. ***2023,*** *62, 10887−10891 (Adopted from ref. 60 © American Chemical Society)*

Chapter-4. *Metallic Conduction at the Interface of Cu(I)-TCNQ/Cu(II)-BPyDC Heterostructured Thin Film*

In this chapter, we have presented a lattice-mismatched heterostructured thin film of Cu(II)-BPyDC and Cu(I)-TCNQ with characteristics of a band insulator and Mott-insulator respectively. Heterostructured thin film of a Mott and a band insulating CPs was successfully achieved on functionalized FTO substrate by LbL method. Electrical transport measurements across the thin film evidenced an interfacial metallic conduction with the electrical conductance values more than ten-fold and million-fold higher than the values of pristine Cu(I)-TCNQ and Cu(II)-BPyDC thin films, respectively. Such an interfacial metallic conduction was duly endorsed by the temperature dependent current-voltage measurement studies and further understood by the first-principles density functional theory calculations (DFT); specifically, via Bader charge analysis. DFT (+U) calculations revealing a strong interlayer hybridization and charge-transfer leading to an overlap of conduction band (CB) and valence band (VB) in the Cu(I)-TCNQ/ Cu(II)-BPyDC interface while finite gaps between CB and VB

for both Cu(I)-TCNQ and Cu(II)-BPyDC. Our results clearly open an avenue for the development of heterostructured CP-based thin film electronic devices in particular, as CPs are most often electrical insulators.[74]

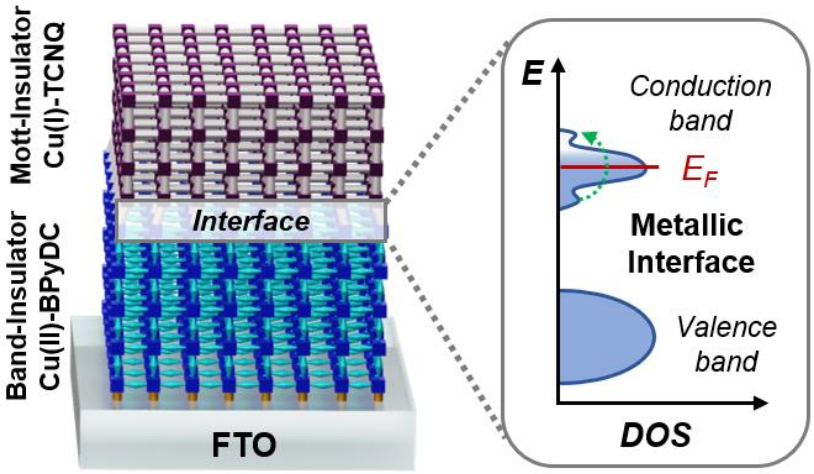

Publication from this chapter:

Charge-Transfer Interface of Insulating Metal-Organic Frameworks with Metallic Conduction

P. Sindhu, K. S. Ananthram, A. Jain, K. Tarafder, N. Ballav

Nat. Commun. ***2022****, 13, 7665 (Adopted from ref. 61 © Nature Publishing Group)*

Chapter-5. *Electrical Transport Properties in Thin Films of Cu(II)(Cys)$_2$ and Cu(I)-TCNQ/ Cu(II)(Cys)$_2$ Heterostructure*

In this chapter, we have designed a lattice-mismatched heterostructured thin film of Cu(II)(Cys)$_2$ and Cu(I)-TCNQ where both CPs are Mott-insulators. Thin films of CPs were fabricated on a functionalized Au substrate by employing LbL method. Electrical transport measurements were conducted across heterostructured thin film and revealed a surprising observation of current rectification and resistive switching at 300 K and 423 K, respectively, wherein both CPs exhibit thermally driven resistive switching behavior. Here, Cu(II)(Cys)$_2$ is being reported for the first time as a bio-CP, generated upon extended coordination of the cystine (dimer of amino acid cysteine) ligand with cupric ion and realized to have a thermally driven and fully reversible resistive switching behavior with an "on-off" ratio of ~10^{10} at slightly above room temperature (333 K) and ambient pressure.

The transition was achieved without a noticeable change in the structure, named insulator-to-metal-like transition (IMLT) and assigned to be of mainly electronic origin, viz., a charge cross-over phenomenon. This work is anticipated to provide a new platform for studying the novel phenomenon at the interface by coupling the charge, spin, and lattice degrees of freedom in the field of device applications.[75]

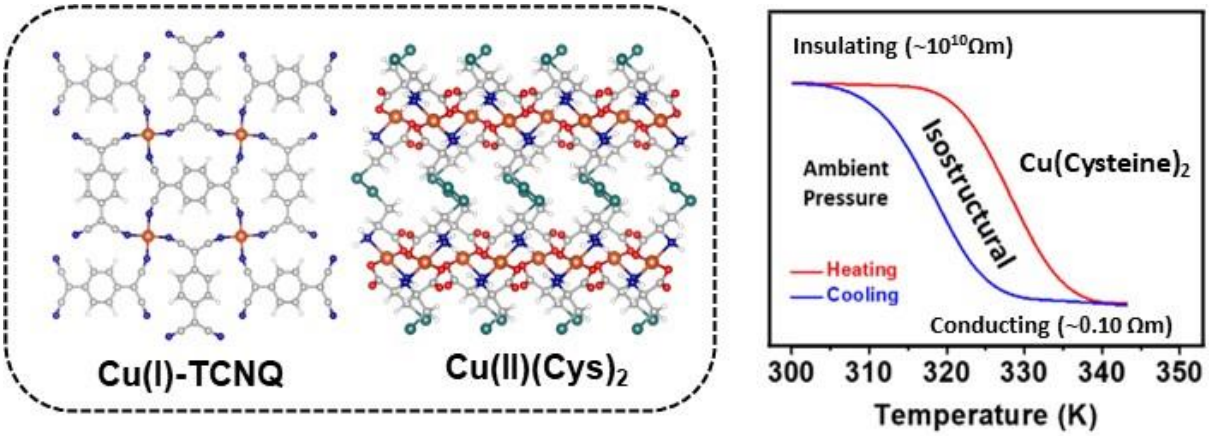

Publication from this chapter:

Insulator-to-Metal-like Transition in Thin Films of a Biological Metal-Organic Framework

P. Sindhu, K. S. Ananthram, A. Jain, K. Tarafder, N. Ballav

Nat. Commun. ***2023****, 14, 2857 (Adopted from ref. 62 © Nature Publishing Group)*

Bistable Interface: Reversible Switching of Rectifying to Non-Rectifying Current across Heterostructured Thin Films of MOFs

P. Sindhu, S. Saha, U. Bhoi, N. Ballav

Under Review ***2023***

1.8 References

1. Liu, Y.; Huang, Y.; Duan, X., Van der Waals integration before and beyond two-dimensional materials. *Nature* **2019,** *567* (7748), 323-333.

2. Heber, J., Materials science: Enter the oxides. *Nature* **2009,** *459* (7243), 28-30.

3. Huang, Z.; Ariando; Renshaw Wang, X.; Rusydi, A.; Chen, J.; Yang, H.; Venkatesan, T., Interface Engineering and Emergent Phenomena in Oxide Heterostructures. *Adv. Mater.* **2018,** *30* (47), 1802439.

4. Mannhart, J.; Schlom, D. G., Oxide Interfaces—An Opportunity for Electronics. *Science* **2010,** *327* (5973), 1607-1611.

5. Ohtomo, A.; Hwang, H. Y., A high-mobility electron gas at the $LaAlO_3/SrTiO_3$ heterointerface. *Nature* **2004,** *427* (6973), 423-426.

6. Ohtomo, A.; Muller, D. A.; Grazul, J. L.; Hwang, H. Y., Artificial charge-modulationin atomic-scale perovskite titanate superlattices. *Nature* **2002,** *419* (6905), 378-380.

7. Reyren, N.; Thiel, S.; Caviglia, A. D.; Kourkoutis, L. F.; Hammerl, G.; Richter, C.; Schneider, C. W.; Kopp, T.; Rüetschi, A. S.; Jaccard, D.; Gabay, M.; Muller, D. A.; Triscone, J. M.; Mannhart, J., Superconducting Interfaces Between Insulating Oxides. *Science* **2007,** *317* (5842), 1196-1199.

8. Takahashi, K. S.; Kawasaki, M.; Tokura, Y., Interface ferromagnetism in oxide superlattices of $CaMnO_3/CaRuO_3$. *Appl. Phys. Lett.* **2001,** *79* (9), 1324-1326.

9. The interface is still the device. *Nat. Mater.* **2012,** *11* (2), 91-91.

10. Chen, Y.; Pryds, N.; Kleibeuker, J. E.; Koster, G.; Sun, J.; Stamate, E.; Shen, B.; Rijnders, G.; Linderoth, S., Metallic and Insulating Interfaces of Amorphous $SrTiO_3$-Based Oxide Heterostructures. *Nano Lett.* **2011,** *11* (9), 3774-3778.

11. Lu, H.-L.; Liao, Z.-M.; Zhang, L.; Yuan, W.-T.; Wang, Y.; Ma, X.-M.; Yu, D.-P., Reversible insulator-metal transition of $LaAlO_3/SrTiO_3$ interface for nonvolatile memory. *Sci. Rep.* **2013,** *3* (1), 2870.

12. Warusawithana, M. P.; Richter, C.; Mundy, J. A.; Roy, P.; Ludwig, J.; Paetel, S.; Heeg, T.; Pawlicki, A. A.; Kourkoutis, L. F.; Zheng, M.; Lee, M.; Mulcahy, B.; Zander, W.; Zhu, Y.; Schubert, J.; Eckstein, J. N.; Muller, D. A.; Hellberg, C. S.; Mannhart, J.; Schlom, D. G., LaAlO3 stoichiometry is key to electron liquid formation at LaAlO3/SrTiO3 interfaces. *Nat. Commun.* **2013,** *4* (1), 2351.

13. Alves, H.; Molinari, A. S.; Xie, H.; Morpurgo, A. F., Metallic conduction at organic charge-transfer interfaces. *Nat. Mater.* **2008,** *7* (7), 574-580.

14. Alves, H.; Pinto, R. M.; Maçôas, E. S., Photoconductive response in organic charge transfer interfaces with high quantum efficiency. *Nat. Commun.* **2013,** *4* (1), 1842.

15. Lezama, I. G.; Nakano, M.; Minder, N. A.; Chen, Z.; Di Girolamo, F. V.; Facchetti, A.; Morpurgo, A. F., Single-crystal organic charge-transfer interfaces probed using Schottky-gated heterostructures. *Nat. Mater.* **2012,** *11* (9), 788-794.

16. Nakano, M.; Alves, H.; Molinari, A. S.; Ono, S.; Minder, N.; Morpurgo, A. F., Small gap semiconducting organic charge-transfer interfaces. *Appl. Phys. Lett.* **2010,** *96* (23), 232102.

17. Introduction to Metal–Organic Frameworks. *Chem. Rev.* **2012,** *112* (2), 673-674.

18. Batten, S. R.; Champness, N. R.; Chen, X.-M.; Garcia-Martinez, J.; Kitagawa, S.; Öhrström, L.; O'Keeffe, M.; Paik Suh, M.; Reedijk, J., Terminology of metal–organic frameworks and coordination polymers (IUPAC Recommendations 2013). **2013,** *85* (8), 1715-1724.

19. Furukawa, H.; Cordova, K. E.; O'Keeffe, M.; Yaghi, O. M., The Chemistry and Applications of Metal-Organic Frameworks. *Science* **2013,** *341* (6149), 1230444.

20. Stavila, V.; Talin, A. A.; Allendorf, M. D., MOF-based electronic and opto-electronic devices. *Chem. Soc. Rev.* **2014,** *43* (16), 5994-6010.

21. Hendon, C. H.; Tiana, D.; Walsh, A., Conductive metal–organic frameworks and networks: fact or fantasy? *Phys. Chem. Chem. Phys.* **2012,** *14* (38), 13120-13132.

22. Talin, A. A.; Centrone, A.; Ford, A. C.; Foster, M. E.; Stavila, V.; Haney, P.; Kinney, R. A.; Szalai, V.; El Gabaly, F.; Yoon, H. P.; Léonard, F.; Allendorf, M. D., Tunable Electrical Conductivity in Metal-Organic Framework Thin-Film Devices. *Science* **2014,** *343* (6166), 66-69.

23. Allendorf, M. D.; Foster, M. E.; Léonard, F.; Stavila, V.; Feng, P. L.; Doty, F. P.; Leong, K.; Ma, E. Y.; Johnston, S. R.; Talin, A. A., Guest-Induced Emergent Properties in Metal–Organic Frameworks. *J. Phys. Chem. Lett.* **2015,** *6* (7), 1182-1195.

24. Guo, Z.; Panda, D. K.; Maity, K.; Lindsey, D.; Parker, T. G.; Albrecht-Schmitt, T. E.; Barreda-Esparza, J. L.; Xiong, P.; Zhou, W.; Saha, S., Modulating the electrical conductivity of metal–organic framework films with intercalated guest π-systems. *J. Mater. Chem. C* **2016,** *4* (5), 894-899.

25. Le Ouay, B.; Boudot, M.; Kitao, T.; Yanagida, T.; Kitagawa, S.; Uemura, T., Nanostructuration of PEDOT in Porous Coordination Polymers for Tunable Porosity and Conductivity. *J. Am. Chem. Soc.* **2016,** *138* (32), 10088-10091.

26. Neumann, T.; Liu, J.; Wächter, T.; Friederich, P.; Symalla, F.; Welle, A.; Mugnaini, V.; Meded, V.; Zharnikov, M.; Wöll, C.; Wenzel, W., Superexchange Charge Transport in Loaded Metal Organic Frameworks. *ACS Nano* **2016,** *10* (7), 7085-7093.

27. Sun, L.; Campbell, M. G.; Dincă, M., Electrically Conductive Porous Metal–Organic Frameworks. *Angew. Chem. Int. Ed.* **2016,** *55* (11), 3566-3579.

28. Usman, M.; Mendiratta, S.; Lu, K.-L., Semiconductor Metal–Organic Frameworks: Future Low-Bandgap Materials. *Adv. Mater.* **2017,** *29* (6), 1605071.

29. Wang, T.; Farajollahi, M.; Henke, S.; Zhu, T.; Bajpe, S. R.; Sun, S.; Barnard, J. S.; Lee, J. S.; Madden, J. D. W.; Cheetham, A. K.; Smoukov, S. K., Functional conductive nanomaterials via polymerisation in nano-channels: PEDOT in a MOF. *Mater. Horiz.* **2017,** *4* (1), 64-71.

30. Bhardwaj, S. K.; Bhardwaj, N.; Kaur, R.; Mehta, J.; Sharma, A. L.; Kim, K.-H.; Deep, A., An overview of different strategies to introduce conductivity in metal–organic frameworks and miscellaneous applications thereof. *J. Mater. Chem. A* **2018,** *6* (31), 14992-15009.

31. Schneider, C.; Ukaj, D.; Koerver, R.; Talin, A. A.; Kieslich, G.; Pujari, S. P.; Zuilhof, H.; Janek, J.; Allendorf, M. D.; Fischer, R. A., High electrical conductivity and high porosity in a Guest@MOF material: evidence of TCNQ ordering within Cu_3BTC_2 micropores. *Chem. Sci* **2018,** *9* (37), 7405-7412.

32. Thürmer, K.; Schneider, C.; Stavila, V.; Friddle, R. W.; Léonard, F.; Fischer, R. A.; Allendorf, M. D.; Talin, A. A., Surface Morphology and Electrical Properties of Cu_3BTC_2 Thin Films Before and After Reaction with TCNQ. *ACS Appl. Mater. Interfaces* **2018,** *10* (45), 39400-39410.

33. Kobayashi, Y.; Jacobs, B.; Allendorf, M. D.; Long, J. R., Conductivity, Doping, and Redox Chemistry of a Microporous Dithiolene-Based Metal−Organic Framework. *Chem. Mater.* **2010,** *22* (14), 4120-4122.

34. Xie, L. S.; Skorupskii, G.; Dincă, M., Electrically Conductive Metal–Organic Frameworks. *Chem. Rev.* **2020,** *120* (16), 8536-8580.

35. Sun, L.; Hendon, C. H.; Park, S. S.; Tulchinsky, Y.; Wan, R.; Wang, F.; Walsh, A.; Dincă, M., Is iron unique in promoting electrical conductivity in MOFs? *Chemical Science* **2017,** *8* (6), 4450-4457.

36. Heintz, R. A.; Zhao, H.; Ouyang, X.; Grandinetti, G.; Cowen, J.; Dunbar, K. R., New Insight into the Nature of Cu(TCNQ): Solution Routes to Two Distinct Polymorphs and Their Relationship to Crystalline Films That Display Bistable Switching Behavior. *Inorg. Chem.* **1999,** *38* (1), 144-156.

37. Dou, J.-H.; Sun, L.; Ge, Y.; Li, W.; Hendon, C. H.; Li, J.; Gul, S.; Yano, J.; Stach, E. A.; Dincă, M., Signature of Metallic Behavior in the Metal–Organic Frameworks M_3(hexaiminobenzene)$_2$ (M = Ni, Cu). *J. Am. Chem. Soc.* **2017,** *139* (39), 13608-13611.

38. Sheberla, D.; Sun, L.; Blood-Forsythe, M. A.; Er, S.; Wade, C. R.; Brozek, C. K.; Aspuru-Guzik, A.; Dincă, M., High Electrical Conductivity in Ni_3(2,3,6,7,10,11-hexaiminotriphenylene)$_2$, a Semiconducting Metal–Organic Graphene Analogue. *J. Am. Chem. Soc.* **2014,** *136* (25), 8859-8862.

39. Ohring, M., *Materials Science of Thin Films: Depositon and Structure*. Elsevier: 2001.

40. Kwon, H.-J. Applications of Thin Films in Microelectronics *Electronics* [Online], 2022.

41. Catania, F.; de Souza Oliveira, H.; Lugoda, P.; Cantarella, G.; Münzenrieder, N., Thin-film electronics on active substrates: review of materials, technologies and applications. *J. Phys. D: Appl. Phys.* **2022,** *55* (32), 323002.

42. Martin, P. M., *Handbook of deposition technologies for films and coatings: science, applications and technology*. William Andrew: 2009.

43. Gliemann, H.; Wöll, C., Epitaxially grown metal-organic frameworks. *Mater. Today* **2012,** *15* (3), 110-116.

44. Zhuang, J.-L.; Terfort, A.; Wöll, C., Formation of oriented and patterned films of metal–organic frameworks by liquid phase epitaxy: A review. *Coord. Chem. Rev.* **2016,** *307*, 391-424.

45. Love, J. C.; Estroff, L. A.; Kriebel, J. K.; Nuzzo, R. G.; Whitesides, G. M., Self-assembled monolayers of thiolates on metals as a form of nanotechnology. *Chem. Rev.* **2005,** *105* (4), 1103-1170.

46. Vericat, C.; Vela, M. E.; Corthey, G.; Pensa, E.; Cortés, E.; Fonticelli, M. H.; Ibañez, F.; Benitez, G.; Carro, P.; Salvarezza, R. C., Self-assembled monolayers of thiolates on metals: a review article on sulfur-metal chemistry and surface structures. *RSC Adv.* **2014,** *4* (53), 27730-27754.

47. Arnold, R.; Azzam, W.; Terfort, A.; Wöll, C., Preparation, modification, and crystallinity of aliphatic and aromatic carboxylic acid terminated self-assembled monolayers. *Langmuir* **2002,** *18* (10), 3980-3992.

48. Kumar, A.; Biebuyck, H. A.; Whitesides, G. M., Patterning self-assembled monolayers: applications in materials science. *Langmuir* **1994,** *10* (5), 1498-1511.

49. Wang, Z.; Wöll, C., Fabrication of Metal–Organic Framework Thin Films Using Programmed Layer-by-Layer Assembly Techniques. *Adv. Mater. Technol.* **2019,** *4* (5), 1800413.

50. Ma, Z.-Z.; Li, Q.-H.; Wang, Z.; Gu, Z.-G.; Zhang, J., Electrically regulating nonlinear optical limiting of metal-organic framework film. *Nat. Commun.* **2022,** *13* (1), 6347.

51. Liu, J.; Wöll, C., Surface-supported metal–organic framework thin films: fabrication methods, applications, and challenges. *Chem. Soc. Rev.* **2017,** *46* (19), 5730-5770.

52. Chen, Y.; Wang, B.; Wang, X.; Xie, L.-H.; Li, J.; Xie, Y.; Li, J.-R., A Copper(II)-Paddlewheel Metal–Organic Framework with Exceptional Hydrolytic Stability and Selective Adsorption and Detection Ability of Aniline in Water. *ACS Appl. Mater. Interfaces* **2017,** *9* (32), 27027-27035.

53. Heinke, L.; Wöll, C., Surface-Mounted Metal–Organic Frameworks: Crystalline and Porous Molecular Assemblies for Fundamental Insights and Advanced Applications. *Adv. Mater.* **2019,** *31* (26), 1806324.

54. Haldar, R.; Wöll, C., Hierarchical assemblies of molecular frameworks—MOF-on-MOF epitaxial heterostructures. *Nano Res.* **2021,** *14* (2), 355-368.

55. Shekhah, O.; Hirai, K.; Wang, H.; Uehara, H.; Kondo, M.; Diring, S.; Zacher, D.; Fischer, R. A.; Sakata, O.; Kitagawa, S., MOF-on-MOF heteroepitaxy: perfectly oriented $[Zn_2(ndc)_2$ (dabco)$]_n$ grown on $[Cu_2(ndc)_2(dabco)]_n$ thin films. *Dalton Trans.* **2011,** *40* (18), 4954-4958.

56. Zacher, D.; Yusenko, K.; Bétard, A.; Henke, S.; Molon, M.; Ladnorg, T.; Shekhah, O.; Schüpbach, B.; de los Arcos, T.; Krasnopolski, M., Liquid-Phase Epitaxy of Multicomponent Layer-Based Porous Coordination Polymer Thin Films of $[M(L)(P)_{0.5}]$ Type: Importance of Deposition Sequence on the Oriented Growth. *Chem. Eur. J.* **2011,** *17* (5), 1448-1455.

57. Knebel, A.; Wulfert-Holzmann, P.; Friebe, S.; Pavel, J.; Strauß, I.; Mundstock, A.; Steinbach, F.; Caro, J., Hierarchical Nanostructures of Metal-Organic Frameworks Applied in Gas Separating ZIF-8-on-ZIF-67 Membranes. *Chem. Eur. J.* **2018,** *24* (22), 5728-5733.

58. Chen, D. H.; Haldar, R.; Neumeier, B. L.; Fu, Z. H.; Feldmann, C.; Wöll, C.; Redel, E., Tunable Emission in Heteroepitaxial Ln-SURMOFs. *Adv. Funct. Mater.* **2019,** *29* (37), 1903086.

59. Ikigaki, K.; Okada, K.; Tokudome, Y.; Toyao, T.; Falcaro, P.; Doonan, C. J.; Takahashi, M., MOF-on-MOF: Oriented Growth of Multiple Layered Thin Films of Metal–Organic Frameworks. *Angew. Chem. Int. Ed.* **2019,** *131* (21), 6960-6964.

60. Heinke, L.; Cakici, M.; Dommaschk, M.; Grosjean, S.; Herges, R.; Bräse, S.; Wöll, C., Photoswitching in two-component surface-mounted metal–organic frameworks: optically triggered release from a molecular container. *ACS nano* **2014,** *8* (2), 1463-1467.

61. Tu, M.; Fischer, R. A., Heteroepitaxial growth of surface mounted metal–organic framework thin films with hybrid adsorption functionality. *J. Mater. Chem. A* **2014,** *2* (7), 2018-2022.

62. Wang, Z.; Liu, J.; Lukose, B.; Gu, Z.; Weidler, P. G.; Gliemann, H.; Heine, T.; Wöll, C., Nanoporous designer solids with huge lattice constant gradients: multiheteroepitaxy of metal–organic frameworks. *Nano Lett.* **2014,** *14* (3), 1526-1529.

63. Wannapaiboon, S.; Tu, M.; Fischer, R. A., Liquid Phase Heteroepitaxial Growth of Moisture-Tolerant MOF-5 Isotype Thin Films and Assessment of the Sorption Properties by Quartz Crystal Microbalance. *Adv. Funct. Mater.* **2014,** *24* (18), 2696-2705.

64. Wannapaiboon, S.; Tu, M.; Sumida, K.; Khaletskaya, K.; Furukawa, S.; Kitagawa, S.; Fischer, R. A., Hierarchical structuring of metal–organic framework thin-films on quartz crystal microbalance (QCM) substrates for selective adsorption applications. *J. Mater. Chem. A* **2015,** *3* (46), 23385-23394.

65. Oldenburg, M.; Turshatov, A.; Busko, D.; Wollgarten, S.; Adams, M.; Baroni, N.; Welle, A.; Redel, E.; Wöll, C.; Richards, B. S., Photon upconversion at crystalline organic–organic heterojunctions. *Adv. Mater.* **2016,** *28* (38), 8477-8482.

66. Chernikova, V.; Shekhah, O.; Spanopoulos, I.; Trikalitis, P. N.; Eddaoudi, M., Liquid phase epitaxial growth of heterostructured hierarchical MOF thin films. *Chem. Commun.* **2017,** *53* (46), 6191-6194.

67. Wang, Z.; Wannapaiboon, S.; Rodewald, K.; Tu, M.; Rieger, B.; Fischer, R. A., Directing the hetero-growth of lattice-mismatched surface-mounted metal–organic frameworks by functionalizing the interface. *J. Mater. Chem. A* **2018,** *6* (43), 21295-21303.

68. Liu, B.; Tu, M.; Zacher, D.; Fischer, R. A., Multi variant surface mounted metal–organic frameworks. *Adv. Funct. Mater.* **2013,** *23* (30), 3790-3798.

69. Meilikhov, M.; Furukawa, S.; Hirai, K.; Fischer, R. A.; Kitagawa, S., Binary Janus porous coordination polymer coatings for sensor devices with tunable analyte affinity. *Angew. Chem.* **2013,** *125* (1), 359-363.

70. Tu, M.; Wannapaiboon, S.; Fischer, R. A., Programmed functionalization of SURMOFs via liquid phase heteroepitaxial growth and post-synthetic modification. *Dalton Trans.* **2013,** *42* (45), 16029-16035.

71. Tang, S.-J.; Lee, C.-Y.; Huang, C.-C.; Chang, T.-R.; Cheng, C.-M.; Tsuei, K.-D.; Jeng, H.-T.; Yeh, V.; Chiang, T.-C., Electronic versus lattice match for metal-semiconductor epitaxial growth: Pb on Ge (111). *Phys. Rev. Lett.* **2011,** *107* (6), 066802.

72. Sindhu, P.; Prasoon, A.; Rana, S.; Ballav, N., Emergent Interface in Heterostructured Thin Films of Cu(II) and Cu(I) Coordination Polymers. *J. Phys. Chem. Lett.* **2020,** *11* (15), 6242-6248.

73. Sindhu, P.; Ballav, N., Thin Films of MOF-on-Guest@MOF: A Simple Strategy of Designing Electronic Heterostructures. *Inorg. Chem.* **2023,** *62* (28), 10887-10891.

74. Sindhu, P.; Ananthram, K. S.; Jain, A.; Tarafder, K.; Ballav, N., Charge-transfer interface of insulating metal-organic frameworks with metallic conduction. *Nat. Commun.* **2022,** *13* (1), 7665.

75. Sindhu, P.; Ananthram, K. S.; Jain, A.; Tarafder, K.; Ballav, N., Insulator-to-metal-like transition in thin films of a biological metal-organic framework. *Nat. Commun.* **2023,** *14* (1), 2857.

Emergent Interface in Cu(II)-BTC and Cu(I)-TCNQ Lattice-mismatched Heterostructured Thin Films

2.1 Introduction

Heterostructures have been a centre of attraction within the scientific community for many decades due to their emergent interfacial properties.[1-5] Nowadays, researchers have started to explore the design of heterostructures in other class of materials,[1, 6-7] coordination polymer (CP) being one among them. Cu-BTC (BTC = 1,3,5-benzenetricarboxylate) and Cu-TCNQ (TCNQ = 7,7,8,8-tetracyanoquinodimethane) are very well-known examples in the field[8-9] and have distinctive properties such as different oxidation states of metal ions, distinctive metal-ligand bonding motifs, and dissimilar lattice constants, therefore, making them interesting to study in the form of heterostructure. Moreover, electrical transport properties across such heterostructured CPs thin films are yet to be realized, which could possibly indicate the emergence of interfacial phenomena similar to well-known oxide heterostructures.[1, 4-5]

However, the fabrication of heterostructured thin films of CPs is quite challenging due to their high porosity.[10-15] The high-porosity of Cu-BTC makes it susceptible to the doping of a redox-active molecule, TCNQ, into the framework leads to a remarkable enhancement of electrical conductivity value by six orders of magnitude (~10^{-8} S/cm to ~10^{-2} S/cm) due to the generation of conducting paths within Cu-BTC framework upon bridging of two Cu paddle wheel dimers via two geminal nitrile groups of TCNQ molecule, facilitating charge-transfer involving the highest occupied molecular orbital (HOMO) of Cu-BTC (localized on the copper atom) and the lowest unoccupied molecular orbital (LUMO) of TCNQ (localized on the π- orbital).[10-11] Therefore, fabrication of Cu-TCNQ on top of Cu-BTC is really challenging and demands a methodology that can provide a scope to avoid doping inside the Cu-BTC framework.

Herein, we have successfully fabricated AB- and BA-type lattice-mismatched heterostructured thin films of Cu-BTC and Cu-TCNQ on functionalized Au substrate by avoiding doping inside the pores of Cu-BTC via layer-by-layer (LbL) approach. Heterostructures of Cu-BTC and Cu-TCNQ have different oxidation states of Cu (Cu(II) and Cu(I)), different coordination motifs (−COO−Cu(II) for Cu-BTC and −CN− Cu(I) for Cu-TCNQ), and mismatched lattices. Additionally, Cu-BTC is a highly porous CP, whereas Cu-TCNQ is a dense CP with a very small porosity and relatively small pores likewise other M-TCNQ CPs.[16-17] Successful growth of Cu(I)-TCNQ thin films on top of a Cu(II)-BTC thin film via the LbL method was assigned to be due to spontaneous reduction of Cu(II) to Cu(I) at the solid−liquid interface - the so-called interfacial reduction reaction (IRR) (Figure 2.1).

Furthermore, we have taken the first attempt to investigate electrical transport properties across such lattice-mismatched heterostructured thin films of CPs.

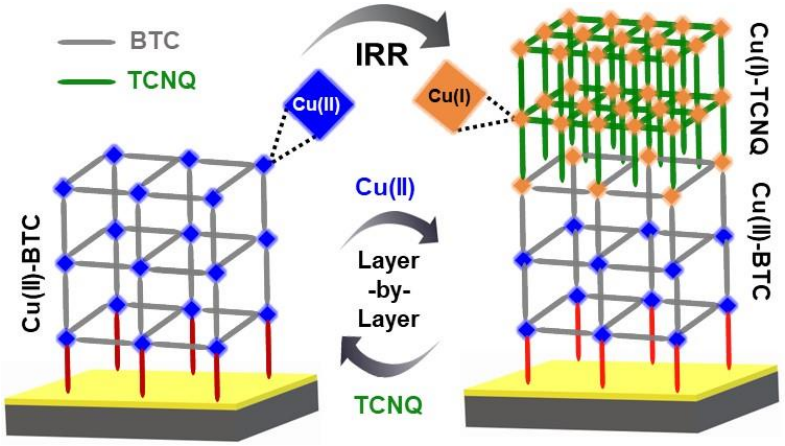

Figure 2.1. *Schematic of LbL growth of Cu(I)-TCNQ (B-type) thin film on top of Cu(II)-BTC (A-type) thin film via IRR leading to AB-type lattice-mismatched heterostructured thin film.*

2.2 Materials and Methods

Materials: Copper acetate [$Cu(OAc)_2.H_2O$], 7,7,8,8-tetracyanoquinodimethane (TCNQ), 1,3,5-benzenetricarboxylic acid (BTC), 11-Merceptoundecanoic acid (MUDA) and Au(111) substrate (100 nm Au coated Si wafer) were purchased from Sigma-Aldrich and ethanol from Merck and used as such, without any further purification except Au(111) substrate.

Fabrication of SAM: Au substrate was cleaned by dipping into Piranha solution (H_2SO_4 (95-98%)/H_2O_2 (30%); v/v 3:1) for 30 minutes (note: proper safety care must be taken) and washed with Milli-Q water followed by ethanol and then dried with N_2 gas. Subsequently, Au substrate was functionalized with a carboxy-terminated (-COOH) SAM by dipping into the 1mM MUDA solution in ethanol/acetic acid (v/v 9:1) for 48 hours followed by washing with ethanol and dried with N_2 gas.

Fabrication of Pristine Cu-BTC Thin Film (A-type): MUDA/Au SAM was immersed in 1mM ethanolic solution of $Cu(OAc)_2.H_2O$ kept at 330 K for 30 minutes followed by washing with ethanol and subsequently in 1mM ethanolic solution of BTC kept at 330 K for 30 minutes (washed with ethanol followed by drying with N_2 gas) to complete one LbL cycle. 20 cycles of LbL were performed to get uniform Cu-BTC thin film (thickness values were estimated to be approximately 700 nm).

Fabrication of Pristine Cu-TCNQ Thin Film (B-type): MUDA/Au substrate was immersed in 1mM ethanolic solution of $Cu(OAc)_2.H_2O$ kept at 330 K for 30 minutes followed by washing with ethanol

and subsequently in 1 mM ethanolic solution of TCNQ kept at 330 K for 30 minutes (washed with ethanol followed by drying with N_2 gas) to complete one LbL cycle. 20 cycles of LbL were performed to get uniform Cu-TCNQ thin film (thickness values were estimated to be approximately 600 nm).

Fabrication of AB-type Heterostructured Thin Film: Pre-fabricated pristine Cu-BTC thin film was subsequently dipped into ethanolic solutions of $Cu(OAc)_2$ and TCNQ (five minutes in each solution at an elevated temperature and washed with ethanol in between followed by drying with stream of N_2 gas to complete one cycle of LbL) for five cycles of LbL to prevent the infiltration of TCNQ within Cu-BTC thin film and afterwards, fifteen consecutive LbL cycles with dipping time of thirty minutes were performed to grow Cu-TCNQ on top of Cu-BTC having well-defined interface (thickness values were estimated to be approximately 1.2-1.3 μm).

Fabrication of BA-type Heterostructured Thin Film: Pre-fabricated pristine Cu-TCNQ thin film was subsequently dipped into ethanolic solutions of $Cu(OAc)_2$ and BTC (thirty minutes in each solution at an elevated temperature and washed with ethanol in between followed by drying with stream of N_2 gas to complete one cycle of LbL) for twenty consecutive cycles of LbL to grow Cu-BTC on top of Cu-TCNQ (thickness values were estimated to be approximately 1.2-1.3 μm).

Characterizations: The surface morphologies of both pristine (A- and B-type) and heterostructured (AB- and BA-type) thin films were performed by Zeiss Ultra Plus Field-emission scanning electron microscopy (FESEM). Contact angle measurements were measured using Holmarc's Contact Angle Meter. Out-of-plane XRD data were recorded at room temperature using a Bruker D8 Advance diffractometer using Cu Kα radiation (λ = 1.5406 Å). Raman spectra (λ_{exc} = 632.8 nm) were recorded at Raman microscope (LabRAM HR, HoribaJobinYvon) with a 50X objective lens and the spectral resolution of the system is ~1 cm^{-1}. Solid state UV-vis absorption spectra were recorded on Shimadzu UV 3600 UV-Vis-NIR spectrophotometer. Electrical transport measurements (*I-V*) on various thin film samples were carried out using a Keithley 4200 SCS Parameter Analyser system attached to an Everbeing probe station with a eutectic gallium indium (EGaIn) alloy and direct Au tip as the top electrode. Capacitance–voltage plots (Mott-Schottky) on heterostructured thin films were recorded in PARSTAT MC PMC-2000 instrument.

2.3 Results and Discussion

Pristine and heterostructured thin films of Cu-BTC and Cu-TCNQ on functionalized Au substrates were successfully fabricated by standard protocols established in our group (Figure 2.2).[15, 17-18] Our

data are consistent with earlier reports on the interfacial growth of pristine Cu-BTC and Cu-TCNQ thin films whereby in each cycle of the LbL growth, multilayers of respective CP were getting deposited at the solid−liquid interface.[19-21]

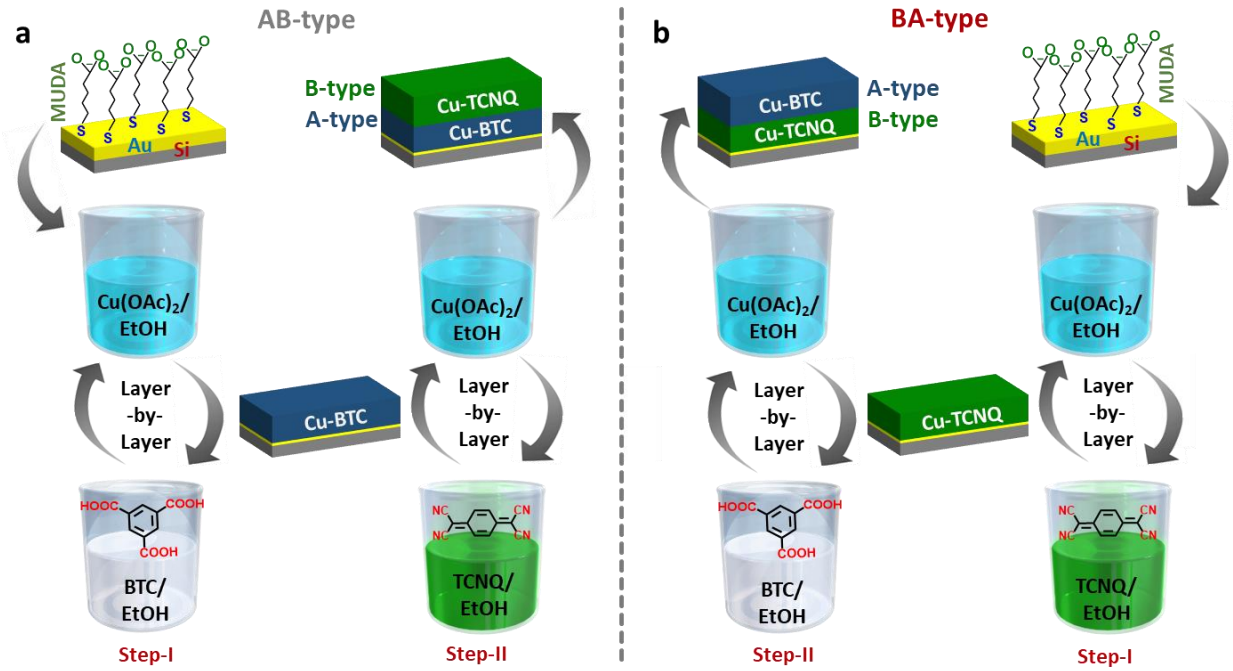

Figure 2.2. *Schematic diagram of heteroepitaxial LbL growth. (a) Sequential dipping of the Au-thiolate SAM substrate into Cu(II) acetate and BTC solutions, constitutes one cycle of LbL growth. After 20 growth cycles, dipping as-synthesised Cu-BTC thin film (from step-I) into Cu(II) acetate and TCNQ solutions alternatively for 20 growth LbL cycles (step-II) and finally fabricated AB-type heterostructured thin film. Similarly, (b) first fabricated Cu-TCNQ thin film in step-I and then sequential dipping of as-synthesized Cu-TCNQ thin film into Cu(II) acetate and BTC solutions (step-II), finally offers a well-oriented BA-type heterostructured thin film.*

In the present study, we have changed the ligand to sequentially deposit Cu-TCNQ on top of Cu-BTC and vice versa, thereby leading to generation of AB- and BA-type heterostructured thin films, and thus, it has been conventionally named LbL growth. It is worthwhile to mention that upon dipping the Cu-BTC thin film into a methanolic solution of TCNQ for a prolonged time, complete conversion of Cu-BTC to Cu-TCNQ can take place,[22] and as a result, it remained really difficult to grow Cu-TCNQ thin film on top of the Cu-BTC thin film by LbL with a well-defined interface. Here, Cu-TCNQ was successfully deposited on Cu-BTC thin film by reducing the dipping time in initial LbL growth cycles of Cu-TCNQ.

Water contact angle values of ~66° and ~130° suggested formation of high-quality pristine Cu-BTC and Cu-TCNQ thin films, respectively (Figure 2.3).[17] An indication of the successful growth of Cu-TCNQ and Cu-BTC, on top of each vis-à-vis formation of AB- and BA-type heterostructures was the modulation of the water contact angle values (Figure 2.4).

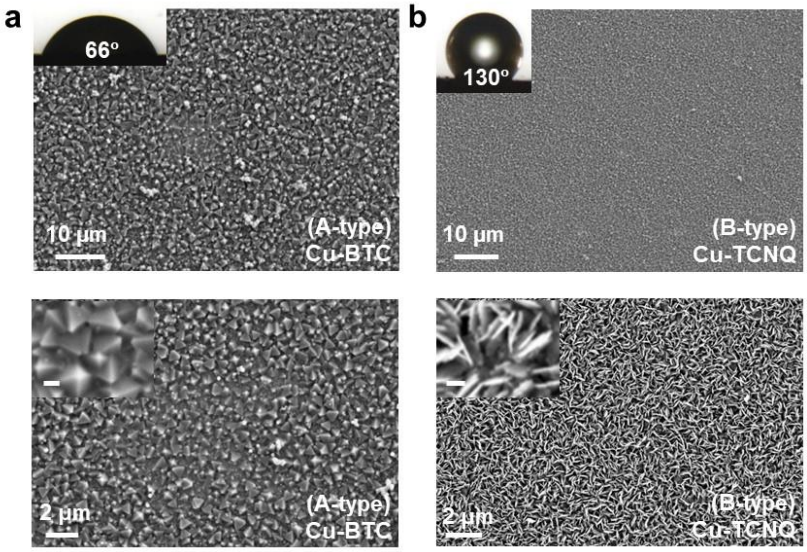

Figure 2.3. *FESEM images of (a) pristine Cu-BTC and (b) pristine Cu-TCNQ thin films (insets: optical images of water contact angles (top panel) and respective zoomed-in images with scale bar of 200 nm).*

Upon growing Cu-TCNQ on top of Cu-BTC, the contact angle of water significantly changed from ~66° to ~132°, so that the noticeable change of contact angle of water from ~130° to ~63° was assigned to when Cu-BTC was grown on Cu-TCNQ (Figure 2.4).

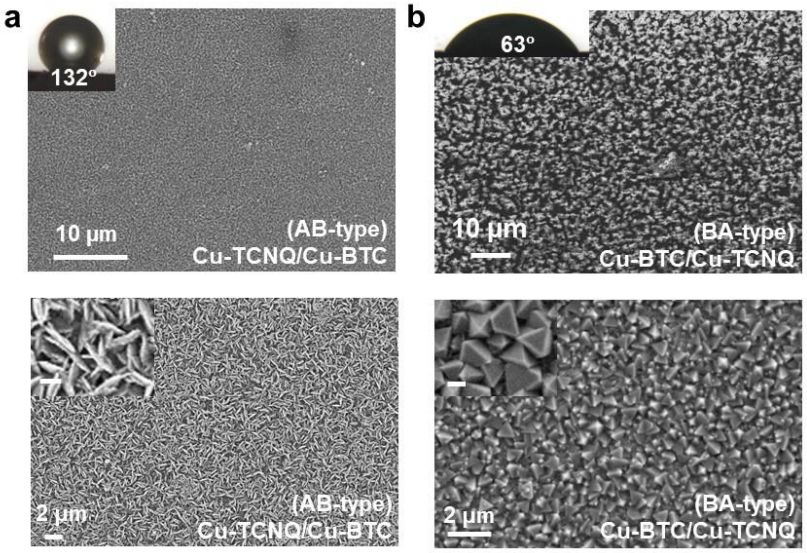

Figure 2.4. *FESEM images of (a) heterostructured AB- and (b) BA-types thin films (insets: optical images of water contact angles (top panel) and respective zoomed-in images with scale bar of 200 nm).*

Cu-BTC crystallizes in the face-centered cubic crystal system[8] with the unit-cell parameters a = b = c = 26.34 Å and α = β = γ = 90° whereas Cu-TCNQ crystallizes in the tetragonal crystal system[9] having unit cell parameters a = b =11.26 Å, c = 3.88 Å, and α = β = γ = 90°. Such different crystal lattices of Cu-BTC and Cu-TCNQ make morphological features of crystallite distinctive, nano-octahedral for the former CP and nanoplate for the latter CP.[17] Field-emission scanning electron microscopy (FESEM) images revealed highly uniform thin film formation for both pristine and heterostructured systems (Figure 2.3 and 2.4). Zoomed-in FESEM images showed characteristic morphological patterns of Cu-BTC and Cu-TCNQ crystallites (Figures 2.3). Specifically, resemblance of surface morphology of pristine B-type for the AB-type thin film and of pristine A-type surface morphology for the BA-type thin film suggested successful fabrication of heterostructured thin films with retention of structural integrity (Figure 2.3 and 2.4).

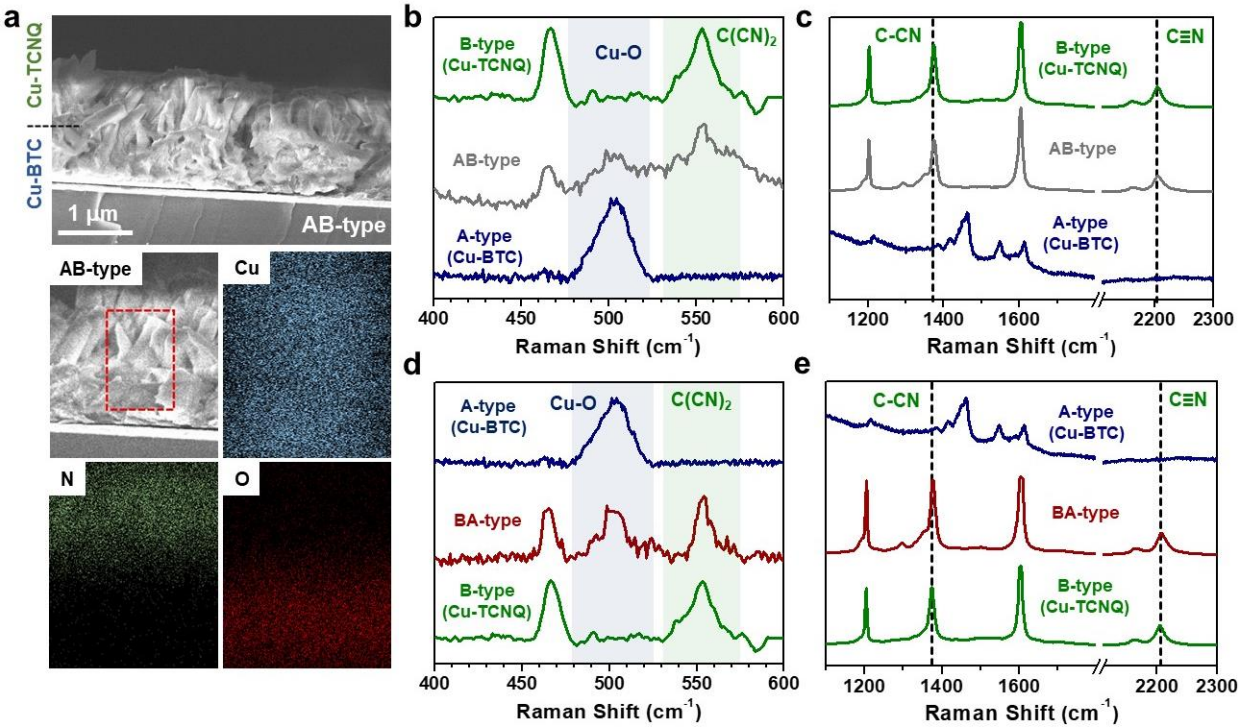

Figure 2.5. *Cross-sectional FESEM image of (a) AB-type heterostructured thin film showing Cu-TCNQ on top of Cu-BTC thin film (top panel) and elemental mapping by EDXS (bottom panel) clearly showing the interface where oxygen (red) and nitrogen (green) act as markers for the Cu-BTC and Cu-TCNQ thin films, respectively. Raman spectra of pristine Cu-BTC (A-type) thin film, pristine Cu-TCNQ (B-type) thin film, (b-c) AB-type heterostructured thin film (grey) and (d-e) BA-type heterostructured thin film (red) (characteristic band ~502*

cm^{-1} is corresponding to Cu-BTC and ~552, ~1377, ~2206 cm^{-1} are corresponding to Cu-TCNQ thin film, which are present in AB-type heterostructured thin film).

A side view of the AB-type heterostructured thin film was also captured in cross-sectional FESEM image whereby elemental mapping by energy-dispersive X-ray spectroscopy (EDXS) clearly disclosed the presence of a well-defined interface (Figure 2.5). Similarly, FESEM images showed the characteristic morphology of Cu-BTC after few initial cycles on the pre-fabricated Cu-TCNQ thin film in BA-type heterostructured thin film (Appendix Fig. 2.1).

To investigate distinctive Cu−OOC− and Cu−NC− metal−ligand coordination bonding motifs, Raman spectra were recorded for both pristine Cu-BTC and Cu-TCNQ thin films and compared with those of AB- and BA-type heterostructured thin films (Figures 2.5). Characteristic vibrational bands of pristine Cu-BTC and Cu-TCNQ thin films were collectively present in the heterostructured AB-type thin film, without notable red or blue shift (Figure 2.5).[23-24] Out-of-plane X-ray diffraction (XRD) patterns of pristine Cu- BTC and Cu-TCNQ thin films were recorded and characteristics diffraction peaks were observed to be present in AB- and BA-type heterostructured thin films (Figure 2.6 and Appendix 2.2). Interestingly, the diffraction peak at 2θ ≈ 11.5° corresponding to the (222) plane of Cu-BTC was found to be the most intense peak for both the pristine thin film and the AB-type heterostructured thin film (Figure 2.6a).[10, 25] Also, the diffraction peak at 2θ ≈ 15.6° corresponding to the (200) plane of Cu-TCNQ (phase-I) remained a highly intense peak for the pristine thin film and the BA-type heterostructured thin film (Figure 2.6b).[9, 17, 26]

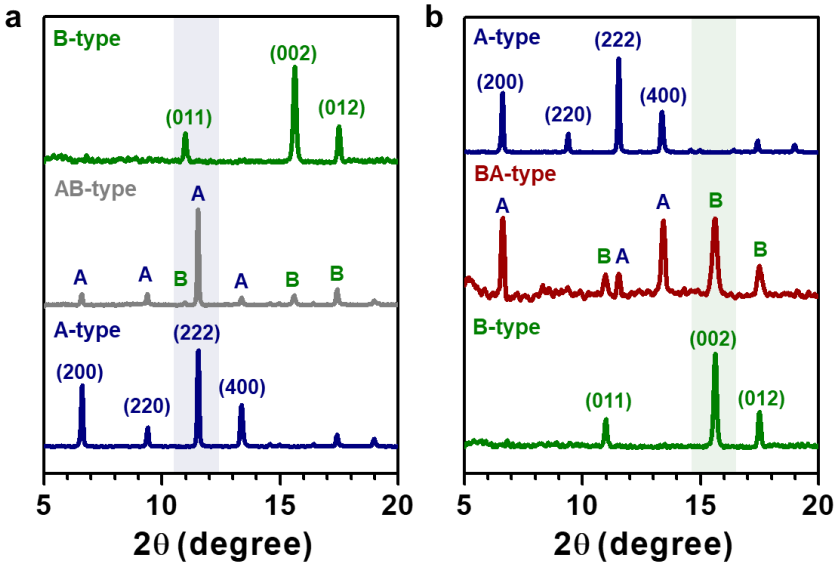

Figure 2.6. *Out-of-plane XRD patterns of (a) AB-type and (b) BA-type hetero-structured thin film with pristine Cu-BTC (A-type), Cu-TCNQ (B-type) thin film showing the preferred orientation in (222) and (002) planes highlighted by blue and green colour respectively.*

To demonstrate thermal stability, we have recorded variable temperature XRD patterns and, indeed, the AB-type heterostructured thin film was found to be thermally very stable up to 400 K (Appendix 2.1) and a similar result is expected for our BA-type heterostructured thin film. Such observations are consistent with previous reports on thin films of CPs, specifically, heterostructures whereby orientation of the initially deposited layers determines the final orientation of thin films.[27-29]

What was responsible for such an unusual growth of a Cu(I)-CP thin film on top of a Cu(II)-CP thin film leading to a well-defined heterostructure? We have recently discovered spontaneous reduction of Cu(II) to Cu(I) at solid−liquid interface−interfacial reduction reaction (IRR), which successfully led to fabrication of a high-quality thin film of pristine Cu(I)-TCNQ on a functionalized Au substrate by LbL involving ethanolic solutions of $Cu^{II}(OAc)_2$ and TCNQ.[21] IRR was consistently observed during LbL growth involving ethanolic solutions of $Cu^{II}(OAc)_2$ and ($K_4[Fe(CN)_6]$) leading to successful fabrication of a high-quality thin film of Cu(I)−hexacyanoferrate.[20] Thus, in course of the growth of Cu(I)-TCNQ thin film on top of Cu(II)-BTC thin film, at every immersion step of LbL into TCNQ solution, Cu(II) was getting converted into Cu(I) by IRR, which finally resulted in the formation of well-defined AB-type heterostructured thin film. As for the BA-type heterostructured thin film, Cu(II) remained Cu(II) due to binding with non-cyanide, carboxylate (COO−) ligand facilitating the growth of a Cu(II)-BTC thin film on top of a Cu(I)-TCNQ thin film. The concomitant oxidation of protic solvents like ethanol/methanol to acetaldehyde/formaldehyde (or acetic acid/formic acid) was assigned to be the source of electron for the IRR of Cu(II) to Cu(I).[21-22] In Cu-BTC, the valence band (VB) exhibits mainly contribution from the oxygen O (2p) state while the conduction band (CB) above the Fermi energy stems predominantly from the Cu (3d) state.[30] The zero-field splitting parameter is smaller and thus of lower spin density on the Cu(II) ions with $3d^9$-electronic configuration and more delocalization of the ground-state spin density on to the acetate linkers may have implications for electrical conductivity.[11] Cu-TCNQ mainly exists in two phases, phase-I and phase-II, having distinct structural properties as well as electrical conductivity values.[9] In the present work, the Cu-TCNQ thin film is realized in the phase-I structure where Cu ions are coordinated to four TCNQ ligands in a highly distorted tetrahedral environment with N−Cu−N bond angles of 92° and 142°.[9] A columnar stack of TCNQ molecules with a distance of 3.24 Å facilitates π–π interaction.[9] Additionally, efficient charge

transfer is possible between Cu(I) ions with $3d^{10}$-electronic configuration and TCNQ ligands leading to generation of the p_{π}–d band. As a result, much higher electrical conductivity is expected for Cu-TCNQ in comparison to Cu-BTC.

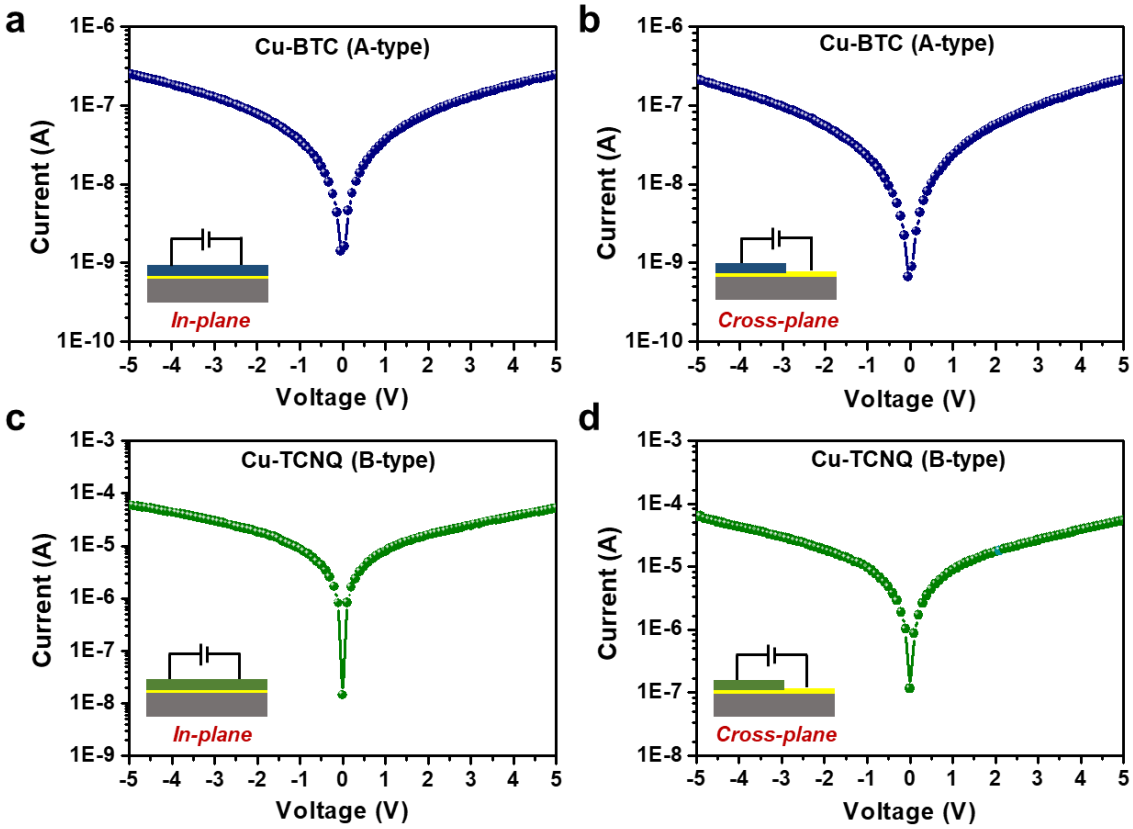

Figure 2.7. *In-plane and cross-plane I–V characteristics at 300 K of (a) pristine Cu-BTC and (b) pristine Cu-TCNQ thin films.*

Electrical conductance values of our pristine and heterostructured thin films were evaluated by performing current-voltage (*I–V*) measurements in both in-plane and cross-plane modes at 300 K. *I–V* characteristics of pristine Cu-BTC thin film, both in-plane and cross-plane, are almost identical and give rise to a conductance value of $\sim 10^{-7}$ S (Figures 2.7a,b).[10] Similar observations were noted for the pristine Cu-TCNQ thin film with a conductance value of $\sim 10^{-5}$ S (Figures 2.7c,d).[31] As for the heterostructured AB- and BA-type thin films, in-plane conductance values were found to be $\sim 10^{-5}$ and $\sim 10^{-7}$ S, respectively (Figures 2.8a,c).

However, rectification of current was observed while performing cross-plane *I–V* measurements on both AB- and BA-type heterostructured thin films and a rectification ratio (RR) of $\sim 10^{2}$ was

consistently obtained, which is a remarkable observation in the domain of thin films of CPs (Figures 2.8b,d). *I–V* measurements were also performed under dark and illumination (365 and 630 nm) conditions for the pristine Cu-BTC and Cu-TCNQ thin films (Appendix 2.3). However, no appreciable change was detected and we expect similar results for our AB- and BA-type heterostructured thin films. The directionality of current flow was reversed from source measure unit (SMU)-2 to source measure unit (SMU)-1 and vice versa.

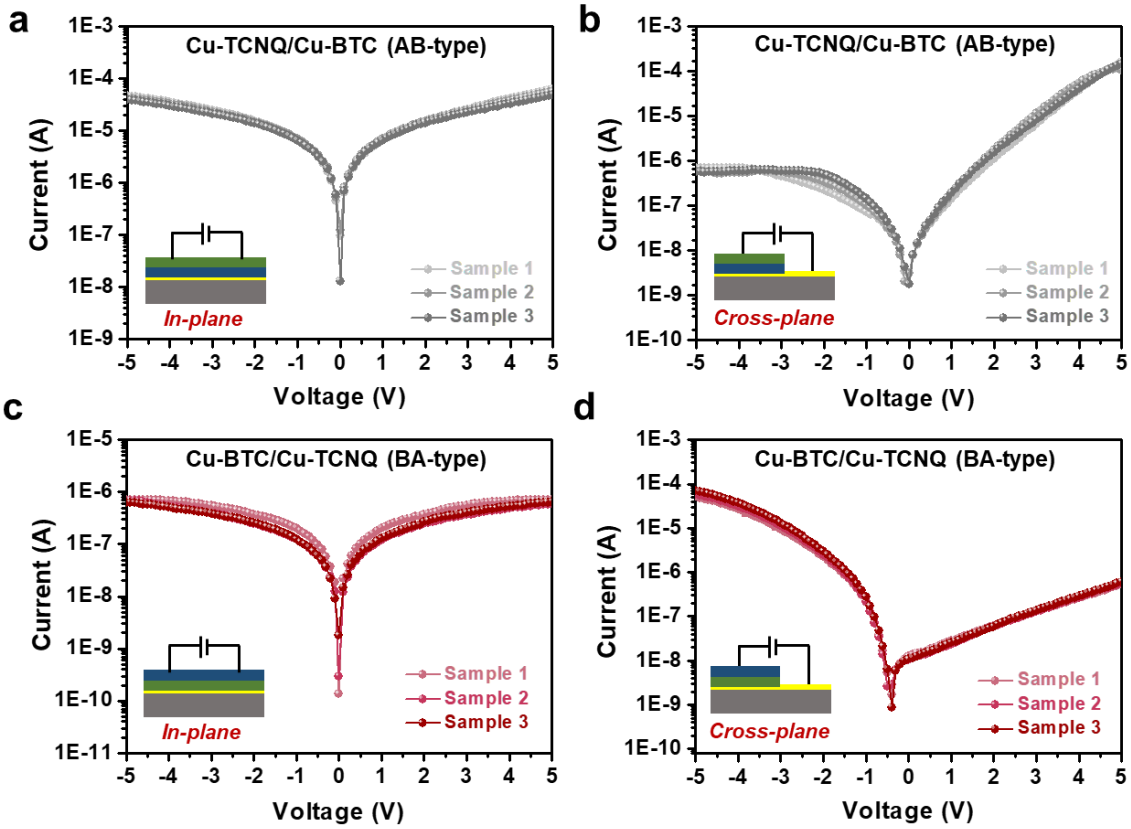

Figure 2.8. *In-plane and cross-plane I–V characteristics at 300 K of (a) AB- and (b) BA-type heterostructured thin film.*

Reverse patterns were observed, thereby confirming the current rectification behavior across heterostructured thin films (Figure 2.9a). Apparently, such current rectification could originate from the Schottky barrier at the metal–semiconductor interfaces, which has been assigned so far for a variety of CPs.[18, 32-40] Subsequently, *I–V* measurements were carried out in both in-plane and cross-plane modes using different contact electrodes, namely, eutectic gallium–indium (EGaIn) and direct Au tips, having different work function values (Figure 2.9b).[18] Similar *I–V* characteristics were consistently

observed for both AB- and BA-type heterostructured thin films, therefore ruling out the possibility of Schottky barrier to be the primary origin of such an electrical rectification. While carrying out in-plane *I–V* measurements in both AB- and BA-type heterostructured thin films, electrical conductance originated mainly from the top layers and thus values were similar to those of pristine Cu-TCNQ and Cu-BTC thin films, respectively.

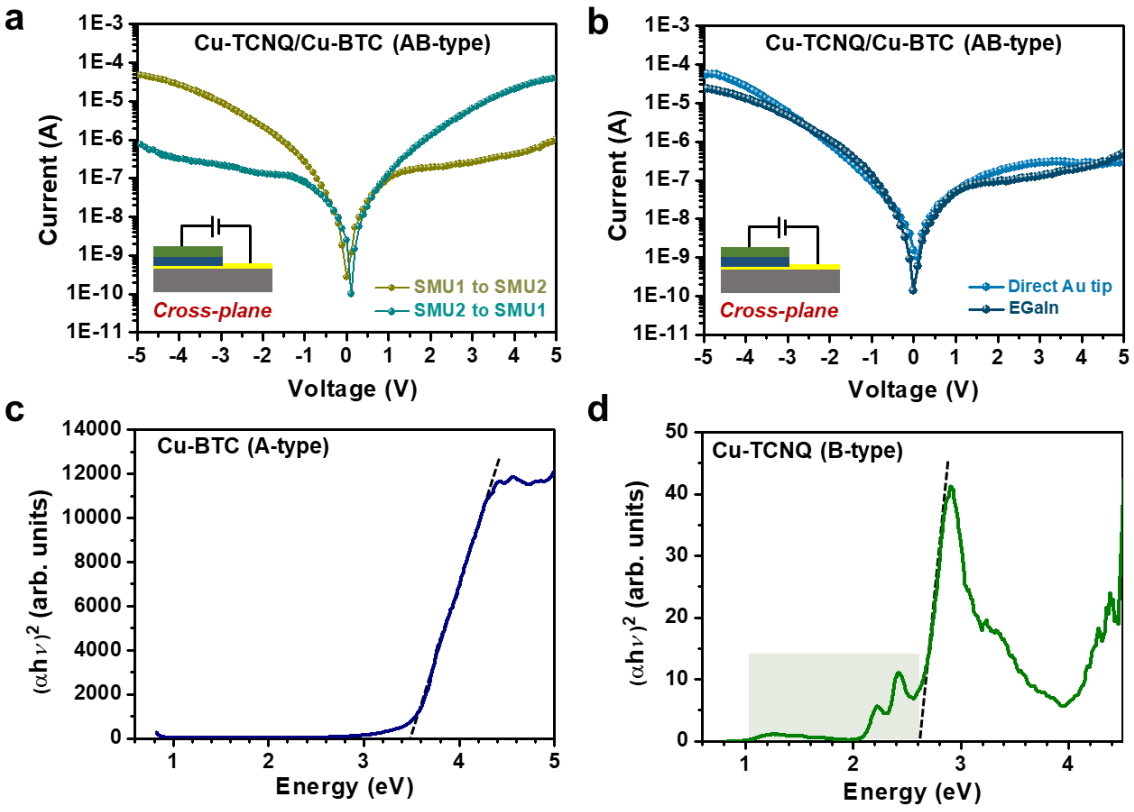

Figure 2.9. *Cross-plane I–V characteristics of (a) and (b) AB-type heterostructured thin film by changing the direction of current flow (by reversing to source measure unit (SMU)-1 from source measure unit (SMU)-2 (dark cyan) and vice-versa (dark yellow)) and by using EGaIn and direct Au tip contact electrodes (having distinct work function values). Tauc plots for (c) pristine Cu-BTC (A-type) thin film and (d) pristine Cu-TCNQ (B-type) thin film where slopes are shown by black lines and highlighted in green part suggests impurity/donor bands in Cu-TCNQ thin film.*

However, upon performing cross-plane *I–V* measurements, the flow of current was restricted at the interface of heterostructure resembling a typical p–n junction.[41] The depletion layer at the interface of the heterostructures could arise due to Cu(I)-TCNQ and Cu-BTC acting as electron donor and acceptor, respectively. Upon looking carefully at the cross-plane *I–V* characteristics of the AB-type

heterostructured thin film (Figure 2.8b), it can be clearly seen that the conductance values pertaining to the negative potential resemble very well those observed for the pristine Cu-BTC thin film (~10^{-7} S) while the conductance values pertaining to positive potential correspond to those of the pristine Cu-TCNQ thin film (~10^{-5} S; ruling out molecular doping[10]) and vice versa for the BA-type heterostructured thin film (Figure 2.8d), which clearly suggests formation of well-defined interfaces. Due to unique Cu−Cu interaction in Cu-BTC, three different spin configurations above the VB in an increasing order of stability are possible: (i) δ-bond state (closed-shell singlet), (ii) ferromagnetic (FM) state (open-shell triplet), and (iii) antiferromagnetic (AFM) state (open-shell singlet).[42-43] Usually, Cu-BTC exists in the AFM ground state whereas other states (FM and δ-bond) can be achieved by means of thermal and photo excitations.[43] These three states have distinct theoretical band gap values: 0.87 eV (δ-bond state), 3.79 eV (FM state), and 3.75 eV (AFM state).[42]

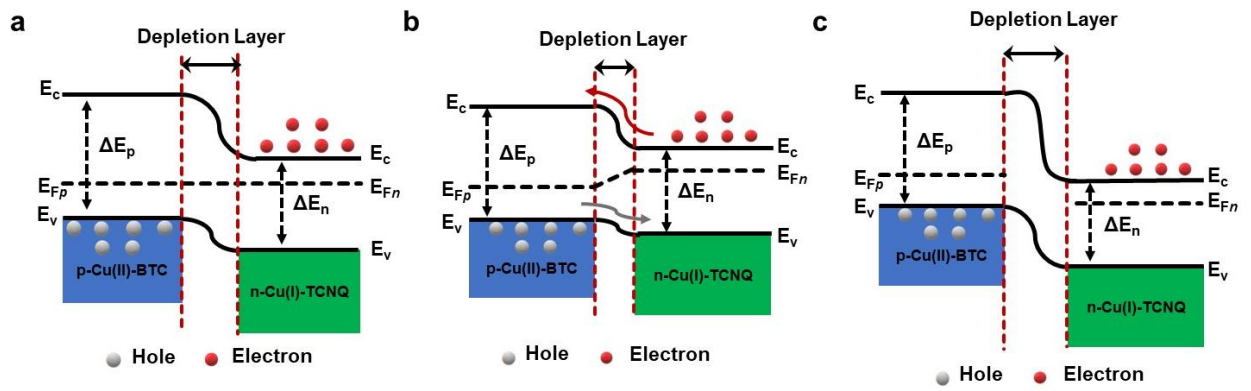

Figure 2.10. *Proposed band diagrams at (a) zero-bias, in (b) forward bias and in (c) reverse bias for heterostructured thin films in qualitative energy scale with standard notations.*

The positions of VB and CB of Cu-BTC were assigned to be at −6.9 and −3.4 eV, respectively.[10] A theoretical band gap value of ~1.8 eV was also reported for Cu-BTC.[44] In the present work, we have estimated an optical band gap value of ~3.5 eV for the pristine Cu-BTC thin film (Figure 2.9c) and attribute it to the presence of a stable AFM ground state. As for the Cu-TCNQ, depending on various experimental methods and theoretical calculations, the band gap energies were reported to be in the range 0.13−0.55 eV.[9, 45-48] The positions of VB and CB of Cu-TCNQ were assigned to be at −5.45 and −5.08 eV, respectively.[48] Interestingly, recent calculations on Cu-TCNQ showed the existence of the Fermi level below 1.0 eV of the CB edge and, also, ultraviolet photoelectron spectroscopy revealed an intense peak at ~0.8 eV below the Fermi level, which was attributed to be characteristic of the donor

state,[49] thereby making the band gap of Cu-TCNQ beyond 1.8 eV. We have realized an optical band gap of ~2.6 eV for the pristine Cu-TCNQ thin film with clear signatures of impurity/donor bands at ~0.9, ~2.0, and ~2.25 eV (Figure 2.9d). Electrochemical analysis on pristine Cu-BTC and Cu-TCNQ thin films could provide additional insights for the relative positions of the VBs and CBs. In view of our measured electrical conductance values and estimated optical band gap values, we have proposed a band diagram for the electrical rectification in our AB- and BA-type heterostructured thin films in a qualitative energy scale (Figure 2.10). Upon applying forward bias, the depletion layer narrowed, and after a certain potential, the depletion layer collapsed and current started to flow (Figure 2.10a). During reverse bias, potential difference increased, which resulted in the broadening of the depletion layer, and flow of current was stopped, resembling an electrical insulator (Figure 2.10c). Such an interesting effect was clearly evident when we performed *I–V* measurements at an elevated temperature of 400 K.

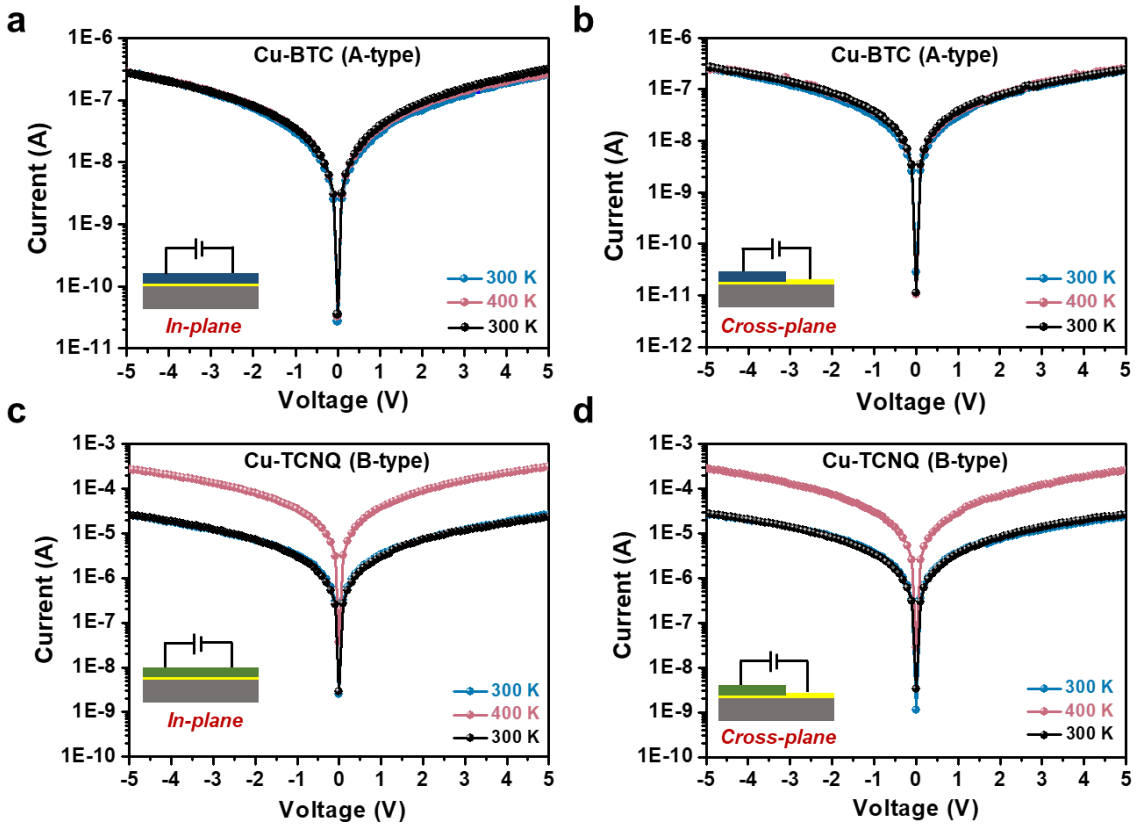

Figure 2.11. *Current-voltage (I-V) characteristics of pristine Cu-BTC thin film at variable temperatures in both (a) in-plane and (b) cross-plane configurations showing no effect of temperature towards electrical conductance, whereas for pristine Cu-TCNQ thin film at variable temperatures in both (c) in-plane and (d) cross-plane modes showing enhancement in electrical conductance by one order of magnitude at 400 K (pink) with respect to 300 K (black) and completely reverting back upon cooling to 300 K (blue).*

In the case of the pristine Cu-BTC thin film, both in-plane and cross-plane electrical conductance values were almost unaltered at 400 K (Figures 2.11a,b) whereas a significant enhancement in electrical conductance value in both in-plane and cross-plane modes for the pristine Cu-TCNQ thin film was observed at 400 K (Figures 2.11c,d). As for the AB-type heterostructured thin film, almost identical enhancement in the in-plane conductance value was noted at 400 K, likewise for the pristine Cu-TCNQ thin film; however, in the cross-plane mode, current values in positive potential were markedly increased (current values in negative potential remained unaltered likewise pristine Cu-BTC thin film), which resulted in a remarkable increase of the RR value from ~10^2 at 300 K to ~10^3 at 400 K (Figure 2.12a,b).

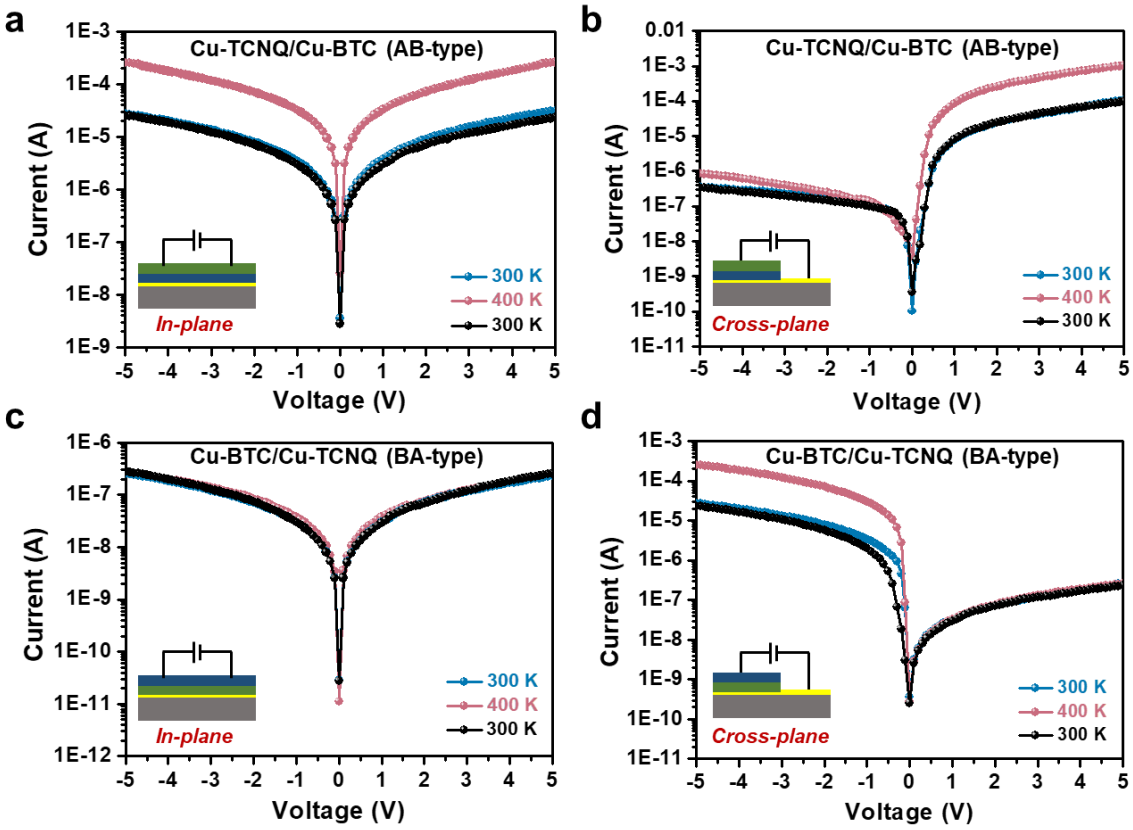

Figure 2.12. *I–V characteristics of AB-type heterostructured thin film at variable temperatures showing (a) in-plane enhancement in positive and negative potentials while (b) cross-plane enhancement only in positive potential at 400 K. Similarly, I–V characteristics of the BA-type heterostructured thin film at variable temperatures showing (c) no in-plane enhancement in positive and negative potentials while (d) cross-plane enhancement only in negative potential at 400 K.*

Consistently, the same influence of temperature on current and RR values in opposite potential was also observed in the BA-type heterostructured thin film (Figures 2.12c,d). In our AB-type heterostructured thin film, when negative and positive terminals of source meter were respectively connected to the upper side (Cu-TCNQ) and the lower side (Cu-BTC), forward bias *I*−*V* characteristics was observed and vice versa in reverse bias. Thus, top and bottom layers of our AB-type heterostructured thin film are behaving as n-type and p-type semiconductors, respectively, complementing *I*−*V* characteristics of commercial p−n junction Si diode (Figure 2.13).[15]

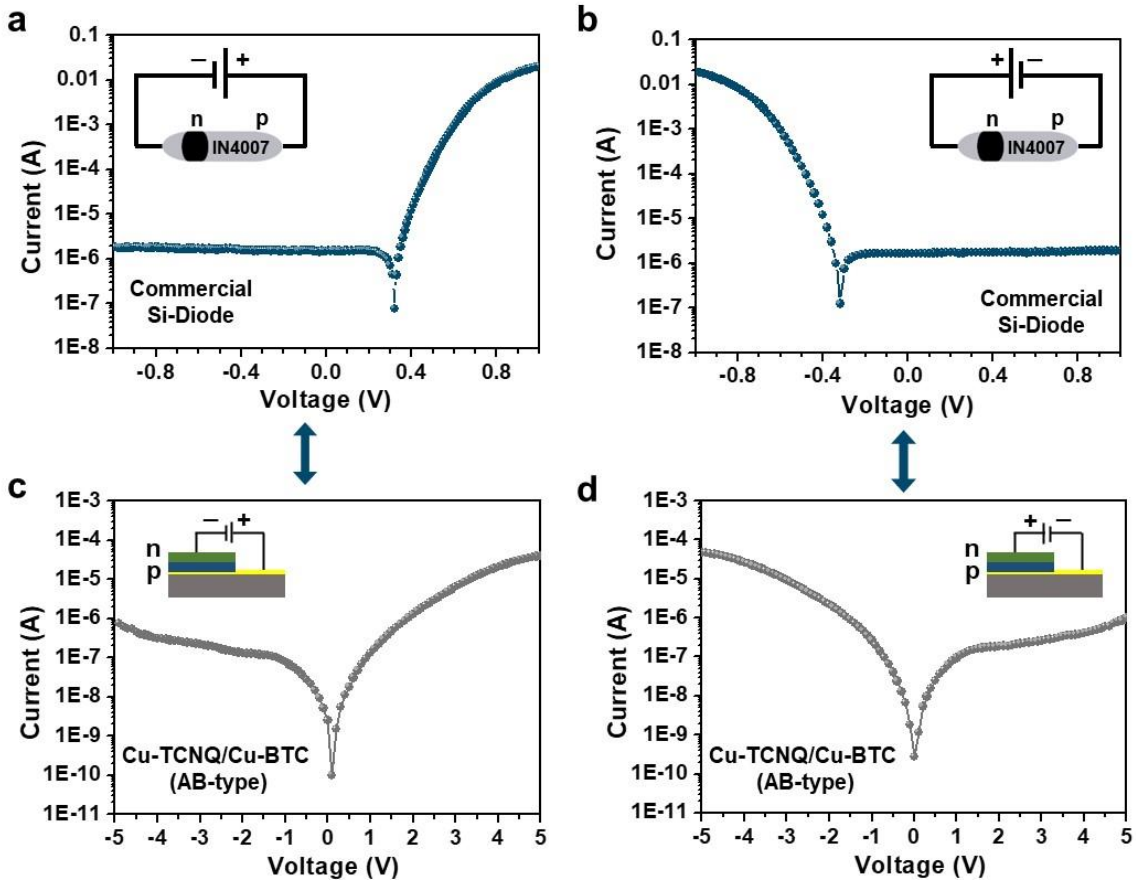

Figure 2.13. *Current-voltage (I-V) characteristic of commercial Si diode (1N4007) showing p-n junction in (a) forward bias and (b) reverse bias along with our AB-type heterostructured thin film in (c) forward bias and (d) reverse bias to correlate the direction of current flow in both.*

To further support our claim on the emergence of p−n junction interface in AB- and BA-type heterostructured thin films, we have recorded capacitance−voltage (C−V) characteristics and plotted $1/C^2$ versus V, the so-called Mott−Schottky (MS) plot. Our MS exhibited both positive and negative slopes with inverted V-like shape (likewise observed for inorganic oxide/sulfide semiconductor

heterostructures[50-51]) where the negative slope represents the p-type semiconductor Cu-BTC with a hole as the majority charge carrier and the positive slope represents the n-type semiconductor Cu-TCNQ with electrons as the majority charge carrier (Figure 2.14).

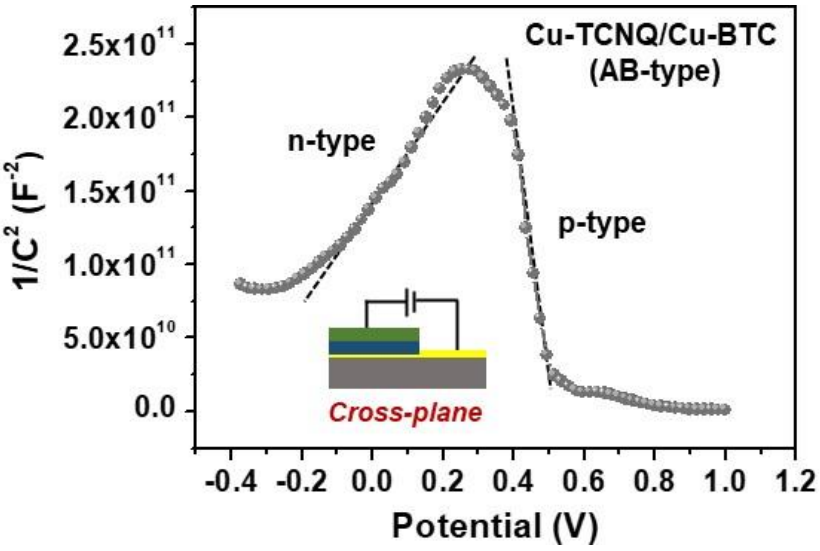

Figure 2.14. *Mott-Schottky ($1/C^2$ versus V; C is capacitance and V is voltage) plot recorded on AB-type heterostructured thin film at 100 Hz showing both n-type and p-type characteristics (slopes are indicated by black lines) suggests the formation of p-n junction.*

2.4 Conclusions

In summary, we have successfully fabricated high-quality thermally stable lattice-mismatched heterostructured thin films of Cu(II)-BTC and Cu(I)-TCNQ by the LbL method. Such an unusual growth of Cu(I)-TCNQ on top of Cu-BTC was possible due to spontaneous reduction of Cu(II) to Cu(I) at the solid−liquid interface, i.e. interfacial reduction reaction (IRR). The rectification of current across AB- and BA-type lattice-mismatched heterostructured thin films at 300 K evidenced an emergent interface due to the formation of p-n junction at the interface and an enhanced RR value was observed at the elevated temperature (400 K).[52] Such heterostructured thin films of CPs, in particular with different oxidation states of metal ions, could provide a new avenue for studying other emergent interfacial phenomena, specifically, electronic reconstruction, viz., formation of a two-dimensional electron gas.

2.5 Appendix

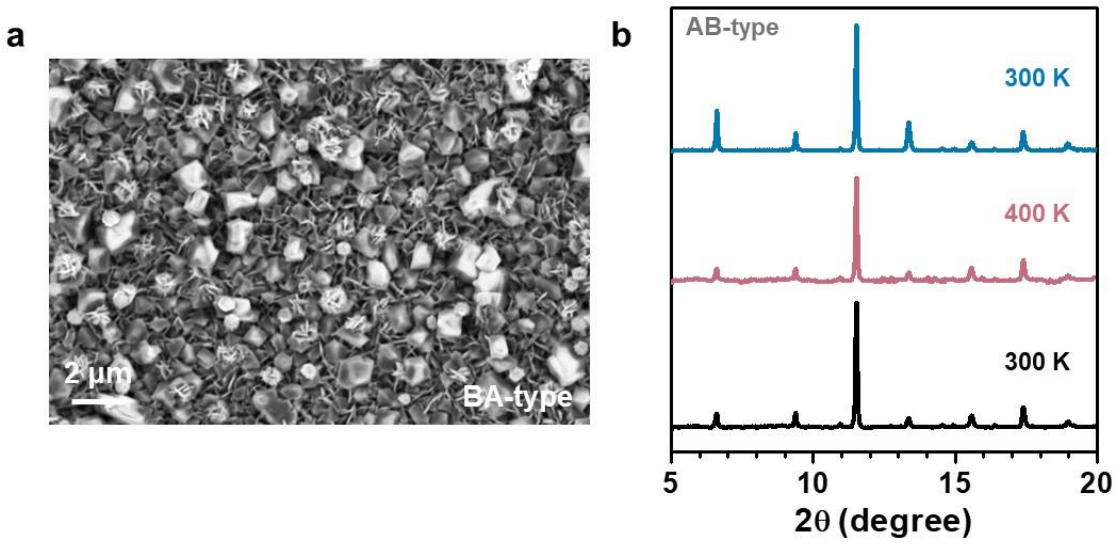

Appendix 2.1. *(a) FESEM image showing Cu-BTC crystallites (up to four LbL cycles) on pre-fabricated Cu-TCNQ thin film in BA-type heterostructured thin film. (b) Out-of-plane XRD patterns of AB-type heterostructured thin film at variable temperatures, 300 K (black), 400 K (pink) and after cooling back to 300 K (blue).*

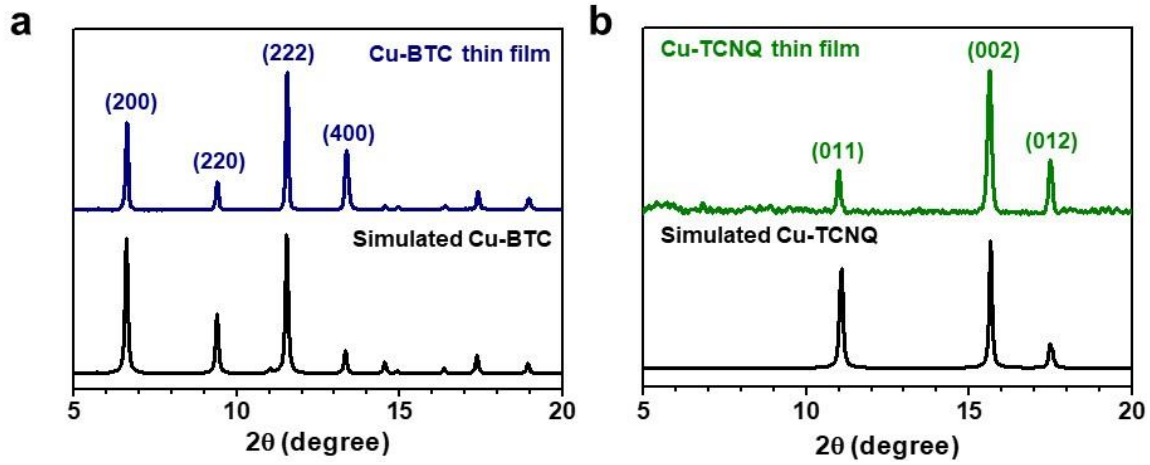

Appendix 2.2. *Out-of-plane XRD patterns of simulated and experimental (a) pristine Cu-BTC and (b) pristine Cu-TCNQ thin films.*

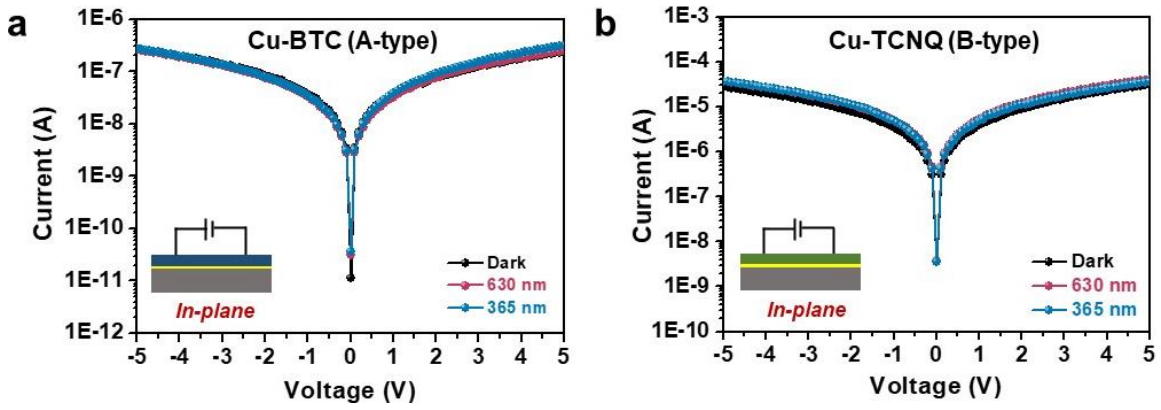

Appendix 2.3. *In-plane current–voltage (I-V) characteristics of (a) pristine Cu-BTC and (b) Cu-TCNQ thin films in dark and illumination (630 nm and 365 nm) conditions by using EGaIn top electrodes.*

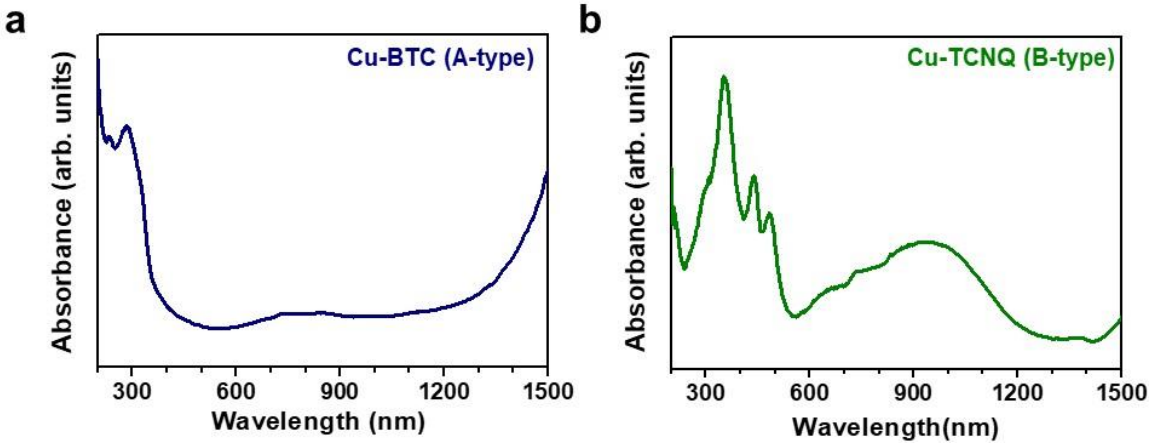

Appendix 2.4. *Solid-state UV-vis spectra of (a) pristine Cu-BTC (A-type) and (b) pristine Cu-TCNQ (B-type) thin films*

2.6 References

1. Ohtomo, A.; Hwang, H., A high-mobility electron gas at the $LaAlO_3/SrTiO_3$ heterointerface. *Nature* **2004,** *427* (6973), 423-426.

2. Reyren, N.; Thiel, S.; Caviglia, A.; Kourkoutis, L. F.; Hammerl, G.; Richter, C.; Schneider, C. W.; Kopp, T.; Ruetschi, A.-S.; Jaccard, D., Superconducting interfaces between insulating oxides. *Science* **2007,** *317* (5842), 1196-1199.

3. Mannhart, J.; Schlom, D. G., Oxide interfaces—an opportunity for electronics. *Science* **2010,** *327* (5973), 1607-1611.

4. Hwang, H. Y.; Iwasa, Y.; Kawasaki, M.; Keimer, B.; Nagaosa, N.; Tokura, Y., Emergent phenomena at oxide interfaces. *Nat. Mater.* **2012,** *11* (2), 103-113.

5. Huang, Z.; Ariando; Renshaw Wang, X.; Rusydi, A.; Chen, J.; Yang, H.; Venkatesan, T., Interface engineering and emergent phenomena in oxide heterostructures. *Adv. Mater.* **2018,** *30* (47), 1802439.

6. Alves, H.; Molinari, A. S.; Xie, H.; Morpurgo, A. F., Metallic conduction at organic charge-transfer interfaces. *Nat. Mater.* **2008,** *7* (7), 574-580.

7. Bera, S.; Pradhan, N., Perovskite Nanocrystal Heterostructures: Synthesis, Optical Properties, and Applications. *ACS Energy Lett.* **2020,** *5* (9), 2858-2872.

8. Chui, S. S. Y.; Lo, S. M. F.; Charmant, J. P. H.; Orpen, A. G.; Williams, I. D., A Chemically Functionalizable Nanoporous Material $[Cu_3(TMA)_2(H_2O)_3]_n$. *Science* **1999,** *283* (5405), 1148-1150.

9. Heintz, R. A.; Zhao, H.; Ouyang, X.; Grandinetti, G.; Cowen, J.; Dunbar, K. R., New Insight into the Nature of Cu(TCNQ): Solution Routes to Two Distinct Polymorphs and Their Relationship to Crystalline Films That Display Bistable Switching Behavior. *Inorg. Chem.* **1999,** *38* (1), 144-156.

10. Talin, A. A.; Centrone, A.; Ford, A. C.; Foster, M. E.; Stavila, V.; Haney, P.; Kinney, R. A.; Szalai, V.; El Gabaly, F.; Yoon, H. P., Tunable electrical conductivity in metal-organic framework thin-film devices. *Science* **2014,** *343* (6166), 66-69.

11. Allendorf, M. D.; Foster, M. E.; Leonard, F.; Stavila, V.; Feng, P. L.; Doty, F. P.; Leong, K.; Ma, E. Y.; Johnston, S. R.; Talin, A. A., Guest-induced emergent properties in metal–organic frameworks. *J. Phys. Chem. Lett.* **2015,** *6* (7), 1182-1195.

12. Guo, Z.; Panda, D. K.; Maity, K.; Lindsey, D.; Parker, T. G.; Albrecht-Schmitt, T. E.; Barreda-Esparza, J. L.; Xiong, P.; Zhou, W.; Saha, S., Modulating the electrical conductivity of metal–organic framework films with intercalated guest π-systems. *J. Mater. Chem. C* **2016,** *4* (5), 894-899.

13. Le Ouay, B.; Boudot, M.; Kitao, T.; Yanagida, T.; Kitagawa, S.; Uemura, T., Nanostructuration of PEDOT in porous coordination polymers for tunable porosity and conductivity. *J. Am. Chem. Soc.* **2016,** *138* (32), 10088-10091.

14. Wang, T.; Farajollahi, M.; Henke, S.; Zhu, T.; Bajpe, S. R.; Sun, S.; Barnard, J. S.; Lee, J. S.; Madden, J. D.; Cheetham, A. K., Functional conductive nanomaterials via polymerisation in nano-channels: PEDOT in a MOF. *Mater. Horiz.* **2017,** *4* (1), 64-71.

15. Prasoon, A.; Dhara, B.; Roy, D.; Rana, S.; Bhand, S.; Ballav, N., Achieving current rectification ratios $\geq 10^5$ across thin films of coordination polymer. *Chem. Sci.* **2019,** *10* (43), 10040-10047.

16. Bhoi, U.; Ray, S.; Bhand, S.; Ninawe, P.; Roy, D.; Rana, S.; Tarafder, K.; Ballav, N., Distal Synergistic Effect in Bimetal–Organic Framework for Superior Catalytic Water Oxidation. *ACS Energy Lett.* **2023,** *8* (10), 4465-4473.

17. Rana, S.; Rajendra, R.; Dhara, B.; Jha, P. K.; Ballav, N., Highly hydrophobic and chemically rectifiable surface-anchored metal-organic framework thin-film devices. *Adv. Mater. Interfaces* **2016,** *3* (13), 1500738.

18. Rana, S.; Prasoon, A.; Jha, P. K.; Prathamshetti, A.; Ballav, N., Thermally driven resistive switching in solution-processable thin films of coordination polymers. *J. Phys. Chem. Lett.* **2017,** *8* (20), 5008-5014.

19. Summerfield, A.; Cebula, I.; Schröder, M.; Beton, P. H., Nucleation and Early Stages of Layer-by-Layer Growth of Metal Organic Frameworks on Surfaces. *J. Phys. Chem. C* **2015,** *119* (41), 23544-23551.

20. Rana, S.; Prasoon, A.; Sadhukhan, P.; Jha, P. K.; Sathe, V.; Barman, S. R.; Ballav, N., Spontaneous Reduction of Copper(II) to Copper(I) at Solid–Liquid Interface. *J. Phys. Chem. Lett.* **2018,** *9* (21), 6364-6371.

21. Rana, S.; Sindhu, P.; Ballav, N., Perspective on the Interfacial Reduction Reaction. *Langmuir* **2019,** *35* (30), 9647-9659.

22. Thürmer, K.; Schneider, C.; Stavila, V.; Friddle, R. W.; Léonard, F.; Fischer, R. A.; Allendorf, M. D.; Talin, A. A., Surface Morphology and Electrical Properties of Cu_3BTC_2 Thin Films Before and After Reaction with TCNQ. *ACS Appl. Mater. Interfaces* **2018,** *10* (45), 39400-39410.

23. Gucciardi, P.; Trusso, S.; Vasi, C.; Patane, S.; Allegrini, M., Nano-Raman imaging of Cu–TCNQ clusters in TCNQ thin films by scanning near-field optical microscopy. *Phys. Chem. Chem. Phys.* **2002,** *4* (12), 2747-2753.

24. Dong, Z.; Mi, Z.; Shi, W.; Jiang, H.; Zheng, Y.; Yang, K., High pressure effects on hydrate Cu-BTC investigated by vibrational spectroscopy and synchrotron X-ray diffraction. *RSC Adv.* **2017,** *7* (87), 55504-55512.

25. Biemmi, E.; Scherb, C.; Bein, T., Oriented growth of the metal organic framework $Cu_3(BTC)_2(H_2O)_3 \cdot xH_2O$ tunable with functionalized self-assembled monolayers. *J. Am. Chem. Soc.* **2007,** *129* (26), 8054-8055.

26. Fernandez, C. A.; Martin, P. C.; Schaef, T.; Bowden, M. E.; Thallapally, P. K.; Dang, L.; Xu, W.; Chen, X.; McGrail, B. P., An electrically switchable metal-organic framework. *Sci. Rep.* **2014,** *4* (1), 1-6.

27. Zacher, D.; Yusenko, K.; Bétard, A.; Henke, S.; Molon, M.; Ladnorg, T.; Shekhah, O.; Schüpbach, B.; de los Arcos, T.; Krasnopolski, M., Liquid-Phase Epitaxy of Multicomponent Layer-Based Porous Coordination Polymer Thin Films of $[M(L)(P)_{0.5}]$ Type: Importance of Deposition Sequence on the Oriented Growth. *Chem. Eur. J.* **2011,** *17* (5), 1448-1455.

28. Wang, Z.; Liu, J.; Lukose, B.; Gu, Z.; Weidler, P. G.; Gliemann, H.; Heine, T.; Wöll, C., Nanoporous designer solids with huge lattice constant gradients: multiheteroepitaxy of metal–organic frameworks. *Nano Lett.* **2014,** *14* (3), 1526-1529.

29. Zhuang, J.-L.; Kind, M.; Grytz, C. M.; Farr, F.; Diefenbach, M.; Tussupbayev, S.; Holthausen, M. C.; Terfort, A., Insight into the oriented growth of surface-attached metal–organic frameworks: surface functionality, deposition temperature, and first layer order. *J. Am. Chem. Soc.* **2015,** *137* (25), 8237-8243.

30. Sun, Y.; Amsler, M.; Goedecker, S.; Caravella, A.; Yoshida, M.; Kato, M., Surfactant-assisted synthesis of large Cu-BTC MOF single crystals and their potential utilization as photodetectors. *CrystEngComm* **2019,** *21* (26), 3948-3953.

31. Liu, S.-G.; Liu, Y.-Q.; Wu, P.-J.; Zhu, D.-B., Multifaceted study of CuTCNQ thin-film materials. Fabrication, morphology, and spectral and electrical switching properties. *Chem. Mater.* **1996,** *8* (12), 2779-2787.

32. Dalapati, S.; Saha, R.; Jana, S.; Patra, A. K.; Bhaumik, A.; Kumar, S.; Guchhait, N., A multifunctional porous organic Schottky barrier diode. *Angew. Chem.* **2012,** *124* (50), 12702-12705.

33. Bhattacharya, B.; Layek, A.; Alam, M. M.; Maity, D. K.; Chakrabarti, S.; Ray, P. P.; Ghoshal, D., Cd (II) based metal–organic framework behaving as a Schottky barrier diode. *Chem. Commun.* **2014,** *50* (58), 7858-7861.

34. Roy, S.; Das, M.; Bandyopadhyay, A.; Pati, S. K.; Ray, P. P.; Maji, T. K., Colossal increase in electric current and high rectification ratio in a photoconducting, self-cleaning, and luminescent schottky barrier nmof diode. *J. Phys. Chem. C* **2017,** *121* (42), 23803-23810.

35. Dutta, B.; Dey, A.; Sinha, C.; Ray, P. P.; Mir, M. H., Photochemical structural transformation of a linear 1D coordination polymer impacts the electrical conductivity. *Inorg. Chem.* **2018,** *57* (14), 8029-8032.

36. Dey, S.; Sil, S.; Dutta, B.; Naskar, K.; Maity, S.; Ray, P. P.; Sinha, C., Designing of Pb (II)-based novel coordination polymers (CPs): structural elucidation and optoelectronic application. *ACS omega* **2019,** *4* (22), 19959-19968.

37. Jana, S.; Jana, R.; Sil, S.; Dutta, B.; Sato, H.; Ray, P. P.; Datta, A.; Akitsu, T.; Sinha, C., Influence of axial linkers on polymerization in paddle-wheel Cu(II) coordination polymers for the application of optoelectronics devices. *Cryst. Growth Des.* **2019,** *19* (11), 6283-6290.

38. Ghorai, P.; Dey, A.; Brandão, P.; Benmansour, S.; Gómez García, C. J.; Ray, P. P.; Saha, A., Multifunctional Ni (II)-Based Metamagnetic Coordination Polymers for Electronic Device Fabrication. *Inorg. Chem.* **2020,** *59* (13), 8749-8761.

39. Naskar, K.; Dey, A.; Maity, S.; Ray, P. P.; Ghosh, P.; Sinha, C., Biporous Cd (II) Coordination Polymer via in Situ Disulfide Bond Formation: Self-Healing and Application to Photosensitive Optoelectronic Device. *Inorg. Chem.* **2020,** *59* (8), 5518-5528.

40. Ghorai, P.; Dey, A.; Hazra, A.; Dutta, B.; Brandão, P.; Ray, P. P.; Banerjee, P.; Saha, A., Cd (II) based coordination polymer series: fascinating structures, efficient semiconductors, and promising nitro aromatic sensing. *Cryst. Growth Des.* **2019,** *19* (11), 6431-6447.

41. Frisenda, R.; Molina-Mendoza, A. J.; Mueller, T.; Castellanos-Gomez, A.; Van Der Zant, H. S., Atomically thin p–n junctions based on two-dimensional materials. *Chem. Soc. Rev.* **2018,** *47* (9), 3339-3358.

42. Butler, K. T.; Hendon, C. H.; Walsh, A., Electronic chemical potentials of porous metal–organic frameworks. *J. Am. Chem. Soc.* **2014,** *136* (7), 2703-2706.

43. Hendon, C. H.; Walsh, A., Chemical principles underpinning the performance of the metal–organic framework HKUST-1. *Chem. Sci.* **2015,** *6* (7), 3674-3683.

44. He, Y.; Talin, A. A.; Allendorf, M. D., Thermoelectric Properties of 2D $Ni_3(HITP)_2$ and 3D $Cu_3(BTC)_2$ MOFs: First-Principles Studies. *ECS J. Solid State Sci. Technol.* **2017,** *6* (12), N236.

45. Siemons, W.; Bierstedt, P.; Kepler, e. R., Electronic properties of a new class of highly conductive organic solids. *Chem. Phys.* **1963,** *39* (12), 3523-3528.

46. Inoue, M.; Inoue, M. B., Infrared spectroscopic study of electrically conducting tetracyanoquinodimethane salts of copper chelates with ethylenediamine. *J. Chem. Soc., Faraday Trans. 2* **1985,** *81* (4), 539-547.

47. Kamitsos, E.; Papavassiliou, G. C.; Karakassides, M., Electronic Spectra of AgTCNQ and CuTCNQ Charge-Transfer Compounds. *Mol. Cryst. Liq. Cryst.* **1986,** *134* (1), 43-51.

48. Mohammadtaheri, M.; Ramanathan, R.; Walia, S.; Ahmed, T.; Weerathunge, P.; Anderson, S. R.; Field, M. R.; Dekiwadia, C. D.; O'Mullane, A. P.; Della Gaspera, E., Broadband light active MTCNQ-based metal–organic semiconducting hybrids for enhanced redox catalysis. *Appl. Mater. Today* **2018,** *13*, 107-115.

49. Capitán, M. J.; Alvarez, J.; Yndurain, F., Organometallic MTCNQ films: a comparative study of CuTCNQ versus AgTCNQ. *Phys. Chem. Chem. Phys.* **2018,** *20* (33), 21705-21715.

50. Mukherjee, B.; Peterson, A.; Subramanian, V. R., 1D CdS/PbS heterostructured nanowire synthesis using cation exchange. *Chem. Commun.* **2012,** *48* (18), 2415-2417.

51. Gultom, N. S.; Abdullah, H.; Kuo, D.-H.; Ke, W.-C., Oriented p–n heterojunction Ag_2O/Zn (O, S) nanodiodes on mesoporous SiO2 for photocatalytic hydrogen production. *ACS Appl. Energy Mater.* **2019,** *2* (5), 3228-3236.

52. Sindhu, P.; Prasoon, A.; Rana, S.; Ballav, N., Emergent Interface in Heterostructured Thin Films of Cu(II) and Cu(I) Coordination Polymers. *J. Phys. Chem. Lett.* **2020,** *11* (15), 6242-6248.

Electrical Transport Properties in Lattice-matched Electronically Heterostructured Thin Films

3.1 Introduction

Heterostructures have a potential to provide new avenues in the domain of electronic as well as electrochemical devices.[1-3] However, the challenge remained in rationally designing a heterostructure with a well-defined electronic interface which could have profound impact in electronic device applications.[4-5] In the fabrication of heterostructured thin films, lattice-matching is one of the critical factors which can minimize the defects at the interface leading to desirable electrical transport properties.[6] Keeping this in mind, what happens if a thin film system is developed by depositing pristine CP layer on top of a molecularly doped CP layers whereby lattice-mismatch can be avoided?

Herein, we have designed a lattice-matched heterostructure of pristine and molecularly-doped CPs, namely CP/Guest@CP and successfully fabricated it by depositing pristine Cu-BTC thin film on top of TCNQ-doped Cu-BTC (TCNQ@Cu-BTC) thin film via LbL method (Figure 3.1). As TCNQ@Cu-BTC system is well-explored and known for its high enhancement in the electrical conductivity after TCNQ doping by six orders of magnitude (~10^{-8} S/cm to ~10^{-2} S/cm) due to the generation of conducting paths within Cu-BTC framework.[7-8] To investigate the interfacial characteristics of a lattice-matched heterostructure composed of two CPs with different electrical conductivities, the electrical transport properties were examined.

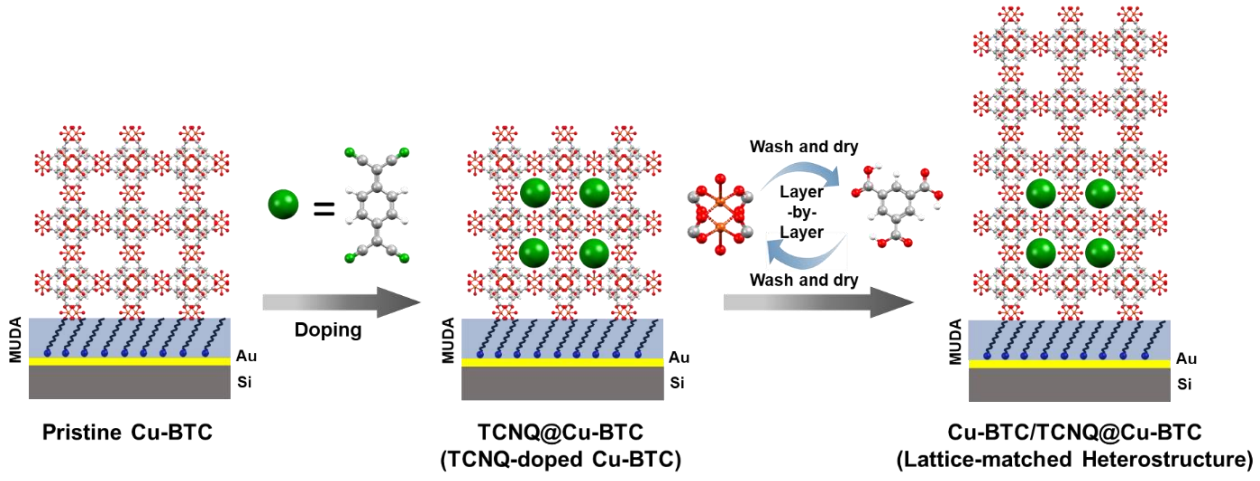

Figure 3.1. *Schematic of the growth of lattice-matched heterostructured thin film of CP/Guest@CP by layer-by-layer (LbL) technique. Fabrication of pristine Cu-BTC by LbL method followed by molecular doping of TCNQ in Cu-BTC and furthermore, Cu-BTC was fabricated on top of TCNQ@Cu-BTC thin film to generate lattice-matched heterostructured thin film.*

3.2 Materials and Methods

Materials: Copper acetate [$Cu(OAc)_2.H_2O$], 1,3,5-benzenetricarboxylic acid (H_3BTC), 7,7,8,8-tetracyanoquinodimethane (TCNQ), Ferrocene (Fc), 11-Merceptoundecanoic acid (MUDA), PET (polyethylene terephthalate) substrate and Au(111) substrate (100 nm Au coated Si wafer) were purchased from Sigma-Aldrich and ethanol from Merck. All the chemicals/materials were used as such, without any further purification except PET and Au(111) substrates.

Functionalization of Au Substrate: Au substrate was cleaned by dipping into Piranha solution (H_2SO_4 (95-98%)/H_2O_2 (30%); v/v 3:1) for 30 minutes (note: proper safety care must be taken) and washed with Milli-Q water followed by ethanol and then dried with N_2. Subsequently, Au substrate was functionalized with a carboxy-terminated (-COOH) SAM by dipping it into the 1mM MUDA solution in ethanol/acetic acid (v/v 9:1) for 48 hours and then washed with ethanol followed by drying under the stream of N_2 gas.

Functionalization of PET Substrate: PET substrate was cleaned with ethanol followed by N_2 drying and Au layer (thickness ≈100 nm was sputtered on clean PET substrate. The same procedure was followed for the functionalization of PET substrate as Au substrate.

Fabrication of Pristine Cu-BTC Thin Film: Carboxy functionalized Au substrate was immersed in 1mM ethanolic solution of $Cu(OAc)_2.H_2O$ kept at 330 K for 30 minutes followed by washing with ethanol to remove unbonded metal ions and subsequently the metal anchored substrate was immersed in 1mM ethanolic solution of H_3BTC kept at 330 K for 30 minutes (washed with ethanol in between followed by drying with stream of N_2 gas) to complete one LbL cycle. 20 cycles of LbL were performed to get uniform Cu-BTC thin film (thickness was estimated to be approximately ~540 nm).

Fabrication of TCNQ@Cu-BTC Thin Film: Pre-fabricated pristine Cu-BTC thin film was first activated at 353 K for 4 hours in vacuum and then immersed into a saturated ethanolic solution of TCNQ for 48 hours followed by washing with ethanol to remove the surface adsorbed TCNQ and dried under a stream of N_2 gas. (Note: no change in the thickness has been estimated after TCNQ doping in Cu-BTC thin film).

Fabrication of Fc@Cu-BTC Thin Film: Pre-fabricated pristine Cu-BTC thin film was first activated at 353 K for 4 hours in vacuum and then immersed into a 100 μM ferrocene solution in n-hexane for

24 hours followed by washing with n-hexane to remove the surface adsorbed ferrocene and dried under a stream of N_2 gas.

Fabrication of Cu-BTC/TCNQ@Cu-BTC Thin Film: Pre-fabricated TCNQ@Cu-BTC thin film was subsequently dipped into ethanolic solutions of $Cu(OAc)_2$ and H_3BTC to fabricate the Cu-BTC thin film on top of TCNQ@Cu-BTC. 20 cycles of LbL with 30 minutes were performed to achieve the uniform heterostructured thin film of doped and undoped Cu_3BTC_2. (thickness value was estimated to be approximately ~1.1 μm).

Fabrication of Fc@Cu-BTC/TCNQ@Cu-BTC Thin Film: Pre-fabricated Cu-BTC/TCNQ@Cu-BTC thin film was activated at 353 K for 4 hours in vacuum and then immersed into a 100 μM ferrocene solution in n-hexane for 24 hours followed by washing with n-hexane to remove the surface adsorbed ferrocene and dried under a stream of N_2 gas.

Characterizations: The surface morphologies of pristine, doped and heterostructured thin films were performed by Zeiss Ultra Plus FESEM. Out-of-plane XRD measurements were performed at room temperature using a Bruker D8 Advance diffractometer using Cu Kα radiation (λ = 1.5406 Å). Contact angle measurements were recorded using Holmarc's Contact Angle Meter. Raman spectra (λ_{exc} = 532 nm) were recorded at Raman microscope (Raman-Renishaw InVia) with the acquisition time of 10 s and Raman microscope (LabRAM HR, HoribaJobinYvon) (λ_{exc} = 632.8 nm) with a 50× objective lens (spectral resolution of the system is ~1 cm^{-1}). Electrical transport measurements (*I-V*) on various thin film samples were carried out using a Keithley 4200 SCS Parameter Analyser system attached to an Everbeing probe station (equipped with a thermal chuck) with a eutectic gallium indium (EGaIn) alloy. The carrier type behaviour along with hall mobility and carrier concentration were confirmed by the M-91 FastHall measurement instrument equipped with 1 T (Tesla) permanent magnet.

3.3 Results and Discussion

Cu-BTC, TCNQ@Cu-BTC, and Cu-BTC/TCNQ@Cu-BTC thin films were fabricated by LbL method (following the standardized protocols in our lab) – as illustrated in Figure 3.1.[1, 9-11] Briefly, Au substrate was functionalized with self-assembled monolayers of carboxy thiol (MUDA = mercaptoundecanoic acid) and sequentially dipped into ethanolic solutions of copper acetate [$Cu(OAc)_2$] and H_3BTC (1,3,5-benzenetricarboxylic acid) resulting in the growth of Cu-BTC thin film. Here, we have explored TCNQ as a redox-active dopant in Cu-BTC framework, aligning with the pervious literature (Section 3.1).[7] TCNQ is an electron-accepting π-acid due to its strong electron-withdrawing properties. It has high

affinity to accept electrons, therefore, can be used as a dopant to induce charge transfer within CPs.[7] In order to carry out molecular doping, the Cu-BTC thin film was first activated at high temperature (353 K) to remove the solvent from the pores and then dipped into ethanolic solution of TCNQ followed by washing and removal of undesired TCNQ leading to the fabrication of TCNQ@Cu-BTC thin film. Finally, the TCNQ@Cu_3BTC_2 thin film was sequentially dipped into [$Cu(OAc)_2$] and H_3BTC solutions to further deposit the Cu-BTC layer on top of the pre-fabricated TCNQ@Cu-BTC layer – so called Cu-BTC/TCNQ@Cu-BTC thin film.

Field-emission scanning electron microscopy (FESEM) images showed uniform coverage on the Au substrate with the characteristic nano-octahedral surface morphology of the Cu-BTC crystallites (Appendix 3.1).[1] Cross-sectional FESEM image suggested a thickness value of ca. 540 nm for the Cu-BTC thin film (Appendix 3.1). After molecular doping of the Cu-BTC thin film with TCNQ, the surface morphology as well as thickness value remained unchanged (Figure 3.2 and Appendix 3.2a) though wettability of the thin film changed dramatically (hydrophilic to hydrophobic) as was indicated by the respective value of contact angle of water (~66º on Cu-BTC thin film and ~138º on TCNQ@Cu-BTC thin film) (Figure 3.2a and Appendix 3.1a).[1]

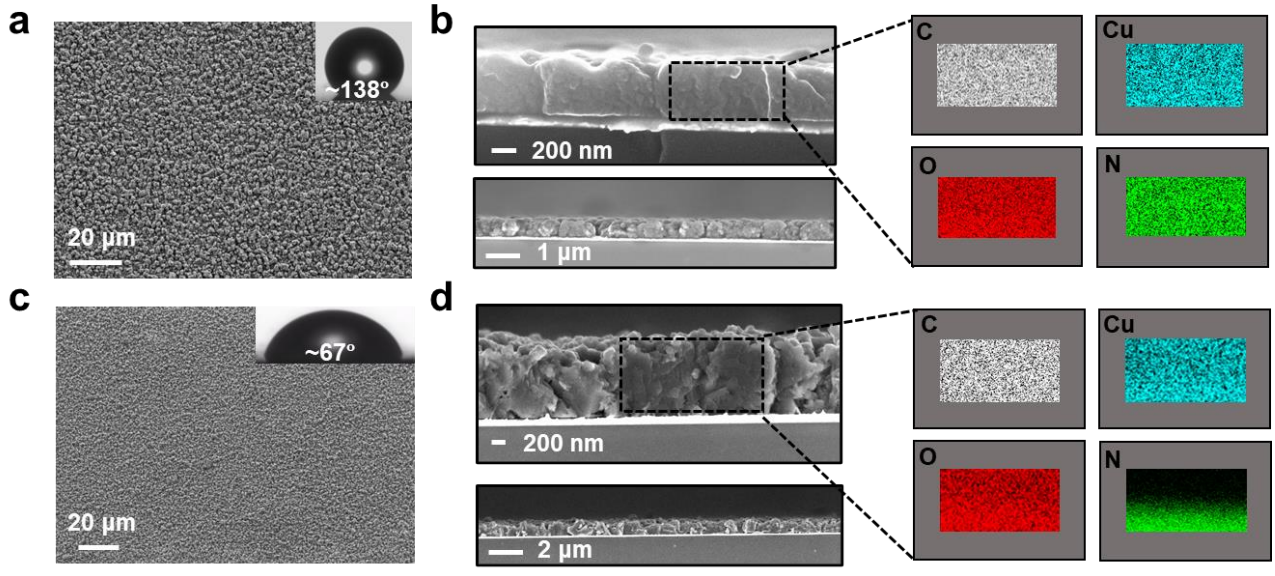

Figure 3.2. *(a) FESEM image (inset: water contact angle) and (b) cross-sectional elemental mapping (top) and cross-sectional FESEM image (bottom: grey, red, cyan, green colors represent carbon, oxygen, copper and nitrogen elements respectively) of TCNQ@Cu-BTC thin film. (c) FESEM image (inset: water contact angle). (d) Cross-sectional elemental mapping (top) and cross-sectional FESEM image (bottom: grey, red, cyan, green*

colors represent carbon, oxygen, copper and nitrogen elements respectively) of Cu-BTC/TCNQ@Cu-BTC thin film.

To check the uniform doping in the TCNQ@Cu-BTC thin film, in-plane and cross-sectional elemental mapping were performed thoroughly using energy-dispersive X-ray spectroscopy (EDXS) analysis where the nitrogen element acted as a marker for the TCNQ molecule. The elemental nitrogen content was found to be uniform, both on the surface and across the thickness of ca. 540 nm, thereby confirming a uniform TCNQ doping in the TCNQ@Cu-BTC thin film (Figure 3.2b and Appendix 3.3). Molecular doping was further supported by Raman spectrum where two vibrational bands at 2207 cm^{-1} and 2224 cm^{-1} were characteristic of two non-equivalent bonding environment of TCNQ (two CN moieties are bound to copper paddle wheel structure and other two are unbounded) (Appendix 3.4). Additionally, a significant red shift was observed from ~1455 cm^{-1} to ~1374 cm^{-1} corresponding to C=C wing stretching mode suggesting the TCNQ incorporation inside the Cu-BTC pores (Appendix 3.4) – very much consistent with earlier findings (Appendix 3.5).[7]

Upon depositing the Cu-BTC layer on top of the TCNQ@Cu-BTC layer, the film thickness value was increased from ca. 540 nm to ca. 1.1 µm with no distinctive change in the surface morphological pattern (Figure 3.2b and Appendix 3.2b). The water contact angle value on the surface of Cu-BTC/TCNQ@Cu-BTC thin film was observed to be ~67º which is similar to water contact angle value on the pristine Cu-BTC thin film (Figure 3.2b and Appendix 3.1a). In the cross-sectional elemental mapping, nitrogen element was present only in bottom layer (from TCNQ molecule) and completely absent in top layer, confirming the successful formation of the Cu-BTC/TCNQ@Cu-BTC thin film and thereby an interface of a doped and undoped CP was realized (Figure 3.2).

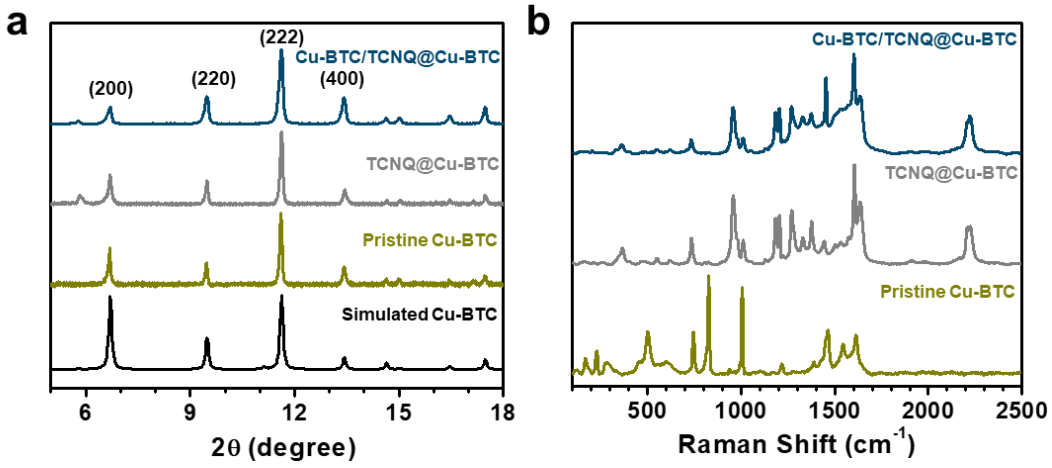

Figure 3.3. *(a) Out-of-plane XRD patterns and (b) Raman spectra of pristine Cu-BTC, TCNQ@Cu-BTC and Cu-BTC/TCNQ@Cu-BTC thin films (for reference, simulated XRD pattern is provided from CCDC number 943008).*

Out-of-plane X-ray diffraction (XRD) patterns of Cu-BTC, TCNQ@Cu-BTC, and Cu-BTC/TCNQ@Cu-BTC thin films were recorded at room-temperature and the peak at $2\boldsymbol{\theta} \approx 11.6^{o}$ corresponding to (222) diffraction plane shows the preferred orientation of pristine Cu-BTC thin film with the presence of other peaks at $2\boldsymbol{\theta} \approx 6.7^{o}$, 9.5^{o} and 13.4^{o} corresponding to (200), (220) and (400) respectively (Figure 3.3).[1, 7, 12] A new peak was emerged at $2\boldsymbol{\theta} \approx 5.8^{o}$ corresponding to (111) diffraction plane in the TCNQ@Cu-BTC thin film which could be assigned to be due to the long-range ordering of TCNQ molecules inside the pores of Cu-BTC (Figure 3.3).[13] In the Cu-BTC/TCNQ@Cu-BTC thin film, the intensity of (222) diffraction plane was further increased as compared to (111) plane which suggested the formation of Cu-BTC layer on top of TCNQ@Cu-BTC layer (Figure 3.3).

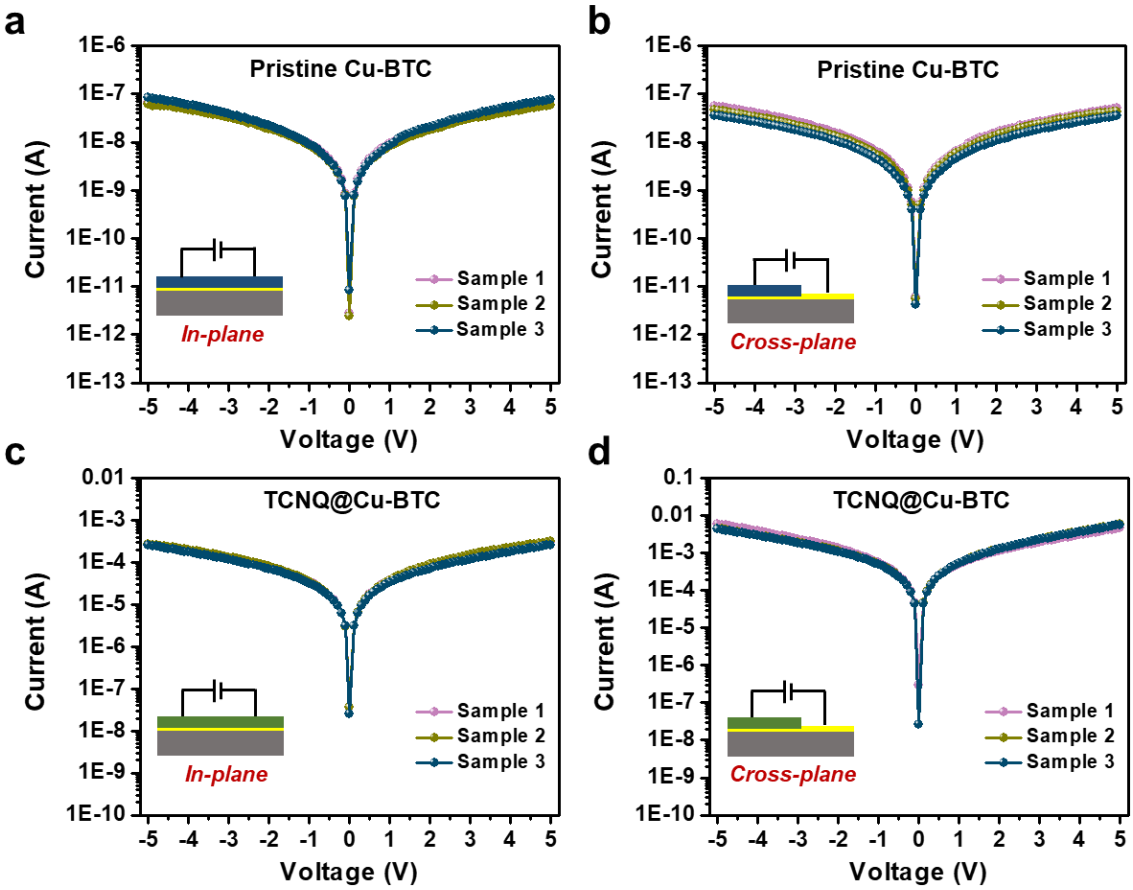

Figure 3.4. *Current-voltage (I-V) characteristics of pristine Cu-BTC and pristine Cu-TCNQ in both (a,c) in-plane and (b,d) cross-plane modes.*

To investigate the electrical transport properties, current-voltage (*I-V*) measurements were performed in both in-plane and cross-plane modes for the Cu-BTC, TCNQ@Cu-BTC, and Cu-BTC/TCNQ@Cu-BTC thin films. *I-V* profiles for the Cu-BTC thin film, both in-plane and cross-plane, were almost identical and suggested an electrical conductance value of ~10^{-8} S (Figure 3.4a,b). In the case of molecularly doped TCNQ@Cu-BTC thin film, in-plane electrical conductance value was ~10^{-4} S and a further increase in the electrical conductance value (~10^{-3} S) in cross-plane mode could be due to the alignment of TCNQ inside the pores of Cu-BTC in out-of-plane [111] direction (Figure 3.4c,d).[14] As for the Cu-BTC/TCNQ@Cu-BTC thin film, in-plane electrical conductance value was expectedly similar to that of the pristine Cu-BTC thin film (Figure 3.5a). Interestingly however, *I-V* profiles revealed a clear-cut rectification of the electrical current in the cross-plane mode with the rectification ratio (RR) of ~10^{5} (Figure 3.5b).

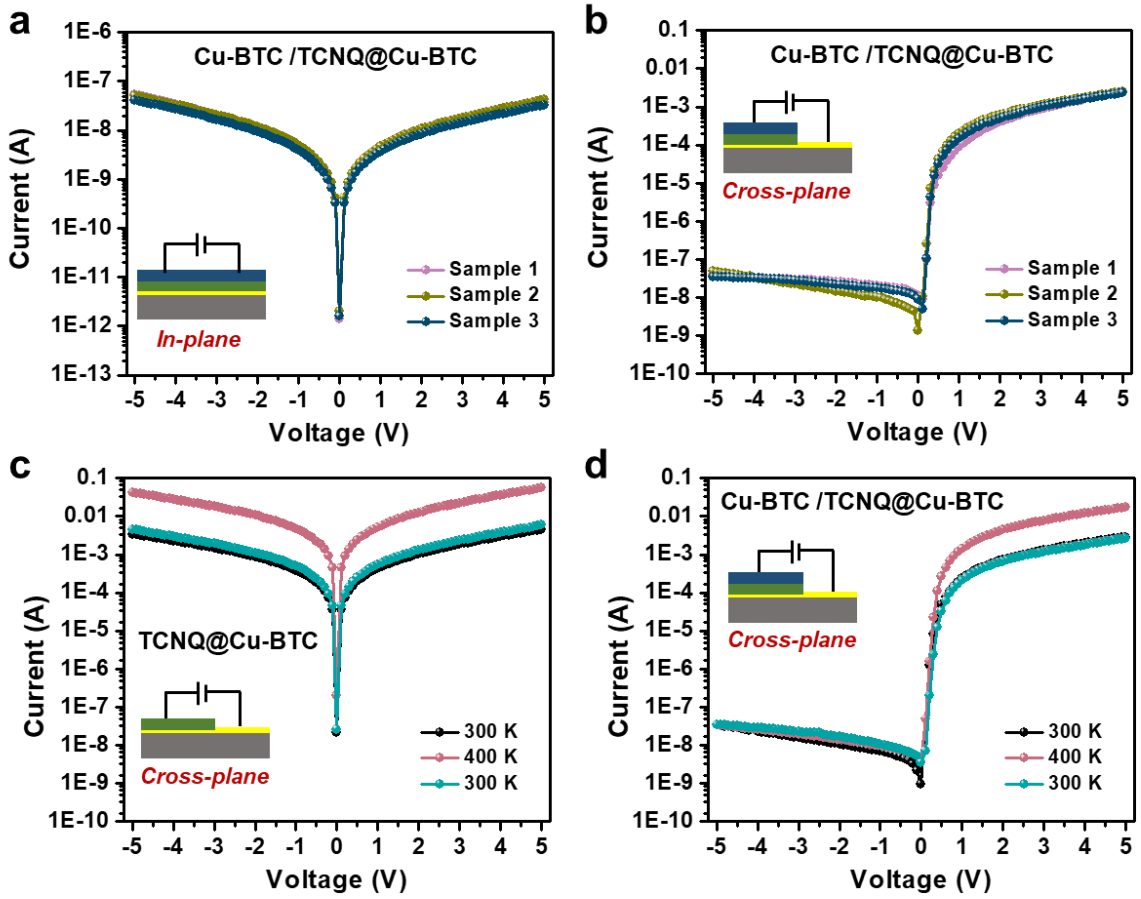

Figure 3.5. *Current-voltage (I-V) characteristics of pristine Cu-BTC/TCNQ@Cu-BTC thin film in both (a) in-plane and (b) cross-plane modes. Temperature-dependent cross-plane I-V characteristics of (c) TCNQ@Cu-*

BTC and (d) Cu-BTC/TCNQ@Cu-BTC thin films showing an order of enhancement in current and current rectification ratio respectively at 400 K (pink) as compared to 300 K (black and dark cyan).

Reverse *I-V* pattern was realized upon changing the direction of the current flow from source measure unit (SMU)-2 to source measure unit (SMU)-1 thereby validating further the current rectification ability of the Cu-BTC/TCNQ@Cu-BTC thin film (Appendix 3.6). In the case of pristine Cu-BTC thin film, cross-plane electrical conductance values remained unchanged at 400 K (Appendix 3.7) whereas an order of enhancement was observed in cross-plane electrical conductance in TCNQ@Cu-BTC thin film at 400 K (Figure 3.5c). Interestingly, a similar enhancement in cross-plane electrical conductance value was realized at 400 K in positive potential of Cu-BTC/TCNQ@Cu-BTC thin film, and values remained unaltered in negative potential likewise pristine Cu-BTC thin film (Figure 3.5d), thereby resulting a rectification ratio of ~10^6 at 400 K which not only justifies the emergence of a well-defined interface in the Cu-BTC/TCNQ@Cu-BTC system but also the RR value stand out as a remarkable figure in the domain of MOFs.

Further, we have successfully fabricated the Cu-BTC/TCNQ@Cu-BTC thin film on flexible substrate (Au coated on PET) and duly characterized. XRD pattern and Raman spectrum showed the similar characteristic features in Cu-BTC/TCNQ@Cu-BTC thin film on flexible PET substrate, thereby confirming successful thin film formation (Appendix 3.8)

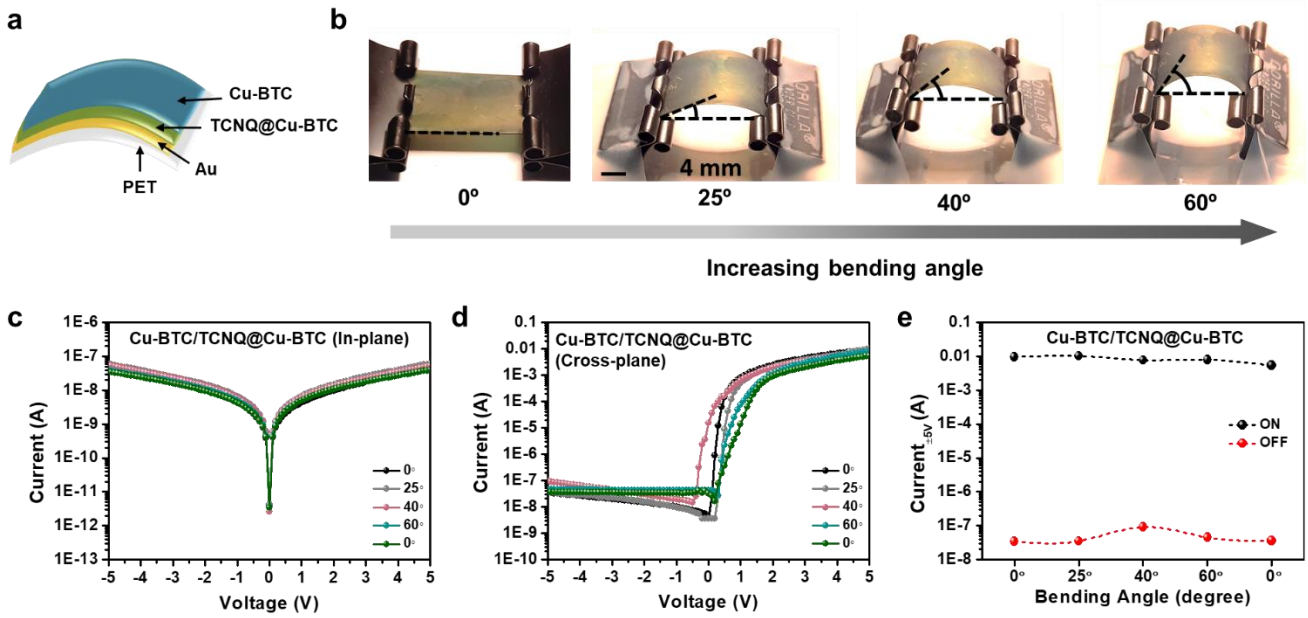

Figure 3.6. *(a) Schematic representation of Cu-BTC/TCNQ@Cu-BTC thin film on Au coated PET flexible substrate. (b) Optical images of Cu-BTC/TCNQ@Cu-BTC on Au coated PET flexible substrate at different*

bending angles. (c) In-plane and (d) cross-plane I-V characteristics of flexible Cu-BTC/TCNQ@Cu-BTC thin film at various bending angles. (e) Bending angle versus current plot for cross-plane I-V measurements of Cu-BTC/TCNQ@Cu-BTC thin film on flexible PET substrate at ±5 V clearly indicating no change in on-off ratios at various bending angles.

Similar *I-V* measurements were performed in both in-plane and cross-plane modes for the Cu-BTC/TCNQ@Cu-BTC thin film on flexible PET substrate and remarkably, identical RR values were observed. Interestingly, on-off ratios and/or RR values were almost retained at various stretching-bending angles (Figure 3.6). Such a hitherto unreported observation can be attributed to the emergence of an electronic heterostructure resembling the classical p-n junction interface. Notably, our Hall-effect measurements on the TCNQ@Cu-BTC thin film confirm it to be a n-type material (carrier mobility ≈ 22.7 $cm^2V^{-1}S^{-1}$; carrier concentration ≈ 770 x 10^{15} cm^{-2}; and Hall coefficient = −8.1 x 10^{-3} cm^2C^{-1}) while Cu-BTC system can act as a p-type material.[1]

The design strategy of our CP-on-Guest@CP over-all provides: (i) a control over the thickness of Cu-BTC and TCNQ@Cu-BTC layers to generate a well-defined electronic interface in the heterostructured Cu-BTC/TCNQ@Cu-BTC thin film, unlike an uncontrolled and gradient-like doping in the TCNQ@Cu-BTEC (BTEC=1,3,5-benzenetetracarboxylic acid) thin film reported earlier;[10] (ii) an opportunity to further modulate the current RR value upon changing the temperature which was found to be not possible with the TCNQ@Cu-BTEC system, perhaps because of the uncontrolled molecular doping;[1, 10] and (iii) an option to modify the top pristine CP layers by molecular doping which can either modulate the RR value or lead to emergence of interesting interfacial property.

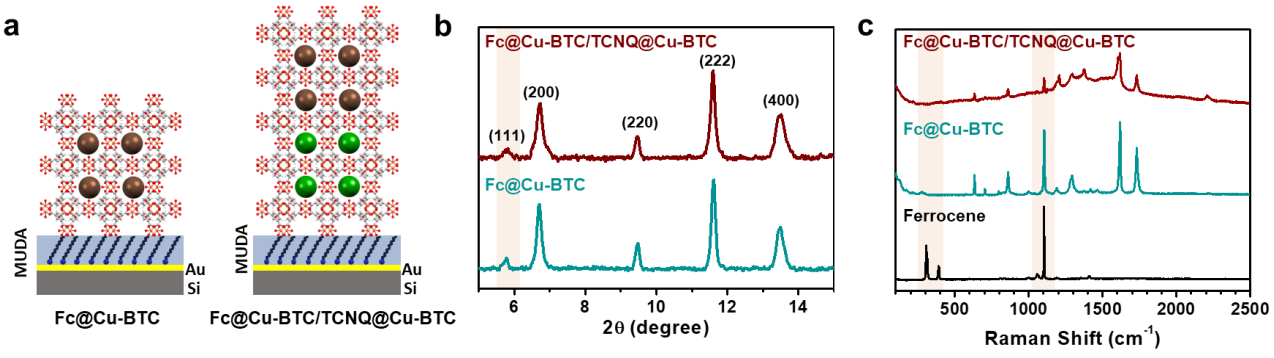

Figure 3.7. *(a) Schematic representation of Fc@Cu-BTC (left) and Fc@Cu-BTC/TCNQ@Cu-BTC (right) heterostructure thin film on functionalized Au substrate. (b) Out-of-plane XRD and (c) Raman spectra of Fc@Cu-BTC and Fc@Cu-BTC/TCNQ@Cu-BTC thin films.*

For this study, we have used ferrocene ($(C_5H_5)_2Fe$, Fc) molecule[15-16] to generate the Fc@Cu-BTC/TCNQ@Cu-BTC thin film by utilizing the accessible pores of Cu-BTC in Cu-BTC/TCNQ@Cu-BTC heterostructure. Ferrocene is a sandwich-like organometallic compound consisting of a central iron atom bonded to two cyclopentadienyl anions. Ferrocene is known for its stability and ability to undergo redox reactions, which can involve transfer of electrons between the iron atom and the cyclopentadienyl rings. Ferrocene was earlier explored as a dopant in Cu-BTC thin film and realized to have voltage-dependent resistive switching by triggering charge hopping transport mechanism.[15-17]

XRD patterns were recorded for Fc@Cu-BTC/TCNQ@Cu-BTC and Fc@Cu-BTC thin films and results were found in line with previous reports[15-16] (Figure 3.7). Similarly, Raman spectra were recorded for Fc@Cu-BTC/TCNQ@Cu-BTC and Fc@Cu-BTC thin films and a signature peak at ~1105 cm^{-1} corresponding to ring breathing mode of ferrocene was observed. Interestingly, vibrational peaks at ~306 cm^{-1} and ~390 cm^{-1} corresponding to *sym.* ring-metal stretch. and *sym.* ring tilt of ferrocene respectively[18] vanished in Fc@Cu-BTC and Fc@Cu-BTC/TCNQ@Cu-BTC thin films due to the restriction of movement in confined pores, thereby strongly suggesting the incorporation of ferrocene inside the pores, not physiosorbed on the surface (Figure 3.7).

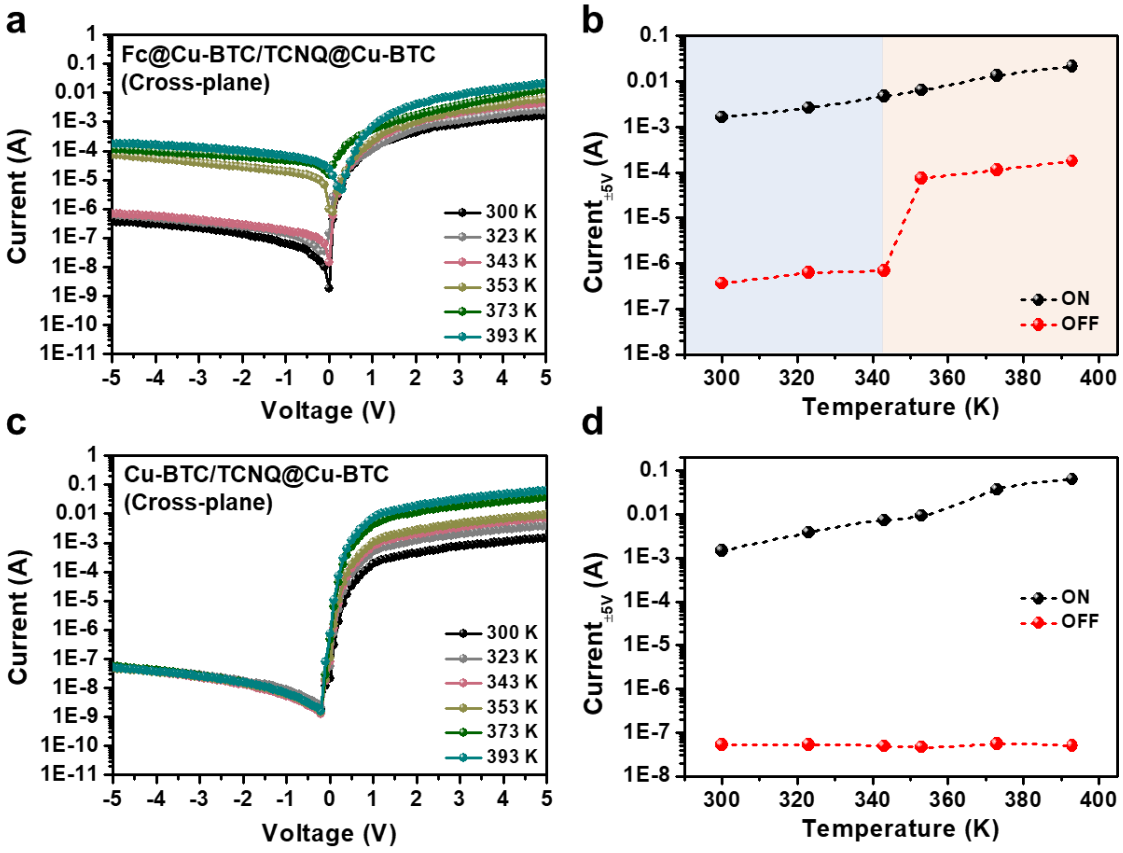

Figure 3.8. *Cross-plane (a,c) I-V characteristics and (b,d) current versus temperature plot at ±5 V for Fc@Cu-BTC/TCNQ@Cu-BTC and Cu-BTC/TCNQ@Cu-BTC heterostructured thin films respectively.*

Furthermore, *I-V* measurements were carried out in both cross-plane mode for Fc@Cu-BTC/TCNQ@Cu-BTC and Cu-BTC/TCNQ@Cu-BTC thin films at variable temperature and interestingly, an anomalous electrical rectification at ~340 K was observed in case of cross-plane *I-V* characteristics of Fc@Cu-BTC/TCNQ@Cu-BTC (Figure 3.8a,b) whereas such effects was absent in Cu-BTC/TCNQ@Cu-BTC heterostructure, clearly reflecting in the current values recorded at ±5V at variable temperature (Figure 3.8c,d).

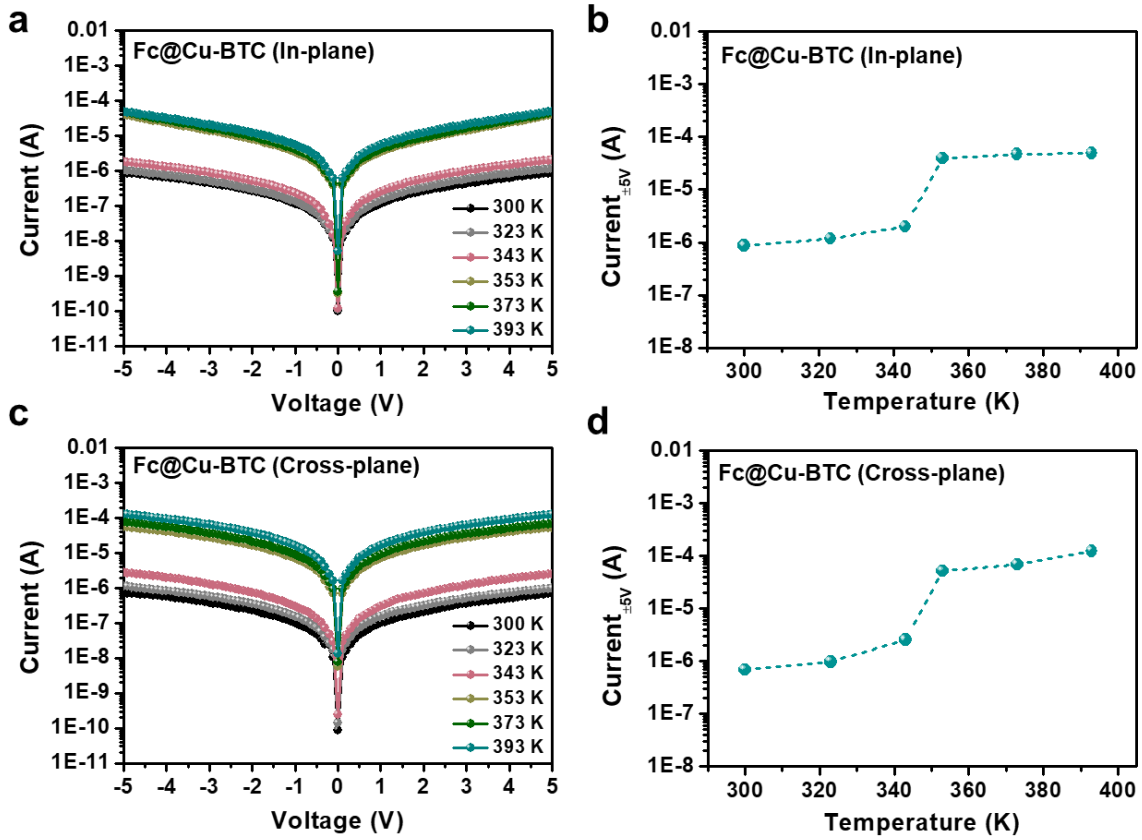

Figure 3.9. *(a,c) I-V characteristics and (b,d) current versus temperature plot at ±5 V for Fc@Cu-BTC thin film in in-plane and cross-plane modes respectively.*

To understand the anomalous electrical rectification behaviour, we have recorded *I-V* characteristics of Fc@Cu-BTC thin film in both in-plane and cross-plane modes, and current values were observed to be reduced by an order (Figure 3.9) similar to pervious reports.[15-16] Such increment in current value can be attributed to increased concentration of charge carrier concentration consisting of oxidised Fc moieties, facilitating hole conduction (p-type).[17] Furthermore, variable-temperature *I-V* measurements

were performed of Fc@Cu-BTC thin film in both in-plane and cross-plane modes and interestingly, resistive switching was observed at ~340 K in both in-plane and cross-planes modes which was similar to the cross-plane *I-V* characteristics of Fc@Cu-BTC/TCNQ@Cu-BTC heterostructured thin film (Figure 3.9). Therefore, a tunable electrical current rectification was achieved with the temperature due to the presence of thermally driven resistive switching behaviour originally coming from Fc@Cu-BTC in case of Fc@Cu-BTC/TCNQ@Cu-BTC heterostructured thin film.

3.4 Conclusions

In summary, we have successfully demonstrated the design principle of generating a lattice-matched electronic heterostructure in thin film configuration upon depositing pristine CP layers on molecularly doped CP layers. Electrical transport properties across the Cu-BTC/TCNQ@Cu-BTC thin film evidenced a rectification of current with remarkable RR value (~10^5) at 300 K which was further enhanced by an order of magnitude upon increasing the temperature to 400 K. Similar behavior was also achieved on the flexible PET substrate and was almost unaltered at various stretching-bending angles. Furthermore, a tunable electrical current rectification behaviour was observed with the temperature in Fc@Cu-BTC/TCNQ@Cu-BTC heterostructure, generated by utilizing the accessible pores of Cu-BTC with another dopant ferrocene.[19] Therefore, such CP-on-Guest@CP or Guest@CP-on-Guest@CP systems can be further improvised by changing the dopant molecules in the accessible pores of pristine CP layers and are in general anticipated to be useful for electronic device applications.

3.5 Appendix

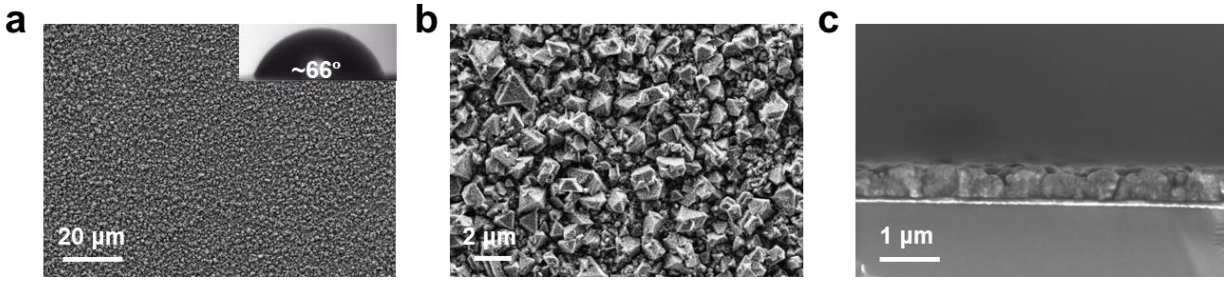

Appendix 3.1. *(a) Zoomed-in (inset: water contact angle) and (b) zoomed-out FESEM images of pristine Cu-BTC in top-view. (c) Cross-sectional FESEM image of pristine Cu-BTC thin film.*

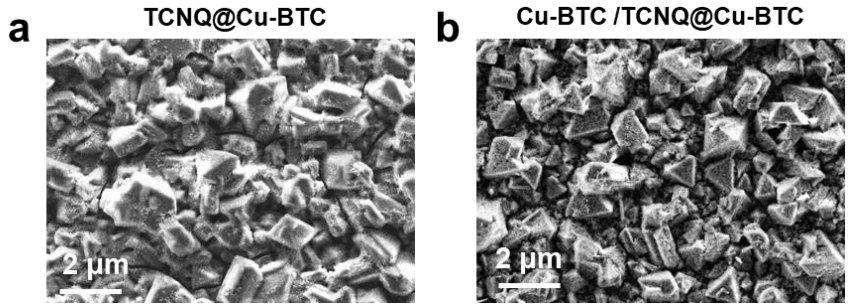

Appendix 3.2. *FESEM images of (a) TCNQ@Cu-BTC and (b) Cu-BTC/TCNQ@Cu-BTC.*

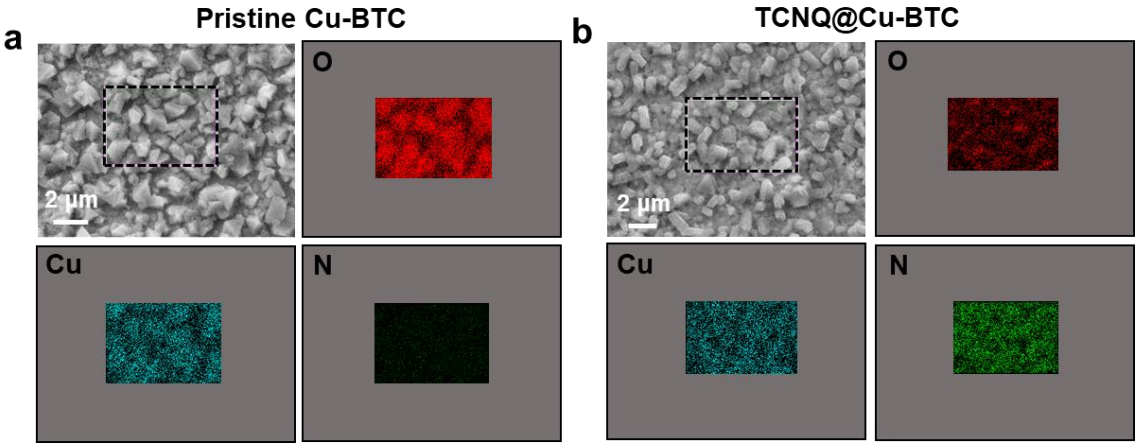

Appendix 3.3. *Elemental mapping on the surface of thin films of (a) pristine Cu-BTC and (b) TCNQ@Cu-BTC.*

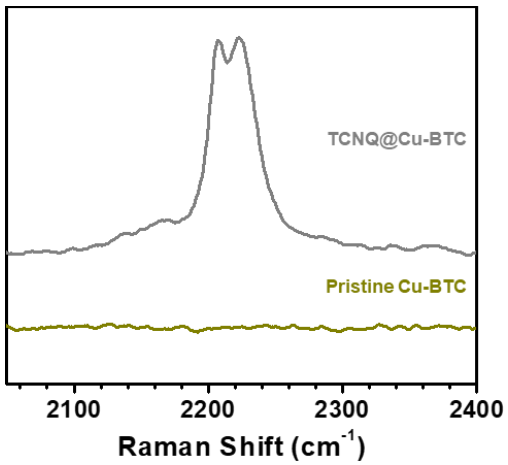

Appendix 3.4. *Raman spectra of pristine Cu-BTC and TCNQ@Cu-BTC thin films.*

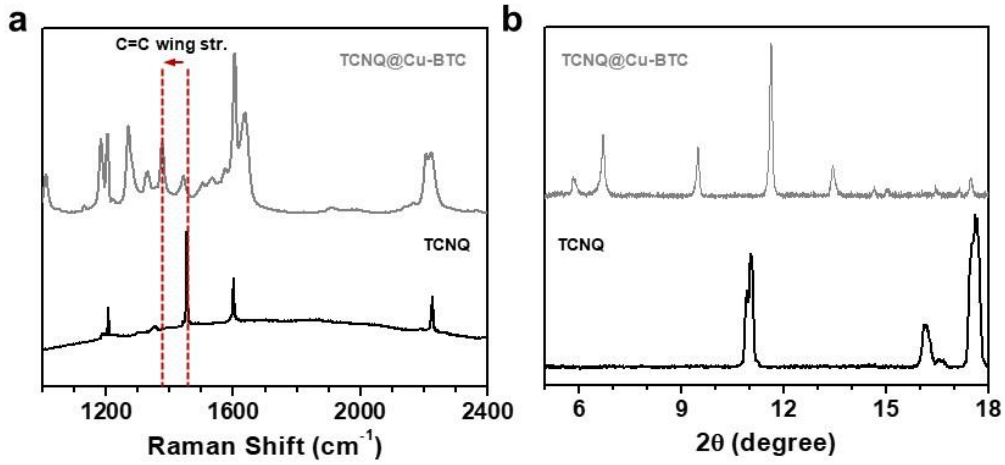

Appendix 3.5. *(a) Raman spectra and (b) out-of-plane XRD patterns of TCNQ and TCNQ@Cu-BTC thin film. A significant red shift of C=C wing stretching mode of TCNQ from ~1455 cm^{-1} to ~1374 cm^{-1} in Raman spectrum of TCNQ@Cu-BTC and absence of signature peak of bulk TCNQ in XRD indicating the incorporation of TCNQ inside the pores of Cu-BTC (not physiosorbed on the surface).*

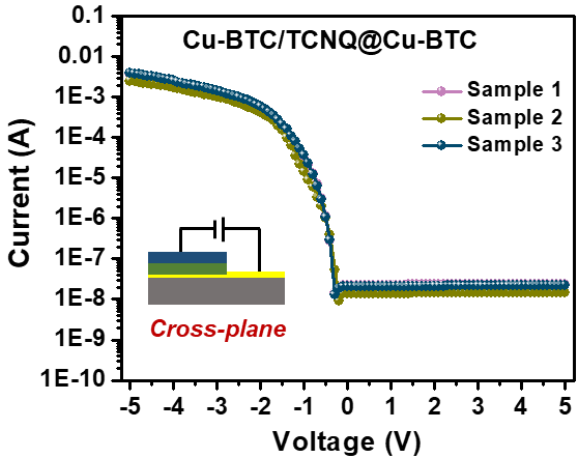

Appendix 3.6. *Cross-plane current-voltage (I-V) characteristics of Cu-BTC/TCNQ@Cu-BTC with changing the direction of current flow from source measure unit (SMU)-2 to source measure unit (SMU)-1.*

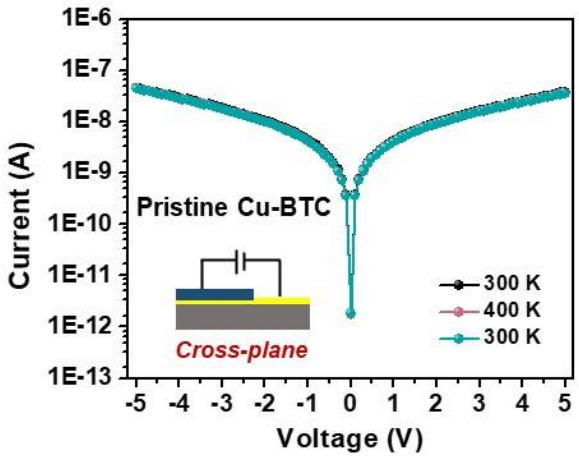

Appendix 3.7. *Cross-plane current-voltage (I-V) characteristics of pristine Cu-BTC at variable temperatures showing no changes in current values at 400 K (pink) and 300 K (black and dark cyan).*

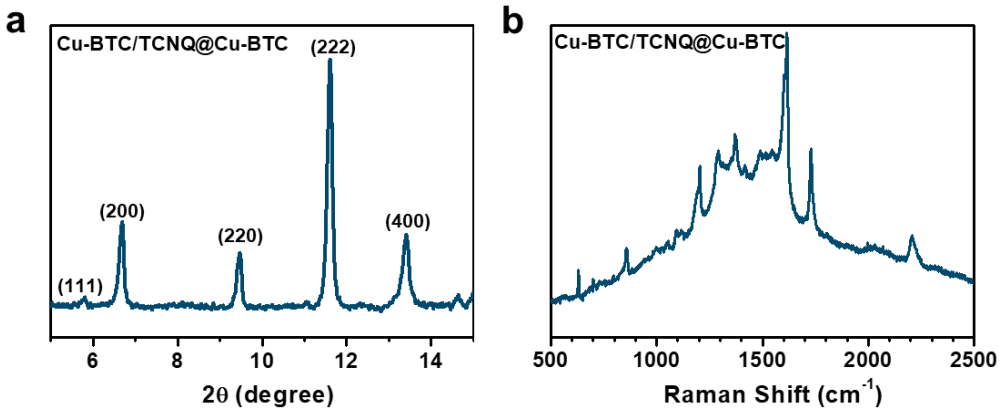

Appendix 3.8. *(a) Out-of-plane XRD and (b) Raman spectrum of Cu-BTC/TCNQ@Cu-BTC thin film on Au coated PET flexible substrate.*

3.6 References

1. Sindhu, P.; Prasoon, A.; Rana, S.; Ballav, N., Emergent Interface in Heterostructured Thin Films of Cu (II) and Cu (I) Coordination Polymers. *J. Phys. Chem. Lett.* **2020,** *11* (15), 6242-6248.

2. Chandresh, A.; Liu, X.; Wöll, C.; Heinke, L., Programmed Molecular Assembly of Abrupt Crystalline Organic/Organic Heterointerfaces Yielding Metal-Organic Framework Diodes with Large On-Off Ratios. *Adv. Sci.* **2021,** *8* (7), 2001884.

3. Hou, S.; Li, W.; Watzele, S.; Kluge, R. M.; Xue, S.; Yin, S.; Jiang, X.; Döblinger, M.; Welle, A.; Garlyyev, B., Metamorphosis of Heterostructured Surface-Mounted Metal–Organic Frameworks Yielding Record Oxygen Evolution Mass Activities. *Adv. Mater.* **2021,** *33* (38), 2103218.

4. Haldar, R.; Wöll, C., Hierarchical assemblies of molecular frameworks—MOF-on-MOF epitaxial heterostructures. *Nano Res.* **2021,** *14* (2), 355-368.

5. Sindhu, P.; Ananthram, K. S.; Jain, A.; Tarafder, K.; Ballav, N., Charge-transfer interface of insulating metal-organic frameworks with metallic conduction. *Nat. Commun.* **2022,** *13* (1), 7665.

6. Shaposhnikov, V. L.; Krivosheeva, A. V.; Borisenko, V. E., Impact of defects on electronic properties of heterostructures constructed from monolayers of transition metal dichalcogenides. *Phys. Status Solidi B* **2019,** *256* (5), 1800355.

7. Talin, A. A.; Centrone, A.; Ford, A. C.; Foster, M. E.; Stavila, V.; Haney, P.; Kinney, R. A.; Szalai, V.; El Gabaly, F.; Yoon, H. P., Tunable electrical conductivity in metal-organic framework thin-film devices. *Science* **2014,** *343* (6166), 66-69.

8. Allendorf, M. D.; Foster, M. E.; Leonard, F.; Stavila, V.; Feng, P. L.; Doty, F. P.; Leong, K.; Ma, E. Y.; Johnston, S. R.; Talin, A. A., Guest-induced emergent properties in metal–organic frameworks. *J. Phys. Chem. Lett.* **2015,** *6* (7), 1182-1195.

9. Rana, S.; Rajendra, R.; Dhara, B.; Jha, P. K.; Ballav, N., Highly Hydrophobic and Chemically Rectifiable Surface-Anchored Metal-Organic Framework Thin-Film Devices. *Adv. Mater. Interfaces* **2016,** *3* (13), 1500738.

10. Prasoon, A.; Dhara, B.; Roy, D.; Rana, S.; Bhand, S.; Ballav, N., Achieving current rectification ratios $\geq 10^5$ across thin films of coordination polymer. *Chem. Sci.* **2019,** *10* (43), 10040-10047.

11. Rana, S.; Sindhu, P.; Ballav, N., Perspective on the Interfacial Reduction Reaction. *Langmuir* **2019,** *35* (30), 9647-9659.

12. Biemmi, E.; Scherb, C.; Bein, T., Oriented growth of the metal organic framework $Cu_3(BTC)_2(H_2O)_3$. x H_2O tunable with functionalized self-assembled monolayers. *J. Am. Chem. Soc.* **2007,** *129* (26), 8054-8055.

13. Schneider, C.; Ukaj, D.; Koerver, R.; Talin, A. A.; Kieslich, G.; Pujari, S. P.; Zuilhof, H.; Janek, J.; Allendorf, M. D.; Fischer, R. A., High electrical conductivity and high porosity in a Guest@ MOF material: evidence of TCNQ ordering within Cu_3BTC_2 micropores. *Chem. Sci.* **2018,** *9* (37), 7405-7412.

14. Okada, K.; Mori, K.; Fukatsu, A.; Takahashi, M., Oriented growth of semiconducting TCNQ@$Cu_3(BTC)_2$ MOF on $Cu(OH)_2$: crystallographic orientation and pattern formation toward semiconducting thin-film devices. *J. Mater. Chem. A* **2021,** *9* (35), 19613-19618.

15. Liu, J.; Wächter, T.; Irmler, A.; Weidler, P. G.; Gliemann, H.; Pauly, F.; Mugnaini, V.; Zharnikov, M.; Wöll, C., Electric Transport Properties of Surface-Anchored Metal–Organic Frameworks and the Effect of Ferrocene Loading. *ACS Appl. Mater. Interfaces* **2015,** *7* (18), 9824-9830.

16. Wang, Z.; Nminibapiel, D.; Shrestha, P.; Liu, J.; Guo, W.; Weidler, P. G.; Baumgart, H.; Wöll, C.; Redel, E., Resistive Switching Nanodevices Based on Metal–Organic Frameworks. *ChemNanoMat* **2016,** *2* (1), 67-73.

17. Dragässer, A.; Shekhah, O.; Zybaylo, O.; Shen, C.; Buck, M.; Wöll, C.; Schlettwein, D., Redox mediation enabled by immobilised centres in the pores of a metal–organic framework grown by liquid phase epitaxy. *Chem. Commun.* **2011,** *48* (5), 663-665.

18. Long, T. V.; Huege, F. R., The laser-Raman spectrum of ferrocene. *Chem. Commun. (London)* **1968,** (20), 1239b-1241.

19. Sindhu, P.; Ballav, N., Thin Films of MOF-on-Guest@MOF: A Simple Strategy of Designing Electronic Heterostructures. *Inorg. Chem.* **2023,** *62* (28), 10887-10891.

Metallic Conduction at the Interface of Cu(I)-TCNQ/Cu(II)-BPyDC Heterostructured Thin Film

4.1 Introduction

Heterostructures are widely explored due to emergent properties at the interface in oxide materials.[1-7] In oxide heterostructures, interface of a band insulator ($SrTiO_3$) and a Mott-insulator ($LaTiO_3$) has captivated the researcher's attention due to the emergence of metallic conduction with remarkably high carrier mobility.[3] Exploring such heterostructure of a band insulator and a Mott-insulator in co-ordination polymers (CPs) can provide new dimensions to the CPs in the field of electronics.[8]

Herein, we have designed a heterostructure of a Mott insulator and a band insulator, and successfully fabricated highly-crystalline lattice-mismatched heterostructured thin film of Cu(I)-TCNQ/Cu(II)-BPyDC on fluorine-doped tin oxide (FTO) substrate by employing layer-by-layer (LbL) method.

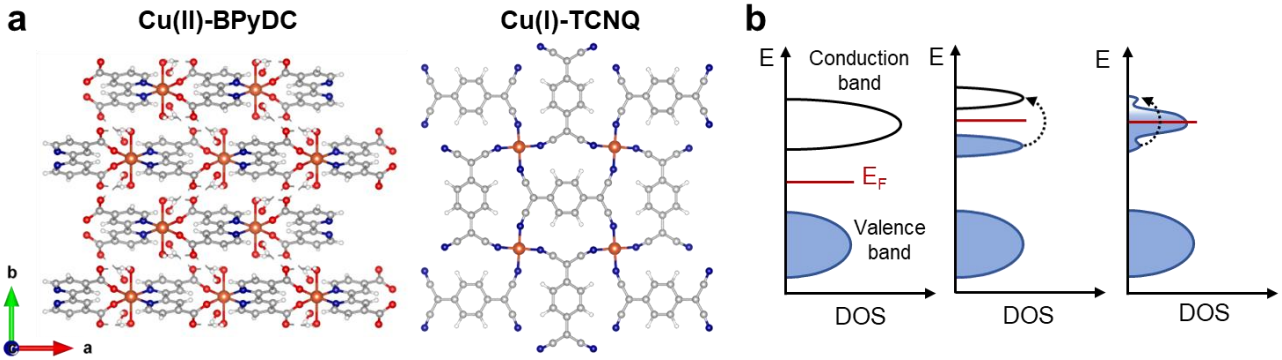

Figure 4.1. *(a) Energy optimized structures of Cu-BPyDC (left) and Cu-TCNQ (right) (view from ab plane) where carbon, hydrogen, nitrogen, oxygen, and copper atoms are represented by colors grey, white, blue, red, and orange, respectively. (b) Band diagram schemes of a band insulator (left), a Mott insulator (middle) and their interface (right). Fermi level is marked by red line (Density functional theory (DFT) calculations were performed by K. S. Ananthram under the supervision of Kartick Tarafder, NITK Surathkal, India).*

Specifically, we have grown thin film of Cu(II)-BPyDC (BPyDC = 2,2'-bipyridine-4,4'-dicarboxylate) which is assigned as a band insulator and on top of it, we have deposited thin film of Cu(I)-TCNQ (TCNQ = 7,7,8,8-tetracyanoquinodimethane) which is a Mott (electron-electron interaction) insulator[9] resulting in the generation of Cu(I)-TCNQ/Cu(II)-BPyDC heterostructured thin film (Figure 4.1). Fabrication of such Cu(II)-Cu(I) ($3d^9$-$3d^{10}$) interface is attributed to the interfacial reduction reaction (IRR)[10-12] whereby solution of $Cu(OAc)_2$ was consistently introduced as the metal ion precursor during two consecutive LbL growth with the BPyDC and TCNQ ligands (Figure 4.2). Electrical transport measurements across the thin film evidenced the emergence of metallic conduction at the interface of a Mott and band insulating CPs likewise oxide heterostructures.

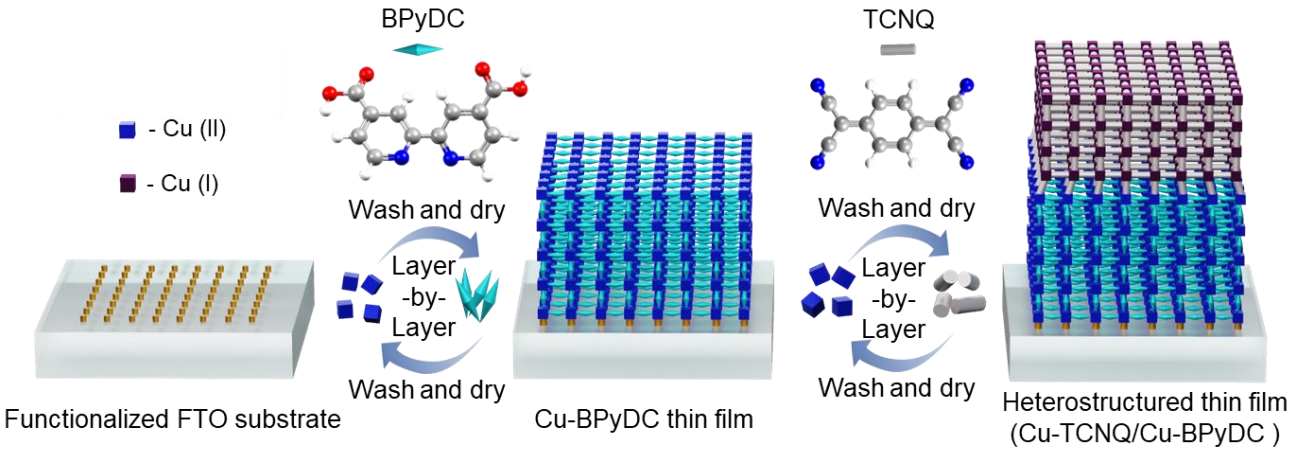

Figure 4.2. *Layer-by-layer (LbL) growth of Cu-TCNQ thin film on top of Cu-BPyDC thin film via IRR leading to heterostructured Cu(I)-TCNQ/Cu-BPyDC thin film by changing the ligand from BPyDC to TCNQ and keeping $Cu(OAc)_2$ as a metal precursor.*

4.2 Materials and Methods

Materials: Copper acetate [$Cu(OAc)_2.H_2O$], 7,7,8,8-tetracyanoquinodimethane (TCNQ), 2,2'-bipyridine-4,4'-dicarboxylic acid (H_2BPyDC), Fluorine doped tin oxide (FTO) coated glass substrate (surface resistivity ~ 7 Ω/sq), and dimethylformamide (DMF) were purchased from Sigma-Aldrich and ethanol from Merck and used as such, without any further purification except FTO coated glass substrate.

Functionalization of FTO Substrate: FTO substrate was first cleaned by sonication in acetone, ethanol and water separately for 15 minutes each, washed with the Milli-Q water and dried under the N_2 flow. Thereafter, the FTO substrate was functionalized by treating it with a mixture of conc. KOH (2 mmol) aqueous solution and H_2O_2 (30%) with the volume ratio of 3:1 at 80ºC for 30 minutes and then rinsed with the Milli-Q water and dried under the stream of N_2 gas.[13]

Fabrication of Pristine Cu-BPyDC Thin Film: Functionalized FTO substrate was immersed in 1mM $Cu(OAc)_2.H_2O$ solution in DMF kept at 330 K for 30 minutes and then washed with DMF solvent to remove the uncoordinated metal ions followed by drying step with N_2 gas and subsequently in 1mM BPyDC solution in DMF kept at 330 K for 30 minutes (washed with DMF in between followed by drying with stream of N_2 gas) to complete one LbL cycle. 20 cycles of LbL were performed to get a uniform Cu-BPyDC thin film (thickness values were estimated to be approximately 400 nm).[12]

Fabrication of Pristine Cu-TCNQ Thin Film: FTO substrate was immersed in 1mM ethanolic solution of $Cu(OAc)_2.H_2O$ kept at 330 K for 30 minutes followed by washing with ethanol and subsequently in 1mM ethanolic solution of TCNQ kept at 330 K for 30 minutes (washed with ethanol in between followed by drying with stream of N_2 gas) to complete one LbL cycle. 20 cycles of LbL were performed to get a uniform Cu-TCNQ thin film (thickness values were estimated to be approximately 600 nm).[12]

Fabrication of Cu-TCNQ/Cu-BPyDC Heterostructured Thin Film: Prefabricated pristine Cu-BPyDC thin film was subsequently dipped into ethanolic solutions of $Cu(OAc)_2.H_2O$ and TCNQ (five minutes in each solution at 330 K and washed with ethanol in between followed by drying with stream of N_2 gas to complete one cycle of LbL) for 5 cycles of LbL to prevent the infiltration of TCNQ within Cu-BPyDC thin film and afterwards, 15 consecutive LbL cycles with dipping time of 30 minutes were performed to grow Cu-TCNQ on top of Cu-BPyDC having well-defined interface (thickness values were estimated to be approximately 1 μm).[12]

Fabrication of TCNQ@Cu-BPyDC Thin Film: Prefabricated pristine Cu-BPyDC thin film was immersed into a saturated ethanolic solution of TCNQ for 48 hours followed by washing with ethanol to remove the surface adsorbed TCNQ and dried under a stream of N_2 gas.[14]

Characterizations: The surface morphologies of both pristine and heterostructured thin films were performed by Zeiss Ultra Plus FESEM. Contact angle measurements were measured using Holmarc's Contact Angle Meter. Out-of-plane XRD data were recorded at room temperature using a Bruker D8 Advance diffractometer using Cu Kα radiation (λ = 1.5406 Å). Rietveld refinement of the PXRD patterns were carried out by a standardized procedure using the FullProf program (performed by Anil Jain, BARC Mumbai, India).[15-16] Raman spectra (λ_{exc} = 632.8 nm) were recorded at Raman microscope (LabRAM HR, HoribaJobinYvon) with a 50X objective lens (spectral resolution of the system is ~1 cm^{-1}). Solid state UV-vis absorption spectra were recorded on Shimadzu UV 3600 UV-Vis-NIR spectrophotometer. The XPS data were collected using Thermo Fisher Scientific ESCALAB Xi+. Electrical transport measurements (*I-V*) on various thin film samples were carried out using a Keithley 4200 SCS Parameter Analyser system attached to an Everbeing probe station with a eutectic gallium indium (EGaIn) alloy[12, 17] as the contact electrode which is similar to earlier explored Hg-drop method for thin films of MOFs.[18-19] Temperature-dependent *I-V* measurements were recorded with the help of a conventional thermal chuck (from room-temperature to high-temperature) and a home-built liquid-

N_2 cooling set-up (from low-temperature to room-temperature) where standard Pt-100 sensor was used to monitor the temperature.

Computational Studies: DFT calculations were performed by K. S. Ananthram under the supervision of Kartick Tarafder, NITK Surathkal, India. The vibrational characteristics of molecular fragments in charge-neutral configurations were investigated using ab-initio DFT as implemented in Gaussian09 software. We have used the B3LYP hybrid functional with a 6-31g basis set for each constituent atom and the Raman spectra were extracted from the frequencies obtained from the second derivative of the energy with respect to the nuclear position and a scaling factor of 30 cm^{-1} was consistently adopted.[20]

The geometrical optimizations as well as the extraction of electronic structure information by considering Cu-BPyDC (Phase-I) as the bottom layer and Cu-TCNQ as the top layer were done by using Vienna Ab-initio Simulation Package (VASP) with projector augmented wave method.[21] The Perdew–Burke–Ernzerhof functional of generalized gradient approximation was employed as exchange-correlation functions.[21] In order to describe the strongly correlated character of the Cu-3*d* orbitals accurately the DFT + U method was employed in the calculation with U value as 5 eV and J value as 1 eV (U_{eff} = 4.0 eV). All the above-mentioned structures are energy optimized using conjugated gradient method until the interatomic forces are reduced to 0.05 eV/ Å. The Brillouin zone integrations were performed using 3x3x5 and 4x4x2 Monkhorst–Pack K-point grids for bulk Cu-TCNQ ($C_{48}H_{16}N_{16}Cu_4$) and bulk Cu-BPyDC ($C_{48}H_{56}N_8O_{32}Cu_4$) systems, respectively. Next we carefully obtained the detailed electronic behavior of the interface in three step process: (i) in the first step, interfacial distance between slabs are optimized and for this purpose, we relaxed the atomic positions of all the atoms in the top layer of Cu-TCNQ only (keeping positions of atoms in the bottom layer of Cu-BPyDC fixed) by using selective dynamics method; in the second step, we relaxed all the atoms in the unit cell to obtain the energy optimized geometric structure of the interface; and (iii) finally, the electronic behavior of the Cu-TCNQ/Cu-BPyDC ($C_{236}H_{200}N_{48}O_{64}Cu_{16}$) interface was calculated from the energy optimized structure for which a 3x3x1 Monkhorst–Pack K-point grid was used. To estimate the proper electronic band structure, we further carried out hybrid functional calculations on top of normal PBE calculation using HSE06[22] functionals. Here we have used 20 percent of Hartree-Fock exchange potential to parametrized the exchange correlation functional. Bader charge analysis[23]: total number of valance electrons contributing to the Bader charge on Cu(I) structure (top layer) = 874; total number of valance electrons contributing to the Bader charge on Cu structure

(bottom layer) = 1048; and total number of valance electrons contributing to the Bader charge on Cu(I)/Cu interface = 1922.

Similarly, DFT(+U) calculations were carried out with the phase-II structure (minor component in our thin film) of Cu-BPyDC as the bottom layer and Cu-TCNQ as the top layer. Structures were energy optimized using conjugated gradient method until the interatomic forces are reduced to 0.01 eV/ Å. The Brillouin zone integrations were performed using 3x3x5, Monkhorst–Pack grid for bulk Cu-TCNQ ($C_{48}H_{16}N_{16}Cu_4$) and bulk Cu-BPyDC ($C_{96}H_{64}N_{16}O_{44}Cu_{10}$) system. Interface structure is made considering the configurations with minimum lattice mismatch and minimum strain on the individual surfaces, staking along (001) plane, for the heterostructure Cu-TCNQ/Cu-BPyDC ($C_{480}H_{224}N_{128}O_{88}Cu_{32}$). The top Cu-TCNQ layer of the interface was relaxed by keeping the bottom Cu-BPyDC undisturbed using selective dynamics to obtain an optimized interfacial distance. To estimate the proper density of states, we have used 3x3x1 Monkhorst–Pack grid and PBE functional. Furthermore, Bader charge analysis were carried out using Henkelman's Group program and the analysis showed the total number of valance electrons contributing to the Bader charge on Cu(I) structure (top layer) = 1860; total number of valance electrons contributing to the Bader charge on Cu structure (bottom layer) = 1804; and total number of valance electrons contributing to the Bader charge on Cu(I)/Cu interface = 3664.

4.3 Results and Discussion

Field-emission scanning electron microscopy (FESEM) images revealed formation of highly-uniform pristine Cu-TCNQ, pristine Cu-BPyDC, and heterostructured Cu-TCNQ/Cu-BPyDC thin films (Figure 4.3). Field-emission scanning electron microscopy (FESEM) images revealed formation of highly-uniform pristine Cu-TCNQ, pristine Cu-BPyDC, and heterostructured Cu-TCNQ/Cu-BPyDC thin films (Figure 4.3). Distinctive morphological patterns of the micro-crystallites of Cu-TCNQ and Cu-BPyDC were visible in the respective zoomed-in FESEM images (Figure 4.2).

In cross-sectional FESEM images of the Cu-TCNQ/Cu- BPyDC system, layers of FTO, Cu-TCNQ, and Cu-BPyDC could be clearly identified thereby attesting the successful formation of heterostructured thin film of an approximate thickness of 1 μm (Figure 4.3). Also, top-view zoomed-in FESEM image on the Cu-TCNQ/Cu-BPyDC thin film revealed Cu-TCNQ crystallites with characteristic morphology as expected[12, 24] (Figure 4.3). Water contact angle values of 140±5° on both

pristine Cu-TCNQ and pristine Cu-BPyDC thin films suggested highly-hydrophobic surfaces so as the surface of the heterostructured Cu-TCNQ/Cu-BPyDC thin film (Figure 4.3).[24]

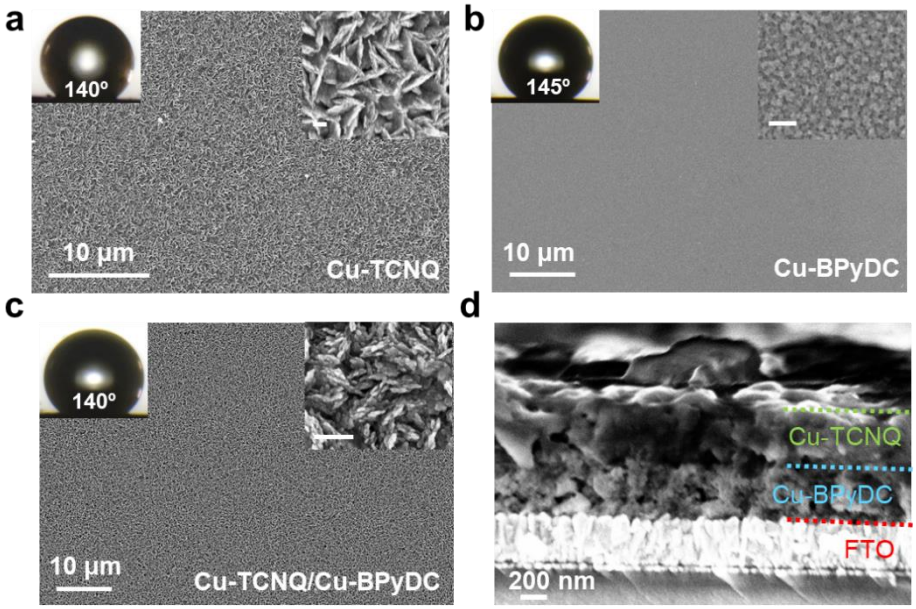

Figure 4.3. *FESEM images of (a) pristine Cu-TCNQ, (b) pristine Cu-BPyDC and (c) heterostructured Cu-TCNQ/Cu-BPyDC thin films showing the uniform coverage in each sample (inset: optical images of water contact angle (top left) and zoomed-in FESEM images at the scale of 200 nm (top right)). (d) Cross-sectional FESEM image of heterostructured Cu-TCNQ/Cu-BPyDC thin film with identifying distinctive layers of FTO, Cu-BPyDC and Cu-TCNQ (marked by dotted lines).*

Room-temperature out-of-plane X-ray diffraction (XRD) patterns of both pristine and heterostructured thin films were recorded which revealed the presence of characteristics diffraction peaks of Cu-TCNQ[25-26] and Cu-BPyDC[27-28] in the Cu-TCNQ/Cu-BPyDC system, and, in general, endorsed formation of highly-crystalline thin films via LbL (Figure 4.4a). XRD pattern of the Cu-TCNQ thin film matched well with the simulated XRD pattern and confirmed the presence of a single-phase system (Appendix 4.1 and 4.2). As for the Cu-BPyDC thin film, the preferred orientation was determined by looking at the peak intensities and was applied during the Rietveld refinement which confirmed the presence of mixed-phase system with one major (assigned as phase-I) and one minor (assigned as phase-II) components (Figure 4.4a,b and Appendix 4.3, 4.4).

Rietveld refinement of the XRD pattern of the heterostructured Cu-TCNQ/Cu-BPyDC thin film was performed considering three-phase system (two-phase of Cu-BPyDC and one-phase of Cu-TCNQ) and

only scale factor was varied whereby a reasonably good match between the experimental and calculated patterns was achieved (Figure 4.4d and Appendix 4.1).

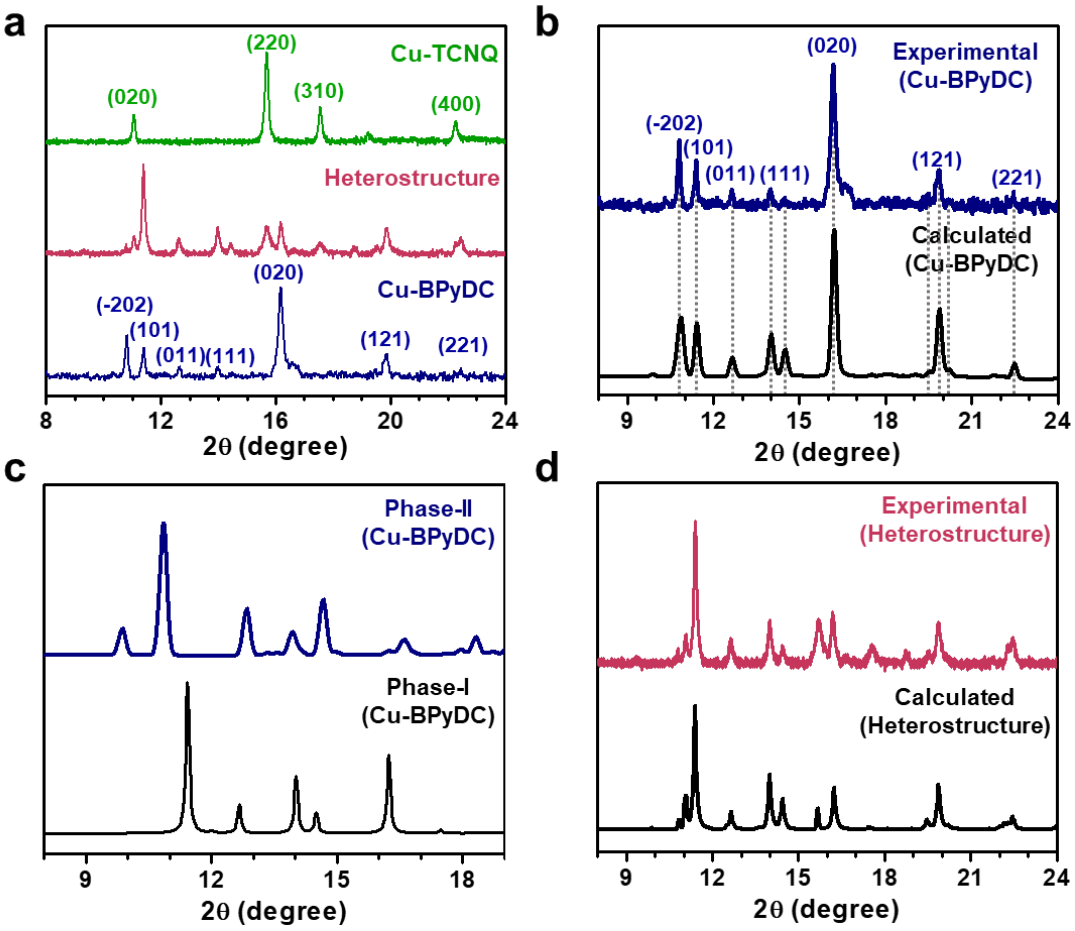

Figure 4.4. *(a) Out-of-plane XRD patterns of pristine Cu-BPyDC (blue), pristine Cu-TCNQ (green) and heterostructured Cu-TCNQ/Cu-BPyDC (pink) thin films. (b) Experimental XRD pattern of Cu-BPyDC thin film and calculated XRD pattern from the Rietveld refinement. For the Rietveld refinement of Cu-BPyDC, a mixed-phase was adopted, starting structural parameters for phase-I and Phase-II were used from Ref. 27, CCDC-710197 and Ref. 28, CCDC-1020991, respectively. The parameters were refined to match the observed and calculated XRD intensities. The refinement shows ratio of phase-I and phase-II as 84.23% and 15.77 %, respectively. Cell parameters for phase-I: a = 14.72(2) Å, b = 10.90(1) Å, c = 9.09(1) Å, α = β = γ = 90°, space group Pnna. Cell parameters for phase-II: a = 17.65(3) Å, b = 7.08(2) Å, c = 26.27(4) Å, α = 90°, β = 106.4°, γ = 90°, space group P1. (c) XRD patterns of phase-I and phase-II structures of Cu-BPyDC. (d) Experimental XRD pattern of the heterostructured Cu-TCNQ/Cu-BPyDC thin film and the calculated XRD pattern from the Rietveld refinements. (Rietveld Refinements were performed by Anil Jain, BARC Mumbai, India).*

Raman spectra of pristine Cu-TCNQ, pristine Cu-BPyDC and heterostructured Cu-TCNQ/Cu-BPyDC thin films were compared and characteristic vibrational signatures of Cu-TCNQ and Cu-BPyDC were found to be clearly present in the Cu-TCNQ/Cu-BPyDC system[12, 20, 24] (Figure 4.5a). Specifically, the peak at ~1374 cm^{-1} corresponding to the C-CN stretching mode represented Cu-TCNQ while the peak at ~1033 cm^{-1} corresponding to the skeletal mode of the bipyridine moiety represented Cu-BPyDC[20] (Figure 4.5a).

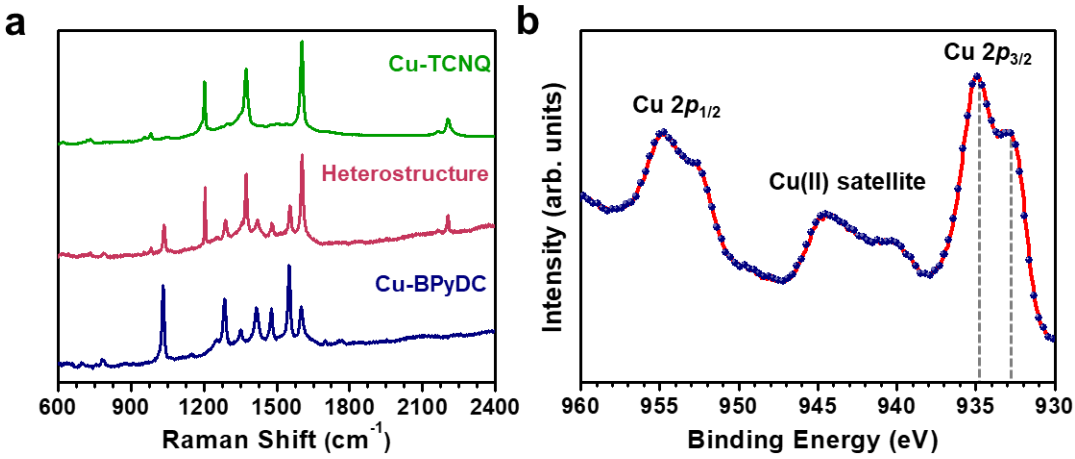

Figure 4.5. *(a) Raman spectra on pristine Cu-BPyDC (blue), pristine Cu-TCNQ (green) and heterostructured Cu-TCNQ/Cu-BPyDC (pink) thin films. (b) Cu 2p XPS data recorded on heterostructured Cu-TCNQ/Cu-BPyDC sample where few layers of Cu-TCNQ (5 cycles) was grown on the pristine Cu-BPyDC thin film showing Cu $2p_{3/2}$ signal at ~934.2 eV (Cu(II) species) and ~932.5 eV (Cu(I) species) – as indicated by dotted grey lines. As for the Cu 2p XPS data on pristine Cu-TCNQ thin film, please refer Ref. 11.*

Therefore, Raman spectra along with FESEM and XRD data confirmed the successful fabrication of heterostructured Cu-TCNQ/Cu-BPyDC thin film with retention of structural integrity. Oxidation states of Cu ions as (II) and (I) in Cu-BPyDC and Cu-TCNQ, respectively, were confirmed by X-ray photoelectron spectroscopy (XPS); upon growing few layers of Cu-TCNQ (5 cycles) on top of the pristine Cu-BPyDC thin film, clear cut signatures of Cu(I) and Cu were identified in the Cu 2*p* XPS signal thereby justifying the formation of $3d^{10}$-$3d^{9}$ Cu(I)/Cu(II) interface in the heterostructured Cu-TCNQ/Cu-BPyDC system (Figure 4.5b and Appendix 4.5). Specifically, Cu $2p_{3/2}$ photoemission signals at binding energy values of ~932.5 and ~934.2 eV with concomitant absence and presence of satellite spectral features, were characteristics of Cu-TCNQ and Cu-BPyDC, respectively[10-11] (Figure 4.5b and Appendix 4.5).

To understand the origin of mixed-phase in the Cu-BPyDC system, we have recorded cycling-dependent Raman spectra, compared with the simulated Raman spectra obtained from density functional theory (DFT) calculations, and recorded cycling dependent out-of-plane XRD patterns (Figure 4.6). In the simulation of Raman spectra, we have considered characteristic molecular fragments of phase-I and phase-II structures of the Cu-BPyDC system (Figure 4.6a). Specifically, in the phase-I structure, along with two water molecules, two oxygen and two nitrogen from three different BPyDC ligands were found to be coordinated to Cu ion (Appendix 4.3) and in the phase-II structure, along with two hydroxyl groups, four nitrogen from two different BPyDC ligand were coordinated to Cu ion (Appendix 4.4).

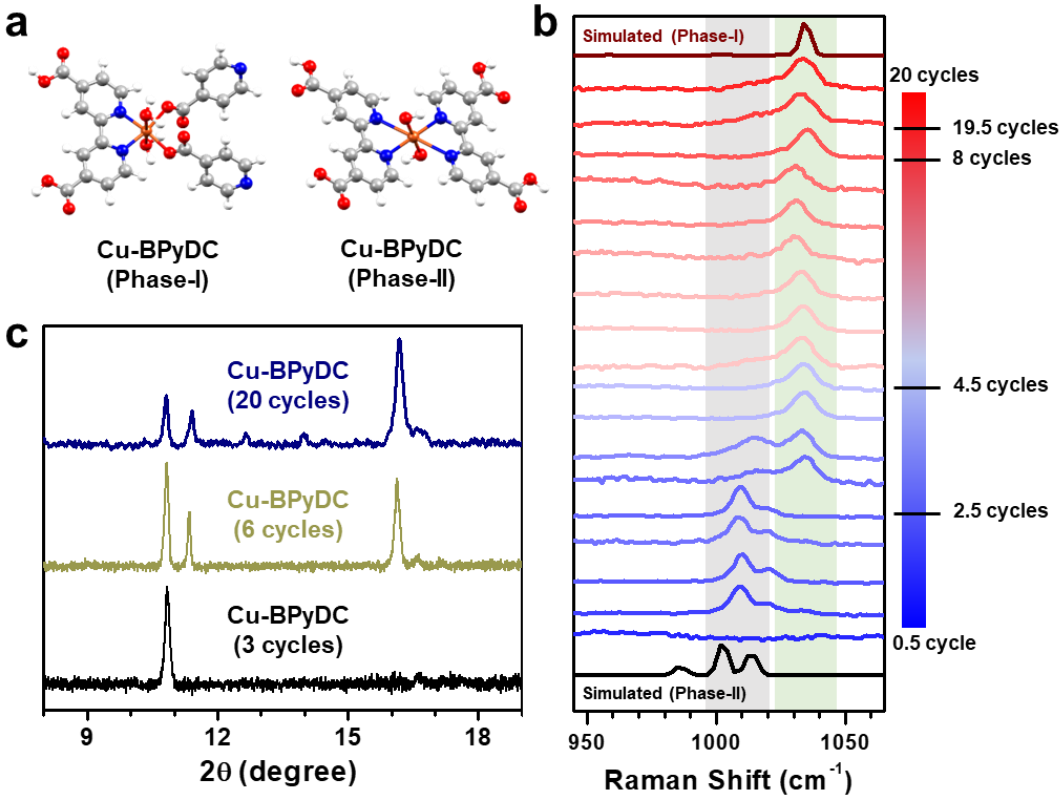

Figure 4.6. *(a) Characteristic molecular fragments isolated from phase-I (left panel) and phase-II (right panel) structures of Cu-BPyDC and subsequently used for the simulation of Raman spectral signatures. (b) Experimental Raman spectra recorded during the growth of Cu-BPyDC thin film, at each step of LbL and up to 20 cycles; and compared with the theoretically simulated Raman spectra for phase-I and phase-II structures of Cu-BPyDC. (c) Out-of-plane XRD patterns recorded during the growth (3 cycles, 6 cycles and 20 cycles) of pristine Cu-BPyDC thin film. (DFT calculations were performed by K. S. Ananthram under the supervision of Kartick Tarafder, NITK Surathkal, India).*

Due to distinctive coordination environments around Cu, vibrational modes associated with the BPyDC ligand are expected to be significantly different. Experimentally, in the Raman spectra (Figure 4.6b), during the initial growth cycles (up to 2.5 cycles) of Cu-BPyDC, one major peak at ~1009 cm^{-1} was observed along with one minor peak at 1020 cm^{-1}. After 2.5 cycles, a new peak was found to emerge at 1033 cm^{-1} along with the small co-existence of the aforementioned peaks which could be considered as the transition point for the onset of a new phase. Beyond 3.5 cycles, a single peak at 1033 cm^{-1} was consistently observed up to 20 cycles. With the help of the simulated Raman spectra, the peak at 1033 cm^{-1} and ~1009 cm^{-1} are assigned to be characteristic of phase-I and phase-II structures of the Cu-BPyDC system, respectively. Raman spectra also endorsed the phase-I structure as the major component (16 cycles of growth) and phase-II structure as the minor component (4 cycles of growth) within the Cu-BPyDC thin film thereby supporting the Rietveld refinement of the XRD patterns. To further strengthen our claim on mixed-phase of Cu-BPyDC, we have recorded cycling dependent out-of-plane XRD patterns during the growth of the pristine Cu-BPyDC thin film; after 3 cycles of growth, presence of phase-II structure was exclusively detected and only after 6 cycles (as well as 20 cycles) appearance of phase-I along with phase-II was clearly identified (Figure 4.6c). Cycling-dependent XPS data complemented the Raman data by showing distinctive Cu 2*p* photoemission signals during the growth of Cu-BPyDC thin film, confirming the presence of almost exclusive presence of Cu in the system (Appendix 4.5b).

Electrical transport properties of pristine Cu-TCNQ, pristine Cu-BPyDC and heterostructured Cu-TCNQ/Cu-BPyDC thin films were evaluated by recording current-voltage (*I-V*) profiles (in-plane and cross-plane modes) at room-temperature (300 K). *I-V* profiles for pristine Cu-TCNQ thin film were found to be similar in both in-plane and cross-plane modes with conductance value of ~6 x 10^{-7} S (Figure 4.7a,b) and so as the *I-V* profiles for pristine Cu-BPyDC thin film with conductance value of ~4 x 10^{-12} S (Figure 4.7c,d). As for the heterostructured Cu-TCNQ/Cu-BPyDC thin film, conductance value was found to be ~5 x 10^{-7} S in the in-plane mode – almost identical to the value observed for the pristine Cu-TCNQ thin film, as expected (Figure 4.8a). Interestingly however, in the cross-plane mode, a conductance value of ~1 x 10^{-5} S for the heterostructured Cu-TCNQ/Cu-BPyDC thin film was realized which is even higher and markedly-higher than the values of pristine Cu-TCNQ and Cu-BPyDC thin films, respectively (Figure 4.8b).

Notably, *I-V* profiles of pristine Cu-TCNQ, pristine Cu-BPyDC and heterostructured Cu-TCNQ/Cu-BPyDC thin films found on various spots in the same sample (Figure 4.7 and 4.8) and across different

batches of samples in both in-plane and cross-plane modes were observed to be consistent (Figure 4.8 and Appendix 4.6). Also, our solution processed interface was realized to be ambient-stable over months – retaining almost identical *I-V* profiles and reflecting a robust electrical transport property (Appendix 4.7).

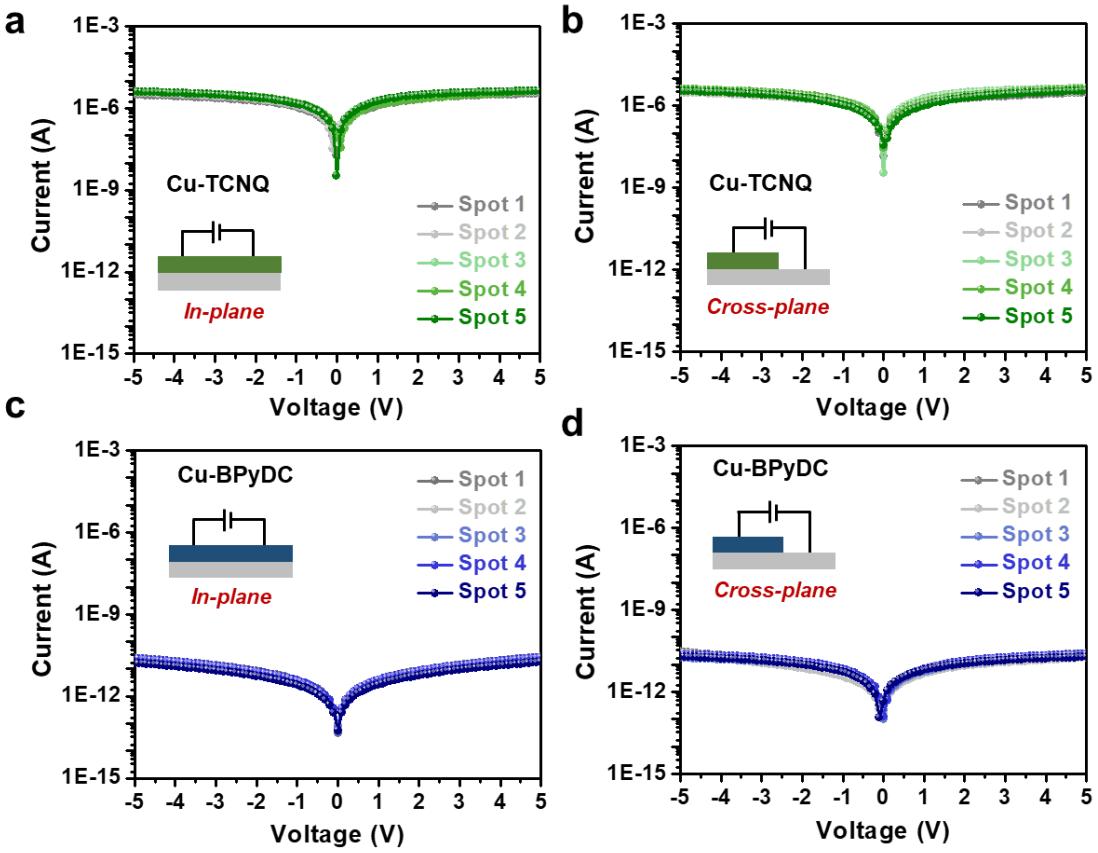

Figure 4.7. *In-plane and cross-plane current-voltage (I-V) characteristics of (a,b) pristine Cu-TCNQ (c,d) pristine Cu-BPyDC respectively (insets: schematic of I-V measurements in in-plane and cross-plane modes).*

One possibility of such a prominent enhancement in electrical conductance value could be due to the fact that TCNQ diffused inside Cu-BPyDC thin film during LbL growth of heterostructured Cu-TCNQ/Cu-BPyDC thin film, as was elegantly demonstrated earlier by Allendorf et al. for the tuning of electrical conductivity upon molecular doping of Cu-BTC by TCNQ. Such an impregnation of TCNQ resulted in successful transformation of an insulating MOF (Cu-BTC) to a semiconductor material (TCNQ@Cu-BTC).[17, 19, 29-30] Motivated by these remarkable observations, we have deliberately impregnated Cu-BPyDC thin film with TCNQ following our standardized procedure[14] (similar to the one reported by Allendorf et al.[29]) and performed a comparative assessment of TCNQ@Cu-BPyDC thin film with heterostructured Cu-TCNQ/Cu-BPyDC thin film.

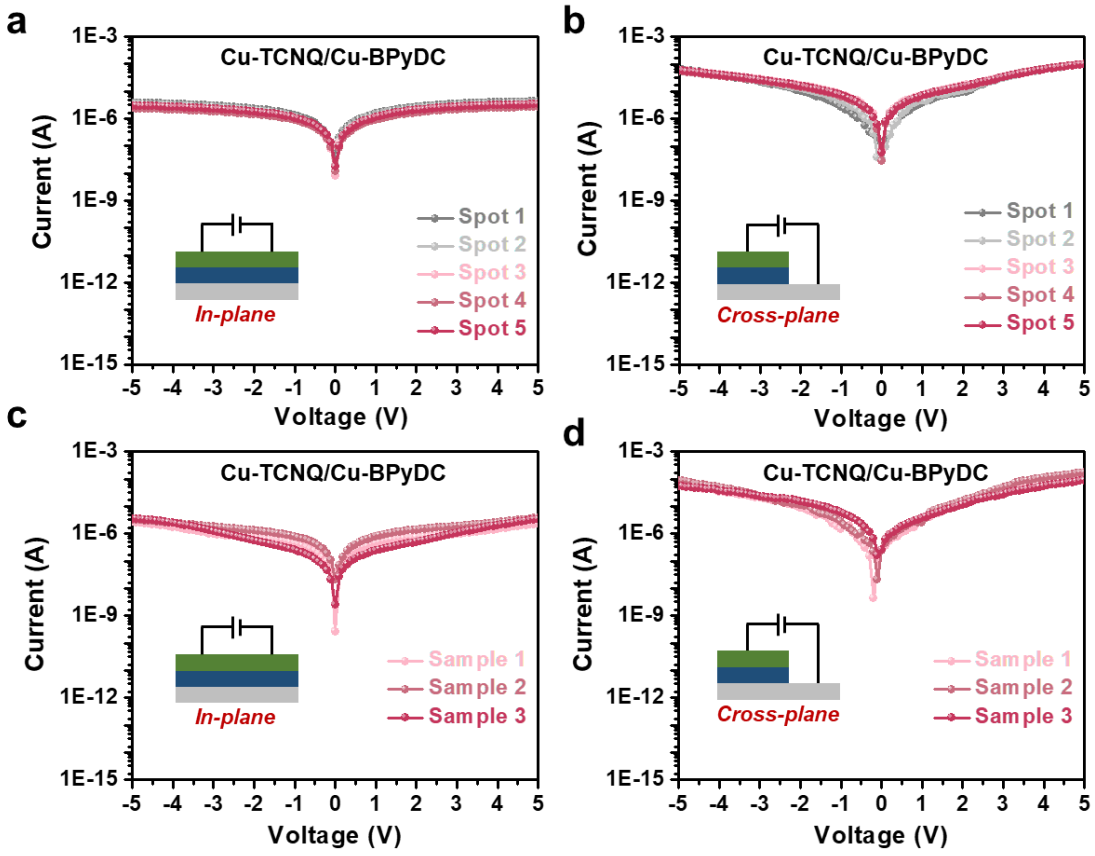

Figure 4.8. *In-plane and cross-plane current-voltage (I-V) characteristics of Cu-TCNQ/Cu-BPyDC heterostructured thin film (a,b) at various spots in the same sample and (c,d) at various samples respectively (insets: schematic of I-V measurements in in-plane and cross-plane modes).*

It is worth to mention here that in a recent study[12], we were able to successfully fabricate heterostructured Cu-TCNQ/Cu-BTC thin film by carefully avoiding the impregnation of TCNQ in Cu-BTC framework, and the same approach has been adopted in the present work i.e., upon reducing the reaction time of the initial few LbL growth cycles of Cu-TCNQ on top of Cu-BPyDC thin film.As revealed by FESEM images, after one LbL growth cycle, Cu-TCNQ crystallites with characteristic morphology were clearly visible on top of Cu-BPyDC thin film (Appendix 4.8a) which is very different from the morphological features on TCNQ@Cu-BPyDC thin film (Appendix 4.8b). The surface wettability after one LbL growth cycle of Cu-TCNQ on Cu-BPyDC thin film was markedly different from that of TCNQ@Cu-BPyDC thin film, as indicated by the water contact angle values of ~140±5° (Appendix 4.8a) and ~55±5° (Appendix 4.8b), respectively.

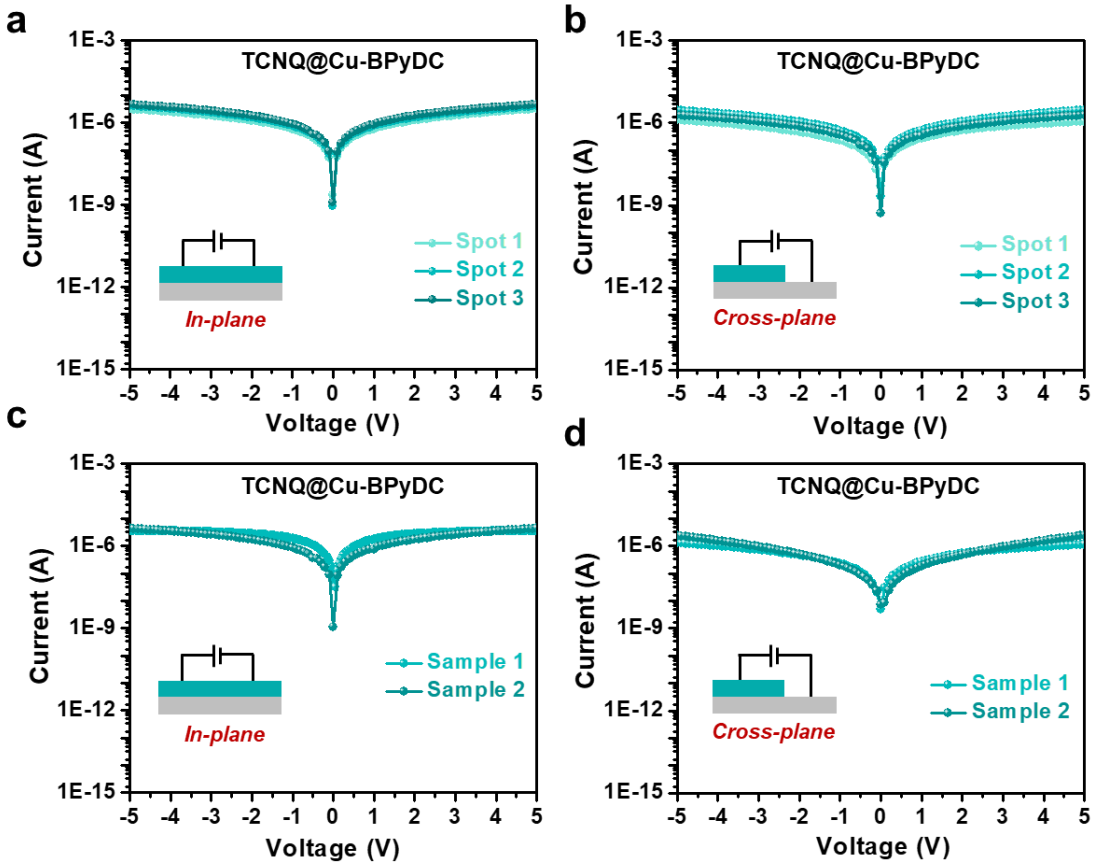

Figure 4.9. *In-plane and cross-plane current-voltage (I-V) characteristics of TCNQ@Cu-BPyDC heterostructured thin film (a,b) at various spots in the same sample and (c,d) at various samples respectively (insets: schematic of I-V measurements in in-plane and cross-plane modes).*

The in-plane *I-V* profiles for TCNQ@Cu-BPyDC thin film (Figure 4.9) with conductance value of ~6 x 10^{-7} S were found to be similar to those of heterostructured Cu-TCNQ/Cu-BPyDC (and pristine Cu-TCNQ) thin film. The cross-plane *I-V* profiles for TCNQ@Cu-BPyDC thin film with conductance value of ~3 x 10^{-7} S (Figure 4.9) were noticeably different from those of heterostructured Cu-TCNQ/Cu-BPyDC thin film. We have also estimated the resistivity values from the respective current-density (*J*)-*V* plots (Figure 4.10). The resistivity values of TCNQ@Cu-BPyDC thin film (~1 × 10^{6} Ωm) and earlier reported TCNQ@Cu-BTC thin film (~5 × 10^{7} Ωm)[19] were found to be more than hundred-fold and thousand-fold higher, respectively, than the resistivity value of heterostructured Cu-TCNQ/Cu-BPyDC thin film (~1 × 10^{4} Ωm). Thus, such a pronounced increment in the cross-plane electrical conductance of heterostructured Cu-TCNQ/Cu-BPyDC thin film, specifically in comparison to pristine Cu-BPyDC thin film, could not be simply attributed to the pore impregnation (by TCNQ)

effect and suggested an emergence of an interfacial phenomenon in the heterostructured thin film viz. metallic conduction.

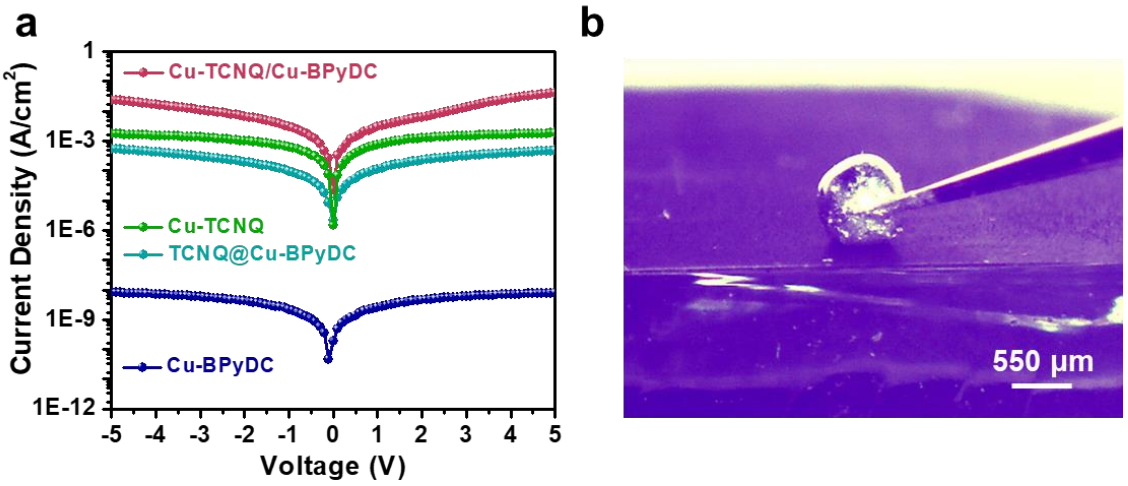

Figure 4.10. *Cross-plane current density-voltage (J-V) characteristics (a) recorded on pristine Cu-TCNQ, pristine Cu-BPyDC, heterostructured Cu-TCNQ/Cu-BPyDC, and TCNQ@Cu-BPyDC thin films; and photograph of EGaIn top contact electrode (b) showing the contact diameter of ca. 550 µm which was used to estimate the resistivity value (similar to the method outlined in Ref. 47). To directly compare the resistivity value of our samples with those in Ref. 22, we have taken the bias voltage at 0.5 V.*

Raman spectra of TCNQ@Cu-BPyDC and heterostructured Cu-TCNQ/Cu-BPyDC thin films were distinctively different (Figure 4.11). Specifically, in addition to the vibrational band at ~ 2205 cm^{-1}, appearance of an additional vibrational band at ~ 2220 cm^{-1} in the Raman spectrum of TCNQ@Cu-BPyDC thin film endorsed two non-equivalent bonding environments of TCNQ with two nitrile groups bonded to the Cu ions while other two nitrile groups remained unbind, as were earlier shown by Allendorf et al.[29] for the TCNQ@Cu-BTC thin film and by our group[14] for the TCNQ@Cu-BTEC (BTEC = 1,2,4,5-benzenetetracarboxylate) thin film. In the Raman spectrum of our heterostructured Cu-TCNQ/Cu-BPyDC thin film, only one vibrational band at ~ 2205 cm^{-1} appeared which is characteristic of Cu-TCNQ (Appendix 4.9) and absence of the vibrational band at ~ 2220 cm^{-1} evidenced no diffusion or impregnation of TCNQ into Cu-BPyDC layers. Further, Raman spectra were recorded during the initial growth of Cu-TCNQ on top of Cu-BPyDC thin film, at each step and up to four consecutive cycles of LbL (Figure 4.10a and Appendix 4.9). Notably, vibrational band at ~2220 cm^{-1}, serving as the fingerprint of a molecular doping phenomenon, was consistently absent (Figure 4.11a). Therefore, our cycling-dependent Raman spectroscopic data clearly ruled out the possibility of

any diffusion or impregnation of TCNQ into Cu-BPyDC layers, even at the microscopic level and our heterostructured thin film is not a system like Cu-TCNQ/TCNQ@Cu-BPyDC.

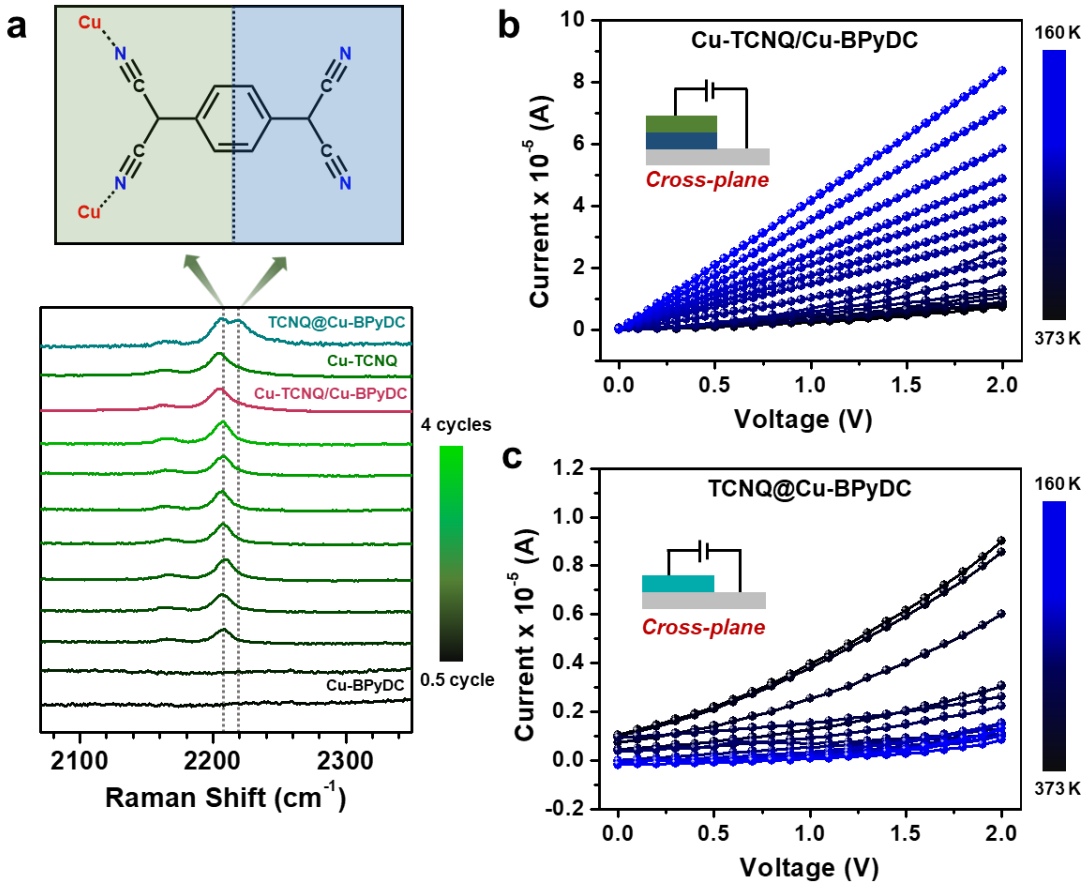

Figure 4.11. *(a) Raman spectra recorded during the growth of Cu-TCNQ on top of Cu-BPyDC thin film (at each step of LbL and up to 4 cycles). Raman spectra of pristine Cu-TCNQ and TCNQ @Cu-BPyDC thin films are also provided for a direct comparison. CN groups of TCNQ will have different vibrational signatures if coordinated to metal ion (like Cu in the present study) – as schematically shown and highlighted by blue and green colors. Positions of the vibrational bands are marked by dotted lines. Current-voltage (I-V) profiles at different temperatures, ranging from 160 K to 373 K, on the (b) heterostructured Cu-TCNQ/Cu-BPyDC thin film and (c) TCNQ@Cu-BPyDC thin film in the cross-plane modes.*

Finally, temperature dependence of the electrical transport property was evaluated by recording the *I-V* profiles, in the cross-plane mode, at various temperature, ranging from low-temperature (160 K) to high-temperature (373 K). In the heterostructured Cu-TCNQ/Cu-BPyDC thin film, a gradual increase in the conductance/conductivity value upon decreasing the temperature from 373 K down to 160 K (Figure 4.11b) confirmed metallic conduction. On the contrary, an opposite trend was realized with the TCNQ@Cu-BPyDC thin film where conductance/conductivity value gradually increased upon

increasing the temperature from 160 K to 373 K (Figure 4.11c) – as expected for a semiconducting system like the well-celebrated TCNQ@Cu-BTC system.[29]

To understand the origin of such an interesting interfacial effect, numerical simulations based on density functional theory (DFT) with additional Hubbard interaction (+U) were performed on Cu-TCNQ, Cu-BPyDC, and heterostructured Cu-TCNQ/Cu-BPyDC systems.[21-22, 31] The bulk structures of Cu-TCNQ ($C_{48}H_{16}N_{16}Cu_4$) and phase-I Cu-BPyDC ($C_{48}H_{56}N_8O_{32}Cu_4$) were modelled by using experimentally obtained crystal structure data[26-27] and duly optimized (Figure 3a and Appendix Table 4.1). After performing bulk geometry optimization of Cu-TCNQ and Cu-BPyDC, an interface structure was constructed by modeling slabs and stacking them along (001) crystal direction of Cu-BPyDC (Appendix 4.10). We found that the (001) crystal direction was most favorable for the formation of the Cu-TCNQ/Cu-BPyDC ($C_{236}H_{200}N_{48}O_{64}Cu_{16}$) interface as the surface energies as well as the lattice mismatch between slabs were minimum. Also, strain on the individual slabs of Cu-TCNQ and Cu-BPyDC was found to be minimum when stacking them along (001) crystal direction of Cu-BPyDC. Our calculations show that Cu-TCNQ and Cu-BPyDC systems have band gap values of 2.1 eV and 2.7 eV respectively (Figure 4.12), corroborating the optical band gap values obtained from the respective solid-state UV-vis absorption spectra viz. Tauc plots[12] (Appendix 4.11).

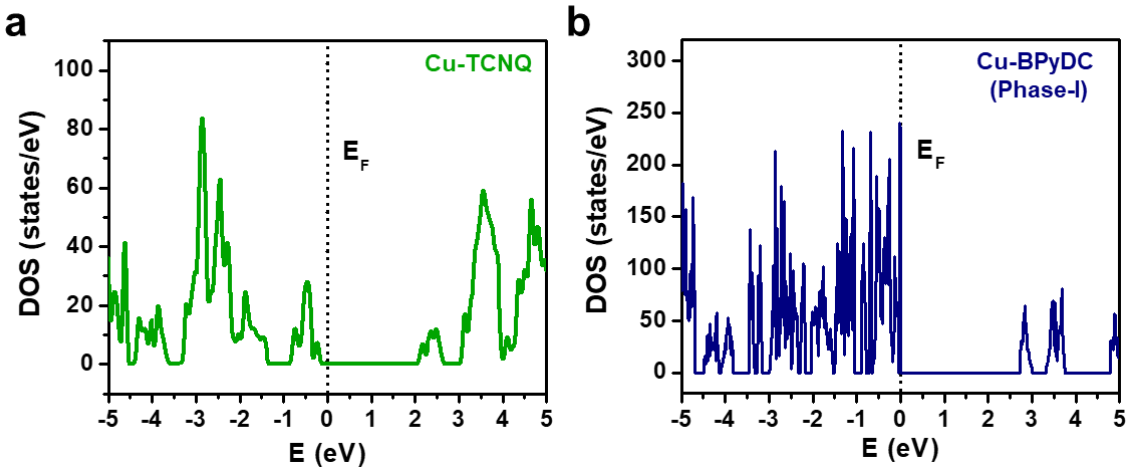

Figure 4.12. *Total density of states (DOS) plots for (a) Cu-TCNQ (green solid line) and (b) Cu-BPyDC Phase-I (blue solid line). Fermi energy is marked by black dotted lines. (DFT calculations were performed by K. S. Ananthram under the supervision of Kartick Tarafder, NITK Surathkal, India).*

Remarkably, interface was found to be metallic with a finite density of states (DOS) at the Fermi level (Figure 4.13a). To recognize this unusual behavior, the difference in charge density due to the

formation of the interface was estimated by using the formula ρ = ρ(AB) – ρ(A) – ρ(B), where ρ(A), ρ(B) and ρ(AB) are the charge densities for Cu-TCNQ, Cu-BPyDC, and Cu-TCNQ/Cu-BPyDC interface, respectively. Significant charge accumulation at the interface is clearly visible in the charge-density plot (Figure 4.13). Specifically, Bader charge analysis[23] was carried out using Henkelman's group program.[32-34] Bader charges are charges of involved atoms defined by an infinitesimal volume of minimal gradient around each atom (Appendix Table 4.2). Charge transfer is estimated to be equal to [Bader charge of the interface (Cu(I)/Cu) – Bader charge of Cu(I) structure – Bader charge of Cu structure].

To find out the charge accumulation at the interface, the distribution of the Bader charge on twenty-eight atoms at the interface is calculated. In this calculation we were only able to specify which atoms are affected and Bader charge analysis was unable to provide the orbital nature of the transferred charges. The details of charges transferred from different atoms at the interface are also summarized (Appendix Table 4.3). The negative Bader charge difference indicates the charge depletion and the positive value indicates the charge accumulation at the atom center (indicated by cyan and yellow isosurfaces, respectively in Figure 4.13). According to our calculations, an approximate net charge of 0.0026 e/Å^3 (or total of 3.52 e per interfacial unit cell) was accumulated at the interface and the charges were estimated to percolate about 7 Å away from the interface. Thus, DFT+U calculations combined with experimental observations evidenced an interfacial metallic conduction. Notably, our cycling-dependent XRD patterns (Figure 4.6c) revealed that with increasing the number of cycles, phase-I structure of Cu-BPyDC became dominant over phase-II and therefore, primarily contributing to the interfacial effects in the heterostructured Cu-TCNQ/Cu-BPyDC thin film.

We have additionally performed similar DFT (+U) calculations upon taking the same crystal structure of Cu-TCNQ ($C_{48}H_{16}N_{16}Cu_4$) but with phase-II crystal structure of Cu-BPyDC ($C_{96}H_{64}N_{16}O_{44}Cu_{10}$) obtained from the Rietveld refinement (Appendix Table 4.4). After performing geometry optimization of both the bulk structures, an interface structure was constructed by stacking them along (001) crystal direction of Cu-BPyDC (Figure 4.14). Bader charge analysis of the Cu-TCNQ/Cu-BPyDC ($C_{480}H_{224}N_{128}O_{88}Cu_{32}$) interface was carried out (Appendix Table 4.5 and Table 4.6) likewise the aforementioned system and in comparison to phase-II structure of Cu-BPyDC, better charge accumulation and percolation across the interface was realized with the phase-I structure of Cu-BPyDC. Remarkably, metallic interface was consistently observed (Figure 4.14) thereby suggesting

that the interfacial charge-transfer chemistry of insulating Cu-BPyDC and Cu(I)-TCNQ MOFs is indeed engrossing and can have far reaching implications.

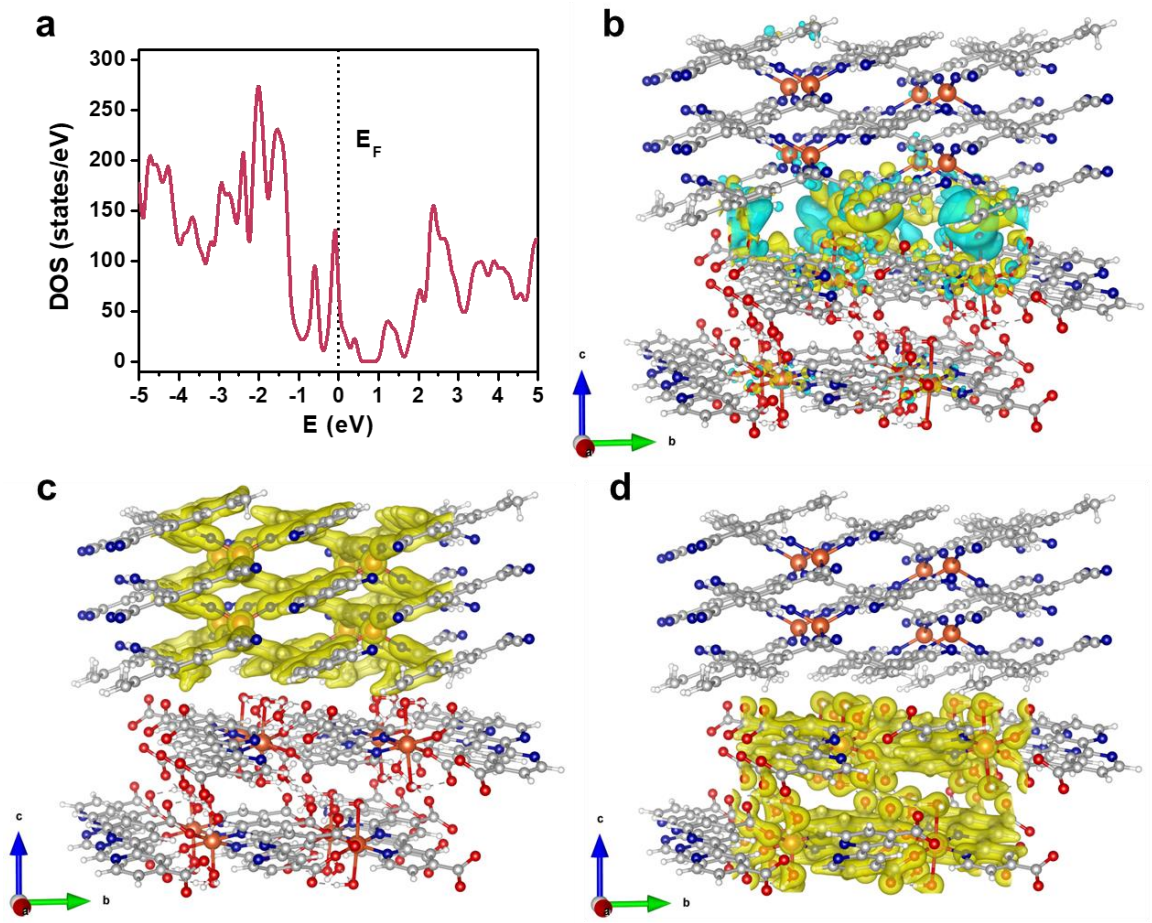

Figure 4.13. *(a) Total density of state (DOS) for the interface structure (pink), a new large peak at the Fermi energy (E_F, marked by dotted black line) appears due to significant charge redistribution and strong hybridization at the interface structure. (b) Percolated charge density due to the formation of the interface is presented (view from bc plane). Total charge density plot for (c) only Cu-TCNQ in heterostructured Cu-TCNQ/Cu-BPyDC system and (d) only Cu-BPyDC structure in heterostructured Cu-TCNQ/Cu-BPyDC system. The atoms carbon, hydrogen, nitrogen, oxygen, and copper are represented by colors grey, white, blue, red, and orange, respectively. Electron accumulation and electron depletion are represented by yellow and cyan isosurfaces, respectively. (DFT calculations were performed by K. S. Ananthram under the supervision of Kartick Tarafder, NITK Surathkal, India).*

Charge-transfer phenomenon has been observed earlier in MOFs upon introducing various design strategies such as incorporation of redox-active guest molecules, integration of mixed donor-acceptor linkers in a single framework, post-synthetic modifications, and many more. An elegant example has

already been discussed where redox-active TCNQ molecules were loaded inside the pores of Cu-BTC and a dramatic enhancement in the electrical conductivity was observed which originated from host-guest charge-transfer interaction.[17, 19, 29-30, 35-36]

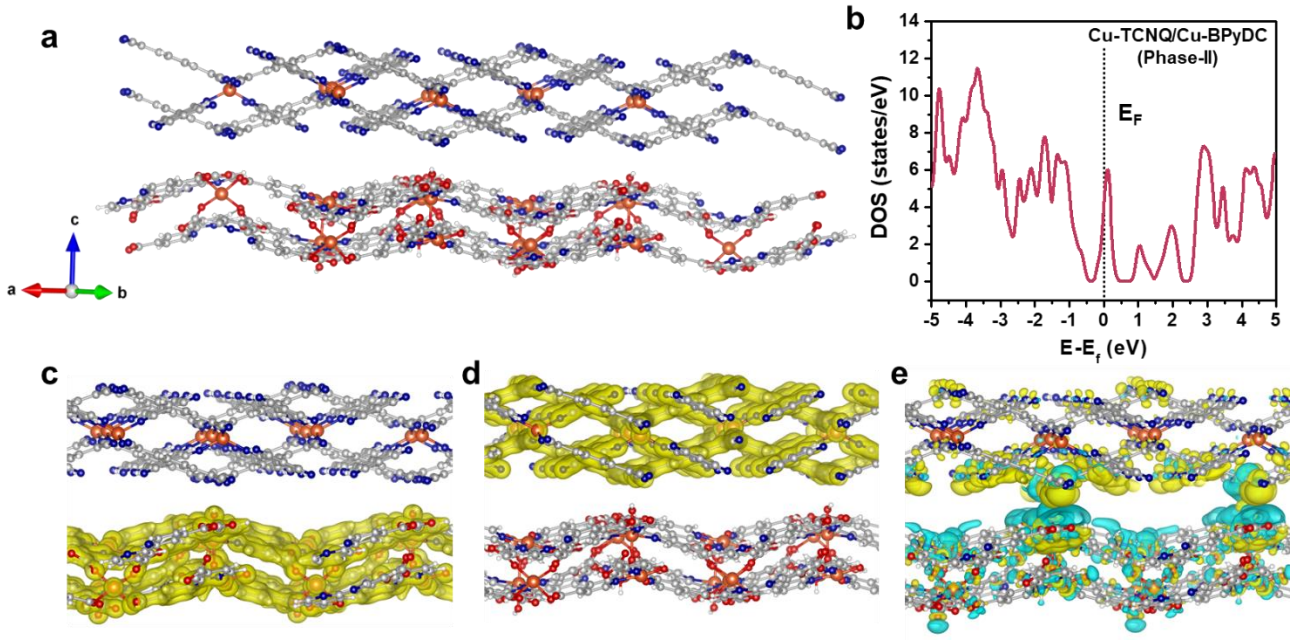

Figure 4.14. *(a) Optimized interface geometric structure of Cu-TCNQ (top, $C_{48}H_{16}N_{16}Cu_4$) and phase-II Cu-BPyDC (bottom, $C_{96}H_{64}N_{16}O_{44}Cu_{10}$) interface where orange, grey, red, blue, and white colours represent copper, carbon, oxygen, nitrogen, and hydrogen atoms, respectively. (b) The total density of state (DOS) for the interface structure, a continuous state at the Fermi energy appeared due to significant charge redistribution and strong hybridization at the interface. (c) Total charge density plot for only Cu-BPyDc (Phase-II) in heterostructured Cu-TCNQ ($C_{48}H_{16}N_{16}Cu_4$)/Cu-BPyDC ($C_{96}H_{64}N_{16}O_{44}Cu_{10}$) system. (d) Total charge density plot for only Cu-TCNQ in heterostructured Cu-TCNQ ($C_{48}H_{16}N_{16}Cu_4$)/Cu-BPyDC ($C_{96}H_{64}N_{16}O_{44}Cu_{10}$) system. (e) Percolated charge density due to the formation of the interface Cu-TCNQ/Cu-BPyDC ($C_{480}H_{224}N_{128}O_{88}Cu_{32}$) is presented where electron accumulation and electron depletion are represented by yellow and cyan isosurfaces, respectively. (DFT calculations were performed by K. S. Ananthram under the supervision of Kartick Tarafder, NITK Surathkal, India).*

The photo-physical effects on infiltration of α,ω-dihexylsexithiophene (DH6T) and [6,6]-phenyl-C_{61}-butyric acid methyl ester (PCBM) inside the pores of MOF-177 ($ZnO_4(BTB)_2$; BTB = 1,3,5-benzenetribenzoate) has been studied with different sample configurations, and consistently, an efficient quenching of MOF-177 luminescence was observed via host-guest Förster resonance energy transfer (FRET) mechanism.[37] Also, host-guest charge-transfer was assigned to occur due to the unique

special arrangements allowing overlapping of p-orbitals of the BTB linkers of MOF host with the fullerene ring of PCBM guest.[37] MOF with mixed donor-acceptor linkers of donor TTFTB (tetrathiafulvalene tetrabenzoate) and acceptor bpmNDI [N,N'-bis(4-pyridylmethyl)-1,4,5,8-naphthalene diimide] exhibited high-degree of charge-transfer from TTF to NDI resulting in a broad absorption in the near infra-red (NIR) region. TTF and NDI moieties were found to interact in a face-to-face manner in the framework with dihedral angle of ca. 8.17° and ca. 3.45 Å distance apart facilitating donor-acceptor charge-transfer and π-π interactions.[38] Wavelength-dependent energy and charge-transfer in a MOF, post-synthetically modified by photo-active porphyrin moiety, also enabled realization of an artificial light harvesting system.[39]

Core-shell heterostructures of Prussian blue-based MOF (core) and porphyrin-based MOF (shell) were developed for the enhancement of photocatalytic properties whereby photo-inspired electrons transfer process can be facilitated while suppressing the recombination of electrons and holes.[40] Heterostructured core-shell system of two Ti-based MOFs also helped to realize multi-stepwise charge transfer during photo-catalytic hydrogen evolution.[41] One-dimensional micro-rods of Eu-BTC and Tb-BTC were successfully grown in tri-block heterostructured configurations for the development of photonic barcodes.[42] Additionally, A-B-A type tri-layer heterostructured thin film was fabricated by LbL technique and Dexter transfer of triplet excitons over the heterojunction demonstrated electron transfer across the layers.[43] AB-type heterostructured thin films of lanthanides (Eu and Tb)-based MOFs with different compositional ratios were fabricated just by varying the growth cycles in LbL and tunable emission was achieved.[44] Also, ABC-type tri-layer heterostructured thin films of Eu, Gd, and Tb-based MOFs exhibited white-light emission.[45] Interestingly however, none of the reports dealing with the charge-transfer phenomenon in MOFs led to observation of metallic conduction in the system, in particular for the heterostructured thin films of MOFs. Only two reports on the electrical transport across heterostructured MOF thin films have been reported till date. In the first report, AB- and BA-type heterostructured thin films of Cu-BTC and Cu-TCNQ were successfully fabricated by LbL technique and rectification of electrical current in the cross-plane mode was consistently observed with similar on-off ratio which was assigned to be due to generation of p-n and n-p junction diode interfaces.[12] In the second report, AB- and BA-type heterostructured thin films of p-type $Cu_2(adc)_2(dabco)$ and n-type $C_{60}@Cu_2(bdc)_2(dabco)$ (adc = 9,10-anthracene dicarboxylate, bdc = 1,4-benzene dicarboxylate and dabco = 1,4-diazabicyclo[2.2.2]octane) MOFs were fabricated by LbL technique and distinctive on-off ratios for the p-n and n-p interfaces were realized.[46] Therefore, in

conjunction with charge/energy transfer across MOF heterostructures, our findings on metallic conduction across the interface of insulating MOFs will certainly open up possibilities in the field.

4.4 Conclusions

In summary, we have presented an interface of Cu(I)($3d^{10}$) and Cu($3d^{9}$) ions-based insulating MOFs coordinated to TCNQ and BPyDC ligands, respectively. Electrical conductance value across the heterostructured Cu-TCNQ/Cu-BPyDC thin film was found to be more than ten-fold and million-fold higher than the values of pristine Cu-TCNQ and Cu-BPyDC thin films, respectively. Raman spectral signatures ruled out the possibility of any pore impregnation of Cu-BPyDC layers by TCNQ in the heterostructured Cu-TCNQ/Cu-BPyDC thin film. Such a pronounced enhancement in the electrical conductivity was attributed to be due to an interfacial metallic conduction and was duly endorsed by the temperature dependence of the *I-V* profiles. Electrical transport measurements were further substantiated by numerical simulations based on DFT (+U) calculations revealing a strong interlayer hybridization and charge-transfer leading to an overlap of CB and VB in the Cu-TCNQ/Cu-BPyDC interface (even consistent with different crystal structures of Cu-BPyDC) while finite gaps between CB and VB for both Cu-TCNQ and Cu-BPyDC.[47] Our results clearly open an avenue for the development of heterostructured MOF-based thin film electronic devices in particular, because most often MOFs are electrical insulators.

4.5 Appendix

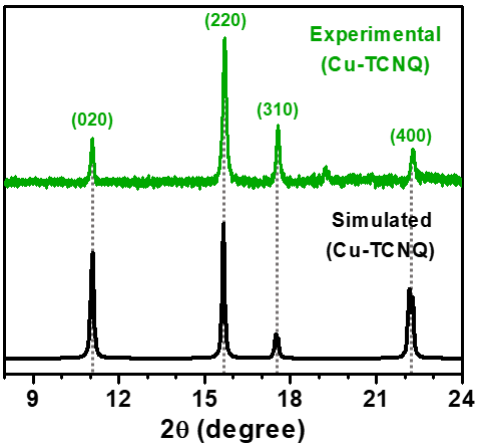

Appendix 4.1. *Experimental XRD pattern of Cu-TCNQ thin film and simulated XRD pattern of Cu-TCNQ (crystal structure data was obtained from the supplementary files of Ref. 31).*

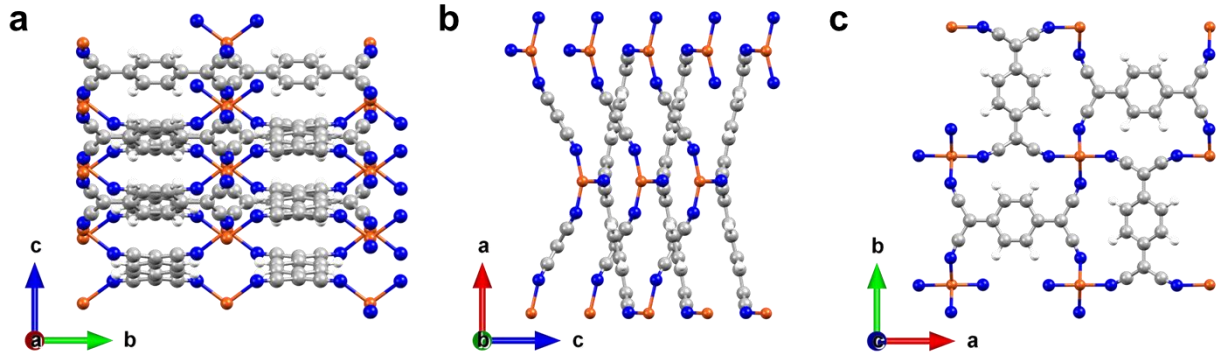

Appendix 4.2. *Insights into structure of Cu-TCNQ; view along (a) a-axis (b) b-axis and (c) c-axis; orange, grey, blue, and white colors represent copper, carbon, nitrogen, and hydrogen atoms, respectively.*

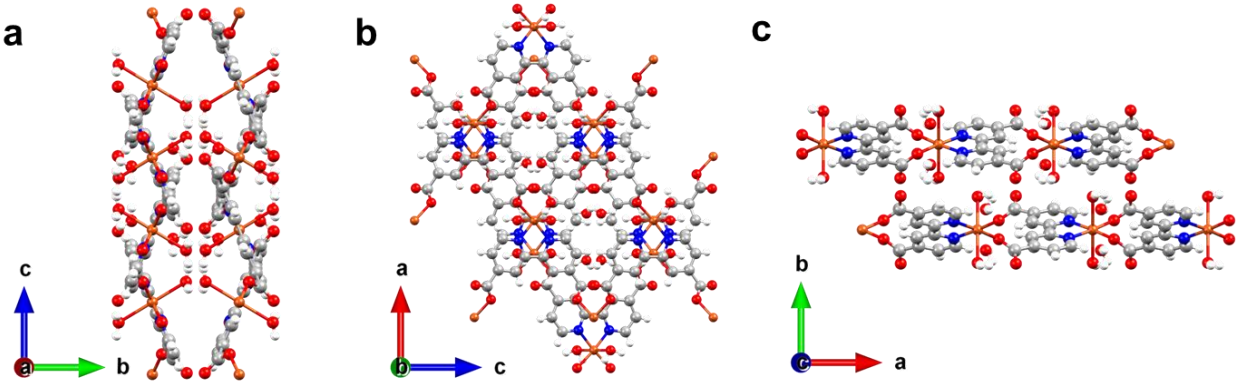

Appendix 4.3. *Insights into phase-I structure of Cu-BPyDC (Phase-I); view along (a) a-axis (b) b-axis and (c) c-axis; orange, grey, red, blue, and white colors represent copper, carbon, oxygen, nitrogen, and hydrogen atoms, respectively. (DFT calculations were performed by K. S. Ananthram under the supervision of Kartick Tarafder, NITK Surathkal, India).*

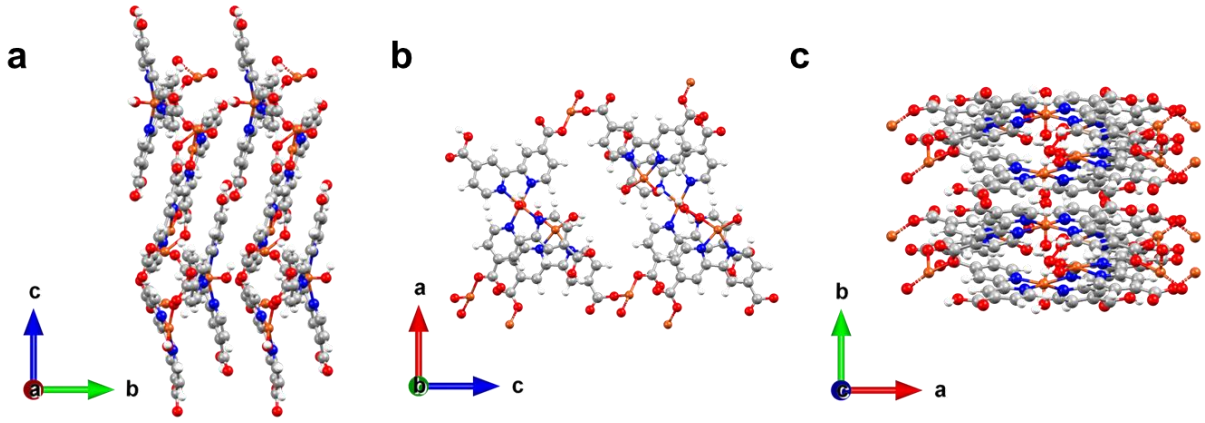

Appendix 4.4. *Insights into phase-II structure of Cu-BPyDC; view along (a) a-axis (b) b-axis and (c) c-axis; orange, grey, red, blue, and white colors represent copper, carbon, oxygen, nitrogen, and hydrogen atoms, respectively. (DFT calculations were performed by K. S. Ananthram under the supervision of Kartick Tarafder, NITK Surathkal, India).*

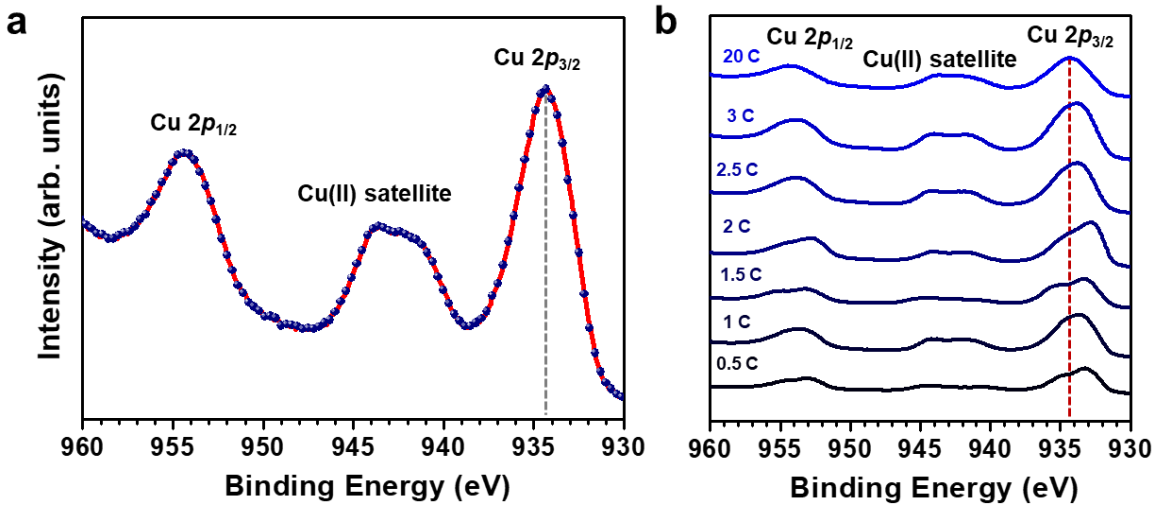

Appendix 4.5. *(a) Cu 2p XPS data recorded on pristine Cu-BPyDC thin film showing the Cu $2p_{3/2}$ signal at ~934.2 eV along with strong satellite feature clearly evidencing the presence of Cu in the thin film. (b) Cu 2p XPS spectra recorded during the growth of pristine Cu-BPyDC thin film at each step of LbL method from 0.5 to 3 cycles and at 20^{th} cycle (C stands for cycle) with strong satellite feature clearly evidencing the presence of Cu in the thin film. During the initial growth (up to 2 cycles), the Cu $2p_{3/2}$ signals at binding energy value of ~933.1 eV and ~935.2 eV could be assigned to two distinctive coordination of Cu ions to four N and four O atoms from BPyDC ligands, respectively, in phase-II structure of Cu-BPyDC. After 2 cycles (up to 3 cycles), the Cu $2p_{3/2}$ signal at binding energy value of ~933.8 eV could be assigned to mixed phase-I and phase-II structures of Cu-BPyDC (note that in phase-I structure of Cu-BPyDC, Cu(II) ion is coordinated simultaneously to two N and*

two O atoms from BPyDC ligands). After 20 cycles, the Cu $2p_{3/2}$ signal at binding energy value of ~934.2 eV could originate predominantly from the phase-I structure of Cu-BPyDC. Therefore, cycling dependent XPS data complemented the cycling dependent Raman spectra as well as XRD patterns.

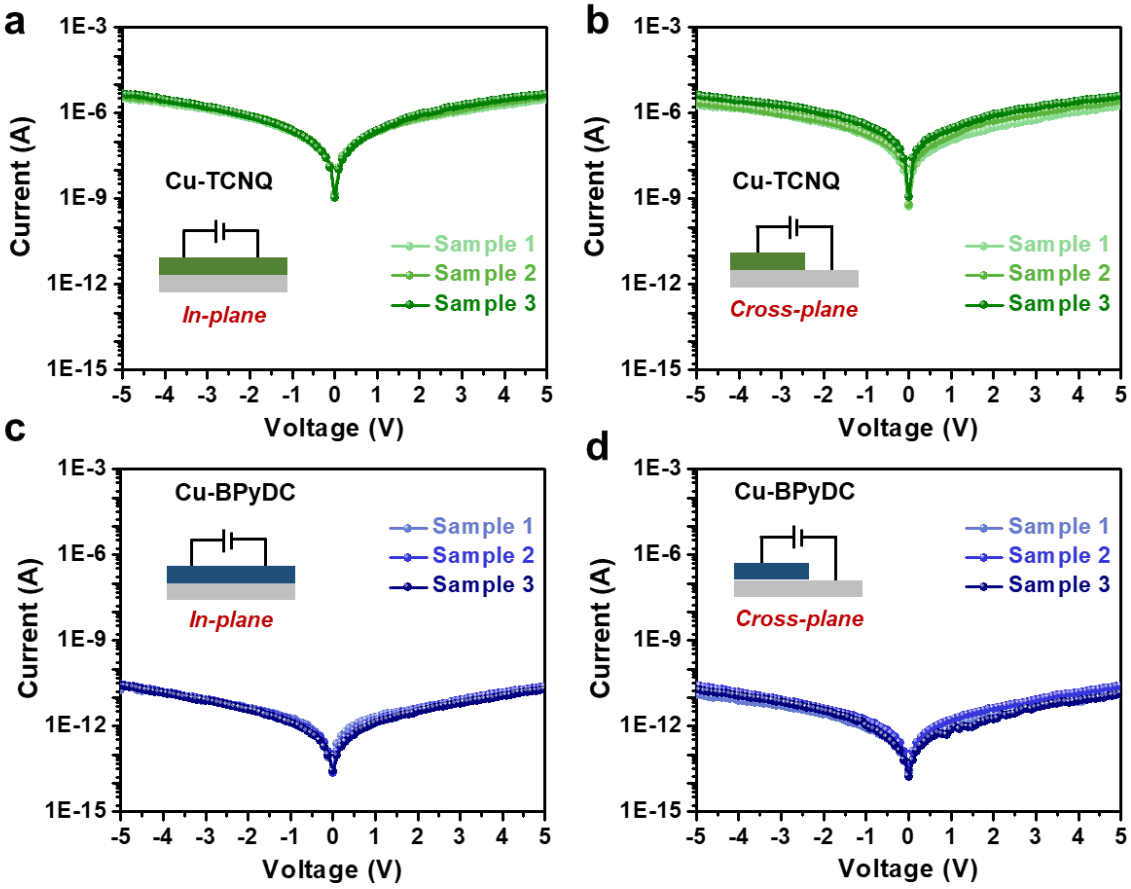

Appendix 4.6. *In-plane and cross-plane current-voltage (I-V) characteristics of (a,b) pristine Cu-TCNQ (c,d) pristine Cu-BPyDC respectively at various samples (insets: schematic of I-V measurements in in-plane and cross-plane modes).*

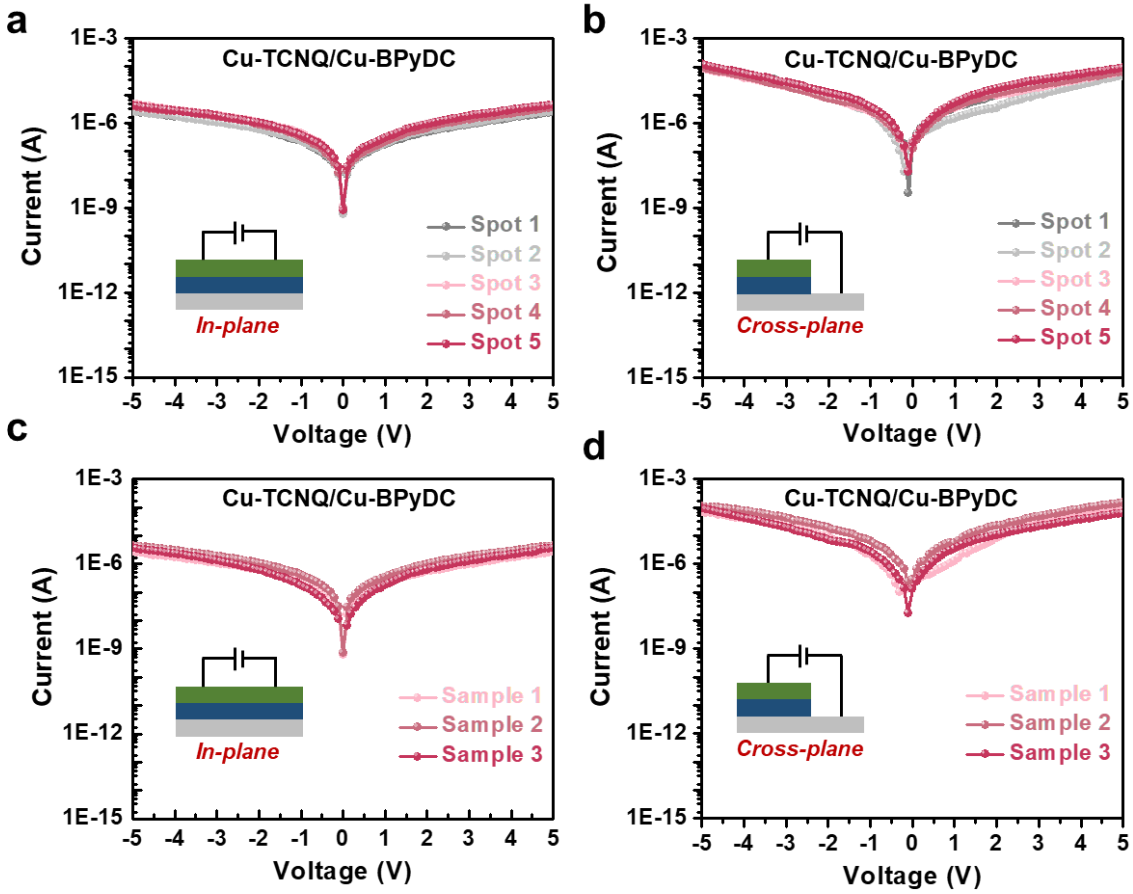

Appendix 4.7. *Current-voltage (I-V) characteristics recorded on 3 months old (kept at ambient conditions) heterostructured Cu-TCNQ/Cu-BPyDC thin films in (a) in-plane and (b) cross-plane modes on various spots in the sample and (c) in-plane and (d) cross-plane modes across different samples. (insets: schematic of I-V measurements in in-plane and cross-plane modes).*

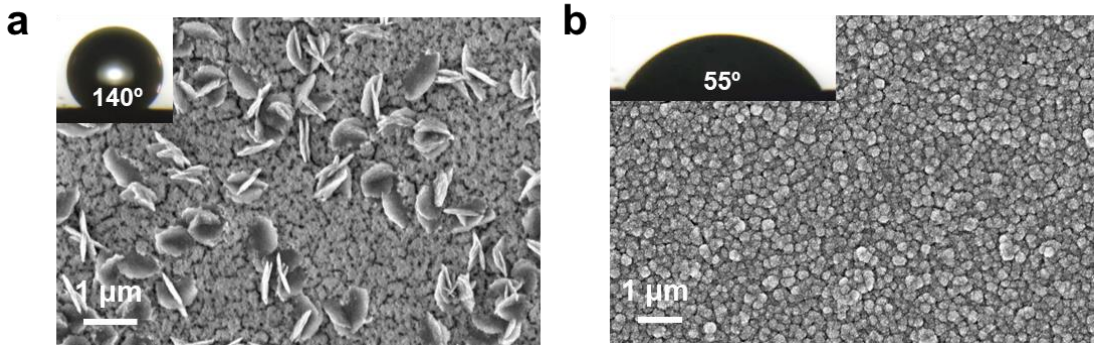

Appendix 4.8. *(a) FESEM image (top-view) showing the initial growth (few LbL cycles) of Cu-TCNQ crystallites with distinctive nanodisc-like morphology on top of the Cu-BPyDC thin film (inset: an optical image*

of the contact angle of water). (b) FESEM image (top-view) showing morphological features of TCNQ@Cu-BPyDC thin film (inset: an optical image of the contact angle of water).

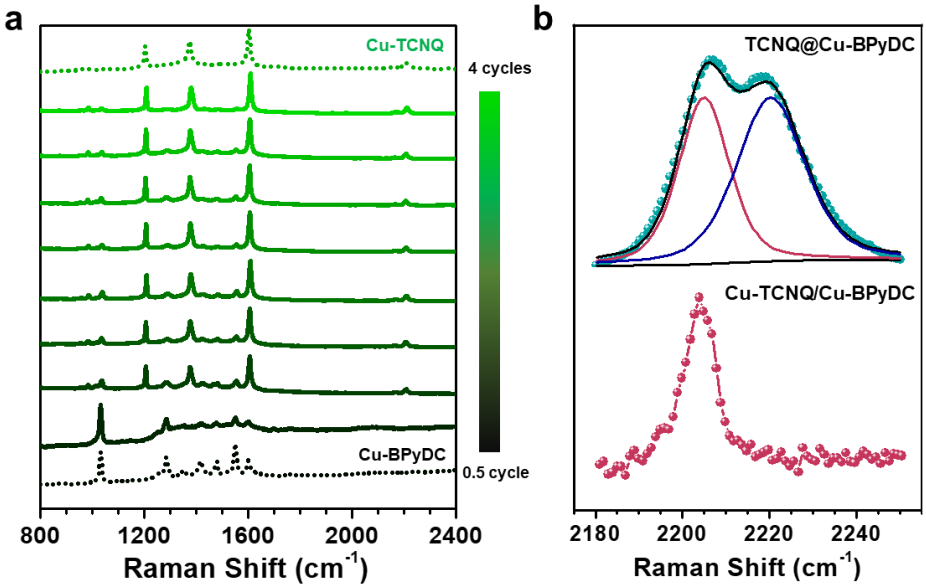

Appendix 4.9. *(a) Raman spectra recorded during the growth of Cu-TCNQ on top of Cu-BPyDC thin film, at each step of LbL and up to 4 cycles; and compared with the Raman spectrum of the pristine Cu-TCNQ thin film. (b) Fitted Raman spectrum of the TCNQ@Cu-BPyDC thin film and as comparison Raman spectrum of heterostructured Cu-TCNQ/Cu-BPyDC thin film is provided.*

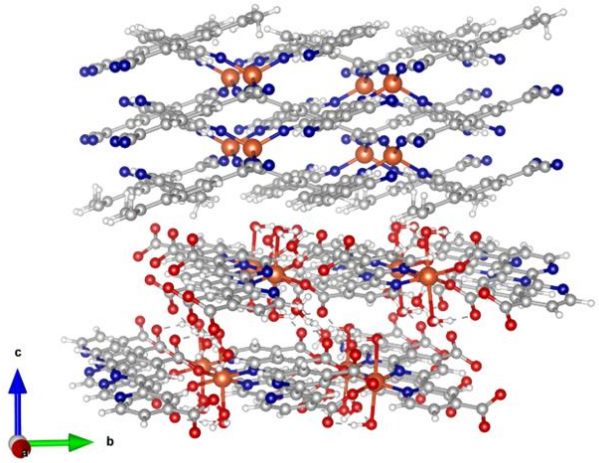

Appendix 4.10. *Energy optimized structure of the interface involving Cu-TCNQ (top) and phase-I of Cu-BPyDC (bottom) where carbon, hydrogen, nitrogen, oxygen, and copper atoms are represented by colors grey, white,*

blue, red, and orange, respectively (view from bc plane). (DFT calculations were performed by K. S. Ananthram under the supervision of Kartick Tarafder, NITK Surathkal, India).

Appendix Table 4.1. Lattice constants information of all optimized structures. (DFT calculations were performed by K. S. Ananthram under the supervision of Kartick Tarafder, NITK Surathkal, India).

Structure	a (Å)	b (Å)	c (Å)	α	β	γ	Space group/HM notation
Cu-TCNQ $C_{48}H_{16}N_{16}Cu_4$	15.53	16.47	3.806	90º	90º	90º	1/P1
Cu-BPyDC (Phase-I) $C_{48}H_{56}N_8O_{32}Cu_4$	17.35	14.89	30.60	90º	90º	90º	52/Pnna
Cu-TCNQ/Cu-BPyDC (Phase-I) interface $C_{236}H_{200}N_{48}O_{64}Cu_{16}$	15.60	15.17	30.48	90º	90º	90º	-nil-

Appendix Table 4.2. Atoms-wise total Bader charge contribution. (DFT calculations were performed by K. S. Ananthram under the supervision of Kartick Tarafder, NITK Surathkal, India).

Atom	Charge (e) in the Layer					
	Total charge on atoms in the top-layer per unit cell		Net charge difference per atom due to formation of interface	Total charge on atoms in the bottom-layer per unit cell		Net charge difference per atom due to formation of interface
	Interface	Individual		Interface	Individual	
Cu	82.71	80.74	0.24	78.78	79.27	-0.06
O	- nil -	- nil -	- nil-	444.30	461.78	-0.27
N	177.33	199.12	-0.68	95.36	99.71	-0.27

Appendix Table 4.3. Details of charge (e) transferred from different atoms at the interface. (DFT calculations were performed by K. S. Ananthram under the supervision of Kartick Tarafder, NITK Surathkal, India).

Atoms [B & T indicate bottom and top layers in the unit cell]	**Total charge on the atoms in the Cu(I)/Cu interface**	**Charge on the atom in the individual layer**	**Net Bader charge at the interface**
Cu-T (4 atoms)	40.36	41.35	-0.99
Cu-B (4 atoms)	39.64	39.44	0.20
N-T (8 atoms)	49.82	47.25	2.57
N-B (8 atoms)	49.8	47.62	2.18
O-B (4 atoms)	28.09	28.53	-0.44
Total effective charge at the interface			**3.52**

Appendix Table 4.4. Lattice constants information of all optimized structures. (DFT calculations were performed by K. S. Ananthram under the supervision of Kartick Tarafder, NITK Surathkal, India).

Structure	**a (Å)**	**b (Å)**	**c (Å)**	**α**	**β**	**γ**	**Space group/HM notation**
Cu-TCNQ $C_{48}H_{16}N_{16}Cu_4$	15.53	16.47	3.806	90º	90º	90º	1/P1
Cu-BPyDC (Phase-II) $C_{96}H_{64}N_{16}O_{44}Cu_{10}$	16.72	6.419	24.03	90º	104º	90º	1/P1
Cu-TCNQ/Cu-BPyDC (Phase-II) interface $C_{480}H_{224}N_{128}O_{88}Cu_{32}$	34.63	23.43	25.50	90º	90º	104.5º	1/P1

Appendix Table 4.5. Atoms-wise total Bader charge contribution by considering Cu-BPyDC (Phase-II) structure. (DFT calculations were performed by K. S. Ananthram under the supervision of Kartick Tarafder, NITK Surathkal, India).

Atom	Charge (e) in the Layer					
	Total charge on atoms in the top-layer per unit cell		Net charge difference per atom due to formation of interface	Total charge on atoms in the bottom-layer per unit cell		Net charge difference per atom due to formation of interface
	Interface	Individual		Interface	Individual	
Cu	120.6684	120.6092	0.0592	201.3270	201.3092	0.0178
O	- nil -	- nil -	- nil-	603.2546	603.4929	-0.2383
N	562.9860	563.2321	-0.2461	184.08198	184.3694	-0.2874

Appendix Table 4.6. Details of charge (e) transferred from different atoms at the interface from Cu-TCNQ and Cu-BPyDC (Phase-II) as top and bottom layers respectively. (DFT calculations were performed by K. S. Ananthram under the supervision of Kartick Tarafder, NITK Surathkal, India).

Atoms [B & T indicate bottom and top layers in the unit cell]	Total charge on the atoms in the Cu(I)/Cu interface	Charge on the atom in the individual layer	Net Bader charge at the interface
Cu-T (12 atoms)	120.66845	120.60922	0.06
Cu-B (10 atoms)	100.545645	100.216273	0.33
N-T (12 atoms)	69.767518	69.710702	0.06
N-B (12 atoms)	69.227223	69.315718	0.09
O-B (18 atoms)	123.720431	123.797303	0.08
Total effective charge at the interface			**0.62**

4.6 References

1. Takahashi, K. S.; Kawasaki, M.; Tokura, Y., Interface ferromagnetism in oxide superlattices of $CaMnO_3/CaRuO_3$. *Appl. Phys. Lett.* **2001,** *79* (9), 1324-1326.

2. Ohtomo, A.; Muller, D. A.; Grazul, J. L.; Hwang, H. Y., Artificial charge-modulationin atomic-scale perovskite titanate superlattices. *Nature* **2002,** *419* (6905), 378-380.

3. Ohtomo, A.; Hwang, H. Y., A high-mobility electron gas at the $LaAlO_3/SrTiO_3$ heterointerface. *Nature* **2004,** *427* (6973), 423-426.

4. Reyren, N.; Thiel, S.; Caviglia, A. D.; Kourkoutis, L. F.; Hammerl, G.; Richter, C.; Schneider, C. W.; Kopp, T.; Rüetschi, A. S.; Jaccard, D.; Gabay, M.; Muller, D. A.; Triscone, J. M.; Mannhart, J., Superconducting Interfaces Between Insulating Oxides. *Science* **2007,** *317* (5842), 1196.

5. Heber, J., Materials science: Enter the oxides. *Nature* **2009,** *459* (7243), 28-30.

6. Mannhart, J.; Schlom, D. G., Oxide Interfaces—An Opportunity for Electronics. *Science* **2010,** *327* (5973), 1607.

7. Huang, Z.; Ariando; Renshaw Wang, X.; Rusydi, A.; Chen, J.; Yang, H.; Venkatesan, T., Interface Engineering and Emergent Phenomena in Oxide Heterostructures. *Adv. Mater.* **2018,** *30* (47), 1802439.

8. Zhou, H.-C.; Long, J. R.; Yaghi, O. M., Introduction to Metal–Organic Frameworks. *Chem. Rev.* **2012,** *112* (2), 673-674.

9. Kojima, H.; Zhang, Z.; Dunbar, K. R.; Mori, T., Energy band structure and metal–organic interactions in tetracyanoquinodimethane (TCNQ) and N,N′-dicyanoquinonediimine (DCNQI) materials. *J. Mater. Chem. C* **2013,** *1* (9), 1781-1790.

10. Rana, S.; Prasoon, A.; Sadhukhan, P.; Jha, P. K.; Sathe, V.; Barman, S. R.; Ballav, N., Spontaneous Reduction of Copper(II) to Copper(I) at Solid–Liquid Interface. *J. Phys. Chem. Lett.* **2018,** *9* (21), 6364-6371.

11. Rana, S.; Sindhu, P.; Ballav, N., Perspective on the Interfacial Reduction Reaction. *Langmuir* **2019,** *35* (30), 9647-9659.

12. Sindhu, P.; Prasoon, A.; Rana, S.; Ballav, N., Emergent Interface in Heterostructured Thin Films of Cu(II) and Cu(I) Coordination Polymers. *J. Phys. Chem. Lett.* **2020,** *11* (15), 6242-6248.

13. Li, D.-J.; Gu, Z.-G.; Zhang, W.; Kang, Y.; Zhang, J., Epitaxial encapsulation of homodispersed CeO2 in a cobalt–porphyrin network derived thin film for the highly efficient oxygen evolution reaction. *J. Mater. Chem. A* **2017,** *5* (38), 20126-20130.

14. Prasoon, A.; Dhara, B.; Roy, D.; Rana, S.; Bhand, S.; Ballav, N., Achieving current rectification ratios ≥ 10^5 across thin films of coordination polymer. *Chem. Sci.* **2019,** *10* (43), 10040-10047.

15. Rodríguez-Carvajal, J., Recent advances in magnetic structure determination by neutron powder diffraction. *Physica B: Condensed Matter* **1993,** *192* (1), 55-69.

16. Gupta, K.; Ninawe, P.; Jain, A.; Dadwal, A.; Anas, M.; Malik, V. K.; Yusuf, S. M.; Joy, P. A.; Ballav, N., Possible electron doping of geometrically perfect spin-1/2 kagome-lattice barlowite by reduced graphene oxide. *Phys. Rev. B* **2021,** *104* (10), L100418.

17. Schneider, C.; Ukaj, D.; Koerver, R.; Talin, A. A.; Kieslich, G.; Pujari, S. P.; Zuilhof, H.; Janek, J.; Allendorf, M. D.; Fischer, R. A., High electrical conductivity and high porosity in a Guest@MOF material: evidence of TCNQ ordering within Cu_3BTC_2 micropores. *Chem. Sci.* **2018,** *9* (37), 7405-7412.

18. Liu, J.; Wächter, T.; Irmler, A.; Weidler, P. G.; Gliemann, H.; Pauly, F.; Mugnaini, V.; Zharnikov, M.; Wöll, C., Electric Transport Properties of Surface-Anchored Metal–Organic Frameworks and the Effect of Ferrocene Loading. *ACS Appl. Mater. Interfaces* **2015,** *7* (18), 9824-9830.

19. Neumann, T.; Liu, J.; Wächter, T.; Friederich, P.; Symalla, F.; Welle, A.; Mugnaini, V.; Meded, V.; Zharnikov, M.; Wöll, C.; Wenzel, W., Superexchange Charge Transport in Loaded Metal Organic Frameworks. *ACS Nano* **2016,** *10* (7), 7085-7093.

20. Prashanth, J.; Konakanchi, R.; Venkatram Reddy, B., Barrier potentials, molecular structure, force filed calculations and quantum chemical studies of some bipyridine di-carboxylic acids using the experimental and theoretical using (DFT, IVP) approach. *Mol. Sim.* **2019,** *45* (16), 1353-1383.

21. Perdew, J. P.; Burke, K.; Ernzerhof, M., Generalized Gradient Approximation Made Simple. *Phys. Rev. Lett.* **1996,** *77* (18), 3865-3868.

22. Heyd, J.; Scuseria, G. E.; Ernzerhof, M., Hybrid functionals based on a screened Coulomb potential. *J. Chem. Phys.* **2003,** *118* (18), 8207-8215.

23. Bader, R. F. W., *Atoms in Molecules: A Quantum Theory*. Clarendon Press: 1994.

24. Rana, S.; Rajendra, R.; Dhara, B.; Jha, P. K.; Ballav, N., Highly Hydrophobic and Chemically Rectifiable Surface-Anchored Metal-Organic Framework Thin-Film Devices. *Adv. Mater. Interfaces* **2016,** *3* (13), 1500738.

25. Heintz, R. A.; Zhao, H.; Ouyang, X.; Grandinetti, G.; Cowen, J.; Dunbar, K. R., New Insight into the Nature of Cu(TCNQ): Solution Routes to Two Distinct Polymorphs and Their Relationship to Crystalline Films That Display Bistable Switching Behavior. *Inorg. Chem.* **1999,** *38* (1), 144-156.

26. Capitán, M. J.; Alvarez, J.; Yndurain, F., Organometallic MTCNQ films: a comparative study of CuTCNQ versus AgTCNQ. *Phys. Chem. Chem. Phys.* **2018,** *20* (33), 21705-21715.

27. Wu, J., Synthesis of a two-dimensional porous framework based on symmetrical organic ligand and linking metal ion. *Cryst. Res. Technol.* **2009,** *44* (4), 453-456.

28. You, L.; Zong, W.; Xiong, G.; Ding, F.; Wang, S.; Ren, B.; Dragutan, I.; Dragutan, V.; Sun, Y., Cooperative effects of lanthanides when associated with palladium in novel, 3D Pd/Ln coordination polymers. Sustainable applications as water-stable, heterogeneous catalysts in carbon–carbon cross-coupling reactions. *Appl. Catal. A: General* **2016,** *511*, 1-10.

29. Talin, A. A.; Centrone, A.; Ford, A. C.; Foster, M. E.; Stavila, V.; Haney, P.; Kinney, R. A.; Szalai, V.; Gabaly, F. E.; Yoon, H. P.; Léonard, F.; Allendorf, M. D., Tunable Electrical Conductivity in Metal-Organic Framework Thin-Film Devices. *Science* **2014,** *343* (6166), 66-69.

30. Allendorf, M. D.; Foster, M. E.; Léonard, F.; Stavila, V.; Feng, P. L.; Doty, F. P.; Leong, K.; Ma, E. Y.; Johnston, S. R.; Talin, A. A., Guest-Induced Emergent Properties in Metal–Organic Frameworks. *J. Phys. Chem. Lett.* **2015,** *6* (7), 1182-1195.

31. Kresse, G.; Furthmüller, J., Efficient iterative schemes for ab initio total-energy calculations using a plane-wave basis set. *Phys. Rev. B* **1996,** *54* (16), 11169-11186.

32. Henkelman, G.; Arnaldsson, A.; Jónsson, H., A fast and robust algorithm for Bader decomposition of charge density. *Comput. Mater. Sci.* **2006,** *36* (3), 354-360.

33. Sanville, E.; Kenny, S. D.; Smith, R.; Henkelman, G., Improved grid-based algorithm for Bader charge allocation. *J. Comput. Chem.* **2007,** *28* (5), 899-908.

34. Tang, W.; Sanville, E.; Henkelman, G., A grid-based Bader analysis algorithm without lattice bias. *J. Phys.: Condensed Matter* **2009,** *21* (8), 084204.

35. Nie, X.; Kulkarni, A.; Sholl, D. S., Computational Prediction of Metal Organic Frameworks Suitable for Molecular Infiltration as a Route to Development of Conductive Materials. *J. Phys. Chem. Lett.* **2015,** *6* (9), 1586-1591.

36. Usov, P. M.; Jiang, H.; Chevreau, H.; Peterson, V. K.; Leong, C. F.; D'Alessandro, D. M., Guest–Host Complexes of TCNQ and TCNE with Cu_3(1,3,5-benzenetricarboxylate)$_2$. *J. Phys. Chem. C* **2017,** *121* (47), 26330-26339.

37. Leong, K.; Foster, M. E.; Wong, B. M.; Spoerke, E. D.; Van Gough, D.; Deaton, J. C.; Allendorf, M. D., Energy and charge transfer by donor–acceptor pairs confined in a metal–organic framework: a spectroscopic and computational investigation. *J. Mater. Chem. A* **2014,** *2* (10), 3389-3398.

38. Yan, T.; Li, Y.-Y.; Su, J.; Wang, H.-Y.; Zuo, J.-L., Charge Transfer Metal-Organic Framework Containing Redox-Active TTF/NDI Units for Highly Efficient Near-Infrared Photothermal Conversion. *Chem. Eur. J.* **2021,** *27* (43), 11050-11055.

39. Li, X.; Yu, J.; Gosztola, D. J.; Fry, H. C.; Deria, P., Wavelength-Dependent Energy and Charge Transfer in MOF: A Step toward Artificial Porous Light-Harvesting System. *J. Am. Chem. Soc.* **2019,** *141* (42), 16849-16857.

40. Luo, Y.; Li, J.; Liu, X.; Tan, L.; Cui, Z.; Feng, X.; Yang, X.; Liang, Y.; Li, Z.; Zhu, S.; Zheng, Y.; Yeung, K. W. K.; Yang, C.; Wang, X.; Wu, S., Dual Metal–Organic Framework Heterointerface. *ACS Central Sci.* **2019,** *5* (9), 1591-1601.

41. Chen, Y.; Yang, D.; Xin, X.; Yang, Z.; Gao, Y.; Shi, Y.; Zhao, Z.; An, K.; Wang, W.; Tan, J.; Jiang, Z., Multi-stepwise charge transfer via MOF@MOF/TiO_2 dual-heterojunction photocatalysts towards hydrogen evolution. *J. Mater. Chem. A* **2022,** *10* (17), 9717-9725.

42. Yao, Y.; Gao, Z.; Lv, Y.; Lin, X.; Liu, Y.; Du, Y.; Hu, F.; Zhao, Y. S., Heteroepitaxial Growth of Multiblock Ln-MOF Microrods for Photonic Barcodes. *Angew. Chem. Int. Ed.* **2019,** *58* (39), 13803-13807.

43. Oldenburg, M.; Turshatov, A.; Busko, D.; Wollgarten, S.; Adams, M.; Baroni, N.; Welle, A.; Redel, E.; Wöll, C.; Richards, B. S.; Howard, I. A., Photon Upconversion at Crystalline Organic–Organic Heterojunctions. *Adv. Mater.* **2016,** *28* (38), 8477-8482.

44. Chen, D.-H.; Haldar, R.; Neumeier, B. L.; Fu, Z.-H.; Feldmann, C.; Wöll, C.; Redel, E., Tunable Emission in Heteroepitaxial Ln-SURMOFs. *Adv. Func. Mater.* **2019,** *29* (37), 1903086.

45. Chen, D.-H.; Sedykh, A. E.; Gomez, G. E.; Neumeier, B. L.; Santos, J. C. C.; Gvilava, V.; Maile, R.; Feldmann, C.; WÖll, C.; Janiak, C.; Müller-Buschbaum, K.; Redel, E., SURMOF Devices Based on Heteroepitaxial Architectures with White-Light Emission and Luminescent Thermal-Dependent Performance. *Adv. Mater. Interfaces* **2020,** *7* (24), 2000929.

46. Chandresh, A.; Liu, X.; Wöll, C.; Heinke, L., Programmed Molecular Assembly of Abrupt Crystalline Organic/Organic Heterointerfaces Yielding Metal-Organic Framework Diodes with Large On-Off Ratios. *Adv. Sci.* **2021,** *8* (7), 2001884.

47. Sindhu, P.; Ananthram, K. S.; Jain, A.; Tarafder, K.; Ballav, N., Charge-transfer interface of insulating metal-organic frameworks with metallic conduction. *Nat. Commun.* **2022,** *13* (1), 7665.

Electrical Transport Properties in Thin Films of Pristine $Cu(II)(Cys)_2$ and $Cu(I)$-TCNQ/$Cu(II)(Cys)_2$ Heterostructure

5.1 Introduction

The heterostructure composed of a band insulator and a Mott insulator of coordination polymers (CPs) has shown highly promising outcomes, revealing the emergence of a metallic interface similar to oxide heterostructures.[1] Bio-CPs are crystalline porous solids and a subclass of conventional CPs where physiological functionalities of bio-molecular ligands along with the structural diversity can primarily be utilized for various biomedical applications. It is apparent from the chemical backbones of biomolecules and the predominant ionic bonding scenario that bio-CPs would be mostly electrical insulators, likewise conventional CPs. Integration of bio-CP into heterostructured thin film configuration with conventional CP may lead to to exhibit intriguing electrical transport properties.

Herein, we have designed a lattice-mismatched heterostructured thin film of Cu(I)-TCNQ with a new bio-CP, Cu(II)$(Cys)_2$, which was generated upon an extended coordination of the cystine (dimer of amino acid cysteine) ligand with cupric ion. Thin films of pristine and heterostructured CPs were fabricated on functionalized Au substrate by employing LbL method. Electrical transport properties were studied in pristine Cu(II)$(Cys)_2$ thin film and exhibited a thermally driven and fully reversible resistive switching behavior with an unprecedented "on–off" ratio, at slightly above room temperature (333 K) and ambient pressure. Electrical transport measurements were also conducted on the Cu-TCNQ/Cu$(Cys)_2$ heterostructured thin film. Note that the individual components of Cu-TCNQ/Cu$(Cys)_2$ heterostructured thin film can undergo thermally driven resistive switching in pristine thin film configurations. However, surprising observations of both current rectification and resistive switching were observed at 300 K and 423 K, respectively.

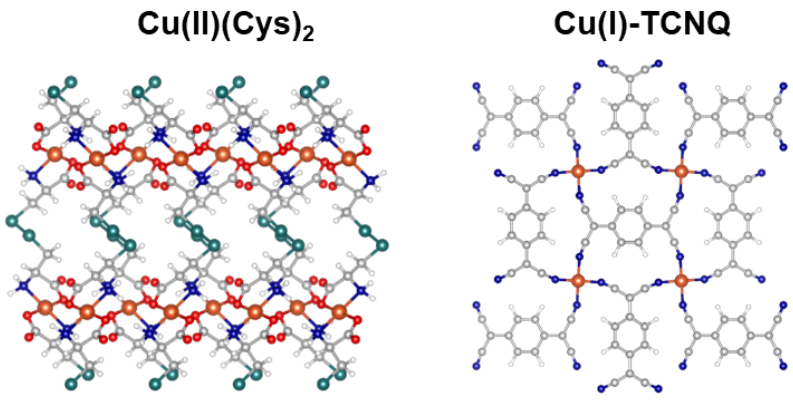

Figure 5.1. *(a) Energy optimized structures of Cu(II)$(Cys)_2$ (left) and Cu(I)-TCNQ (right) (view from ac and ab plane respectively) where carbon, hydrogen, nitrogen, oxygen, sulfur, and copper atoms are represented by grey,*

white, blue, red, dark cyan and orange colors, respectively. (Density functional theory (DFT) calculations were performed by K. S. Ananthram under the supervision of Kartick Tarafder, NITK Surathkal, India).

5.2 Materials and Methods

Materials: Copper acetate [$Cu(OAc)_2.H_2O$], L-Cysteine (Cys), TCNQ (7,7,8,8-tetracyanoquinodimethane), 11-Merceptoundecanoic acid (MUDA) and Au(111) substrate (100 nm Au coated Si wafer) were purchased from Sigma-Aldrich and ethanol from Merck and used without any further purification except Au(111) substrate.

Functionalization of Au substrate: Au substrate was cleaned by dipping into Piranha solution (H_2SO_4 (95-98%)/H_2O_2 (30%); v/v 3:1) for 30 minutes (note: proper safety care must be taken) and washed with Milli-Q water followed by ethanol and then dried under the stream of N_2 gas. Subsequently, Au substrate was functionalized with a carboxy-terminated (-COOH) self-assembled monolayer (SAM) by dipping into the 1 mM MUDA solution in ethanol/acetic acid (v/v 9:1) for 48 hours followed by washing with ethanol and dried with N_2 gas.[2-3]

Fabrication of $Cu(Cys)_2$ thin film: MUDA functionalized Au substrate was immersed in 1 mM ethanolic solution of $Cu(OAc)_2.H_2O$ kept at 330 K for 30 minutes followed by washing with ethanol and subsequently in 2 mM Cysteine solution in ethanol-water (1:1) mixture kept at 330 K for 30 minutes (washed with ethanol in between followed by drying with stream of N_2 gas) to complete one LbL cycle.[4] 30 cycles of LbL were performed to get uniform $Cu(Cys)_2$ thin film (thickness values were estimated to be ~1.2 μm). Employing same experimental conditions, thin films of $Cu(Cys)_2$ with thickness values of ~750 nm, ~980 nm and ~1.5 μm were also fabricated corresponding to LbL growth of 20 cycles, 25 cycles, and 35 cycles, respectively.

Fabrication of Cu-TCNQ/$Cu(Cys)_2$ Heterostructured Thin Film: Pre-fabricated pristine $Cu(Cys)_2$ thin film was subsequently dipped into ethanolic solutions of $Cu(OAc)_2.H_2O$ and TCNQ each at an elevated temperature for 30 minutes and washed with ethanol in between followed by drying with stream of N_2 gas to complete one cycle of LbL and it was repeated for 20 consecutive LbL cycles to grow Cu-TCNQ on top of $Cu(Cys)_2$ with well-defined interface (thickness values were estimated to be ~1.8 μm with the contribution of ~1.2 μm and ~600 nm from $Cu(Cys)_2$ and Cu-TCNQ, respectively).

Synthesis of $Cu(Cys)_2$ powder: $Cu(OAc)_2.H_2O$ (1 mM) and Cysteine (2 mM) solutions were prepared in ethanol and ethanol-water (1:1) mixture respectively and mixed together in a round bottom flask. The solution was kept at 330 K with the constant stirring for next 3 days. A sky-blue coloured powder was collected after centrifugation with water and ethanol three times alternatively.

Characterizations: The surface morphologies of thin film and bulk performed by Zeiss Ultra Plus FESEM. Contact angle measurements were measured using Holmarc's Contact Angle Meter. Out-of-plane XRD data were recorded at room temperature and high temperature using a Bruker D8 Advance diffractometer using Cu Kα radiation (λ = 1.5406 Å). Raman spectra (λ_{exc} = 632.8 nm) were recorded at Raman microscope (LabRAM HR, HoribaJobinYvon) with a 50X objective lens and the spectral resolution of the system is ~1 cm^{-1}. FTIR spectra were collected in the range of 400 to 4000 cm^{-1} with a resolution of ~4 cm^{-1} using KBr pellets (NICOLET 6700 spectrophotometer). High-resolution XPS spectra were recorded by using a Thermo Fisher Scientific ESCALAB Xi+ for both bulk and thin film; and a hand-book58 was referred for the assignments of various photoemission signals. ESR was recorded using JES - FA200 ESR Spectrometer with X band on bulk sample. Gas adsorption and desorption isotherms were collected at 77 K for N_2 gas on the BelSorpmax instrument (pore size distribution was obtained from the standard H-K model). HRTEM images were recorded on drop casted samples (methanolic dispersion) over a 200 mesh Cu grid using JEOL USA JEM-2200 FS Transmission Electron Microscope (scratched sample in case of thin film). TGA profiles were recorded using Perkin-Elmer thermal analyzer STA 6000 model. Photolithography was performed by LW405 Laser writer, followed by the deposition of Au by using LTE sputter 080. Electrical transport measurements (current-voltage, *I-V* profiles) on various thin film samples were carried out using a Keithley 4200 SCS Parameter Analyser system attached to an Everbeing probe station with a eutectic gallium indium (EGaIn) alloy, tungsten tip, Au and Pt pads and direct Au tip as the contact electrodes, in two-probe configuration. During the electrical transport measurements at ambient pressure, relative humidity (RH) values at 300 K and 333 K were noted to be ~46% and ~38%, respectively.

Computational studies: DFT calculations and molecular dynamics (MD) simulations were performed by K. S. Ananthram under the supervision of Kartick Tarafder, NITK Surathkal, India. The unit cell of the $Cu(Cys)_2$ system was modelled by considering experimentally obtained data on the $Zn(Cys)_2$ system[5] (CCDC 971360) where Zn metal ions were replaced with Cu ions using an open-source molecular builder and visualization tool Avogadro[6]. The geometrical optimizations and the extraction of electronic structure information were achieved by using the Vienna Ab-initio Simulation Package

(VASP) with projector augmented wave method.[7] The Perdew–Burke–Ernzerhof (PBE) functional of generalized gradient approximation (GGA)[8] was employed as exchange-correlation functions to estimate the accurate density of states (DOS) and band structure[9] of the $Cu(Cys)_2$ system. The conjugate gradient method was used to obtain the energy-optimized structure and the optimization process was carried out until the interatomic forces in the system were reduced to 0.001 eV/Å. The Brillouin zone integration is performed using a 5x5x3, Monkhorst–Pack grid. To study the temperature-dependent electronic structure and calculate the electronic conductivity, MD simulations were carried out at different temperatures using Parrinello and Rahman method as implemented in VASP. In our simulation process we have used Langevin dynamics[10-12] for the isobaric-isothermal ensemble where Brillouin zone was sampled at the Gamma point 1x1x1 and a PAW basis-set with energy cut-off of 600 eV was considered. To equilibrate the sample at a particular temperature, we have used 1.0 fs per step and simulated the sample for a minimum 150000 MD steps. Simulated mean temperatures achieved at thermal equilibrium were 279.16 K and 350.61 K for 280 K and 350 K, respectively. The thermally equilibrated samples were further used to study the electrical conductivity of the system at different temperatures. Conductivity calculations were performed by using Boltzmann transport method implemented in BOLTZWANN code[13] distributed with Wannier90 package[14]. In this method, the semi-classical Boltzmann transport equations were solved for the periodic infinite system under the constant relaxation-time approximation where the band energies and band derivatives were obtained via Wannier interpolations. We have used plane wave (PW) results obtained from VASP to construct the maximally localized Wannier functions and were interpolated accurately to calculate transport quantities on a coarse k-point reciprocal space grid. In the present calculation, highly dense 40x40x40 k-mesh was used for the interpolation in constructing tight binding Hamiltonian matrix elements. All individual snapshots at different temperatures obtained from MD simulations were considered as the initial configuration. And maximally localized Wannier functions were derived by choosing the individual projection. Electrical conductivity was calculated for chemical potential equal to 0 eV by minimizing the real space spread of individual Wannier functions. Bader charge analysis[15] were performed using Henkelman's Group program.[16-18]

Crystal structure analysis: Rietveld Refinements were performed by Anil Jain, BARC Mumbai, India. Structural characterization of the thin film was carried out by performing the Rietveld analysis of the XRD data using the FullProf program.[19] Our analysis shows that crystallites are preferentially oriented toward three directions which makes a real refinement using the traditional software packages

such as FullProf and GSAS difficult because in these packages it is onerous to include more than one preferred orientation direction. The initial crystal structural parameters for the refinement were taken from the $Zn(Cys)_2$ system (CCDC 971360)[5], with Zn(II) ions replaced by Cu(II) ions and energy optimized by DFT calculations. In the present case, diffraction pattern was simulated by considering the three preferred orientation (110), (-101), (01-1) with lattice parameters, a = 19.999(3) Å, b = 9.434(2) Å, c = 5.484(1) Å, $\alpha = \beta = \gamma = 90^{o}$. To account for the spectrum shifting, variation along longer a-axis was expected due to the strain in thin films or existence of defect state during the initial cycles of the LbL growth at solid-liquid interface. Therefore, contraction along a-axis (a = 18.980 Å) was considered during the simulation along with the aforementioned cell parameters, with preferred orientation along (100), with the maximum fraction of 5% which led to the good match of refined diffraction pattern to the experimental diffraction pattern.

5.3 Results and Discussion

Field-emission scanning electron microscopy (FESEM) images revealed the formation of a highly-uniform pristine $Cu(Cys)_2$ thin film extending over hundreds of microns, with a thickness of 1.2 µm.

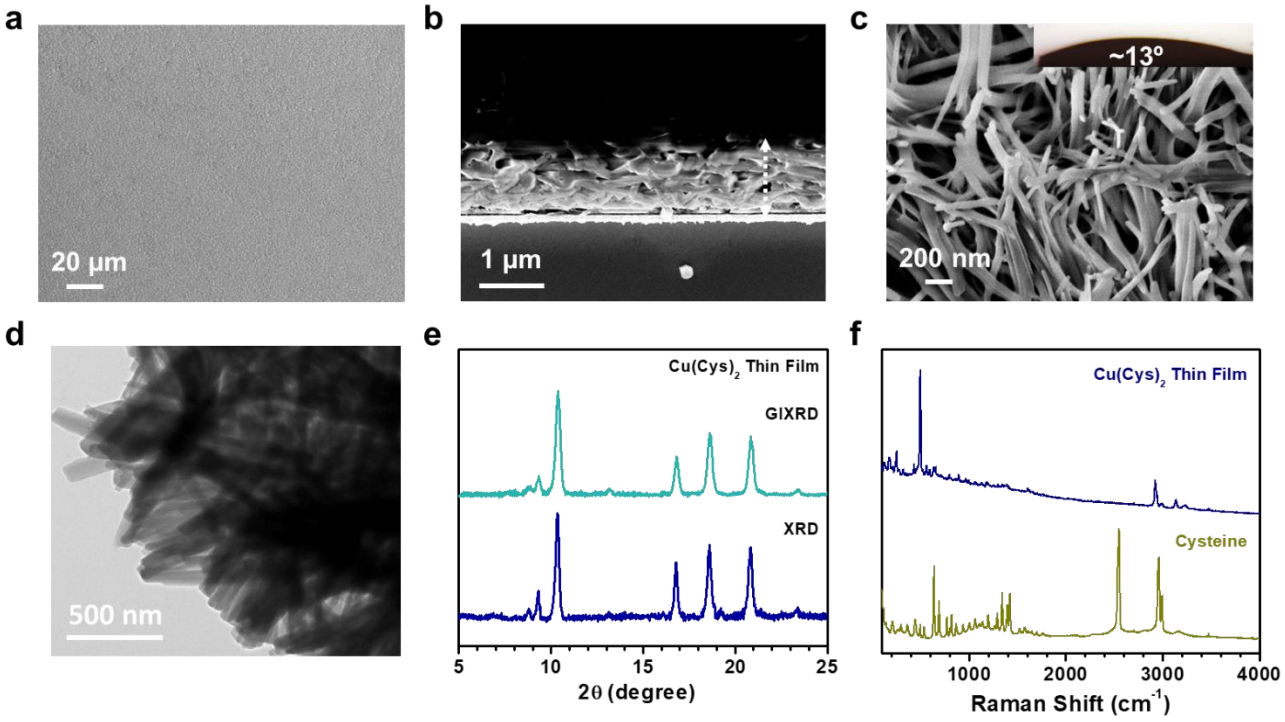

Figure 5.2. *(a) Uniform surface coverage of the $Cu(Cys)_2$ thin film by FESEM image and (b) the cross-sectional FESEM image showing the thickness as ~1.2 µm and (c,d) FESEM and TEM images of $Cu(Cys)_2$ thin film clearly indicating the rod-like morphology (inset of (c): water contact angle). (e) XRD and GIXRD patterns*

revealing crystalline nature of the Cu(Cys)$_2$ thin film. (f) Raman spectra of the Cu(Cys)$_2$ thin film and the cysteine ligand.

Additionally, rod-like morphology was observed in FESEM and transmission electron microscopy (TEM) images, and the thin film exhibited a highly hydrophilic water contact angle of ~13º (Figure 5.2 and Appendix 5.1). Out-of-plane X-ray diffraction (XRD) and grazing-incidence X-ray diffraction (GIXRD) patterns of the thin film confirmed the highly crystalline nature of Cu(Cys)$_2$ thin film.

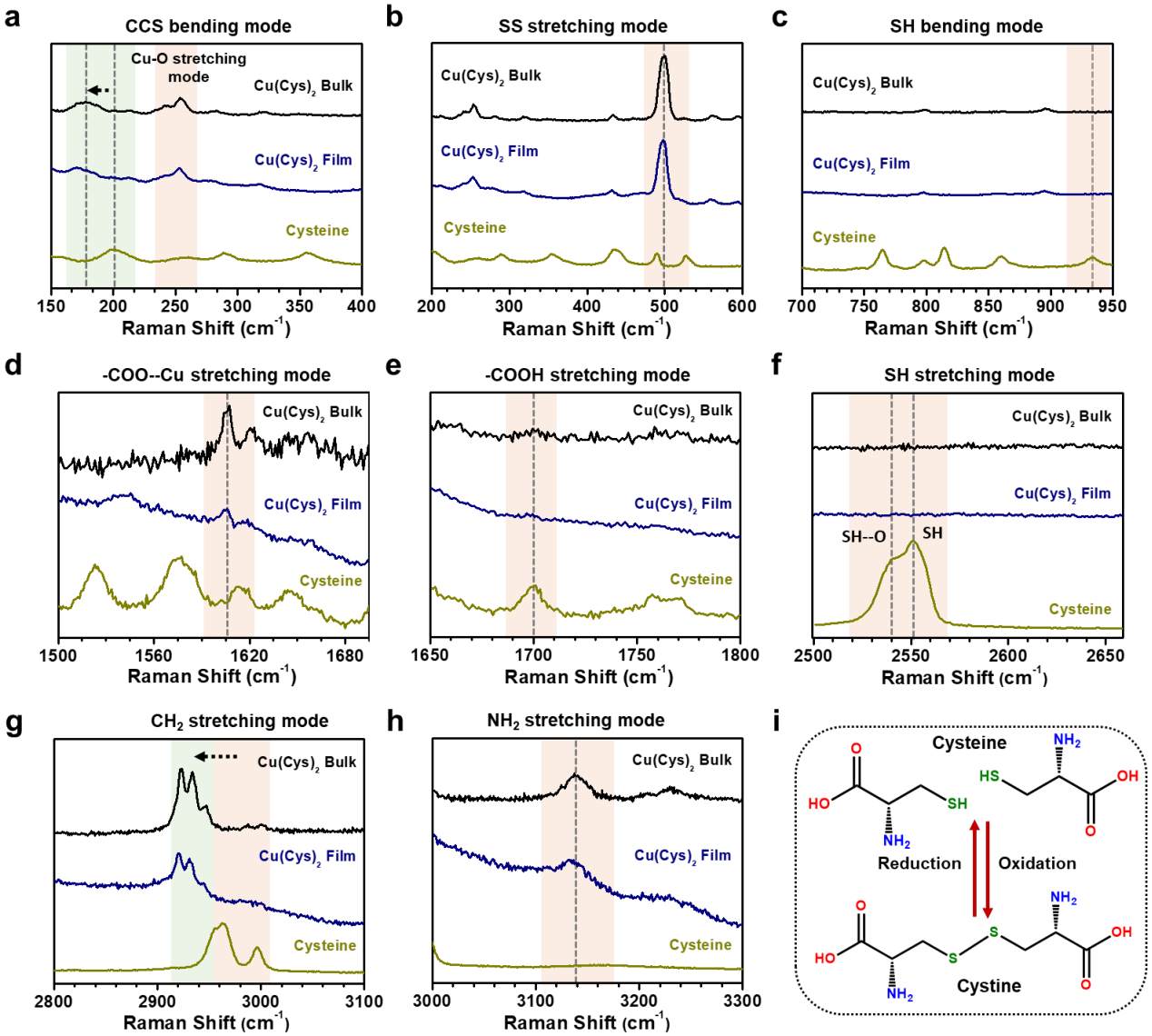

Figure 5.3. *(a-h) Raman spectra of Cysteine (dark yellow), Cu(Cys)$_2$ thin film (blue) and Cu(Cys)$_2$ bulk (black). (i) Schematic representation of the conversion of cysteine to cystine. Our thorough analysis of the Raman spectra combined with the information from XPS data and other complementary characterizations confirmed the presence of Cu(Cys)$_2$ in bulk as well as in thin film.*

Raman spectra of cysteine ligand, $Cu(Cys)_2$ thin film, and $Cu(Cys)_2$ bulk were compared, and notable differences in the vibrational signatures were observed The characteristic vibrational signals of the S-H bending mode (933 cm^{-1}), -COOH stretching mode (1700 cm^{-1}), S-H stretching mode (2551 cm^{-1}) were absent in the $Cu(Cys)_2$ thin film.[20-21] However, new vibrational modes emerged in the thin film, including the C-C-S bending mode (175 cm^{-1}), Cu-O (240 cm^{-1}), S-S stretching mode (496 cm^{-1}), COO-Cu stretching mode (1603 cm^{-1}), C-H ($-CH_2-$) stretching modes (2921 cm^{-1}, 2932 cm^{-1}, and 2945 cm^{-1}), and N-H ($-NH_2$) stretching mode (3136 cm^{-1}) in $Cu(Cys)_2$ samples (Figures 5.2 and 5.3).[20-21]

The evidence of the conversion of cysteine to cystine in $Cu(Cys)_2$ was observed and further confirmed using X-ray photoemission spectroscopy (XPS). The XPS analysis revealed the presence of S-S and C-S bonds ($S2p_{3/2}$ peak at 163.0 eV and no Cu-S bond, indicated by the absence of a peak at ~162.0 eV), as well as the NH_2 moiety (N1s peak at ~399 eV, characteristic of amine). Additionally, the presence of Cu(II) was detected with the $Cu2p_{3/2}$ peak at ~934.0 eV, along with characteristic satellite features[22] (Figures 5.3 and 5.4). Similar results were also observed in $Cu(Cys)_2$ bulk samples, confirming the consistency of the findings (Figure 5.3 and Appendix 5.2, 5.3, 5.4).

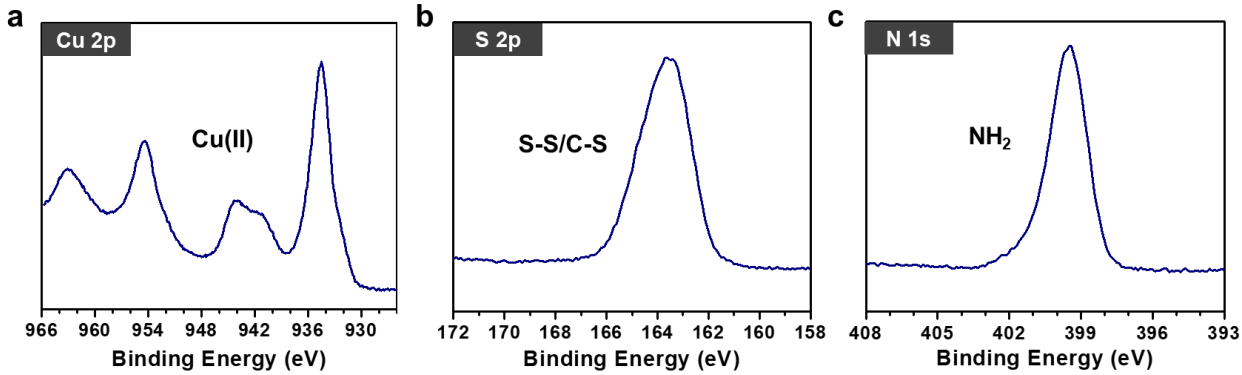

Figure 5.4. *(a) Cu2p, (b) S2p and (c) N1s XPS spectra of the $Cu(Cys)_2$ thin film confirming the presence of Cu(II) S-S and C-S bonds and NH_2 moiety.*

Electrical transport measurements were carried out in pristine $Cu(Cys)_2$ thin film and thermally resistive switching was observed with the values of ~10^{11} Ω in the high-resistance state (HRS) at 300 K and ~10 Ω in the low-resistance state (LRS) at 333 K (Figure 5.5a). Furthermore, $Cu(Cys)_2$ thin film was realized to be highly-durable under thermal stress whereby the respective resistance values at 300 K and 333 K were found to be almost unaltered over ten continued cycles of heating and cooling viz. retention of the 'on-off' ratio of ~10^{10} (Figure 5.5b). Also, resistance value at 333 K was found to be highly-stable over long period of time and the time-dependent stability was successfully reproduced

in the subsequent cycles (Figure 5.5c). A thermally driven and fully reversible resistive switching behavior was observed upon cooling with an additional hysteretic effect (Figure 5.5d and Appendix 5.5 and 5.6) – resembling the recently demonstrated electrical field-induced IMT in thin films of archetypal TMO, vanadium dioxide (VO_2; spin-1/2), little above room-temperature (340 K).[23] Considering the remarkable change in the resistance value (~10^{10} times), such a thermally-driven phenomenon in the $Cu(Cys)_2$ thin film can be assigned to an insulator-to-metal-like transition (IMLT). Estimated resistivity values for the $Cu(Cys)_2$ thin film at 300 K and 333 K were found to be ~10^{10} Ωm and ~10^{-1} Ωm, respectively (Appendix 5.5 and 5.6). Further we have recorded the current-voltage (*I-V*) profiles for the $Cu(Cys)_2$ thin film from room-temperature down to 160 K and no appreciable change in the conductance value was observed, even though the trend was similar to that of an insulator (Appendix 5.7).

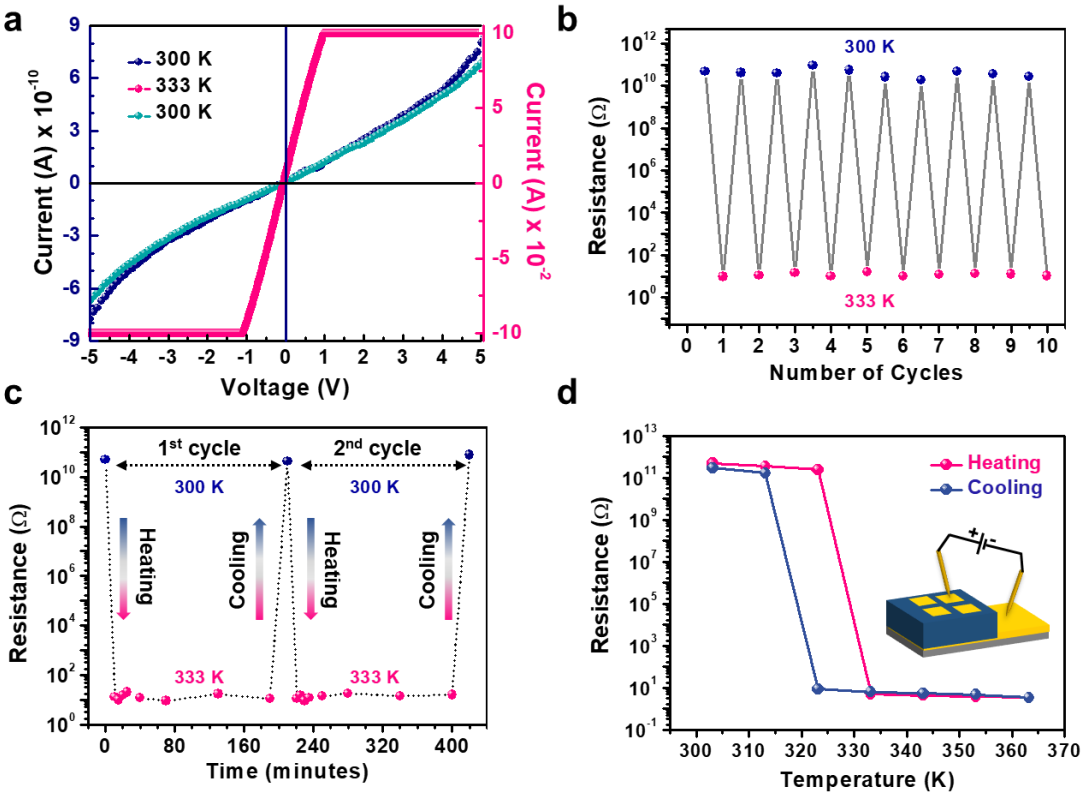

Figure 5.5. *(a) Temperature-dependent current-voltage (I-V) profiles and (b) cycling stability of the IMLT of $Cu(Cys)_2$ thin film in in-plane mode. (c) Time-dependent cycling stability: after measuring the resistance value at 300 K (0 h), the sample was heated to 333 K and kept for a few hours at 333 K; the resistance values were measured at different time intervals, and indeed, no significant change was observed (even by 10 times). Subsequently, the sample was cooled back to 300 K, and the resistance value was measured to be the same as*

the value at the starting point (0 h). Such behavior was successfully reproduced in the second heating-cooling cycle. (d) Temperature-dependent resistance values of the Cu(Cys)$_2$ thin film in the cross-plane mode during heating and cooling of the sample with a clearly visible hysteretic effect (inset: schematic of the transport measurement with top patterned Au contact and bottom Au substrate as electrodes). Reversible modulation of the resistance values ensured that no diffusion of Au from the contact pads across the Cu(Cys)$_2$ thin film took place during the microfabrication process as well during the heating-cooling cycle.

In case of the IMT involving band-type and Mott-type insulators where the resistivity can be altered over tens of orders of magnitude are most often accompanied by structural phase transition in the system.[24] It is expected that for inherent Mott insulators, IMT, usually induced by temperature, should be of purely electronic origin (without structural change).[25-27] However, strong Coulomb interaction over bandwidth leads to coupling of charge, spin and lattice; and eventually, IMT (including the transition to semimetal state[28-29]) involving Mott insulators are also frequently associated with structural change. Notable exceptions of temperature-induced IMT in Mott insulators, without structural change, are surface-tailored layered perovskite $Ca_{1.9}Sr_{0.1}RuO_4$ and compositionally tuned heterostructured VO_2 thin film.[27, 30]

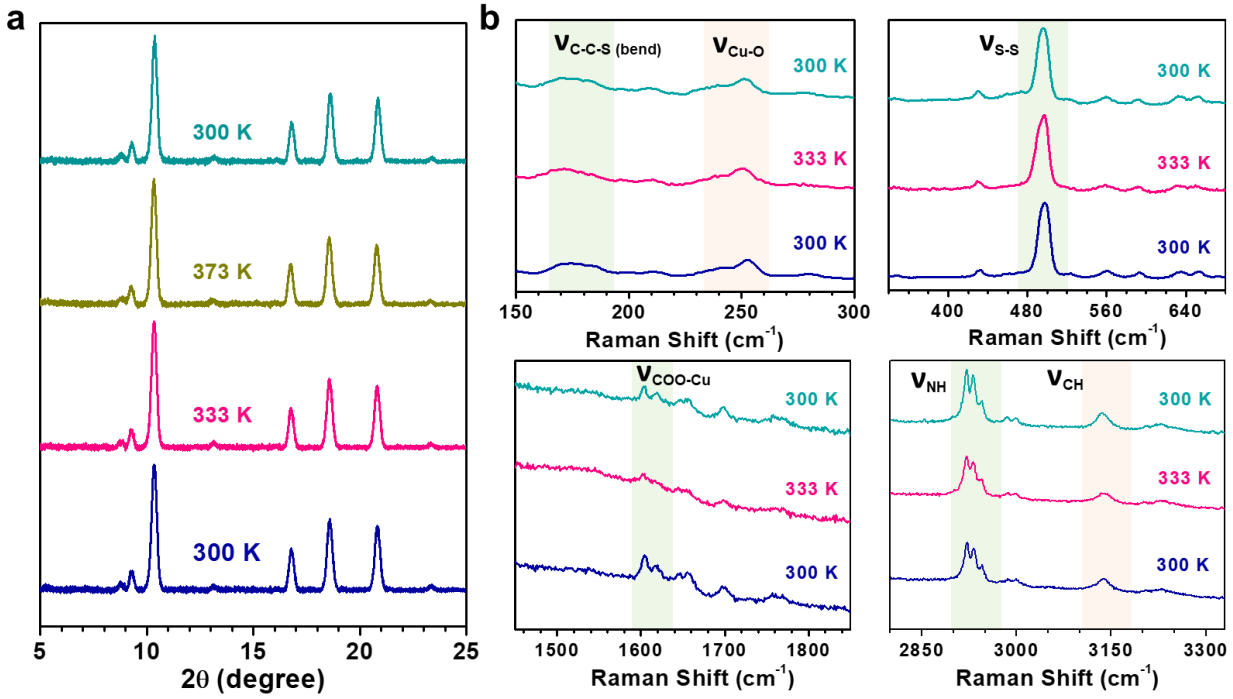

Figure 5.6. *(a) XRD patterns and (b) Raman spectra recorded on the Cu(Cys)$_2$ thin film sample at variable temperatures. The pattern remained almost identical across various temperatures. Characteristic vibrational features mentioned and spectral regions are highlighted.*

We have recorded X-ray diffraction (XRD) patterns on the $Cu(Cys)_2$ thin film by systematically varying the temperature from 300 K up to 373 K (and back to 300 K) which could serve as the key marker to investigate any structural change in the system (Figure 5.6 and Appendix 5.8). Interestingly, no appreciable change in the XRD patterns could be detected during the heating and cooling cycle. Grazing-incidence X-ray diffraction (GIXRD) pattern at 300 K ensured that the sharp and separated pattern was not related to any interface-effect but the material itself (Figure 5.2) and notably, similar XRD patterns were consistently observed in our earlier reports on thin films of coordination polymers. Therefore, in course of the IMLT structural order parameters were almost retained in the $Cu(Cys)_2$ thin film – primarily an electronic phenomenon likewise in $Ca_{1.9}Sr_{0.1}RuO_4$ and VO_2.

To complement the temperature-dependent XRD data, we have recorded Raman spectra on the $Cu(Cys)_2$ thin film at 300 K, 333 K and back to 300 K (Figure 5.6 and Appendix 5.9). Characteristic vibrational signatures were found to be unaltered at different temperatures; specifically, C-C-S bending mode (175 cm^{-1}), Cu-O (240 cm^{-1}), S-S stretching mode (496 cm^{-1}), COO-Cu stretching mode (1603 cm^{-1}), C-H (-CH_2-) stretching modes (2921 cm^{-1}, 2932 cm^{-1}, and 2945 cm^{-1}), and N-H (-NH_2) stretching mode (3136 cm^{-1}).[20-21] Therefore, Raman spectra confirmed that IMLT in the $Cu(Cys)_2$ thin film did not accompany any change in the coordination environment viz. chemical bonding integrity was retained in the system. One relevant example is the intertwining of redox-chemistry and IMT in a MOF induced by oxygen (O_2) adsorption-desorption chemistry leading to profound change in the electronic structure throughout the material.[31] Another example is the insulator-to-proton-conductor transition in a dense MOF upon exposure to humidity.[32] Also, solvation-desolvation with water molecules was observed to significantly impact the electrical conductivity of an one-dimensional MOF.[33] However, these examples dealt with a change in the chemical integrity of the systems resembling the chemically-driven IMT in oxides[34] and unlike the temperature-induced IMLT presented here with a bio-MOF. Notably, in the spectral range of 3000-3800 cm^{-1}, no signature of water adsorption-desorption could be detected in our temperature-dependent Raman spectra on the $Cu(Cys)_2$ thin film; specifically peaks at 3215 cm^{-1} and 3371 cm^{-1} (respective symmetric and asymmetric OH stretch modes of hydrogen-bonded water) as well as peak at 3683 cm^{-1} (water adsorbed in the pores)[35] (Appendix 5.9).

One-dimensional (1D) zig-zag chains can be visualized in the simulated crystal structure of our $Cu(Cys)_2$ system [$Cu(C_3H_5NO_2S)_2$] with four coordination around the Cu(II) ion (two N and two O)

and these 1D chains are inter connected by H-bonding giving rise to three-dimensional (3D) framework structure (Figure 5.7a).

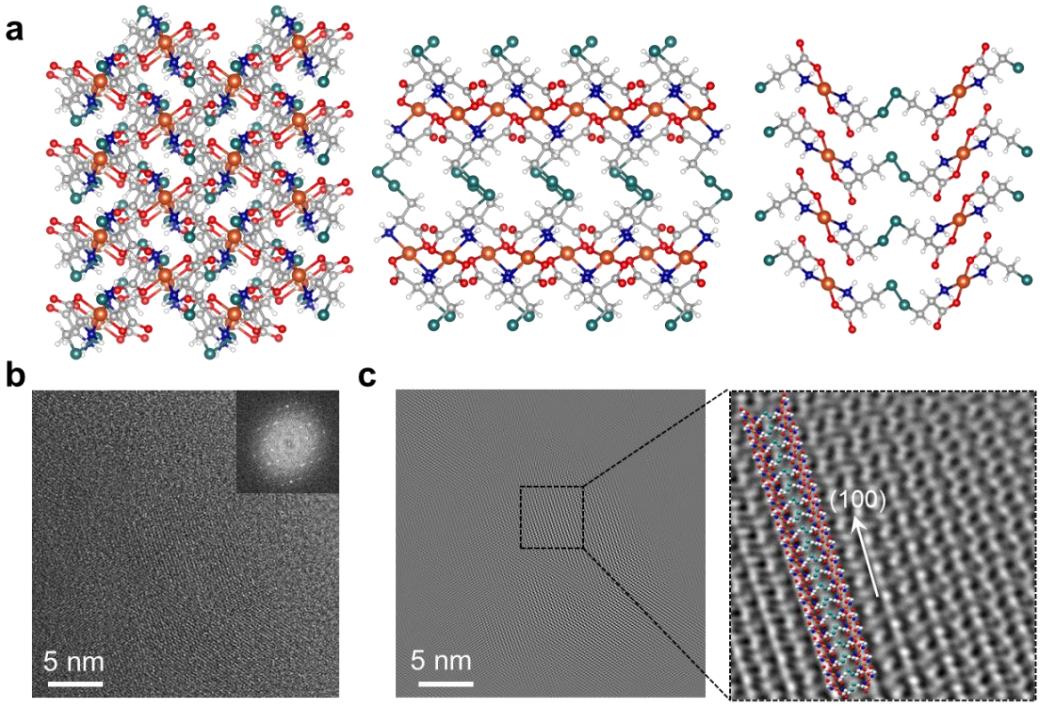

Figure 5.7. *(a) Structural view from the a-axis (left panel), b-axis (middle panel), and c-axis (right panel) where carbon, hydrogen, nitrogen, oxygen, sulfur, and copper atoms are represented by grey, white, blue, red, dark cyan and orange colors, respectively. (b) HRTEM image of the Cu(Cys)$_2$ sample (inset: corresponding fast-Fourier transform (FFT) image).(c) Inverse fast-Fourier transform (IFFT) pattern extracted from the HRTEM image showing a good overlap with the crystal structure along (100) direction. (DFT calculations were performed by K. S. Ananthram under the supervision of Kartick Tarafder, NITK Surathkal, India).*

Initial geometry of the Cu(Cys)$_2$ unit cell was constructed from the reported Zn(Cys)$_2$ [Zn($C_3H_5NO_2S$)$_2$] crystal structure[5], in which Zn(II) ions were replaced with Cu(II) ions and then the Cu(Cys)$_2$ energy-optimised ground state geometry was obtained by performing the density functional theory (DFT) calculations. The energy optimized structure was subjected to Rietveld refinement of the XRD pattern of the Cu(Cys)$_2$ thin film.[19] Preferred orientation was determined by looking at the XRD peak intensities and was applied during the Rietveld refinement[1] whereby a reasonably fair match between the experimental and calculated XRD patterns was achieved (Figure 5.8a). To complement the XRD data, high-resolution transmission electron microscopy (HRTEM) analysis was performed on extracted sample from the Cu(Cys)$_2$ thin film; and HRTEM image along with the corresponding

fast-Fourier transformed (FFT) and inverse fast-Fourier transformed (IFFT) patterns clearly revealed existence of highly-periodic 1D zig-zag chains (Figure 5.7).[36-37]

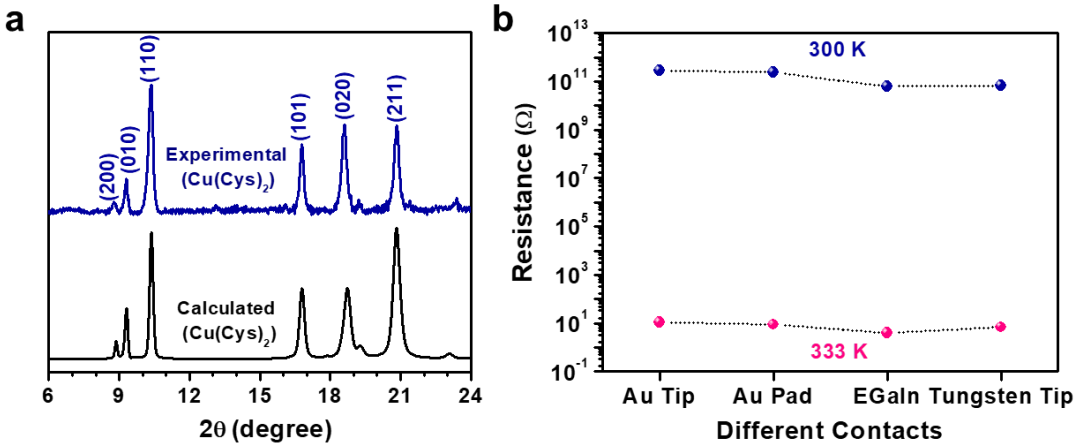

Figure 5.8. *(a) Experimental XRD pattern of $Cu(Cys)_2$ thin film and calculated XRD pattern from the Rietveld refinement. (b) Plot of resistance of the Cu(Cys)2 thin film with different contact electrodes, at 300 K and 333 K, consistently showing a change in the value by ~10^{10} fold with the temperature. (Rietveld Refinements were performed by Anil Jain, BARC Mumbai, India).*

Barring structural phase transition, such a dramatic change in the resistance value in the $Cu(Cys)_2$ system can be associated with the contact interface. In an earlier work, we have shown thermally-driven resistive switching in Cu-TCNQ and Ag-TCNQ (TCNQ = 7,7,8,8-tetracyanoquinodimethane) which was attributed to the alternation of a Schottky barrier at the contact interface i.e., primarily an interface effect.[38] Specifically, change in the in-plane resistance value in the Ag-TCNQ thin film at 400 K was varied from 10^4 fold to 10^6 fold in comparison to the value at 300 K, depending on the type of the contact electrode. As for the Cu-TCNQ thin film, the enhancement factor was observed to be 10^4. Later on, upon increasing the temperature from 300 K to 400 K, both in-pane and cross-plane modes, we realized a significant change in the resistance value for the thin film of Cu-TCNQ; and interestingly, no change in the resistance value for the thin film of Cu-BTC (BTC = 1,3,5-benzenetricarboxylate).[4] Therefore, it is the intrinsic property of the material, for example Mott-type (Cu-TCNQ) or band-type (Cu-BTC) insulator,[1, 39] which played more important role than the influence of the interfaces. In the present study, successful capture of the IMLT for the $Cu(Cys)_2$ thin film (thickness ~1.2 μm) in both cross-plane and in-plane modes (consistent change in the resistance by 10^{10} fold) clearly endorses that it is not primarily an interface effect. Also, in-plane *I-V* profiles on the $Cu(Cys)_2$ thin film with various metallic contacts having different work function values (Au, W and

Eutectic-GaIn)[38] revealed mainly Ohmic-type electrical transport, both at 300 K and 333 K; and the change in the resistance by 10^{10} fold was consistent (Figure 5.8b and Appendix 5.10). Even, upon performing in-plane *I-V* measurements with patterned Pt pads (having relatively higher work function value of ~6.3 eV) on top of the $Cu(Cys)_2$ thin film gave the same results (Appendix 5.11).

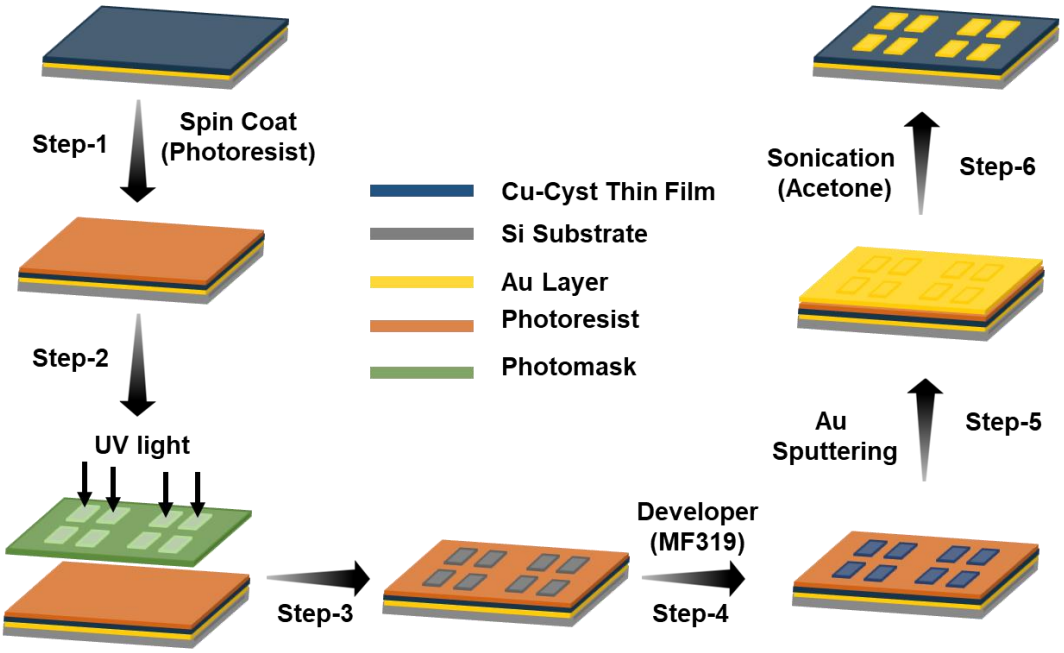

Figure 5.9. *Schematic of the fabrication of patterned Au pads on top of the $Cu(Cys)_2$ thin film by photolithography. Step-1: Spin coating of photoresist (S1813; ~0.2 to ~0.3 ml; thickness ~2 µm) on the $Cu(Cys)_2$ thin film; Step-2: A patterned mask was applied to block the UV light, and only unmasked regions of the material were exposed to the UV light; Step-3: the exposed photo-sensitive material is degraded by the UV light; Step-4: the degraded material is dissolved in developer (MF319) solution; Step-5: Au (~100 nm) was sputtered on the patterned thin film; and Step-6: Resulted patterned thin film was sonicated in acetone for 1-2 minutes to dissolve the photoresist and resulted into the well-defined Au pads on the $Cu(Cys)_2$ thin film.*

The robustness of the IMLT phenomenon motivated us to test the device functionality, and accordingly, we have employed photolithography followed by sputtering Au contact pads on the $Cu(Cys)_2$ thin film (Figure 5.9). Well-defined patterns with various channel lengths (Figure 5.10a) as well as sizes of the Au contact pads (Figure 5.10b) can be clearly visualized in the optical and FESEM images. After the microfabrication process involving multi-steps, structural integrity of the $Cu(Cys)_2$ thin film was fully retained, as was reflected in the FESEM images, XRD patterns and the Raman spectra (Appendix 5.12). The IMLT captured in the cross-plane mode (Figure 5.5d) was also successfully captured in our patterned sample in the in-plane mode.

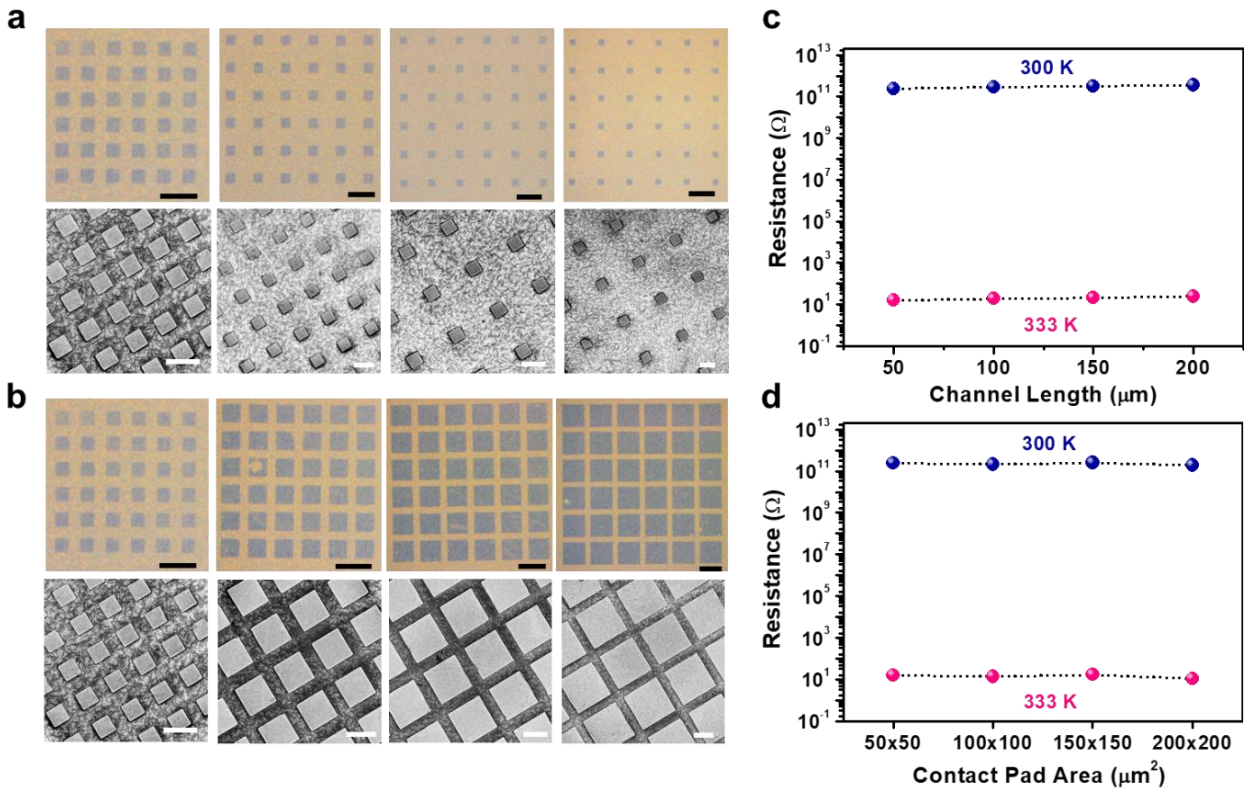

Figure 5.10. *(a) Optical (top panels; scale bars represent 200 μm length) and FESEM (bottom panels; scale bars represent 100 μm length) images of the 50 μm, 100 μm, 150 μm, and 200 μm channels (left to right) with Au contact pads on the top of $Cu(Cys)_2$ thin film. Scale bars are provided. (b) Optical (top panels; scale bars represent 200 μm length) and FESEM (bottom panels; scale bars represent 100 μm length) images of the 50x50 μm^2, 100x100 μm^2, 150x150 μm^2 and 200x200 μm^2 (left to right) Au contact pads. (c) Plot of resistance values versus and channel length at 300 K (blue spheres) and 333 K (pink spheres). (d) Plot of resistance values versus and contact pad area at 300 K (blue spheres) and 333 K (pink spheres).*

Upon systematic variation of the channel length (50 μm, 100 μm, 150 μm and 200 μm) while keeping the contact area same (50x50 μm^2), no appreciable change in the resistance value was observed, both at 300 K as well as 333 K (Figure 5.10c and Appendix 5.13). Also, systematically varying the contact pad area (50x50 μm^2, 100x100 μm^2, 150x150 μm^2 and 200x200 μm^2) while keeping the channel length same (50 μm), the resistance values did not change noticeably, both at 300 K and 333 K (Figure 5.10d and Appendix 5.14).

To strengthen the IMLT effect, we have fabricated $Cu(Cys)_2$ thin films of different thickness values (~750 nm, ~980 nm, and ~1.5 μm) and upon changing the temperature of the samples from 300 K to 333 K, an increase in the conductance value by 10^{10} fold was consistently observed (Figures 5.11 and

5.12). It is noteworthy to mention here that the effect of thickness on electric transport properties in such Cu-based CP thin films was observed below 100 nm as per earlier literature.[40]

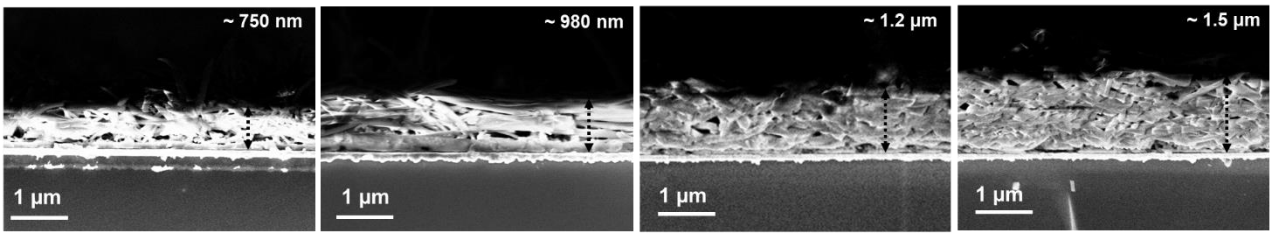

Figure 5.11. *Cross-sectional FESEM images of the Cu(Cys)$_2$ thin films with different thickness values from ~750 nm to ~1.5 µm corresponding to LbL growth of 20 cycles, 25 cycles, 30 cycles and 35 cycles, respectively.*

Such robustness in the *I-V* profiles along with the reversibility of the IMLT phenomenon further ruled out the possibility of diffusion of Au from the contact pads into the Cu(Cys)$_2$ thin film. Therefore, keeping in mind an intricate role of the electronic structure of the interface, our various complementary electrical transport measurements highlighting the consistent linear *I-V* profiles within ± 0.5 V, in both in-plane and cross-plane modes, endorsed IMLT phenomenon as a unique property of the Cu(Cys)$_2$ thin film.

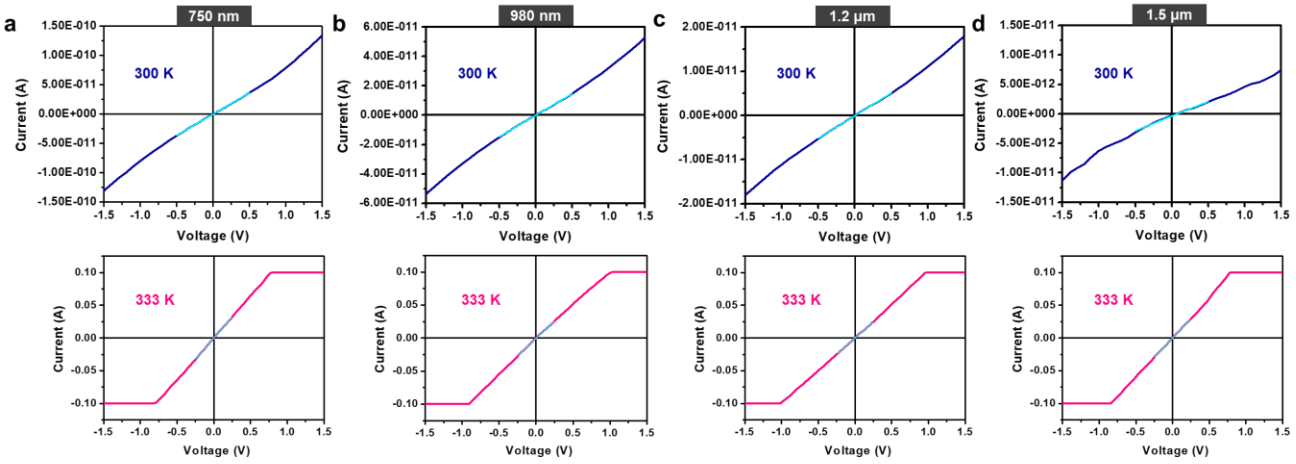

Figure 5.12. *(a) I-V characteristic curves at 300 K (RT) and 333 K (HT) upon varying the thickness from 750 nm to 1.5 µm in Cu(Cys)$_2$ thin film. Please note that the electrical conductance values are calculated by linear fitting (cyan line) at 300 K and 333 K from -0.5 V to +0.5 V and -0.25 V to +0.25 V respectively.*

In order to get mechanistic insights into the origin of such an electronically-driven IMLT phenomenon, DFT calculations combined with molecular dynamics (MD) simulations were performed on the Cu(Cys)$_2$ system at three different temperatures (0 K, 280 K and 350 K).

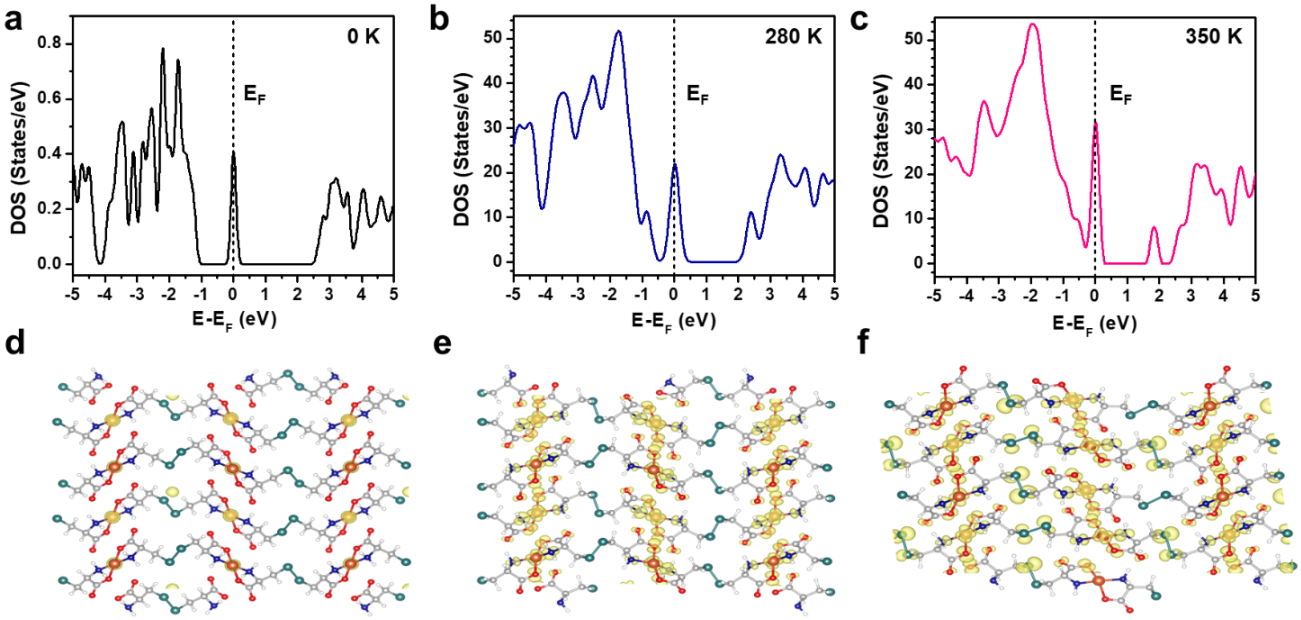

Figure 5.13. *(a) Total density of state (DOS) plots for the $Cu(Cys)_2$ structure at 0 K (a), 280 K (b) and 350 K (c) (E_F is marked by the dotted black lines). Partial charge density plots for the $Cu(Cys)_2$ structure around E_F (±0.5 eV eV) at 0 K (d), 280 K (e) and 350 K (f) where carbon, hydrogen, nitrogen, oxygen, sulphur and copper atoms are represented by grey, white, blue, red, dark cyan and orange colours, respectively; and electron accumulation is represented by yellow isosurfaces. (DFT calculations and MD simulations were performed by K. S. Ananthram under the supervision of Kartick Tarafder, NITK Surathkal, India).*

The total density of states (DOS) plots obtained at 0 K, 280 K and 350 K are presented in Figure 5.13. An important observation in the DOS plot at 0 K was the appearance of a discrete state around Fermi energy (E_F, ± 0.25 eV) which was mainly originating from the Cu atoms, as identified in the atom-projected partial density of states (PDOS) plot (Figure 5.14 and Appendix 5.15). Also, the discrete state was populated by approximately one electron density, residing mostly on the t_{2g} set of the 3*d* orbitals of Cu (Figure 5.14); and the energy gap between the valence band (VB) minimum and the discrete state was found to be ~ 1.0 eV. Therefore, $Cu(Cys)_2$ can be ascribed as a Mott-type insulator[24, 41]. Upon increasing the temperature from 0 K to 280 K, the width of the discrete state around E_F was increased (± 0.5 eV) and with a significant contribution from S atoms (Figure 5.14 and Appendix 5.15), the VB minimum shifted towards E_F, thereby reducing the energy gap. Remarkably, at 350 K, the discrete state at E_F was merged with the VB and a metal-like continuous density of states was realized viz. overlapping of the Cu-based states via the S-based state (Figure 5.14 and Appendix Figure 5.15).

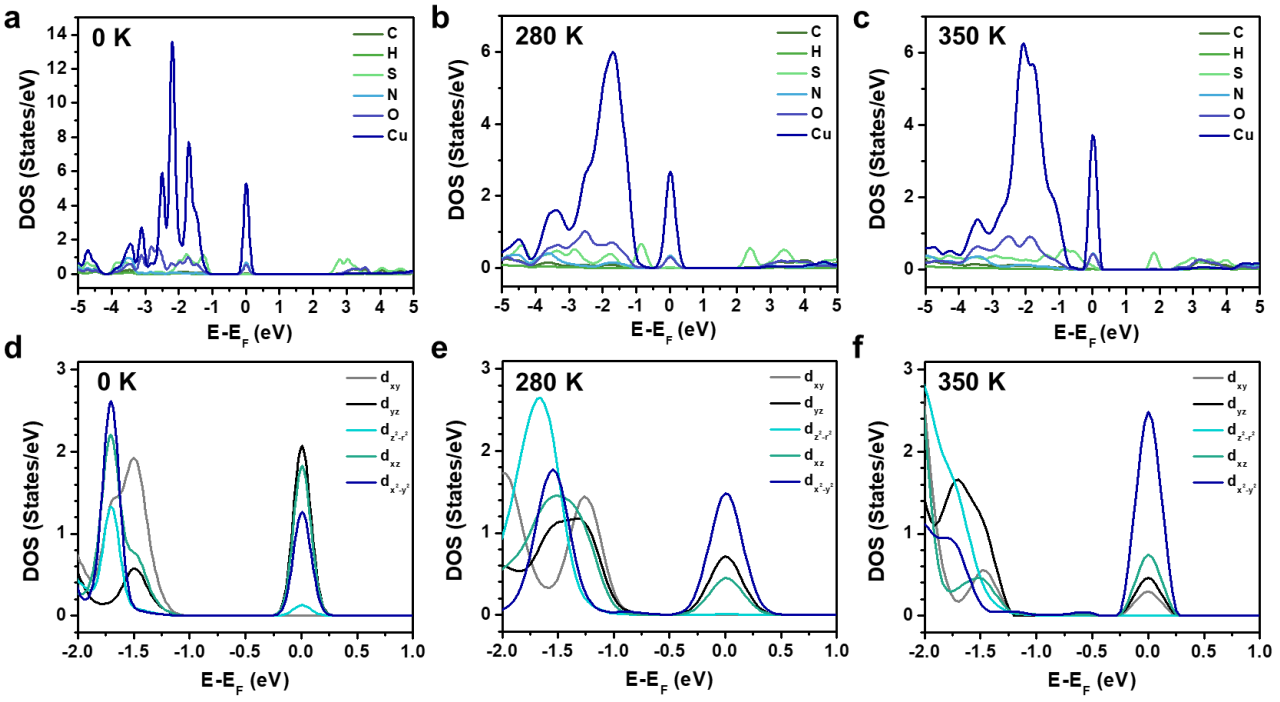

Figure 5.14. *(a-c) Atom-projected partial density of states (PDOS) plots at 0 K, 280 K and 350 K. (d-f) d-orbitals contribution of Cu atom in the atom-project partial density of states at 0 K, 280 K and 350 K. (DFT calculations and MD simulations were performed by K. S. Ananthram under the supervision of Kartick Tarafder, NITK Surathkal, India).*

Additionally, total charge density plots (Appendix 5.16) and partial charge density plots (Figure 5.13) were carefully examined and Bader charge analysis[1, 15, 31] was carried out to understand the distribution of charge on various atoms at different temperatures which showed that S atom released and Cu atom accumulated charges at higher temperatures (Appendix Table 1) so that the respective electronic band structures were affected by the overall charge re-distribution across the high-symmetry points (Appendix 5.17). Thus, IMLT in our $Cu(Cys)_2$ system can be attributed to be due to the onset of an electronic coupling primarily involving 3*d* and 3*p* orbitals of Cu and S atoms, respectively (possibly, via 2*p* orbitals of N atoms) – without any appreciable change in the structure and/or coordination. Notably, earlier studies revealed that infinite chains and planes of $(\text{-M-S-})_\infty$ in MOF structures (so called 'through-bond' approach),[42-44] specifically the $(\text{-Cu-S-})_\infty$ linkage, could enable efficient charge-transport leading to high-electrical conductivity in the systems. The present study is clearly unravelling the innovative 'through-space' avenue $(\text{-Cu----S-})_\infty$ as well as stimulating the usage of Mott-type insulator $Cu(Cys)_2$ in neuromorphic device applications[41]. Finally, we have theoretically calculated electrical conductivity values for the $Cu(Cys)_2$ system at different temperatures which qualitatively

complemented our experimental observation on the IMLT phenomenon, specifically the trend, and certainly encourage further investigations (Appendix 5.18 and Table 2).

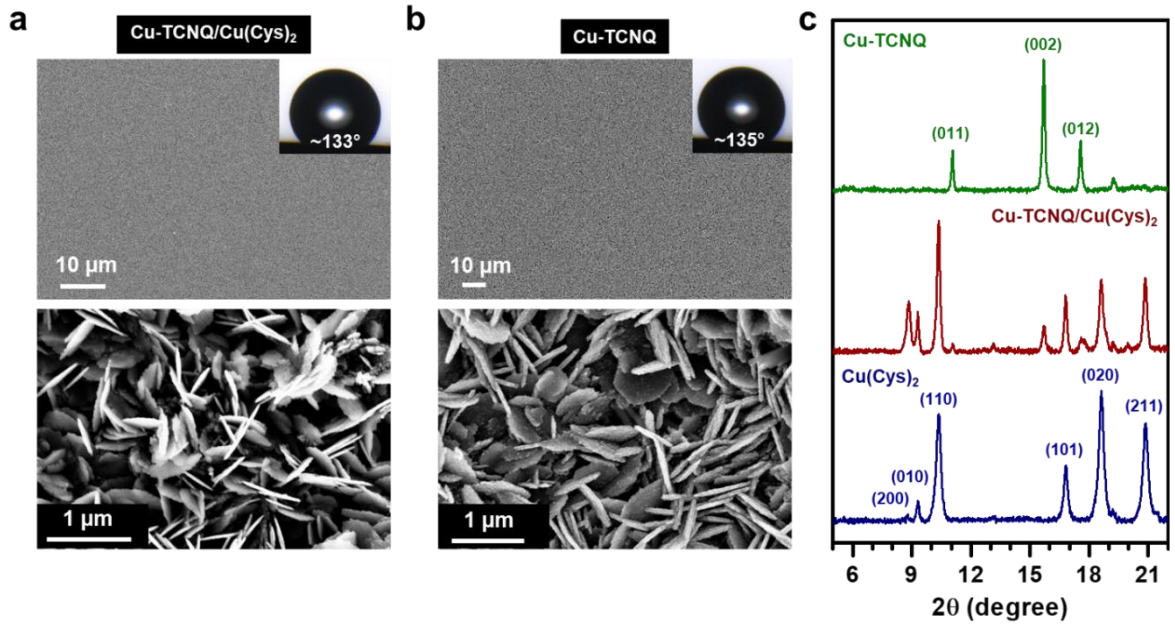

Figure 5.15. *FESEM images of (a) Cu-TNQ/Cu(Cys)₂ and Cu-TCNQ thin films showing uniform formation and their characteristic morphology. (insets: respective water contact angle in top panels). (c) Out-of-plane XRD patterns of pristine Cu(Cys)₂, pristine Cu-TCNQ and heterostructured Cu-TCNQ/Cu(Cys)₂ thin films.*

After studying the electrical transport properties of pristine $Cu(Cys)_2$ thin film, a new heterostructured thin film was fabricated by combining two Mott-like insulators: $Cu(Cys)_2$ and Cu-TCNQ.[1, 45] This is in contrast to the previous case of Cu-TCNQ/Cu-BPyDC.[1] The fabrication process involved depositing a Cu-TCNQ thin film onto a pre-fabricated $Cu(Cys)_2$ thin film on a functionalized Au substrate using the LbL method. The successful growth of Cu-TCNQ on top of the $Cu(Cys)_2$ thin film was indicated by the observed modulation of the water contact angle, which transitioned from highly hydrophilic (~13º) to highly hydrophobic (~133º) (Figure 5.2 and 5.15). Furthermore, FESEM images revealed the presence of nanoplate morphology in the Cu-TCNQ/$Cu(Cys)_2$ thin film, resembling the characteristic morphology of Cu-TCNQ[4] (Figure 5.15). To check the interface in the Cu-TCNQ/$Cu(Cys)_2$ thin film, cross-sectional elemental mapping were performed by using energy dispersive X-ray spectroscopy (EDXS) analysis, where the sulfur element acted as a marker for the cysteine molecule. The sulfur element was found to be present only in bottom layer and completely absent in top layer, whereas Cu element was present throughout, thereby supporting the successful formation of Cu-TCNQ on top of the $Cu(Cys)_2$ thin film (Appendix 5.19) Out-of-plane XRD patterns of both pristine and

heterostructured thin films were compared, which revealed the presence of characteristics diffraction peaks of Cu-TCNQ and $Cu(Cys)_2$ in the Cu-TCNQ/$Cu(Cys)_2$ thin film, and, in general, endorsed the formation of highly-crystalline thin films via LbL (Figure 5.15). Interestingly, the peak ~ 10.36º was found to be the most intense peak for both pristine $Cu(Cys)_2$ thin film and Cu-TCNQ/$Cu(Cys)_2$ heterostructured thin film. This observation aligns with previous findings where the initial deposition layers determine the final orientation of the thin films.[4, 46-48]

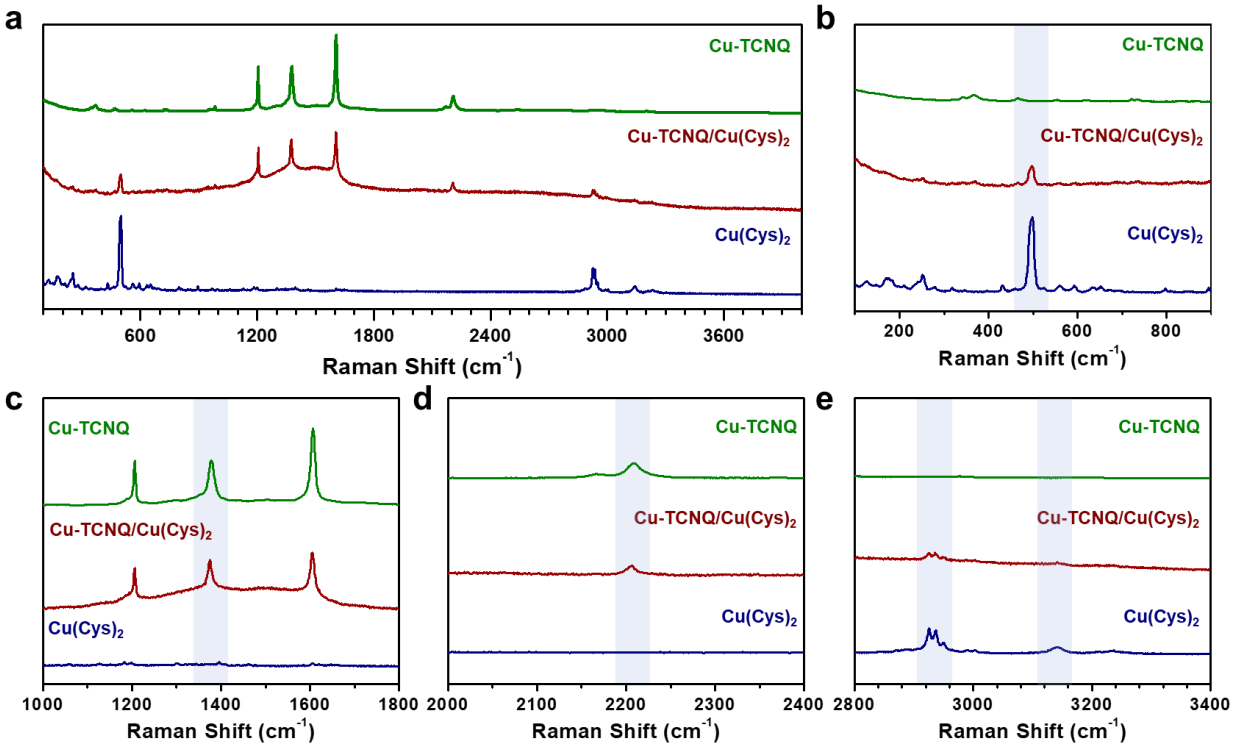

Figure 5.16. *(a-e) Raman spectra of pristine $Cu(Cys)_2$, pristine Cu-TCNQ and heterostructured Cu-TCNQ/$Cu(Cys)_2$ thin films. Characteristic vibrational features mentioned and spectral regions are highlighted.*

Similarly, Raman spectra were recorded for pristine $Cu(Cys)_2$, pristine Cu-TCNQ and heterostructured Cu-TCNQ/$Cu(Cys)_2$ thin films and characteristic vibrational signatures of Cu-TCNQ and $Cu(Cys)_2$ were found to be clearly present in the Cu-TCNQ/$Cu(Cys)_2$ system. Specifically, the characteristic vibrational peaks at ~ 1374 cm^{-1}, ~ 2206 cm^{-1} corresponded to the C–CN and C≡N stretching modes, respectively, indicating the presence of Cu-TCNQ[3-4, 16] while the peaks at ~ 496 cm^{-1}, ~ 2921 cm^{-1}, ~ 2932 cm^{-1}, ~ 2945 cm^{-1} and ~ 3136 cm^{-1} represented the S-S stretching mode, C-H ($-CH_2-$) stretching modes, and N-H ($-NH_2$) stretching mode, respectively, confirming the existence of the $Cu(Cys)_2$ system[20-21, 45] (Figure 5.16).

Electrical transport measurements were conducted in both in-plane and cross-plane modes on the heterostructured thin film of Cu-TCNQ/Cu(Cys)$_2$. The in-plane *I-V* characteristics of the Cu-TCNQ/Cu(Cys)$_2$ thin film exhibited an electrical conductance of ~10^{-5} S, which is the same as of the pristine Cu-TCNQ film, as previously observed in our studies[4] (Figure 5.17a). However, cross-plane *I-V* measurements revealed rectification of current, with a rectification ratio (RR) of ~10^2 at ±5V (Figure 5.17b).

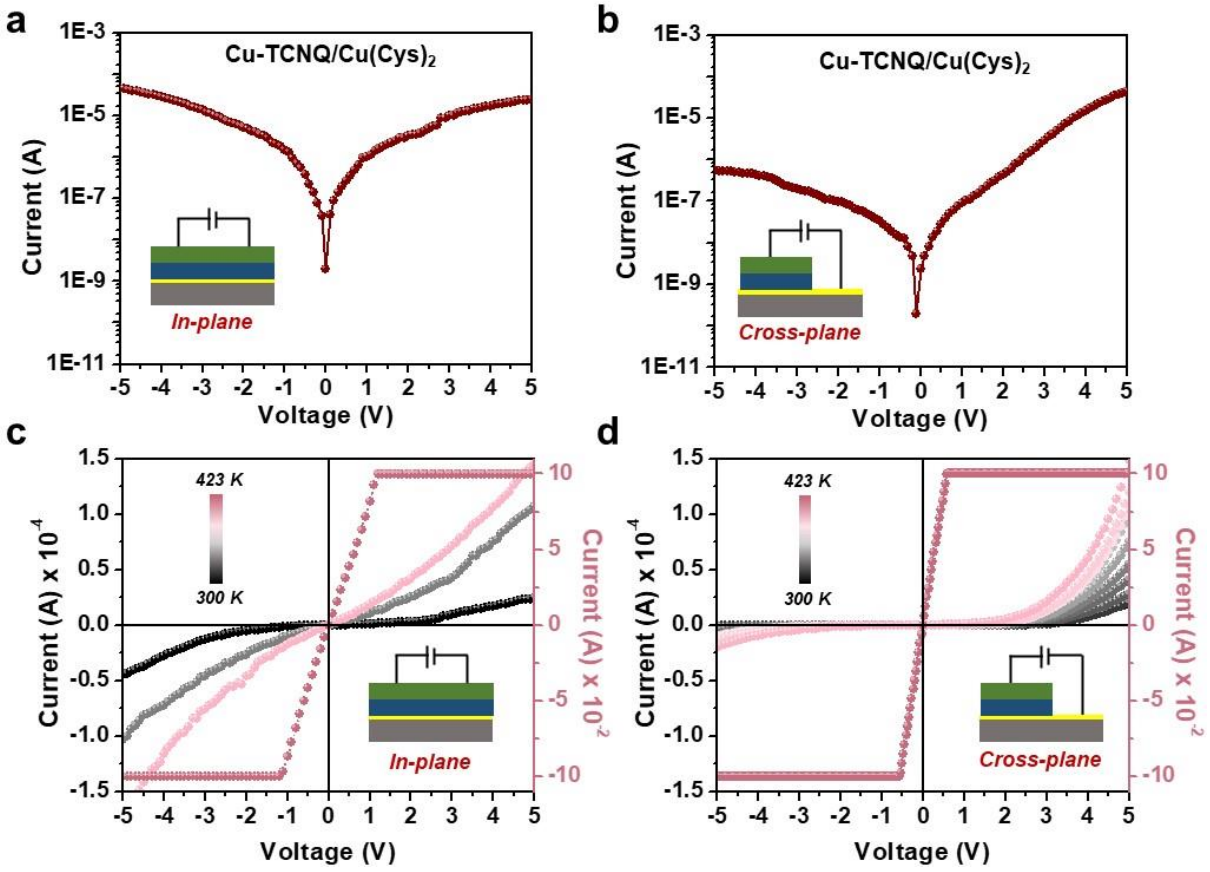

Figure 5.17. *I-V characteristic curves (a,b) at room-temperature and (c,d) at variable temperature (ranging from 300 K to 423 K) of Cu-TCNQ/Cu(Cys)$_2$ in in-plane and cross-plane modes (insets: schematic of in-plane and cross-plane I-V modes).*

Both pristine thin films, Cu-TCNQ and Cu(Cys)$_2$, display resistive switching behavior at different transition temperatures. Therefore, an investigation of the temperature dependence of electrical transport properties across the Cu-TCNQ/Cu(Cys)$_2$ heterostructured thin film is anticipated to be interesting. The in-plane *I-V* profile of Cu-TCNQ/Cu(Cys)$_2$ thin film was found to be similar to that of the pristine Cu-TCNQ thin film at variable temperatures (Figure 5.17c). Remarkably, the cross-

plane *I-V* profiles demonstrate an exponential increase in current primarily on the positive potential side, accompanied by a slight increase on the negative potential side as the temperature rises, resulting in a decrease in the RR. No significant changes are observed at the transition temperature of $Cu(Cys)_2$ (333 K), but a resistive switching behavior occurs at 423 K (transition temperature of Cu-TCNQ) (Figure 5.17d). This anomalous behavior is primarily attributed to the formation of a p-n junction-like interface, wherein Cu(I)-TCNQ acts as the electron donor (n-type) and $Cu(II)(Cys)_2$ functions as the electron acceptor (p-type), as validated by comparing the current directionality with a commercial Si diode, similar to our previous studies.[4, 49-50] Moreover, the emergence of a low-resistance state (LRS) with a value of ~10 Ω at the elevated temperature of 423 K can be attributed to a significant reduction and/or vanishing of the depletion region (possibly higher degree of charge transfer), leading to symmetrical current flow in both forward and reverse bias conditions.

5.4 Conclusions

In summary, we have presented an interface of two Mott insulating CPs with $Cu(I)(3d^{10})$ and $Cu(II)(3d^{9})$ coordinated to TCNQ and cysteine ligands, respectively. Electrical conductance value across the pristine $Cu(Cys)_2$ thin film showed a thermally driven and fully reversible IMT-like transition with an"on–off" ratio of $\sim 10^{10}$ at ambient pressure and a little above room temperature (333 K). The transition was achieved without a noticeable change in the structure and assigned to be of mainly electronic origin, viz., a charge cross-over phenomenon.[45] The electrical transport properties of the Cu-TCNQ/$Cu(Cys)_2$ thin film were studied at variable temperatures, revealing an intriguing phenomenon of current rectification (at 300 K) coupled with resistive switching at an elevated temperature (423 K). This anomalous behaviour is attributed to the emergence of a p-n junction-like interface and the occurrence of LRS at 423 K could be due to significant reduction and/or vanishing of the depletion region. This research is expected to establish a fresh platform for investigating novel phenomena at the interface, where the interplay of charge, spin, and lattice degrees of freedom can be coupled. Such investigations hold great potential for advancing the field of device applications.

5.5 Appendix

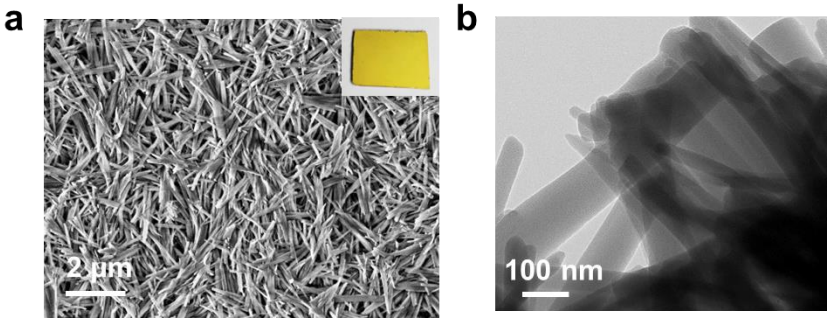

Appendix 5.1. *(a) FESEM (inset: optical image of $Cu(Cys)_2$ thin film) and (b) TEM images of $Cu(Cys)_2$ thin film.*

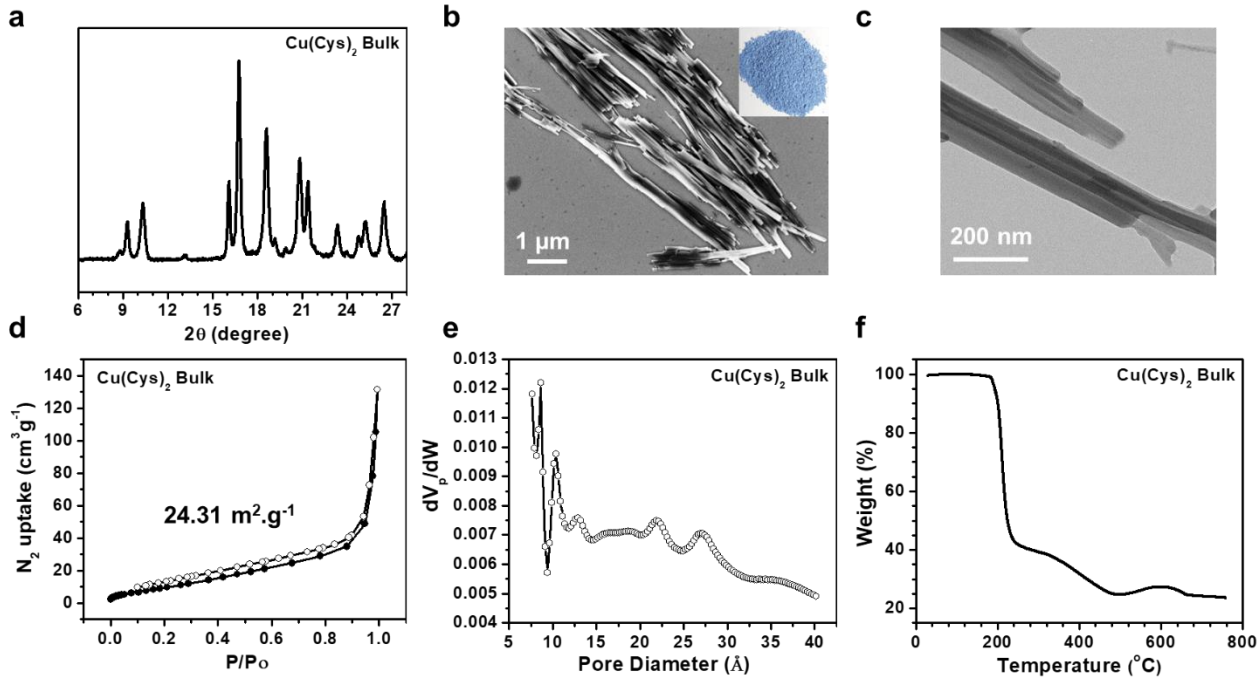

Appendix 5.2. *(a) Powder-XRD pattern revealing crystalline nature of the bulk $Cu(Cys)_2$. (b) FESEM image (inset: optical image of the powder) and (c) TEM image indicating the rod-like morphology of the $Cu(Cys)_2$ crystallites. (d) N_2 gas sorption profile along with the estimated BET surface area and (e) pore diameter profile obtained from standard H-K model showing its porous nature. (f) TGA profile depicting the thermal stability of the $Cu(Cys)_2$ bulk.*

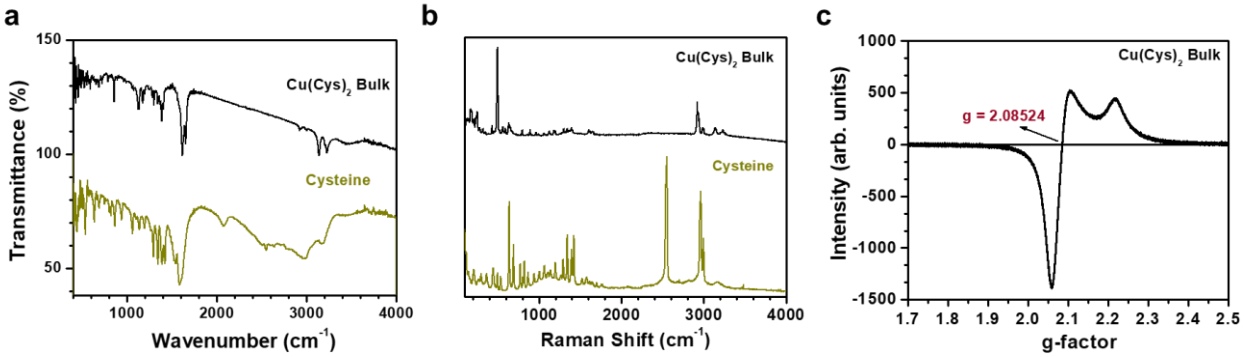

Appendix 5.3. *FTIR (a) and Raman (b) spectra of cysteine and $Cu(Cys)_2$ bulk. (c) EPR spectrum of the $Cu(Cys)_2$ bulk indicating the presence of Cu(II) (spin-1/2 system with g = 2.08) ion in the system.*

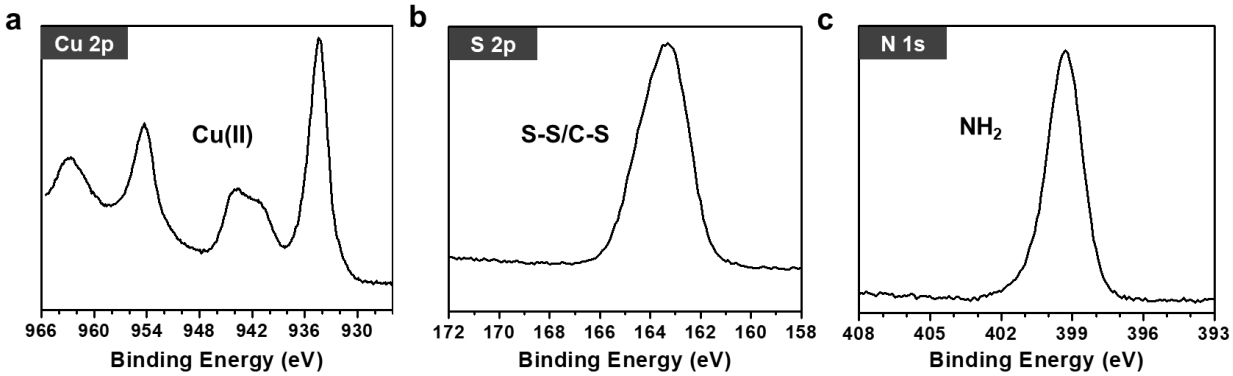

Appendix 5.4. *(a) Cu2p, (b) S2p and (c) N1s XPS spectra of the $Cu(Cys)_2$ bulk confirming the presence of Cu(II) S-S and C-S bonds and NH_2 moiety.*

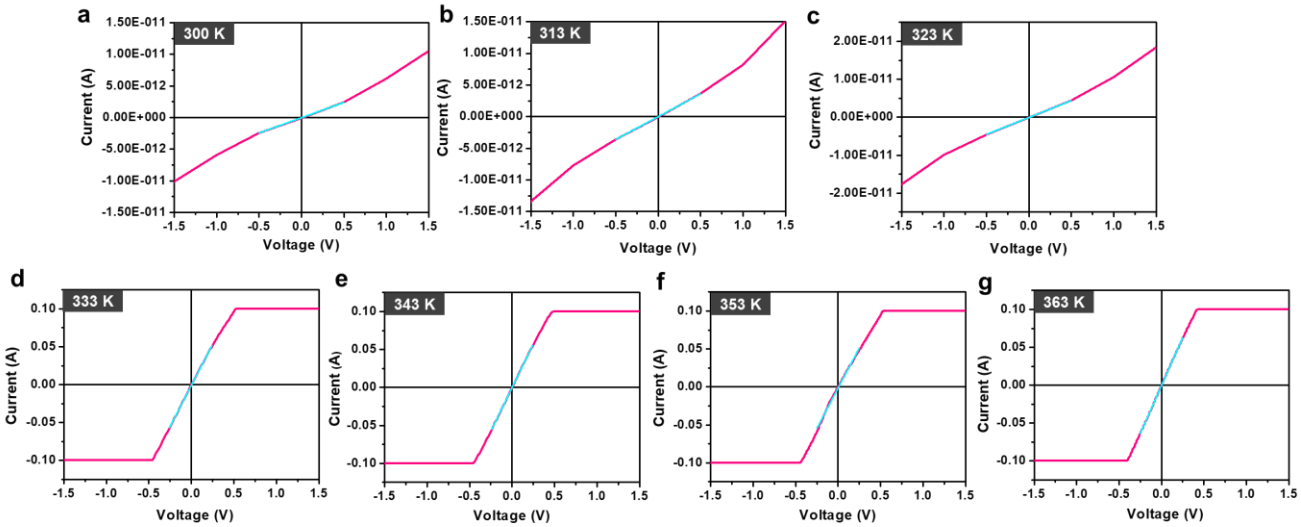

Appendix 5.5. *Temperature-dependent I-V profiles of the $Cu(Cys)_2$ thin film in the cross-plane mode during heating from 300 K to 363 K using patterned Au pad (200x200 μm^2) as top electrode. Please note that the electrical conductance values are calculated by linear fitting (cyan line) at 300 K and 333 K from -0.5 V to +0.5 V and -0.25 V to +0.25 V respectively. Resistivity values calculated at 300 K and 333 K are 1.28 x 10^{10} Ωm and 10^{-1} Ωm, respectively.*

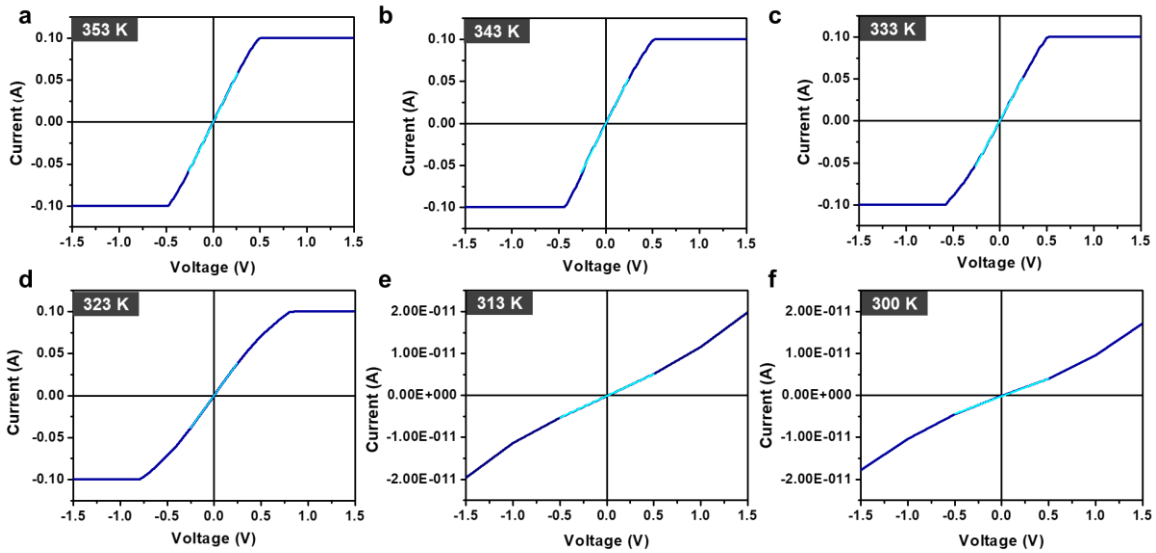

Appendix 5.6. *(a-f) Temperature-dependent I-V profiles of the $Cu(Cys)_2$ thin film in the cross-plane mode during cooling from 353 K to 300 K using patterned Au pad (200x200 μm^2) as top electrode. Please note that the electrical conductance values are calculated by linear fitting (cyan line) at 300 K and 333 K from -0.5 V to +0.5 V and -0.25 V to +0.25 V respectively.*

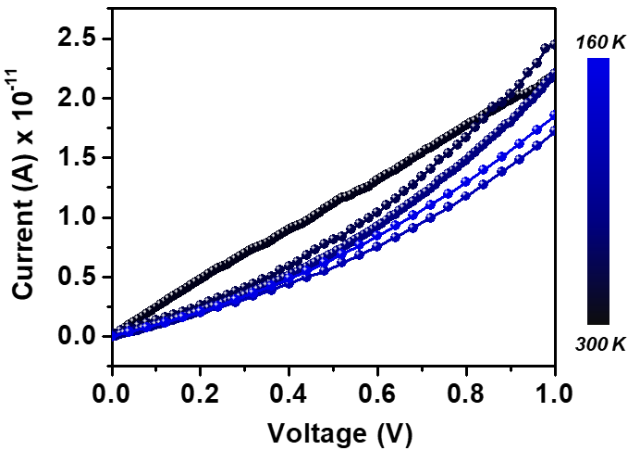

Appendix 5.7. *In-plane I-V profiles of the Cu(Cys)$_2$ thin film from room temperature (300 K) to low-temperature (160 K) indicating no appreciable change even by an order of magnitude. Low-temperature measurements were carried out by following the procedure recently standardized in our lab (Ref. 1).*

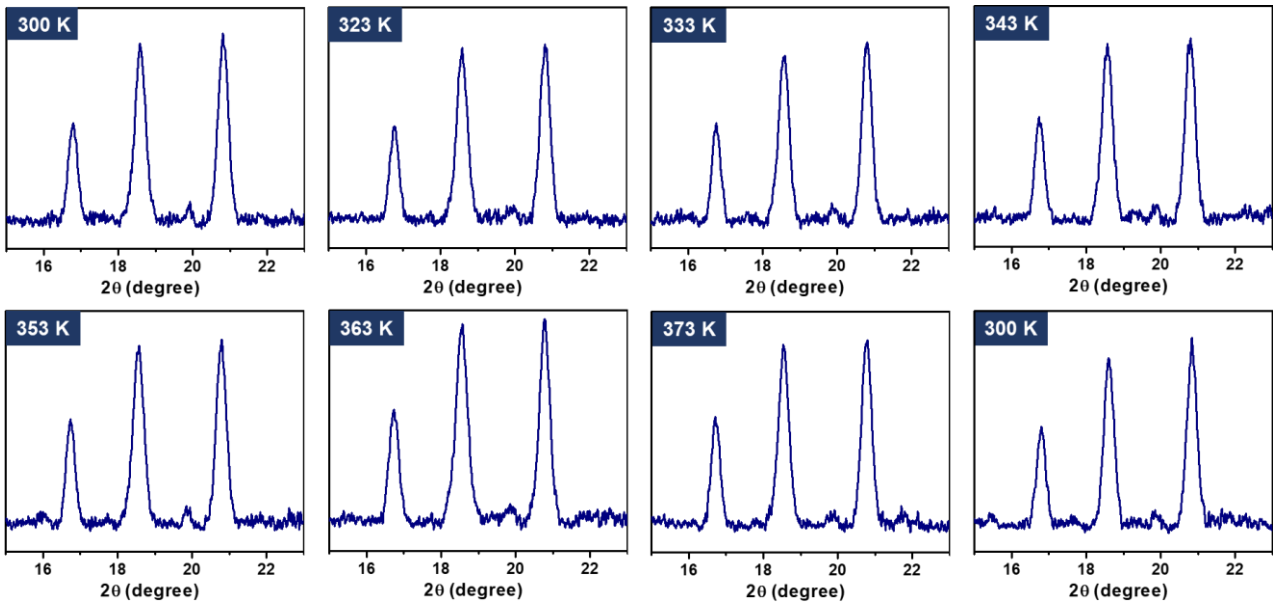

Appendix 5.8. *Temperature-dependent out-of-plane XRD patterns of the Cu(Cys)2 thin film upon systematically varying the temperature from 300 K to 373 K (above the transition temperature) and back to 300 K. Apparently, no change in the pattern was observed.*

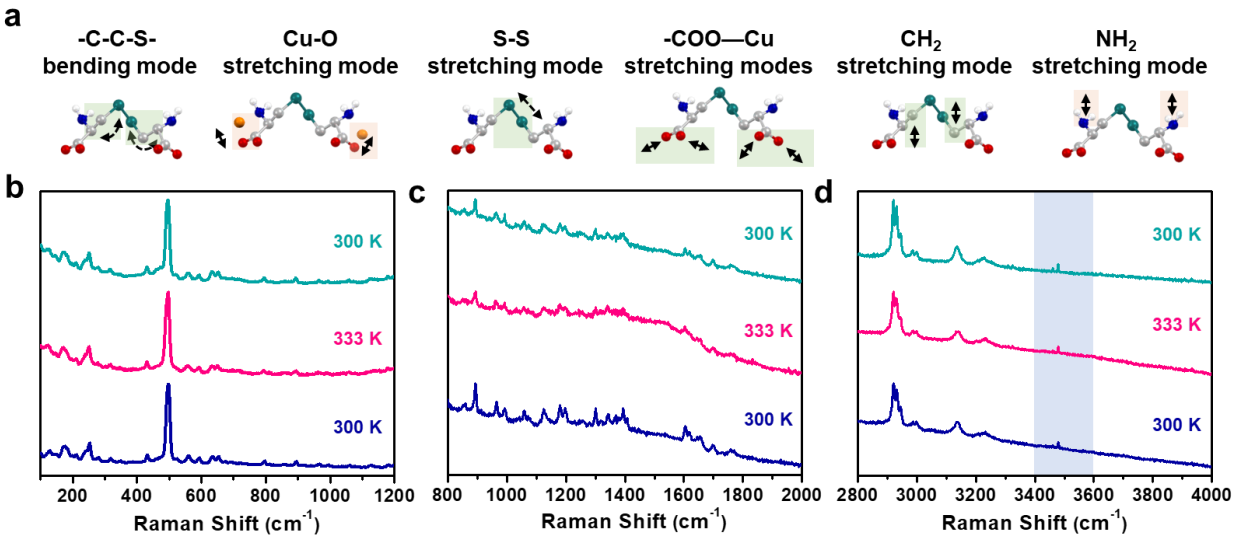

Appendix 5.9. *(a) Schematic representation of Raman spectral modes. (b-d) Raman spectra of the $Cu(Cys)_2$ thin film at various temperatures (300 K, 333 K and back to 300 K) indicating no change in the local structure and desorption-adsorption of water (characteristic vibrations are marked by dotted lines).*

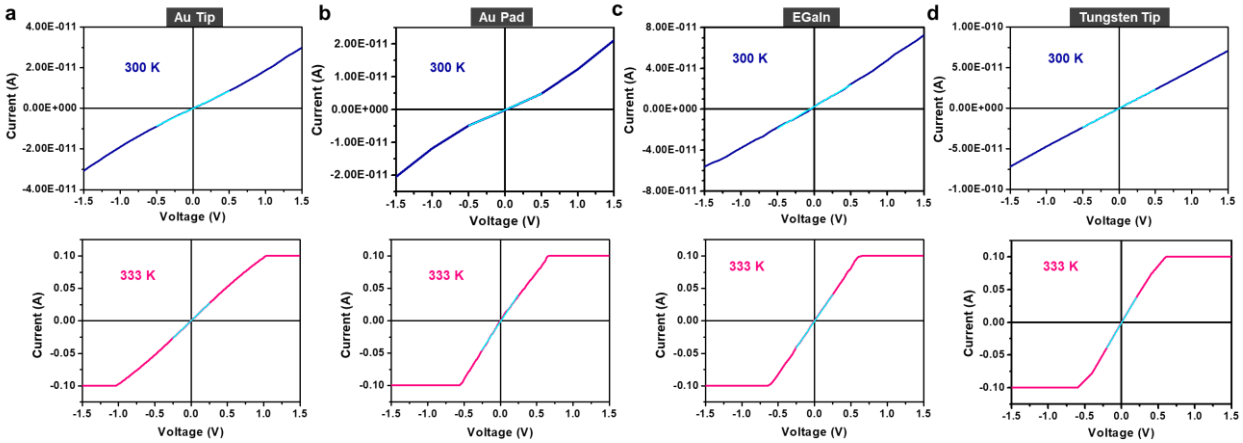

Appendix 5.10. *In-plane I-V profiles of the $Cu(Cys)_2$ thin film with different contact electrodes (a) Au tip (b) Au pad (c) EGaIn and (d) W tip, at 300 K and 333 K. Please note that the electrical conductance values are calculated by linear fitting (cyan line) at 300 K and 333 K from -0.5 V to +0.5 V and -0.25 V to +0.25 V respectively.*

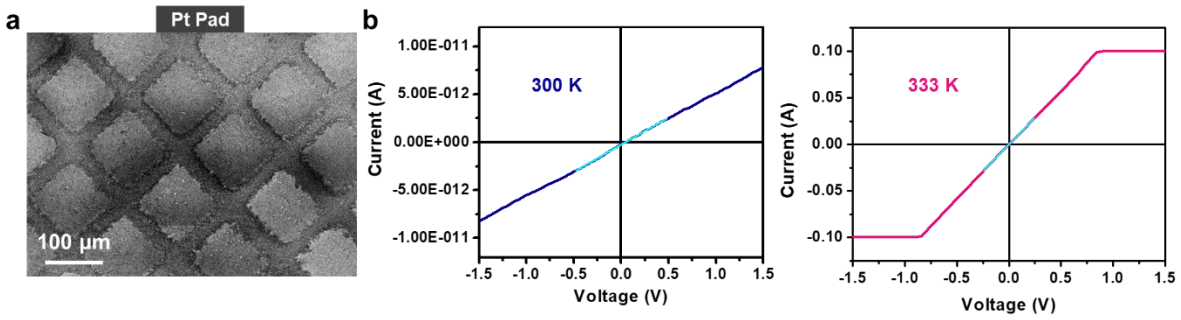

Appendix 5.11. *(a) FESEM image of Pt contact pad on the top of the $Cu(Cys)_2$ thin film (b) In-plane I-V profiles of the $Cu(Cys)_2$ thin film with Pt contact pads at 300 K and 333 K. Please note that the electrical conductance values are calculated by linear fitting (cyan line) at 300 K and 333 K from -0.5 V to +0.5 V and -0.25 V to +0.25 V respectively.*

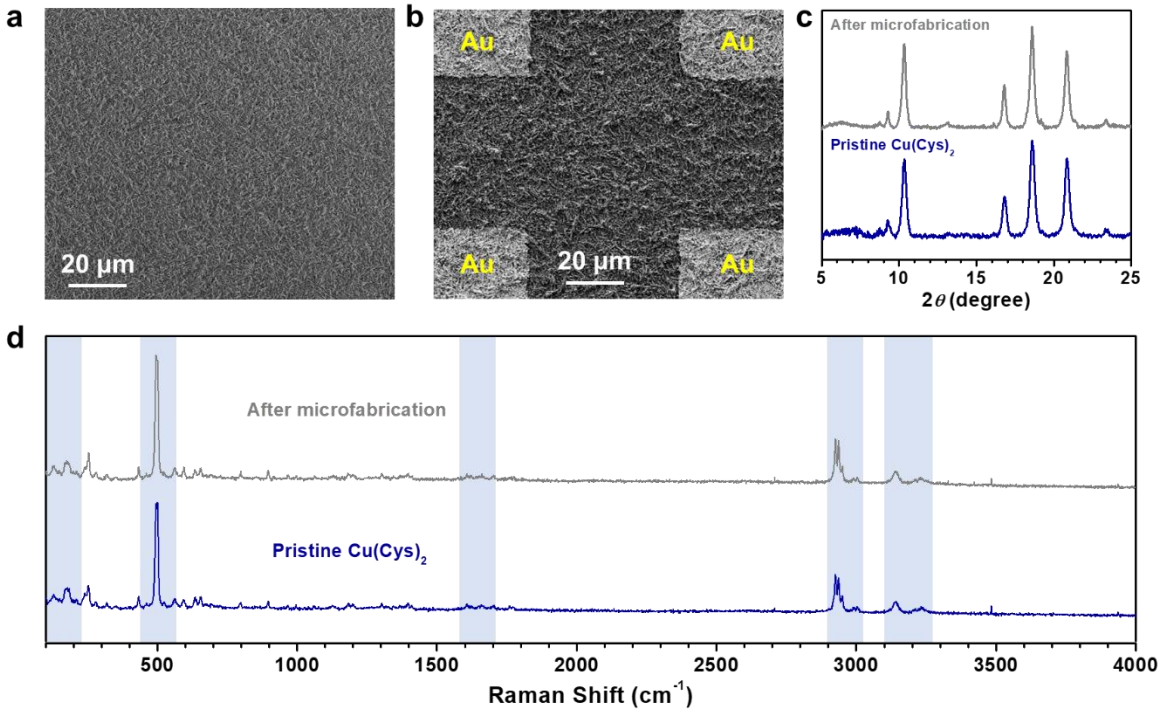

Appendix 5.12. *(a-b) FESEM images (c) XRD and (d) Raman spectra of the $Cu(Cys)_2$ thin film before and after microfabrication of the Au contact pads indicating no changes in the morphology as well as the structural integrity.*

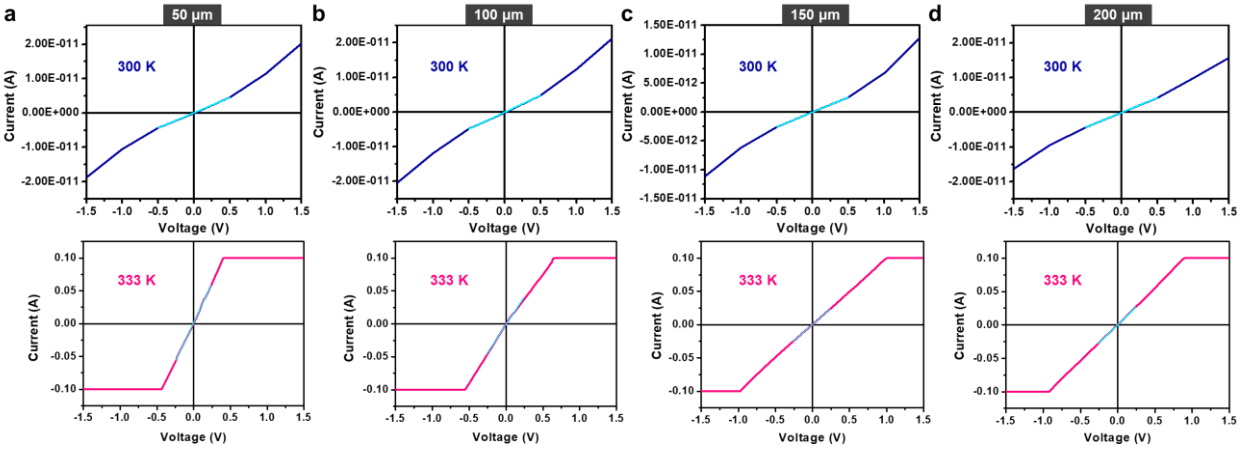

Appendix 5.13. *In-plane I-V profiles of the $Cu(Cys)_2$ thin film with the variation of channel length from 50 μm to 200 μm (a-d) at 300 K and 333 K. Please note that the electrical conductance values are calculated by linear fitting (cyan line) at 300 K and 333 K from -0.5 V to +0.5 V and -0.25 V to +0.25 V respectively.*

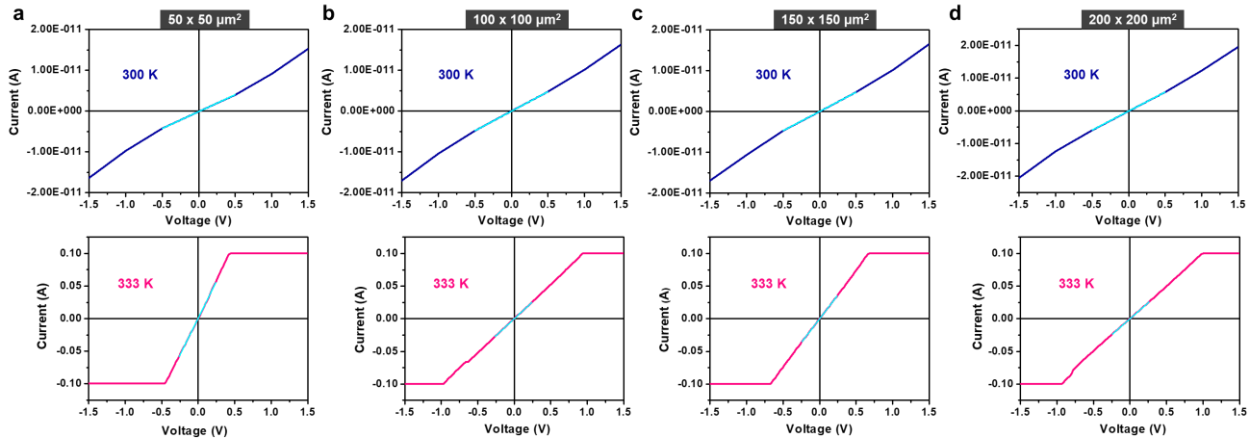

Appendix 5.14. *In-plane I-V profiles of the Cu(Cys)$_2$ thin film with the variation of contact area from 50 x 50 µm2 to 200 x 200 µm2 (a-d) at 300 K and 333 K. Please note that the electrical conductance values are calculated by linear fitting (cyan line) at 300 K and 333 K from -0.5 V to +0.5 V and -0.25 V to +0.25 V respectively.*

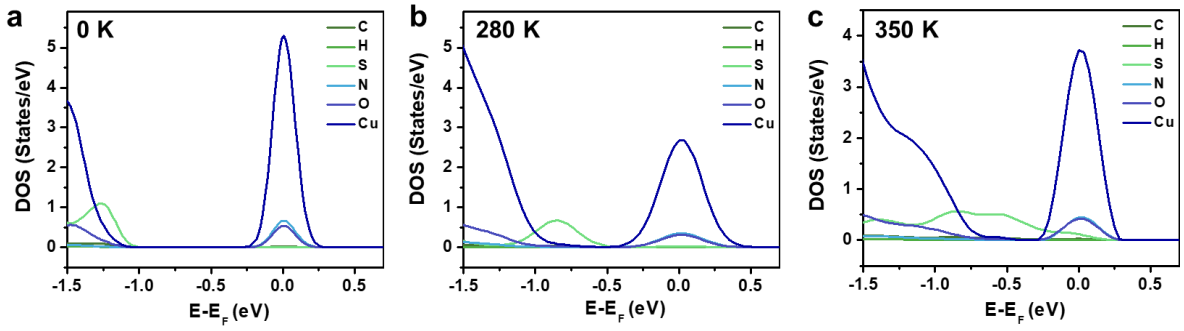

Appendix 5.15. *Energy Atom-projected partial density of states (PDOS) plots (zoomed-in sections around E_F) at 0 K, 280 K and 350 K. (DFT calculations and MD simulations were performed by K. S. Ananthram under the supervision of Kartick Tarafder, NITK Surathkal, India).*

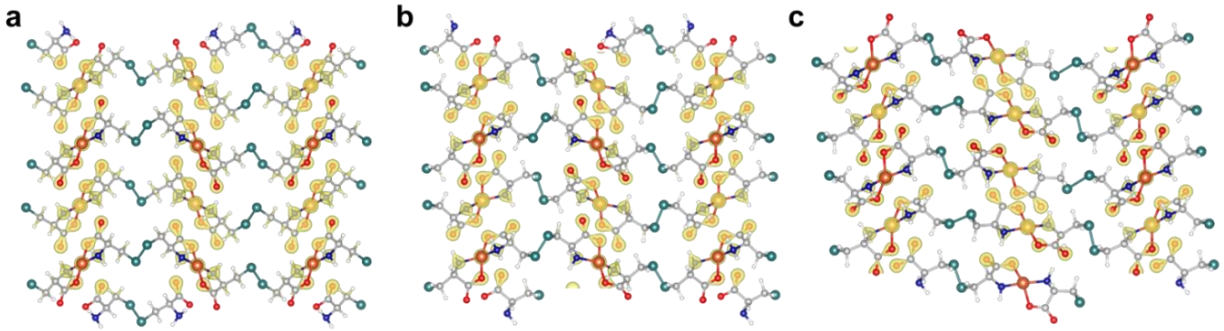

Appendix 5.16. *(a-c) Total charge density plots of $Cu(Cys)_2$ at 0 K (left panel), 280 K (middle panel) and 350 K (right panel) where carbon, hydrogen, nitrogen, oxygen, sulphur and copper atoms are represented by colors grey, white, blue, red, dark cyan and orange, respectively and electron accumulation is represented as yellow isosurface. (DFT calculations and MD simulations were performed by K. S. Ananthram under the supervision of Kartick Tarafder, NITK Surathkal, India).*

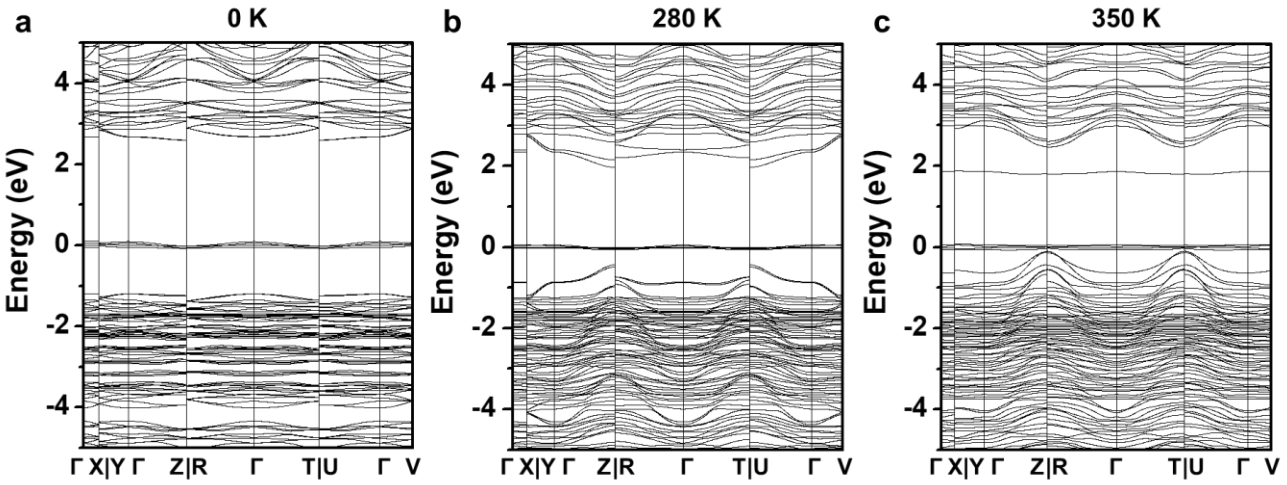

Appendix 5.17. *Band structures of the $Cu(Cys)_2$ system at (a-c) 0 K, 280 K and 350 K. Standard notations are used for the high-symmetry points (Ref. 9). (DFT calculations and MD simulations were performed by K. S. Ananthram under the supervision of Kartick Tarafder, NITK Surathkal, India).*

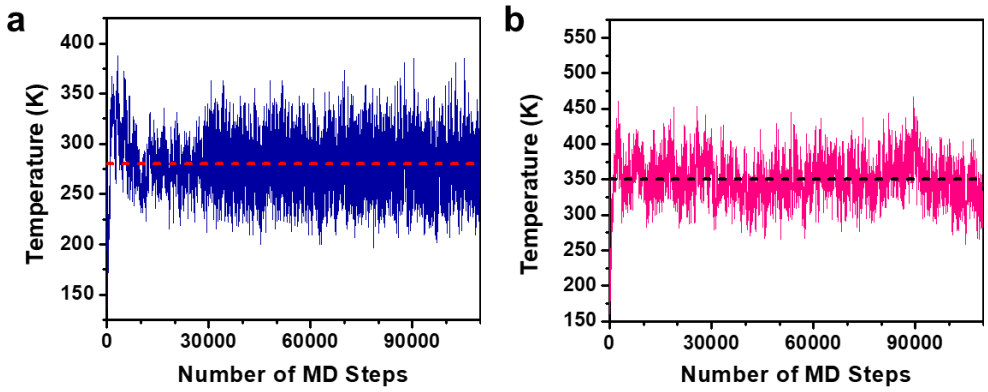

Appendix 5.18. *Temperature fluctuation during MD simulation at (a) 280 K and (b) 350 K. (DFT calculations and MD simulations were performed by K. S. Ananthram under the supervision of Kartick Tarafder, NITK Surathkal, India).*

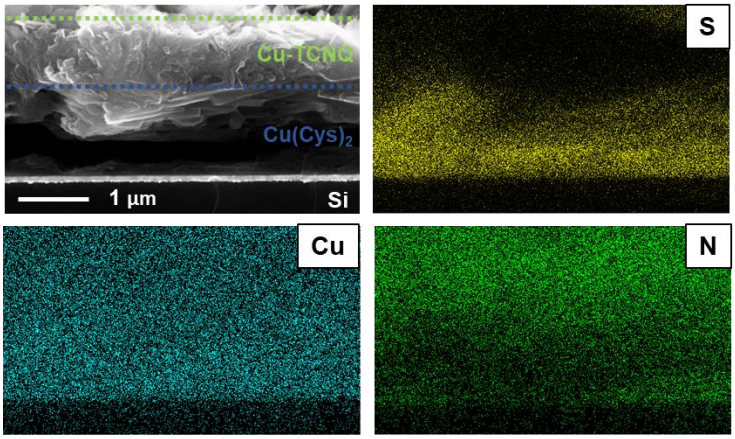

Appendix 5.19. *Cross-sectional elemental mapping by using EDXS analysis in Cu-TCNQ/Cu(Cys)$_2$ Thin film, where the sulfur element acted as a marker for the cysteine molecule.*

Appendix Table 5.1. *Atoms-wise Bader charge contribution in the Cu(Cys)$_2$ structure at different temperatures. (DFT calculations and MD simulations were performed by K. S. Ananthram under the supervision of Kartick Tarafder, NITK Surathkal, India).*

Atoms (total number of atoms in the cell)	**Effective Bader Charge (in electron)**		
	0 K	**280 K**	**350 K**
Cu (4 atoms)	39.65	40.42	41.24
S (8 atoms)	46.95	46.19	45.22
N (8 atoms)	46.33	44.81	44.15
O (16 atoms)	111.71	109.04	109.48
C (24 atoms)	80.60	82.38	82.11
H (40 atoms)	38.74	41.13	41.77

Appendix Table 5.2. *Theoretical conductivity values from the Boltzmann transport method at various temperature. Temperature in MD simulations has a fluctuation of ± 20 K, hence the equilibrium*

temperature might not be the exact temperature that the system is mimicking. The deviation from the simulated temperature could be the reason why a higher conductivity value at 300 K (since it is close to experimental transition temperature of 333 K). (DFT calculations and MD simulations were performed by K. S. Ananthram under the supervision of Kartick Tarafder, NITK Surathkal, India).

Conductivity calculated in BOLTZWANN (in 1/Ohm/m)	
1 K	764.74
280 K	10065.44
350 K	580924.35

5.6 References

1. Sindhu, P.; Ananthram, K. S.; Jain, A.; Tarafder, K.; Ballav, N., Charge-transfer interface of insulating metal-organic frameworks with metallic conduction. *Nat. Commun.* **2022,** *13* (1), 7665.

2. Arnold, R.; Azzam, W.; Terfort, A.; Wöll, C., Preparation, Modification, and Crystallinity of Aliphatic and Aromatic Carboxylic Acid Terminated Self-Assembled Monolayers. *Langmuir* **2002,** *18* (10), 3980-3992.

3. Rana, S.; Rajendra, R.; Dhara, B.; Jha, P. K.; Ballav, N., Highly Hydrophobic and Chemically Rectifiable Surface-Anchored Metal-Organic Framework Thin-Film Devices. *Adv. Mater. Interfaces* **2016,** *3* (13), 1500738.

4. Sindhu, P.; Prasoon, A.; Rana, S.; Ballav, N., Emergent Interface in Heterostructured Thin Films of Cu(II) and Cu(I) Coordination Polymers. *J. Phys. Chem. Lett.* **2020,** *11* (15), 6242-6248.

5. Ferrer, P.; da Silva, I.; Rubio-Zuazo, J.; Castro, G. R., Synthesis and crystal structure of the novel metal organic framework Zn(C3H5NO2S)2. *Powder Diffr.* **2014,** *29* (4), 366-370.

6. Hanwell, M. D.; Curtis, D. E.; Lonie, D. C.; Vandermeersch, T.; Zurek, E.; Hutchison, G. R., Avogadro: an advanced semantic chemical editor, visualization, and analysis platform. *J. Cheminfor.* **2012,** *4* (1), 17.

7. Kresse, G.; Furthmüller, J., Efficient iterative schemes for ab initio total-energy calculations using a plane-wave basis set. *Phys. Rev. B* **1996,** *54* (16), 11169-11186.

8. Perdew, J. P.; Burke, K.; Ernzerhof, M., Generalized Gradient Approximation Made Simple. *Phys. Rev. Lett.* **1996,** *77* (18), 3865-3868.

9. Hinuma, Y.; Pizzi, G.; Kumagai, Y.; Oba, F.; Tanaka, I., Band structure diagram paths based on crystallography. *Comput. Mater. Sci.* **2017,** *128*, 140-184.

10. Hoover, W. G.; Ladd, A. J. C.; Moran, B., High-Strain-Rate Plastic Flow Studied via Nonequilibrium Molecular Dynamics. *Phys. Rev. Lett.* **1982,** *48* (26), 1818-1820.

11. Evans, D. J., Computer ‘‘experiment’’ for nonlinear thermodynamics of Couette flow. *J. Chem. Phys.* **1983,** *78* (6), 3297-3302.

12. Allen, M. P.; Tildesley, D. J., *Computer Simulation of Liquids*. Oxford University Press, New York: 1991.

13. Pizzi, G.; Volja, D.; Kozinsky, B.; Fornari, M.; Marzari, N., BoltzWann: A code for the evaluation of thermoelectric and electronic transport properties with a maximally-localized Wannier functions basis. *Comput. Phys. Commun.* **2014,** *185* (1), 422-429.

14. Mostofi, A. A.; Yates, J. R.; Lee, Y.-S.; Souza, I.; Vanderbilt, D.; Marzari, N., wannier90: A tool for obtaining maximally-localised Wannier functions. *Comput. Phys. Commun.* **2008,** *178* (9), 685-699.

15. Bader, R. F. W., *Atoms in Molecules : A Quantum Theory*. Clarendon Press: 1994.

16. Henkelman, G.; Arnaldsson, A.; Jónsson, H., A fast and robust algorithm for Bader decomposition of charge density. *Comput. Mater. Sci.* **2006,** *36* (3), 354-360.

17. Sanville, E.; Kenny, S. D.; Smith, R.; Henkelman, G., Improved grid-based algorithm for Bader charge allocation. *J. Comput. Chem.* **2007,** *28* (5), 899-908.

18. Tang, W.; Sanville, E.; Henkelman, G., A grid-based Bader analysis algorithm without lattice bias. *J. Phys.: Condens. Matter* **2009,** *21* (8), 084204.

19. Rodríguez-Carvajal, J., Recent advances in magnetic structure determination by neutron powder diffraction. *Physica B: Condens. Matter* **1993,** *192* (1), 55-69.

20. Diaz Fleming, G.; Finnerty, J. J.; Campos-Vallette, M.; Célis, F.; Aliaga, A. E.; Fredes, C.; Koch, R., Experimental and theoretical Raman and surface-enhanced Raman scattering study of cysteine. *J. Raman Spec.* **2009,** *40* (6), 632-638.

21. Minkov, V. S.; Goryainov, S. V.; Boldyreva, E. V.; Görbitz, C. H., Raman study of pressure-induced phase transitions in crystals of orthorhombic and monoclinic polymorphs of L-cysteine: dynamics of the side chain. *J. Raman Spec.* **2010,** *41* (12), 1748-1758.

22. Moulder, J. F.; Stickle, W. F.; Sobol, P. E.; Bomben, K. D., *Handbook of X-ray photoelectron spectroscopy : a reference book of standard spectra for identification of XPS data*. Perkin-Elmer: Minsesota, 1992.

23. Valle, J. d.; Vargas, N. M.; Rocco, R.; Salev, P.; Kalcheim, Y.; Lapa, P. N.; Adda, C.; Lee, M.-H.; Wang, P. Y.; Fratino, L.; Rozenberg, M. J.; Schuller, I. K., Spatiotemporal characterization of the field-induced insulator-to-metal transition. *Science* **2021,** *373* (6557), 907-911.

24. Imada, M.; Fujimori, A.; Tokura, Y., Metal-insulator transitions. *Rev. Mod. Phys.* **1998,** *70* (4), 1039-1263.

25. Mott, N. F., The Basis of the Electron Theory of Metals, with Special Reference to the Transition Metals. *Proc. Phys. Soc. London Sect. A* **1949,** *62* (7), 416.

26. Mott, N. F., *Metal-insulator transitions* **Taylor & Francis, London, 1974**.

27. Moore, R. G.; Zhang, J.; Nascimento, V. B.; Jin, R.; Guo, J.; Wang, G. T.; Fang, Z.; Mandrus, D.; Plummer, E. W., A Surface-Tailored, Purely Electronic, Mott Metal-to-Insulator Transition. *Science* **2007,** *318* (5850), 615-619.

28. Sow, C.; Yonezawa, S.; Kitamura, S.; Oka, T.; Kuroki, K.; Nakamura, F.; Maeno, Y., Current-induced strong diamagnetism in the Mott insulator Ca_2RuO_4. *Science* **2017,** *358* (6366), 1084-1087.

29. Bertinshaw, J.; Gurung, N.; Jorba, P.; Liu, H.; Schmid, M.; Mantadakis, D. T.; Daghofer, M.; Krautloher, M.; Jain, A.; Ryu, G. H.; Fabelo, O.; Hansmann, P.; Khaliullin, G.; Pfleiderer, C.; Keimer, B.; Kim, B. J., Unique Crystal Structure of Ca_2RuO_4 in the Current Stabilized Semimetallic State. *Phys. Rev. Lett.* **2019,** *123* (13), 137204.

30. Lee, D.; Chung, B.; Shi, Y.; Kim, G.-Y.; Campbell, N.; Xue, F.; Song, K.; Choi, S.-Y.; Podkaminer, J. P.; Kim, T. H.; Ryan, P. J.; Kim, J.-W.; Paudel, T. R.; Kang, J.-H.; Spinuzzi, J. W.; Tenne, D. A.; Tsymbal, E. Y.; Rzchowski, M. S.; Chen, L. Q.; Lee, J.; Eom, C. B., Isostructural metal-insulator transition in VO_2. *Science* **2018,** *362* (6418), 1037-1040.

31. Maximoff, S. N.; Smit, B., Redox chemistry and metal–insulator transitions intertwined in a nano-porous material. *Nat. Commun.* **2014,** *5* (1), 4032.

32. Tominaka, S.; Coudert, F.-X.; Dao, T. D.; Nagao, T.; Cheetham, A. K., Insulator-to-Proton-Conductor Transition in a Dense Metal–Organic Framework. *J. Am. Chem. Soc.* **2015,** *137* (20), 6428-6431.

33. Kon, K.; Uchida, K.; Fuku, K.; Yamanaka, S.; Wu, B.; Yamazui, D.; Iguchi, H.; Kobayashi, H.; Gambe, Y.; Honma, I.; Takaishi, S., Electron-Conductive Metal–Organic Framework, Fe(dhbq)(dhbq = 2,5-Dihydroxy-1,4-benzoquinone): Coexistence of Microporosity and Solid-State Redox Activity. *ACS Appl. Mater. Interfaces* **2021,** *13* (32), 38188-38193.

34. Nagarajan, L.; De Souza, R. A.; Samuelis, D.; Valov, I.; Börger, A.; Janek, J.; Becker, K.-D.; Schmidt, P. C.; Martin, M., A chemically driven insulator–metal transition in non-stoichiometric and amorphous gallium oxide. *Nat. Mater.* **2008,** *7* (5), 391-398.

35. Tan, K.; Nijem, N.; Gao, Y.; Zuluaga, S.; Li, J.; Thonhauser, T.; Chabal, Y. J., Water interactions in metal organic frameworks. *CrystEngComm* **2015,** *17* (2), 247-260.

36. Peng, X.; Pelz, P. M.; Zhang, Q.; Chen, P.; Cao, L.; Zhang, Y.; Liao, H.-G.; Zheng, H.; Wang, C.; Sun, S.-G.; Scott, M. C., Observation of formation and local structures of metal-organic layers via complementary electron microscopy techniques. *Nat. Commun.* **2022,** *13* (1), 5197.

37. Tong, L.; Huang, S.; Shen, Y.; Liu, S.; Ma, X.; Zhu, F.; Chen, G.; Ouyang, G., Atomically unveiling the structure-activity relationship of biomacromolecule-metal-organic frameworks symbiotic crystal. *Nat. Commun.* **2022,** *13* (1), 951.

38. Rana, S.; Prasoon, A.; Jha, P. K.; Prathamshetti, A.; Ballav, N., Thermally Driven Resistive Switching in Solution-Processable Thin Films of Coordination Polymers. *J. Phys. Chem. Lett.* **2017,** *8* (20), 5008-5014.

39. Dolgopolova, E. A.; Brandt, A. J.; Ejegbavwo, O. A.; Duke, A. S.; Maddumapatabandi, T. D.; Galhenage, R. P.; Larson, B. W.; Reid, O. G.; Ammal, S. C.; Heyden, A.; Chandrashekhar, M.; Stavila, V.; Chen, D. A.; Shustova, N. B., Electronic Properties of Bimetallic Metal–Organic Frameworks (MOFs): Tailoring the Density of Electronic States through MOF Modularity. *J. Am. Chem. Soc.* **2017,** *139* (14), 5201-5209.

40. Neumann, T.; Liu, J.; Wächter, T.; Friederich, P.; Symalla, F.; Welle, A.; Mugnaini, V.; Meded, V.; Zharnikov, M.; Wöll, C.; Wenzel, W., Superexchange Charge Transport in Loaded Metal Organic Frameworks. *ACS Nano* **2016,** *10* (7), 7085-7093.

41. Zhou, Y.; Ramanathan, S., Mott Memory and Neuromorphic Devices. *Proc. IEEE* **2015,** *103* (8), 1289-1310.

42. Sun, L.; Miyakai, T.; Seki, S.; Dincă, M., Mn2(2,5-disulfhydrylbenzene-1,4-dicarboxylate): A Microporous Metal–Organic Framework with Infinite (−Mn–S−)$_\infty$ Chains and High Intrinsic Charge Mobility. *J. Am. Chem. Soc.* **2013,** *135* (22), 8185-8188.

43. Pathak, A.; Shen, J.-W.; Usman, M.; Wei, L.-F.; Mendiratta, S.; Chang, Y.-S.; Sainbileg, B.; Ngue, C.-M.; Chen, R.-S.; Hayashi, M.; Luo, T.-T.; Chen, F.-R.; Chen, K.-H.; Tseng, T.-W.; Chen, L.-C.; Lu, K.-L., Integration of a (–Cu–S–)n plane in a metal–organic framework affords high electrical conductivity. *Nat. Commun.* **2019,** *10* (1), 1721.

44. Xie, L. S.; Skorupskii, G.; Dincă, M., Electrically Conductive Metal–Organic Frameworks. *Chem. Rev.* **2020,** *120* (16), 8536-8580.

45. Sindhu, P.; Ananthram, K. S.; Jain, A.; Tarafder, K.; Ballav, N., Insulator-to-metal-like transition in thin films of a biological metal-organic framework. *Nat. Commun.* **2023,** *14* (1), 2857.

46. Zacher, D.; Yusenko, K.; Bétard, A.; Henke, S.; Molon, M.; Ladnorg, T.; Shekhah, O.; Schüpbach, B.; de los Arcos, T.; Krasnopolski, M., Liquid-Phase Epitaxy of Multicomponent Layer-Based Porous Coordination Polymer Thin Films of $[M(L)(P)_{0.5}]$ Type: Importance of Deposition Sequence on the Oriented Growth. *Chem. Eur. J.* **2011,** *17* (5), 1448-1455.

47. Wang, Z.; Liu, J.; Lukose, B.; Gu, Z.; Weidler, P. G.; Gliemann, H.; Heine, T.; Wöll, C., Nanoporous designer solids with huge lattice constant gradients: multiheteroepitaxy of metal–organic frameworks. *Nano letters* **2014,** *14* (3), 1526-1529.

48. Zhuang, J.-L.; Kind, M.; Grytz, C. M.; Farr, F.; Diefenbach, M.; Tussupbayev, S.; Holthausen, M. C.; Terfort, A., Insight into the Oriented Growth of Surface-Attached Metal–Organic Frameworks: Surface Functionality, Deposition Temperature, and First Layer Order. *J. Am. Chem. Soc.* **2015,** *137* (25), 8237-8243.

49. Prasoon, A.; Dhara, B.; Roy, D.; Rana, S.; Bhand, S.; Ballav, N., Achieving current rectification ratios $\geq 10^5$ across thin films of coordination polymer. *Chem. Sci.* **2019,** *10* (43), 10040-10047.

50. Sindhu, P.; Ballav, N., Thin Films of MOF-on-Guest@MOF: A Simple Strategy of Designing Electronic Heterostructures. *Inorg. Chem.* **2023,** *62* (28), 10887-10891.

Emergent Interface in Heterostructured Thin Films of Cu(II) and Cu(I) Coordination Polymers

Author: Pooja Sindhu, Anupam Prasoon, Shammi Rana, et al
Publication: Journal of Physical Chemistry Letters
Publisher: American Chemical Society
Date: Aug 1, 2020

PERMISSION/LICENSE IS GRANTED FOR YOUR ORDER AT NO CHARGE

This type of permission/license, instead of the standard Terms and Conditions, is sent to you because no fee is being charged for your order. Please note the following:

- Permission is granted for your request in both print and electronic formats, and translations.
- If figures and/or tables were requested, they may be adapted or used in part.
- Please print this page for your records and send a copy of it to your publisher/graduate school.
- Appropriate credit for the requested material should be given as follows: "Reprinted (adapted) with permission from {COMPLETE REFERENCE CITATION}. Copyright {YEAR} American Chemical Society." Insert appropriate information in place of the capitalized words.
- One-time permission is granted only for the use specified in your RightsLink request. No additional uses are granted (such as derivative works or other editions). For any uses, please submit a new request.

If credit is given to another source for the material you requested from RightsLink, permission must be obtained from that source.

BACK CLOSE WINDOW

Thin Films of MOF-on-Guest@MOF: A Simple Strategy of Designing Electronic Heterostructures

Author: Pooja Sindhu, Nirmalya Ballav
Publication: Inorganic Chemistry
Publisher: American Chemical Society
Date: Jul 1, 2023

PERMISSION/LICENSE IS GRANTED FOR YOUR ORDER AT NO CHARGE

This type of permission/license, instead of the standard Terms and Conditions, is sent to you because no fee is being charged for your order. Please note the following:

- Permission is granted for your request in both print and electronic formats, and translations.
- If figures and/or tables were requested, they may be adapted or used in part.
- Please print this page for your records and send a copy of it to your publisher/graduate school.
- Appropriate credit for the requested material should be given as follows: "Reprinted (adapted) with permission from {COMPLETE REFERENCE CITATION}. Copyright {YEAR} American Chemical Society." Insert appropriate information in place of the capitalized words.
- One-time permission is granted only for the use specified in your RightsLink request. No additional uses are granted (such as derivative works or other editions). For any uses, please submit a new request.

If credit is given to another source for the material you requested from RightsLink, permission must be obtained from that source.

BACK CLOSE WINDOW

Charge-transfer interface of insulating metal-organic frameworks with metallic conduction

Author: Pooja Sindhu et al

Publication: Nature Communications

Publisher: Springer Nature

Date: Dec 12, 2022

Insulator-to-metal-like transition in thin films of a biological metal-organic framework

Author: Pooja Sindhu et al

Publication: Nature Communications

Publisher: Springer Nature

Date: May 19, 2023